Inaugural dissertation

for

obtaining the doctoral degree

of the

Combined Faculty of Mathematics, Engineering and Natural Sciences

of the

Ruprecht - Karls - University

Heidelberg

Presented by

M.Sc. Sarina Norell

born in: Heilbronn, Germany

Oral examination: 22.07.2022

The regulation of kinetochore capturing *versus* spindle stabilization by Slk19

Referees: Prof. Dr. Michael Brunner

PD Dr. Johannes Lechner

Table of contents

Abbreviations

α-factor	alpha factor
aa	amino acid
ADE	adenine
AID	auxin-induced degradation
AMCA	aminomethylcoumarin acetate
APC	anaphase promoting complex
APS	ammonium persulfate
APTES	3-aminopropyltriethoxysilane
atKT	attached kinetochore
ATP	adenosine triphosphate
Biotin-PEG-NHS	alpha-biotin-omega-carboxy succinimidyl ester polyethylene glycol
bp	base pair
cc	coiled coil
CEN	centromere
CFP	cyan fluorescent protein
ChIP	chromatin immunoprecipitation
CIAP	calf intestinal alkaline phosphatase
CL	C-terminal loop (of Stu1)
CLASP	cytoplasmic linker–associated protein
CoIP	co-immunoprecipitation
CSM	complete supplement mixture
C-terminus	carboxyl-terminus (-COOH)
D3	domain three (of Stu1)
D4	domain four (of Stu1)
DNA	deoxyribonucleic acid
dNTP	deoxynucleotide triphosphate
DTT	dithiothreitol
E. coli	Escherichia coli
EDTA	ethylenediaminetetraacetic acid
EGTA	ethylene glycol-bis(β-aminoethyl ether)-N,N,N′,N′-tetraacetic acid

FEAR	Cdc14 early anaphase release
GD	globular domain
GFP	green fluorescent protein
GTP	guanosine triphosphate
GDP	guanosine diphosphate
HEAT	huntingtin, elongation factor 3 (EF3), protein phosphatase 2A (PP2A), target of rapamycin 1 (TOR1)
HEPES	4-(2-hydroxyethyl)-1-piperazineethanesulfonic acid
HRP	horseradish peroxidase
IAA	indole acetic acid
IDPR	two long intrinsically disordered protein regions
ipMT	interpolar microtubule
kMT	kinetochore microtubule
KT	kinetochore
MAP	microtubule-associated protein
MBD	microtubule-binding domain
MC/C buffer	methylcellulose/β-casein buffer
MEN	mitotic exit network
MeO-PEG-NHS	alpha-Methoxy-omega-carboxylic acid succinimidyl ester polyethylene glycol
Met	methionine
ML	middle loop
mpH2O	millipore water
MT	microtubule
NFM	non-fluorescent media
nrMT	nuclear random microtubule
N-terminus	amino-terminus ($-NH_2$)
Nz	nocodazole
o/n	overnight
PAGE	polyacrylamide gel electrophoresis
PBS	phosphate buffered saline
PBST	phosphate-buffered saline/Tween®

PCR	polymerase chain reaction
PEG	polyethylene glycol
PLD	prion-like domain
PMSF	phenylmethylsulfonyl fluoride
PNK	T4 polynucleotide kinase
PVDF	polyvinylidene fluoride
qPCR	quantitative PCR
RE	restriction enzyme
Rho	rhodamine
RT	room temperature
S. cerevisiae	*Saccharomyces cerevisiae*
SAC	spindle assemby checkpoint
SC	synthetic complete
SDC	synthetic dextrose complete
SDS	sodium dodecyl sulfate
SPB	spindle pole body
S. pombe	*Schizosaccharomyces pombe*
ssSTD	single stranded salmon testes DNA
TACC	transforming acid coiled coil
TEMED	N,N,N′,N′-tetramethylethylene-diamine
TOG	tumor overexpressed gene
TOGL	TOG-like
uaKT	unattached kinetochore
Ura	uracil
vs.	*versus*
WCE	whole cell extract
WT	wild type
YPD	yeast extract peptone dextrose

Summary

Slk19 (**S**ynthetic **L**ethal with **K**ar3) is a non-essential protein in *Saccharomyces cerevisiae* with multiple functions during the cell cycle required for error-free chromosome segregation in mitosis (Pfiz et al., 2002). Slk19 localizes to attached kinetochores (atKTs) throughout the cell cycle and localizes to the spindle midzone in anaphase (Zeng et al., 1999). Slk19 together with the microtubule (MT) rescue factor Stu1 efficiently sequesters at unattached KTs (uaKTs) (Funk et al., 2014),(Ortiz et al., 2009),(Kolenda et al., 2018). The interdependent sequestering of the two proteins results in their withdrawal from the spindle and to a reorganization of the MT network, which facilitates KT capturing (Kolenda et al., 2018). Whether KT-bound Slk19 is involved in initiating this sequestering process is so far unclear. There have been several indications that Slk19 must play a role for metaphase spindle stability (Zeng et al., 1999),(Ye et al., 2005),(T. Zhang et al., 2006),(Richmond et al., 2013). However, whether Slk19 can localize to the metaphase spindle per se and what exact function it has at the spindle was also so far unknown. This study should shed more light on these aspects. Furthermore, Slk19 is a component of the Cdc**14** **E**arly **A**naphase **R**elease (FEAR) pathway and thus is involved in the formation of the anaphase midzone and anaphase spindle stabilization (Sullivan et al., 2001),(Stegmeier et al., 2002),(Khmelinskii et al., 2007). At the meta-to-anaphase transition, binding of Stu1 at the anaphase spindle switches from a binding via the microtubule-binding domain (MBD) to a (probably indirect) binding via the domain 4 (D4) (Funk et al., 2014). So far, it is not known how this altered binding mode is achieved and whether the FEAR function of Slk19 might regulate the D4-mediated Stu1 binding in anaphase.

This study is focused on the questions below and led to new valuable insights into the Slk19 functions for KT capturing, spindle stabilization and possible regulation mechanisms summarized in the following:

What is the role of Slk19 in the sequestering process?

- There are at least two prerequisites for Slk19 for functional sequestering at uaKTs: 1) Slk19-Stu1 interaction and 2) Slk19-Slk19 homotetramerization. Slk19 is a protein with 821 amino acid (aa) residues and seven predicted coiled coil (cc) domains (referred to as cc1-7). It was found here, that two Slk19 domains are essential for sequestering: the C-terminus (cc6+7, aa 709–821) and the cc1 domain (aa 300–410). Both domains were shown to contribute to Stu1 interaction, while the C-terminus is required for Slk19 tetramerization and for its KT localization.
- A minimal Slk19 construct, consisting only of the C-terminus (cc6+7) and the cc1+2 domain (aa 300–502), was sufficient to restore the sequestering process at uaKTs, while the C-terminus alone was not. Thus, both domains are essential and sufficient for sequestering.

- Spc105 was determined as the KT protein that mediates the basal Slk19 binding at uaKTs. However, whether this basal Slk19 binding at uaKTs is required for the initiation of the sequestering process could not be finally clarified.

What functional role does Slk19 have for metaphase spindle stabilization?

The data obtained in this study suggest that Slk19 contributes to increased interpolar MT (ipMT) crosslinking and spindle stabilization by enhancing the binding of Stu1 and of the MT-crosslinking protein Ase1 at the metaphase spindle overlaps. Thus, tetrameric Slk19 might promote protein network formation specifically stabilizing ipMT overlaps of metaphase spindles. This hypothesis is based on the following results of this study:

- Slk19 does not possess an intrinsic MT binding activity but can efficiently bind to MTs via prebound Stu1 or Ase1 *in vitro*. Also *in vivo*, Slk19 localization to the metaphase spindle depends on Ase1 and Stu1.
- Slk19 localizes to the center of the metaphase spindle rather than along the complete spindle, indicative for a localization specifically at the ipMT overlaps.
- Slk19 enhances Ase1 and Stu1 amounts at the spindle *in vivo* and at MTs *in vitro*.
- Ase1 as well as Stu1 can both bind and crosslink MTs by themselves *in vitro* (Schuyler et al., 2003),(Funk et al., 2014). Slk19 can enhance this MT crosslinking when incubated together with Stu1 or Ase1, while Slk19 alone could not crosslink MTs.
- Absence of Slk19 from metaphase spindles results in defective ipMT overlaps as assessed by reduced tubulin levels at the spindle center, increased appearance of long unaligned nuclear MTs and by altered Ase1 and Stu1 localizations at the ipMT overlaps.

Is Slk19 localization at the metaphase spindle tension-regulated?

It was found here, that Slk19 amounts at the metaphase spindle center are increased in situations with high tension and decreased in situations with low/no tension at the KTs and the spindle. Thus, the results suggest a tension-regulated mechanism controlling Slk19 spindle localization according to demand.

Can Slk19 confer MBD-independent Stu1 binding to the anaphase midzone?

Slk19 promotes the midzone localization of Stu1 by two distinct mechanisms, a FEAR-dependent and a FEAR-independent mechanism:

- The FEAR function of Slk19 (Cdc14 release) plays a dual role for the midzone formation in anaphase. Firstly, released Cdc14 is required for the formation of a centered and restricted overlap zone (via Ase1 dephosphorylation) to which Stu1 preferentially binds (Khmelinskii et al., 2007). Here, it was shown that the physical presence of Slk19 at the spindle is not required for this function. Secondly, released Cdc14 is required to promote D4-mediated Stu1 binding at the midzone.
- Physical presence of Slk19 at the anaphase spindle is required in a direct manner for D4-mediated Stu1 binding at the midzone in addition to the FEAR pathway. Possibly, Slk19 directly or indirectly interacts with D4 of Stu1 at the midzone (enabled by Cdc14).

Zusammenfassung

Slk19 (**S**ynthetisch **L**etal mit **K**ar3) ist ein nicht-essentielles Protein in *Saccharomyces cerevisiae* mit mehreren Funktionen im Zellzyklus, das für eine fehlerlose Chromosomensegregation in der Mitose benötigt wird (Pfiz et al., 2002). Slk19 lokalisiert während des gesamten Zellzyklus an den Kinetochoren (KTs) und in Anaphase an der Spindelmittelzone (Zeng et al., 1999). Slk19 sequestriert effizient mit dem Mikrotubuli (MT)-Rettungsfaktor Stu1 an unangehefteten Kinetochoren (uaKTs) (Funk et al., 2014),(Ortiz et al., 2009),(Kolenda et al., 2018). Die voneinander abhängige Sequestrierung der beiden Proteine führt zu deren Entzug von der Spindel und zu einer Reorganisation des Mikrotubuli-Netzwerks, welches das Einfangen von uaKTs erleichtert (Kolenda et al., 2018). Ob KT-gebundenes Slk19 an der Initiierung dieser Sequestrierung beteiligt ist, ist bisher unklar. Es gibt mehrere Hinweise darauf, dass Slk19 eine Rolle für die Metaphasenspindel-Stabilität spielen muss (Zeng et al., 1999),(Ye et al., 2005),(Zhang et al., 2006),(Richmond et al., 2013). Ob Slk19 aber per se an der Metaphasenspindel binden kann und welche genaue Funktion es an der Spindel hat, war bisher unbekannt. Diese Arbeit soll diese Aspekte näher beleuchten. Des Weitern ist Slk19 eine Komponente des Cdc**14** **E**arly **A**naphase **R**elease (FEAR) Signalwegs und ist somit an der Bildung der Spindelmittelzone und der Spindelstabilisierung in Anaphase beteiligt (Sullivan et al., 2001),(Stegmeier et al., 2002),(Khmelinskii et al., 2007). Beim Übergang von Meta- zu Anaphase wechselt Stu1 die Art der Spindelbindung von einer Bindung über die Mikrotubuli-bindende Domäne (MBD) zu einer (wahrscheinlich indirekten) Bindung über die Domäne 4 (D4) (Funk et al., 2014). Bisher ist nicht bekannt, wie diese veränderte Bindung erreicht wird und ob die FEAR-Funktion von Slk19 die D4-vermittelte Stu1-Bindung in Anaphase regulieren könnte.

Diese Arbeit konzentriert sich auf die folgenden Fragen und führte zu neuen wertvollen Einblicken in die Slk19-Funktionen für das Einfangen von KTs, die Spindelstabilisierung und mögliche Regulationsmechanismen, welche im Folgenden zusammengefasst sind:

Welche Rolle spielt Slk19 im Sequestrierungsprozess?

- Es gibt mindestens zwei Voraussetzungen für Slk19 für die Sequestrierung an uaKTs: 1) Slk19-Stu1 Interaktion und 2) Slk19-Slk19 Homotetramerisierung. Slk19 ist ein Protein mit 821 Aminosäure (aa)-Resten und sieben vorhergesagten Coiled-Coil (cc)-Domänen (als cc1-7 bezeichnet). Es stellte sich heraus, dass zwei Slk19-Domänen für die Sequestrierung essentiell sind: der C-Terminus (cc6+7, aa 709–821) und die cc1-Domäne (aa 300–410). Beide Domänen tragen zur Stu1-Interaktion bei, während der C-Terminus für die Slk19-Tetramerisierung und KT-Lokalisierung erforderlich ist.
- Ein minimales Slk19-Konstrukt, das nur aus dem C-Terminus (cc6+7) und der cc1+2-Domäne (aa 300–502) bestand, war ausreichend, um die Sequestrierung an uaKTs wiederherzustellen während der C-Terminus allein nicht ausreichend war. Somit sind beide Domänen für die Sequestrierung ausreichend und zugleich unerlässlich.

- Spc105 wurde als das KT-Protein identifiziert, welches die basale Slk19-Bindung an uaKTs vermittelt. Ob diese basale Slk19-Bindung an uaKTs jedoch für die Initiierung des Sequestrierungsprozesses erforderlich ist, konnte nicht abschließend geklärt werden.

Welche funktionelle Rolle spielt Slk19 für die Stabilisierung der Metaphasenspindel?

Die Daten dieser Arbeit deuten darauf hin, dass Slk19 zu einer erhöhten Vernetzung von interpolaren MT (ipMT) und Spindelstabilisierung beiträgt, indem es die Bindung von Stu1 und des MT-vernetzenden Proteins Ase1 an der Metaphasenspindel erhöht. Das Tetramer Slk19 könnte die Bildung von Proteinnetzwerken fördern, welche die ipMT-Überlappungen stabilisieren. Diese Hypothese basiert auf folgenden Ergebnissen dieser Arbeit:

- Slk19 besitzt keine intrinsische MT-Bindungsaktivität, kann aber über vorgebundenes Stu1 oder Ase1 *in vitro* effizient an MTs binden. Auch *in vivo* ist die Lokalisierung von Slk19 an der Metaphasenspindel von Ase1 und Stu1 abhängig.
- Slk19 lokalisiert eher im Zentrum der Metaphasenspindel als entlang der gesamten Spindel, was auf eine Lokalisierung spezifisch an den ipMT-Überlappungen hindeutet.
- Slk19 erhöht die Ase1- und Stu1-Mengen an der Spindel *in vivo* und an MTs *in vitro*.
- Sowohl Ase1 als auch Stu1 können *in vitro* an MTs binden und diese vernetzen (Schuyler et al., 2003),(Funk et al., 2014). Slk19 kann diese MT-Vernetzung verstärken, wenn es zusammen mit Stu1 oder Ase1 inkubiert wird. Slk19 allein führte zu keiner Vernetzung.
- Fehlendes Slk19 an den Spindeln führte zu defekten ipMT-Überlappungen, was durch verringertes Tubulin im Spindelzentrum, vermehrtes Auftreten langer, unausgerichteter nukleärer MTs und veränderten Ase1- und Stu1-Lokalisationen an ipMTs gezeigt wurde.

Wird die Slk19-Lokalisation an der Metaphasenspindel durch Spannung reguliert?

Die Slk19-Mengen im Zentrum der Metaphasenspindel waren in Situationen mit hoher Spannung am KT und der Spindel erhöht und in Situationen mit geringer/keiner Spannung verringert. Die Ergebnisse deuten somit auf einen spannungsregulierten Mechanismus hin, der die Lokalisierung von Slk19 an der Spindel je nach Bedarf steuern kann.

Kann Slk19 eine MBD-unabhängige Stu1-Bindung an die Mittelzone vermitteln?

Slk19 fördert die Lokalisierung von Stu1 in der Mittelzone durch zwei unterschiedliche Mechanismen, einen FEAR-abhängigen und einen FEAR-unabhängigen Mechanismus:

- Die FEAR-Funktion von Slk19 (Cdc14-Freisetzung) spielt eine doppelte Rolle für die Bildung der Mittelzone in Anaphase. Erstens wird Cdc14 für die Bildung einer zentrierten und kompakten Überlappungszone benötigt (über Ase1-Dephosphorylierung), an die Stu1 bindet (Khmelinskii et al., 2007). Es konnte hier gezeigt werden, dass die Präsenz von Slk19 an der Spindel hierfür nicht nötig ist. Zweitens ist Cdc14 erforderlich, um die D4-vermittelte Stu1-Bindung an der Mittelzone zu fördern.
- Anwesenheit von Slk19 an der Anaphasenspindel ist, zusätzlich zu FEAR, direkt für die D4-vermittelte Stu1-Bindung an der Mittelzone erforderlich. Möglicherweise interagiert Slk19 direkt oder indirekt mit D4 von Stu1 in der Mittelzone (ermöglicht durch Cdc14).

1 Introduction

1.1 The importance of accurate chromosome segregation

One of the most essential characteristics of all living organisms is the ability of cell division and passing on hereditary information via chromosome segregation (separation of duplicated sister chromatids). Chromosome segregation occurs during the process of mitosis, which is finalized by cytokinesis, creating two new daughter cells with identical genetic information. The described principle of cell division is the most basic form of reproduction in form of binary fission and is found in many unicellular organisms, e.g. in prokaryotes such as bacteria and archaea (Margolin, 2005),(Bernander & Ettema, 2010). In multicellular organisms, cell division and the associated chromosome segregation is required for the creation of an entire organism starting from only one single cell.

Chromosome segregation is a precisely regulated and timely coordinated process and any kind of defect during this step can lead to severe genomic damages and chromosomal aberrations. In humans, for example, defective chromosome segregation can lead to aneuploidy and severe congenital malformations. Aneuploidy often causes chromosomal instability (CIN) and *vice versa* CIN can reinforce aneuploidy. These events can eventually lead to cell death or carcinogenesis (Weaver & Cleveland, 2006),(Mcclelland & Mcclelland, 2017),(Lengauer et al., 1997),(Thompson & Compton, 2008),(Ganem et al., 2009), (Duesberg et al., 1998),(Thompson et al., 2010),(Chandhok & Pellman, 2009),(Holland & Cleveland, 2009),(Orr & Compton, 2013). Indeed, chromosomal abnormalities are a common characteristic of cancer cells (Hanahan & Weinberg, 2011),(Yoon et al., 2002), (Haruki et al., 2001) and can be caused by defects in cell cycle checkpoints, instability of the mitotic spindle or defective microtubule (MT) attachments at the kinetochores (KTs) (Thompson & Compton, 2008),(Cimini et al., 2001),(Bakhoum et al., 2009),(Silkworth et al., 2009),(D. J. Gordon et al., 2012).

Basic research on the molecular processes occurring during chromosome segregation, including their key players and their spatial and temporal regulation, is a prerequisite for a deeper understanding of how accurate distribution of genetic material is ensured. Furthermore, it paves the way for future research aimed at new cancer treatments and improved diagnostics. This work aimed to contribute to the understanding of conserved mechanisms of chromosome segregation.

1.2 *Saccharomyces cerevisiae* as model organism

To study the conserved mechanisms of chromosome segregation, the model organism *Saccharomyces cerevisiae* (short: *S. cerevisiae* or budding yeast) was chosen. *S. cerevisiae* is a widely used unicellular eukaryotic model organism and is taxonomically assigned to the kingdom of fungi. Budding yeast is one of the most intensively studied model organisms and

its genome was the first eukaryotic genome to be fully sequenced (Engel et al., 2014). Many critical proteins are conserved between humans and yeast and it was shown that human orthologous can even replace 47 % of the tested essential yeast genes (Kachroo et al., 2015). It was also shown that approximately 30 % of disease related genes in humans have orthologues in *S. cerevisiae* (Foury, 1997). The functional conservation of proteins between human and yeast cells makes *S. cerevisiae* an optimal model organism for protein function analyses in different pathways.

S. cerevisiae reproduces via budding. Budding is a process of asymmetric cell division, creating one new smaller daughter cell besides the aging mother cell. One mother cell can undergo the process of budding approximately 20–25 times before the cell dies (Mortimer & Johnston, 1959). Unbudded cells of *S. cerevisiae* have a diameter of approximately 5 µm and are easy to examine by microscopy. Under optimal conditions, budding yeast has a doubling time of 100–120 min (Hartwell, 1974), which allows fast culturing of cell populations. In contrast, human cells divide every 24 h depending on the specific cell type (24 h is referred to as a rapidly proliferating cell) (Cooper, 2000b).

There are two viable forms of *S. cerevisiae*: cells with either a haploid or a diploid chromosome set. Both forms can grow and reproduce via budding. Under stress conditions, e.g. nutrient deprivation, haploid cells eventually die, while diploid cells can undergo meiosis and thus create haploid spores within their cytoplasm, a process called sporulation (Freese et al., 1982),(Neiman, 2005). In laboratory conditions, the haploid form is often used for genetic analyses since genetic manipulations are easily implemented and comparatively cost-effective.

S. cerevisiae has two types of sexual differentiation called mating type a and mating type α. Haploid cells with mating type a can only mate with haploid α-cells and *vice versa*. Cells with opposite mating types differ from each other in the gene expression of certain proteins and peptides. The different expressional programs are determined by two different mating type alleles MATa (encodes a1 gene) and MATα (encodes α1 and α2 genes). Cells with the mating type α produce a mating pheromone called alpha factor (α-factor) to attract cells with the mating type a in the surrounding (and *vice versa*). Cells respond to pheromone signals by growing a cell projection called “shmoo” towards the source to the signal, which enables mating. Mating can only take place in early G1 phase of the cell cycle (Hartwell, 1974) and cells arrest in this phase in presence of the mating pheromone (Bücking-Throm et al., 1973). Laboratory yeast strains are mostly haploid a-cells that can respond to α-factor (13 amino acid (aa) peptide). Treatment with α-factor is often utilized to achieve a synchronized cycling cell population after release from this reversible G1 arrest. The a-cells express a protease called Bar1 that allows α-factor cleavage and thus recovery from the α-factor induced arrest. Thus, the BAR1 gene is deleted in most laboratory yeast strains to allow an effective α-factor arrest.

Moreover, *S. cerevisiae* can switch its mating type by a gene conversion event. This is highly regulated and performed via a deoxyribonucleic acid (DNA) endonuclease encoded by the

HO-gene. Therefore, the HO-gene is mostly altered in laboratory yeast strains to prevent the mating type switch and to maintain a homogenous haploid cell population (Meiron et al., 1995).

1.3 The budding yeast cell cycle

1.3.1 Overview over the cell cycle stages

The cell cycle is roughly divided into four phases: the first gap phase (G1), the synthesis phase (S-phase), the second gap phase (G2) and mitosis phase (M-phase). In mammalian cells, the G1-, S- and G2-phase are collectively referred to as interphase, which makes up 95 % of the cell cycle and separates two consecutive mitotic events (Cooper, 2000b). During interphase, RNA and protein expression as well as DNA replication occurs and cells grow in size (Harper & Brooks, 2005). In most eukaryotes, the start of M-phase is characterized by the breakdown of the nuclear envelope (Alberts et al., 2002). In contrast, budding yeast performs a closed mitosis during which the nuclear envelope stays fully intact (Boettcher & Barral, 2013). Therefore, there is no strictly characterized boundary between G2 and onset of mitosis and the phases are often collectively referred to as G2/M-phase. Notably, the transition between the different cell cycle stages must be tightly regulated to ensure accurate chromosome segregation and cell division. Thus, surveillance mechanisms have evolved that control each critical step of the cell cycle and, if necessary, halt the cell cycle until impediments are resolved. Figure I-1 shows an overview over the budding yeast cell cycle.

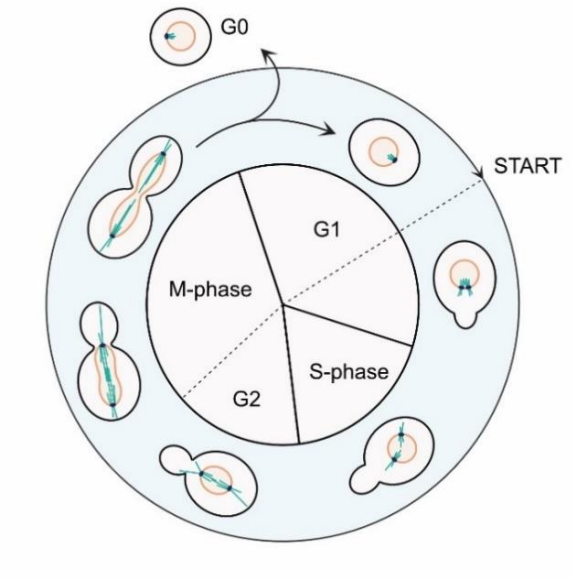

Figure I-1: Phases of the budding yeast cell cycle. Figure is based on (Winey & O'Toole, 2001) and (Hartwell, 1974). The budding yeast cell cycle is divided into four phases: the first gap phase (G1), the synthesis phase (S-phase), the second gap phase (G2) and mitosis phase (M-phase).

G1-phase:

In G1, budding yeast cells grow in size and volume. The cell cycle "START" is defined by activation of Cdc28 (the sole budding yeast cyclin-dependent kinase (Cdk)) associated with the G1 cyclins Cln1, Cln2 and Cln3 (cell cycle regulation by Cdk and cyclins described in more detail below, chapter 1.3.2) (Hartwell, 1974),(Cross, 1995),(Schneider et al., 1998). At this point cells are committed to the cell cycle and processes such as bud emergence and actin cytoskeleton assembly take place in late G1 (Daniel J Lew, 2003). During G1, the spindle pole body (SPB) duplication is initiated by the formation of a new SPB precursor, the satellite. The duplicated SPBs eventually separate during S-phase (Byers & Goetsch, 1975),(reviewed in Jaspersen & Winey, 2004). This separation to the opposite poles constitutes the basis for the establishment of a bipolar mitotic spindle (see chapter 1.4.3.3) and is especially important for accurate chromosome segregation. The budding yeast morphogenesis checkpoint monitors and coordinates the events of bud formation and delays the onset of mitosis and nuclear division until bud formation was successful. Thus, the morphogenesis checkpoint also prevents the accumulation of multiple nuclei in the cell (Daniel J Lew, 2003).

S-phase:

In S-phase, DNA replication takes place. To guarantee that DNA replication takes place only once per cell cycle, this process is controlled by several conserved proteins (Nishitani & Lygerou, 2002). A so called pre-replicative complex (Diffley et al., 1994), consisting of the origin recognition complex (ORC), Ctd1, Cdc6 and the minichromosome maintenance (MCM) complex, is assembled at the replication origins in G1 and thereby the replication origins become "licensed" for the next round of replication. The MCM complex possesses a helicase function and leaves the origins of replication associated with a post-replicative complex after replication (consisting of less components than the pre-replicative complex). Thus, the replication origins become "unlicensed" until the end of mitosis (Labib et al., 2000),(Diffley et al., 1994),(Nishitani & Lygerou, 2002). Additionally, increasing Cdc28 activity in S-Phase is required to initiate replication and high Cdc28 activity in G2 inhibits extra rounds of DNA replication. Cdc6 expression as well as Sic1 expression increases again at the end of mitosis resulting in downregulation of Cdc28 and this prepares a new round of replication for the next cell cycle (Calzada et al., 2001).

Moreover, the genome must be duplicated precisely and completely prior to mitosis to ensure genome integrity. Replication stress, such as DNA lesions, breakage or recombination are sensed by the DNA replication checkpoint (DRC) or the DNA damage checkpoint (DDC) that delay the cell cycle until errors are corrected (Pardo et al., 2017), (Jossen & Bermejo, 2013). The DRC is especially important during DNA replication in S-phase, while the DDC is important during the complete cell cycle. S-phase is followed by the G2/M-phase in which cells grow further and undergo mitosis.

Mitosis:

Mitosis is divided into four consecutive phases: prometa-, meta-, ana- and telophase. During budding yeast mitosis and most of the cell cycle, chromosomes are attached to MTs via the KT (MTs originate from two opposing spindle pole bodies, described in more detail in chapter 1.4.3). Only during replication of the centromeric region in S-Phase, KTs are transiently detached from MTs and must be recaptured again after KT reassembly in prometaphase (Kitamura et al., 2007). The spindle assembly checkpoint (SAC) halts the progression of the cell cycle until all uaKTs are captured, while the tension checkpoint ensures the bipolar orientation of KT attachments prior to anaphase onset (M. Andrew Hoyt et al., 1991),(T. U. Tanaka et al., 2002). As soon as all duplicated sister chromatids are bipolarly attached to MTs in metaphase and a bipolar metaphase spindle is established, anaphase is initiated by removal of cohesions that hold sister chromatids together (Uhlmann et al., 1999). During anaphase A, the sister chromatids are pulled to the opposite poles by shortening of the kinetochore microtubules (kMTs), while during anaphase B the spindle elongates and slides apart (Kahana et al., 1995). Simultaneously, also the nucleus elongates and migrates through the bud neck. The correct positioning of the mitotic spindle and the migration of one spindle pole through the mother-bud neck is especially important, since defects in this step might result in chromosome segregation errors and aneuploidy. Therefore, the spindle position checkpoint (SPOC) senses unaligned spindles and inhibits the mitotic exit until the spindle is in the correct position (Caydasi et al., 2010). Moreover, sister chromatids need to be fully separated before abscission (cell cleavage) to prevent chromosome breakage. Therefore, the NoCut checkpoint senses the appearance of chromatin bridges at the midzone in anaphase in budding yeast (Norden et al., 2006) and prevents premature abscission until chromosomes are completely segregated. As soon as the spindle is correctly positioned at the mother-bud axis and all chromosomes are accurately segregated, the cytokinesis is finalized in telophase and the abscission eventually gives rise to a new daughter cell (reviewed in Johnson & Walker, 2003). After cell division, cells can either undergo the next cell cycle or go into quiescent phase (G0) dependent on stress and nutrient conditions, e.g. availability of carbon source or other factors (Hartwell, 1974).

1.3.2 Cell cycle events are regulated by a single Cdk and associated cyclins

In general, the cell cycle is a timely coordinated sequence of processes including altering gene-expression patterns, the activity of kinases and opposing phosphatases as well as controlled protein degradation.

The cell cycle in budding yeast is regulated by one single cyclin-dependent kinase (Cdk) called Cdc28 (Cdk1 in other eukaryotes) (Nasmyth, 1993). Cdc28 is activated by associating with different cell cycle specific cyclins and regulates various processes throughout the cell cycle (reviewed in Bloom & Cross, 2007). In G1-phase, the cyclins Cln1, Cln2 and Cln3

are expressed and regulate processes such as bud morphogenesis (D J Lew & Reed, 1993) and SPB duplication (Kovacs et al., 2008). B-type cyclins (Clb) regulate processes in S-phase as well as mitotic events and are activated by G1-phase cyclins (reviewed in Nasmyth, 1996 and Bloom & Cross, 2007). The early expressed B-type cyclins Clb5 and Clb6 are required for DNA replication in S-Phase (Epstein & Cross, 1992),(Schwob & Nasmyth, 1993) and the B-type cyclins Clb1–4 are required for mitotic functions such as spindle formation and cytokinesis (Fitch et al., 1992). The exit from mitosis and the completion of the cell cycle requires the degradation of the B-type cyclins, which are substrates of the anaphase promoting complex (APC) (APC described in detail in part 1.3.3.1) (R. Visintin et al., 1998),(Zachariae et al., 1998), (Thornton & Toczyski, 2003).

Besides Cdc28, there are also other mitotic kinases that regulate the progression of the cell cycle such as the spindle assembly checkpoint (SAC) kinase Mps1 (described within SAC in part 1.4.2.1) (Jones et al., 1999), the tension checkpoint kinase Ipl1 (Biggins & Murray, 2001), the kinase Bub1 (Robertst et al., 1994) (component of the SAC and tension checkpoint, described in more detail in part 1.4.2.2) and the polo-like kinase Cdc5 (described within the FEAR pathway in part 1.3.3.3)(Kitada et al., 1993). The action of these kinases is counteracted in the course of the cell cycle by opposing phosphatases such as Cdc14 (R. Visintin et al., 1998), Glc7 (Z. Feng et al., 1991) or PP2A (Sneddon et al., 1990).

1.3.3 The delicate process of meta-to-anaphase transition

Anaphase onset is a strictly regulated irreversible step of the cell cycle and is initiated by the activation of a caspase-related protease named separase (Esp1 in budding yeast) (Uhlmann et al., 2000). Once activated, Esp1 induces anaphase onset by cleaving the cohesion subunit Scc1/Mcd1 that holds sister chromatids together. This cleavage is an irreversible step of the cell cycle that initializes anaphase by promoting the separation and poleward movement of the sister chromatids (Uhlmann et al., 1999),(Uhlmann et al., 2000). Securin (Pds1 in budding yeast) functions as inhibitor of Esp1 until anaphase onset (Cohen-Fix et al., 1996),(Ciosk et al., 1998).

1.3.3.1 The anaphase promoting complex (APC)

The anaphase promoting complex/cyclosome is a large protein complex with over thirteen subunits functioning as E3-ubiquitin-ligase and plays several important roles in cell cycle regulation (Lamb et al., 1994),(Zachariae et al., 1996),(Passmore et al., 2005). The APC targets its substrates for degradation via the 26S proteasome by polyubiquitination (reviewed in Peters, 2002). As its name already suggests, the anaphase promoting complex plays an essential role in initializing anaphase in budding yeast by mediating the degradation of Pds1 (Irniger et al., 1995),(Cohen-Fix et al., 1996). Thus, APC-dependent degradation of Pds1 activates Esp1, which in turn cleaves Scc1 and induces anaphase (Uhlmann et al., 1999)

(illustrated in Figure I-2). The APC also promotes degradation of the mitotic B-type cyclins (Clb2 and Clb5) necessary for mitotic exit (Wäsch & Cross, 2002),(Masaid Shirayama et al., 1999),(Irniger et al., 1995),(Schwab et al., 1997),(Masaki Shirayama et al., 1998).

Moreover, the APC is the main target of the SAC: If spindle assembly and attachment of KTs is disturbed, the SAC inhibits the APC and thus anaphase onset until all impediments are resolved (SAC described in more detail in chapter 1.4.2.1).

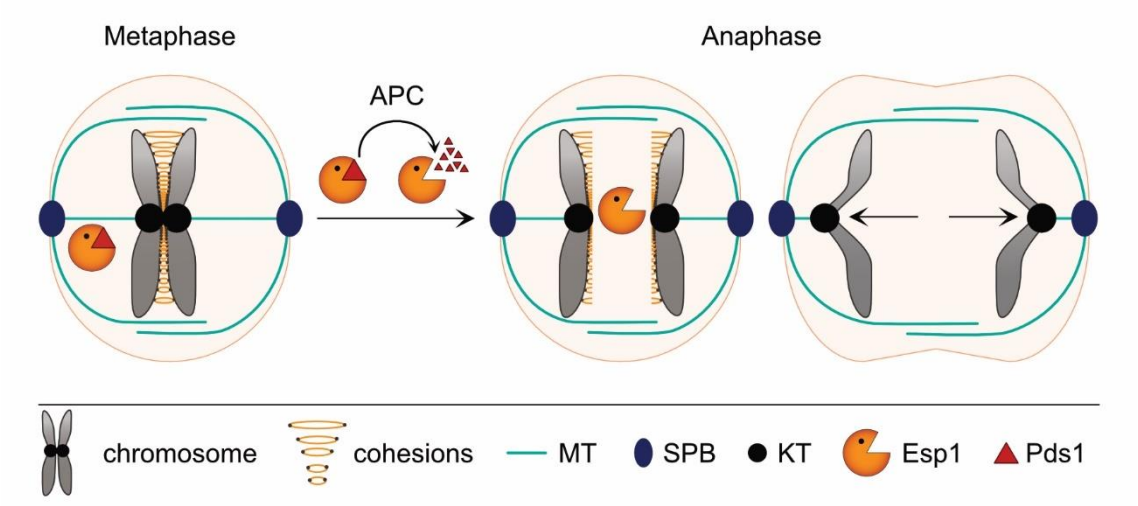

Figure I-2: Cohesion cleavage by Esp1 induces anaphase. Figure is based on (Marston, 2014). The figure illustrates the process of cohesion cleavage at the meta-to-anaphase transition. Activation of the APC results in Pds1 degradation and thus Esp1 activation. Esp1 cleaves cohesions and initiates separation of sister chromatids. APC = anaphase promoting complex, SPB = spindle pole body, KT = kinetochore.

The APC itself is also regulated by cell cycle specific factors: The two APC subunits, Cdc20 and Cdh1/Hct1, function as APC activators and associate with the APC in a cell cycle dependent manner (Rosella Visintin et al., 1997). Cdc20 and Cdh1 both confer substrate specificity of the APC in budding yeast by directly binding APC substrates (Pfleger et al., 2001). APC that is bound to its activator Cdc20 (APC^{Cdc20}) is activated by Cdc28-dependent phosphorylation (Rudner & Murray, 2000) and responsible for the described role in Pds1 degradation (Irniger et al., 1995),(Cohen-Fix et al., 1996),(reviewed in Peters, 2002). Furthermore, APC^{Cdc20} regulates spindle dynamics by degradation of the kinesin-5 Kip1 after anaphase onset (D. M. Gordon & Roof, 2001). In contrast, the APC activator Cdh1 is kept inactive by Cdc28-dependent phosphorylation in early cell cycle stages (Jaspersen et al., 1999). In early anaphase, the phosphatase Cdc14 is released (FEAR pathway described in detail below, part 1.3.3.3) and this leads to the dephosphorylation of Cdh1 (Stegmeier et al., 2002),(Jaspersen et al., 1999). Consequently, Cdh1 can bind and activate the APC (APC^{Cdh1}) (Jaspersen et al., 1999). APC^{Cdh1} leads for example to the degradation of the MT-

crosslinking protein Ase1 and the kinesin-5 Cin8 in the G1-phase of the cell cycle to promote a timely spindle disassembly (Juang et al., 1997),(Hildebrandt & Hoyt, 2001).

1.3.3.2 Regulation levels of cohesion cleavage

The described activation of Esp1 by APC-dependent degradation of Pds1 is not the only cellular mechanism that regulates the delicate process of meta-to-anaphase transition. Scc1-cleavage is additionally regulated by several distinct mechanisms:

The first level of regulation for cohesion cleavage is the regulation of the APC activity that targets Pds1 for degradation. While the kinase activity of Cdc28 leads to phosphorylation and activation of the APC^{Cdc20} (Rudner & Murray, 2000), the phosphatase $PP2A^{Cdc55}$ opposes this activating Cdc28 phosphorylation and thereby hinders premature Pds1 degradation and Scc1 cleavage (Rossio et al., 2013).

Another level of regulation is the regulation of Esp1. Cdc28-dependent phosphorylation of Esp1 activates Esp1 (in parallel to APC-dependent Pds1 degradation) and thereby promotes the cleavage of Scc1 and anaphase onset (Lianga et al., 2018). A phosphomimetic Esp1 mutant (*esp1-3D*) in combination with induced Pds1 depletion is sufficient for premature spindle elongation (Lianga et al., 2018). On the other hand, $PP2A^{Cdc55}$ counteracts the activating Cdc28-dependent phosphorylation of Esp1 to prevent anaphase initiation (Lianga et al., 2018). Moreover, it was shown that the KT- and spindle-localizing protein Slk19 has a regulatory function in inhibiting Esp1-activity. Thereby, Slk19 functions in parallel with Pds1 and $PP2A^{Cdc55}$ to prevent premature anaphase onset (Lianga et al., 2018) (illustrated in Figure I-3).

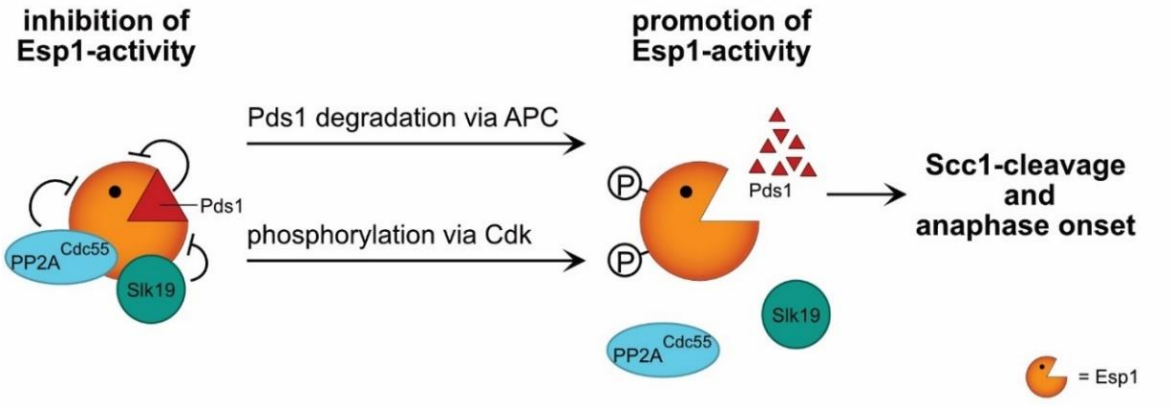

Figure I-3: Slk19 inhibits Esp1 in parallel with Pds1 and $PP2A^{Cdc55}$. Figure is based on (Lianga et al., 2018). The figure illustrates the regulation of Esp1 activity. The proteins Slk19, $PP2A^{Cdc55}$ and Pds1 inhibit Esp1 activity, while phosphorylation via Cdk and Pds1 degradation promote its activity. APC = anaphase promoting complex, Cdk = cyclin dependent kinase.

Supportingly, premature anaphase spindle elongation is induced upon Pds1-degradation in *Δcdc55* or *Δslk19* cells (Lianga et al., 2018). Pds1 depletion in *Δslk19* cells resulted in premature spindle elongation that goes along with premature Scc1-cleavage, which is not observed in *Δslk19* cells where Pds1 is present (Lianga et al., 2018). This finding indicates a premature activation of Esp1 in those cells and gives Slk19 a regulatory role for anaphase initiation (together with Pds1). The above-mentioned phosphorylation of Esp1 by Cdc28 can again oppose the Slk19-dependent inhibition of Esp1, promoting Esp1 activation (Lianga et al., 2018) (illustrated in Figure I-3). However, this is only one of the regulatory functions of Slk19 and further roles of Slk19 as component of the FEAR pathway are described below (in chapter 1.3.3.3).

A further regulatory level for cohesion cleavage is given by the activity of the polo-kinase Cdc5. Like Slk19, also Cdc5 is a component of the FEAR pathway and its FEAR functions are described in more detail below (in chapter 1.3.3.3). Cdc5 regulates cohesion cleavage by directly phosphorylating the cohesion subunit Scc1 itself (*in vivo* and *in vitro*) and thereby promoting its cleavage by Esp1 (Alexandru et al., 2001),(Hornig & Uhlmann, 2004). This direct regulation of Scc1 cleavage by Scc1 phosphorylation is a crucial regulation step for sister chromatid separation especially in cells without Pds1 (Alexandru et al., 2001).

1.3.3.3 The FEAR pathway – Cdc14 early anaphase release

Once Esp1 is fully activated and cohesion cleavage is initialized, the cell needs to regulate the next stage of the cell cycle. The Cdc-**F**ourteen **E**arly **A**naphase **R**elease (FEAR) pathway is an important cell cycle regulation step that guides the cell through anaphase and prepares mitotic exit. It is required for midzone organization, spindle stability, segregation of ribosomal DNA and nuclear positioning in anaphase (Caydasi et al., 2010)**.** The FEAR pathway leads to the transient release of the phosphatase Cdc14 from the nucleolus into the nucleus. The key players of this pathway include Esp1, Slk19, Spo12, the polo-like kinase Cdc5, PP2A and its regulatory subunit Cdc55 ($PP2A^{Cdc55}$) as well as the $PP2A^{Cdc55}$ regulators Zds1 and Zds2 (Stegmeier et al., 2002). The phosphatase Cdc14 is the key effector of the FEAR pathway due to its role in counteracting the activity of mitotic kinases (R. Visintin et al., 1998). An overview over the FEAR pathway and the functions of its components is given in Figure I-4.

During most of the cell cycle, Cdc14 is trapped in the nucleolus by its inhibitor Cfi1/Net1 (R Visintin et al., 1999). The phosphatase $PP2A^{Cdc55}$ keeps Cfi1/Net1 in a dephosphorylated state to prevent Cdc14 release during metaphase. Moreover, the FEAR component Fob1 interacts with Spo12 and in turn binds to Cfi1/Net1. Fob1 binding to Cfi1/Net1 prevents Cdc14 release from its inhibitor prior to anaphase (Stegmeier et al., 2004). Spo12 phosphorylation upon anaphase onset reduces the affinity to Fob1. Phosphorylated Spo12 antagonizes the Fob1 function and thus promotes FEAR (Stegmeier et al., 2004). However, Spo12 must have at least one additional (unknown) function in promoting Cdc14 release in early anaphase, since the FEAR defects caused by deletion of *SPO12* and *BNS1* (Bns1 =

Spo12 homolog) could only partially be rescued by *Δfob1* (Stegmeier et al., 2004). Although sequestered in the nucleolus by its inhibitor Cfi1/Net1, Cdc14 is able to keep Spo12 dephosphorylated prior to anaphase (Tomson et al., 2009).

In anaphase, Esp1 binds and downregulates the activity of $PP2A^{Cdc55}$ (E. Queralt et al., 2006). Thereby, Esp1 promotes the phosphorylation of Cfi1/Net1 by the polo-like kinase Cdc5 and Cdc28 (in association with Clb1, Clb2) and this phosphorylation is required for the release of Cdc14 from its inhibitor (Manzoni et al., 2010), (Ethel Queralt & Uhlmann, 2008),(Azzam et al., 2004). Esp1 physically interacts with the FEAR component Slk19 and this is required for a functional FEAR pathway (Sullivan & Uhlmann, 2003). Notably, Esp1 cleaves Slk19 at its amino-terminus (N-terminus) (at aa 77) at anaphase onset (Sullivan et al., 2001). However, this protease function of Esp1 neither influences the interaction with Slk19 nor is it required for a functional FEAR pathway (Sullivan & Uhlmann, 2003). Esp1 together with Slk19 promotes Cdk-dependent phosphorylation of Spo12 (Tomson et al., 2009) thereby further promoting Cdc14 release (Stegmeier et al., 2004).

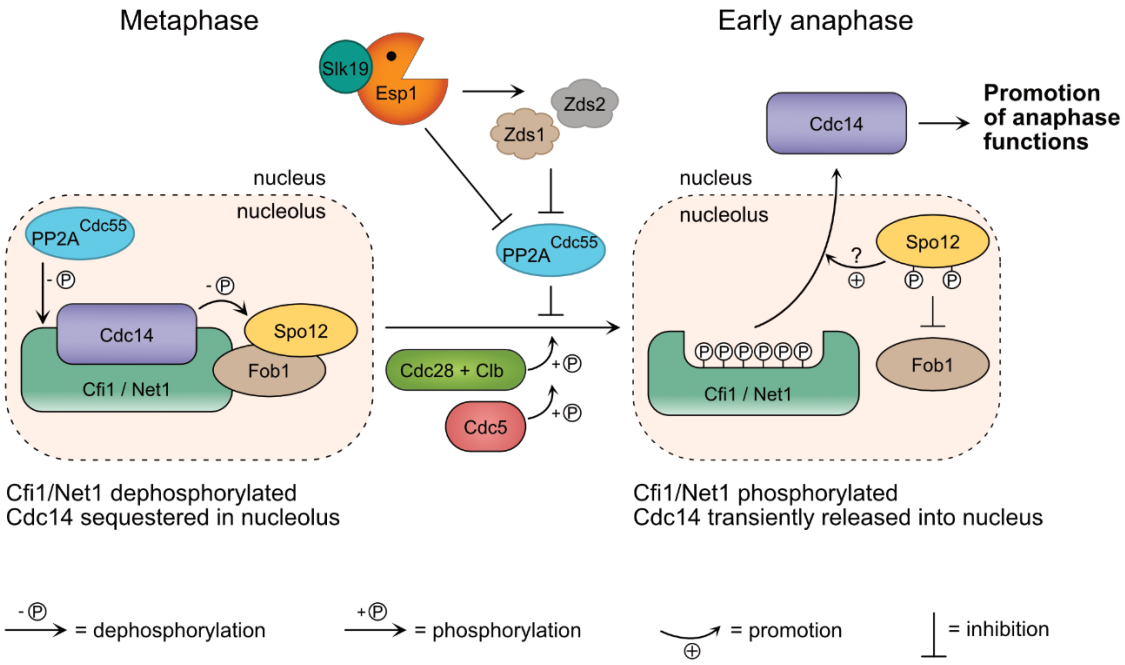

Figure I-4: Overview of the FEAR pathway. Figure is based on (Marston, 2014). The figure illustrates the Cdc-**F**ourteen **E**arly **A**naphase **R**elease (FEAR) pathway and its components. The FEAR pathway results in dephosphorylation of several Cdc14-substrates at anaphase onset with the overall goal to guide the cell through anaphase. In metaphase, Cdc14 is trapped in the nucleolus by its inhibitor Cfi1/Net1. Dephosphorylation of Cfi1/Net1 by $PP2A^{Cdc55}$ and binding of the Fob1-Spo12 complex to the inhibitor prevents Cdc14 release. In early anaphase, Cfi1/Net1 and Spo12 are phosphorylated by the kinases Cdc28 and Cdc5, which promotes Cdc14 release from its inhibitor. The FEAR-components Esp1 and Slk19 as well as Zds1 and Zds2 also promote Cdc14 release by downregulating the activity of the phosphatase $PP2A^{Cdc55}$.

The role of the FEAR components Zds1 and Zds2 is the inhibition of the nuclear activity of $PP2A^{Cdc55}$ by recruiting its regulator Cdc55 to the cytoplasm (Rossio & Yoshida, 2011),(Ethel Queralt & Uhlmann, 2008). Furthermore, Zds1 promotes Cdc28-dependent Cfi1/Net1 phosphorylation (Ethel Queralt & Uhlmann, 2008). These functions also promote the Cdc14 release into the nucleus.

Since $PP2A^{Cdc55}$ can dephosphorylate and thereby inhibit the APC^{Cdc20} (as mentioned above) (Rossio et al., 2013),(Rudner & Murray, 2000), the downregulation of nuclear $PP2A^{Cdc55}$ by Zds1, Zds2 or via Esp1 (E. Queralt et al., 2006) promotes anaphase also by activating the APC (besides releasing Cdc14).

The FEAR pathway is only one out of two consecutive steps in releasing Cdc14 during the budding yeast cell cycle. The FEAR pathway is followed by a second wave of Cdc14-release, which is mediated by the mitotic exit network (MEN). MEN is essential for the exit from mitosis (unlike FEAR) and results in the sustained release of Cdc14 from the nucleolus into the cytoplasm. This permanently released Cdc14 dephosphorylates Cdk targets within the cytoplasm and this is one of the most important functions for mitotic exit and cytokinesis (Caydasi et al., 2010).

1.4 The macromolecular machines that drive chromosome segregation

Besides a tight regulation of cell cycle events, chromosome segregation requires two main macromolecular machineries that drive accurate chromosome segregation: The kinetochore and the mitotic spindle apparatus.

1.4.1 The kinetochore – attachment site for microtubules

The KT is a macromolecular protein complex assembled at the centromere region of each sister chromatid. KTs are inevitable for the process of chromosome segregation since they constitute the site of attachment of chromosomes to MTs. Thus, the movement of each sister chromosome is coupled with the dynamics of MTs that distributes them to the two opposite poles (T. U. Tanaka & Desai, 2008),(Kern & Cheeseman, 2012),(Gonen et al., 2012), (Cheeseman, Drubin, et al., 2002),(Joglekar et al., 2008),(Brinkley et al., 1992),(Biggins, 2013).

In *S. cerevisiae*, the KT has a total mass of approximately 5–10 MDa and is made up of approximately 250 proteins (McAinsh et al., 2003),(A. Gupta et al., 2018). *In vitro* purified KT particles from budding yeast showed a KT length of 126 nm in electron microscope data when bound to a MT (Gonen et al., 2012). The budding yeast KT consists of over 60–70 different protein components (Joglekar et al., 2006),(Meraldi et al., 2006). In comparison, the human KT is composed of over 80 protein components (Cheeseman & Desai, 2008). In both budding yeast and humans, the different KT proteins are organized into several subcomplexes and are present at the KT in multiple copies. However, the exact sizes and

protein copy numbers are hard to determine since the KT composition varies during the course of the cell cycle (Hara & Fukagawa, 2020).

In humans, the KT structure can be roughly divided into three layers based on electron microscopy data: an electron-dense inner layer that is in direct contact with the centromeric DNA (the inner KT), a 20–30 nm middle layer with low contrast (the central KT) and a 40–50 nm electron-dense outer layer (the outer KT). The outer KT constitutes the contact site for MTs. In vertebrate cells, an additional fibrous corona is visible on the outer layer of the KTs that have no MT attachment and this corona can extend up to 200 nm (McEwen et al., 1998),(Dong et al., 2007b),(Wan et al., 2009),(Craig et al., 1999),(Hara & Fukagawa, 2020). Although the different layers are not visible by electron microscopy in *S. cerevisiae*, also here the KT can be functionally categorized into an inner KT (in contact to centromeric DNA), an outer KT (in contact with the attached MT) and a central KT (connecting the two layers) (De Wulf et al., 2003).

1.4.1.1 The centromere – a platform for inner KT assembly

The centromeres constitute the platform on which KTs are assembled and thus play a crucial role in chromosome segregation.

Centromeric DNA sequences are not conserved and differ between humans and budding yeast. The budding yeast centromere spans a relatively small DNA region of 125 base pairs (bp) and is therefore referred to as “point centromere”. This region contains the three **C**entromere **D**NA **E**lements CDE I, CDEII and CDEIII (Fitzgerald-Hayes et al., 1982) (illustrated in Figure I-5A). The CDEI and CDEIII sequences are conserved between the yeast chromosomes. In contrast, the CDEII sequence is not conserved and represents a A/T-rich region of 76–84 bp length (Cleveland et al., 2003),(Cheeseman, Drubin, et al., 2002). In budding yeast, one KT is assembled at each point centromere and each KT is attached to only one MT (Winey et al., 1995) (Figure I-5A). In contrast, human centromeres are much larger compared to budding yeast centromeres and consist of highly repetitive sequences, the alpha satellite DNA. Information about the exact size of human centromeres varies between 0.3–5 Mb (Yamagishi et al., 2014),(Wevrick & Willard, 1989),(Willard, 1990) or even between 5–10 Mb (K. Bloom & Costanzo, 2017). Also the human KT structure assembled on the centromeres is much larger compared to budding yeast, since it contains multiple copies of KT complexes that give rise to 20–25 MT attachment sites (Joglekar et al., 2008),(Maiato et al., 2004) (Figure I-5B). Thus, these centromeres are called regional centromeres (Spence et al., 2002),(Schueler et al., 2001) (illustrated in Figure I-5B). Although the centromeric DNA-sequences differ from each other (point centromeres in budding yeast and regional centromeres in humans), the molecular architecture of the thereon assembled KT, the function of the KT subcomplexes as well as the regulation mechanisms are quite conserved between the species (Andy Choo, 2001),(Joglekar et al., 2008),(Joglekar et al., 2009).

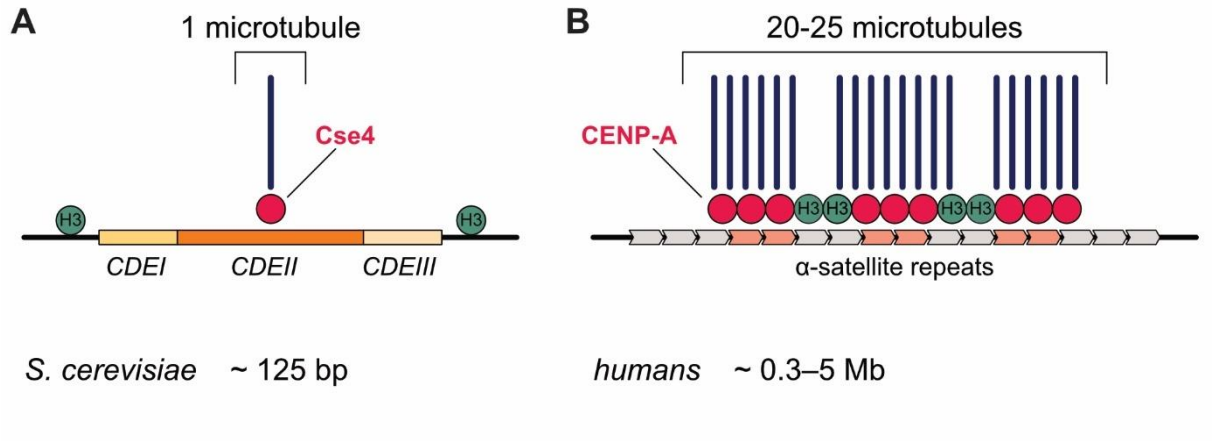

Figure I-5: Comparison of centromeres in budding yeast and humans. Figure is based on (Yamagishi et al., 2014) and (Willard, 1990). The figure illustrates the differences between the point centromere in *S. cerevisiae* (~ 125 bp region) with only one microtubule attached to the KT (A) and the regional centromeres in humans (~ 0.3–5 Mb region) with 20–25 microtubules attached to multiple copies of KT complexes (B). KT = kinetochore.

Both, the human and the budding yeast centromeres contain an atypical histone variant as substitute for histone H3, called CENP-A in humans (D. K. Palmer et al., 1991),(Henikoff et al., 2000),(De Rop et al., 2012) and Cse4 in budding yeast (Meluh et al., 1998),(Earnshaw et al., 2013). The KT assembles on Cse4/CENP-A containing nucleosomes. In humans, the loading of CENP-A to the centromeric nucleosomes is determined by epigenetic mechanisms (reviewed in Stellfox et al., 2013), while in budding yeast, Cse4-loading is determined by the centromeric DNA-sequence.

Budding yeast Cse4 interacts directly with the unconserved CDEII element of the centromeric DNA region (Stoler et al., 1995). Furthermore, also the **C**entromere DNA **B**inding **F**actor CBF3 (complex consisting of the four essential inner KT proteins Ndc10, Cep3, Ctf13 and Skp1) interacts directly with CDEIII (Lechner & Carbon, 1991). Importantly, binding of the CBF3-complex to CDEIII is essential for the assembly of the entire budding yeast KTs, since Cse4 deposition to the centromeric region is dependent on the CBF3-complex (Ho et al., 2014),(Yan et al., 2018). Cse4 loading is additionally facilitated by other proteins, such as Scm3 and the outer KT complex Dam1-DASH (Camahort et al., 2007),(Ho et al., 2014). CBF3 is also required for the integrity of the inner KT by its interaction with the centromere binding protein Cbf1. Cbf1 is a non-essential protein that interacts *in vitro* with the inner KT protein Ndc10 (part of the CBF3 complex) (Cho & Harrison, 2012). Moreover, Cbf1 binds to CDEI and bends the DNA, which is important for chromosome function (Mellor et al., 1990),(Niedenthal et al., 1993). Components of the CBF3-complex were shown to enhance DNA binding of Cbf1 *in vitro* (Hemmerich et al., 2000). Moreover, the CBF3-complex is required for KT assembly by recruiting further KT components such as Okp1, Ctf19 and Mcm21 (Ortiz et al., 1999) and the chromosomal passenger complex (CPC, consisting of Ipl1, Sli15, Nbl1 and Bir1)

(Biggins & Murray, 2001),(Sandall et al., 2006). Together, these proteins constitute the inner KT (Biggins, 2013),(A. Gupta et al., 2018),(De Wulf et al., 2003) (for illustration of the budding yeast KT see Figure I-6 in chapter 1.4.1.2).

The molecular connections between the human centromeric DNA and CENP-A are less clear compared to budding yeast (K. Bloom & Costanzo, 2017). CENP-A is loaded on the alpha satellite DNA with the help of the DNA-binding protein CENP-B, which is structurally similar to Cbf1 and also induces DNA bending (Y. Tanaka et al., 2001). *In vitro*, nucleosomes containing CENP-A can induce KT assembly by the recruitment of different KT proteins (Weir et al., 2016),(Guse et al., 2011). Taken together, CENP-A /Cse4 and the interplay of several factors at the centromeric DNA and inner KT eventually leads to the hierarchical assembly of the macromolecular kinetochore complex.

1.4.1.2 The central KT and the KT-MT interface

The inner KT is connected to the outer KT by several protein complexes that are collectively referred to as central KT. The central KT includes the COMA complex (consisting of Ctf19, Okp1, Mcm21 and Ame1) and the MIND complex (consisting of Mtw1, Nnf1, Nsl1 and Dsn1) (Figure I-6). The COMA complex (part of the constitutive centromere associated network (CCAN) complex in humans) leads to the recruitment of the MIND complex (human central KT Mis12 complex). The MIND complex is required for recruiting the Spc105 and the Ndc80 complex of the outer KT. The Spc105 complex consists of the proteins Spc105 and Kre28 (KNL1 and Zwint in humans respectively) and constitutes a site for checkpoint regulation (Biggins, 2013),(A. Gupta et al., 2018). The Ndc80 complex consists of four proteins: the Spc24-Spc25 heterodimer and the Ndc80-Nuf2 heterodimer. Spc24-Spc25 binds to the MIND complex of the inner KT and the Ndc80-Nuf2 heterodimer is placed at the KT-MT interface (Wei et al., 2006) (Figure I-6).

The Ndc80-complex is essential for KT-MT attachment: the calponin-homology (CH) domain at the N-terminus of Ndc80 (HEC1 in humans) forms the attachment site for MTs (Wei et al., 2007). The Ndc80 complex interacts with the Dam1 complex (consisting of Ask1, Dad1, Dad2, Dad3, Dad4, Dam1, Duo1, Spc19, Spc34, Hsk1) (Shang et al., 2003),(Wong et al., 2007) and this interaction is important for stable KT-MT interaction (Tien et al., 2010). The Dam1 complex forms a ring around MTs (Miranda et al., 2005), (Gonen et al., 2012) and guides the Ndc80 complex to the plus ends of dynamic MTs (Lampert et al., 2010). Furthermore, the Dam1 complex is needed for stable attachment of the KTs and for end-on pulling (K. Tanaka et al., 2007). Thus, the Ndc80 and Dam1 complexes are required to convert the energy from depolymerizing MTs into the movement of chromosomes (Koshland et al., 1988),(Wan et al., 2009). Although there are no human homologues for the Dam1 complex, there is evidence that the human Ska1 complex is functionally related to the Dam1-complex in budding yeast (Welburn et al., 2009). Further components of the outer KT are also Stu1 (Yin et al., 2002) and Slk19 (Zeng et al., 1999). Budding yeast Stu1 localizes to KTs only until anaphase and then translocates to the

anaphase midzone (Funk et al., 2014),(Yin et al., 2002). Stu1 is essential for the stabilization of MTs that are attached to KTs (kinetochore MTs = kMTs) and sequesters together with Slk19 at uaKTs, a process that facilitates KT recapturing upon MT detachment (sequestering process described in chapter 1.5.3.2) (Ortiz et al., 2009),(Funk et al., 2014),(Kolenda et al., 2018). The functions of both Stu1 and Slk19 are of major importance for this work and are described in more detail below (see section 5.3 for Stu1 and 5.4 for Slk19).

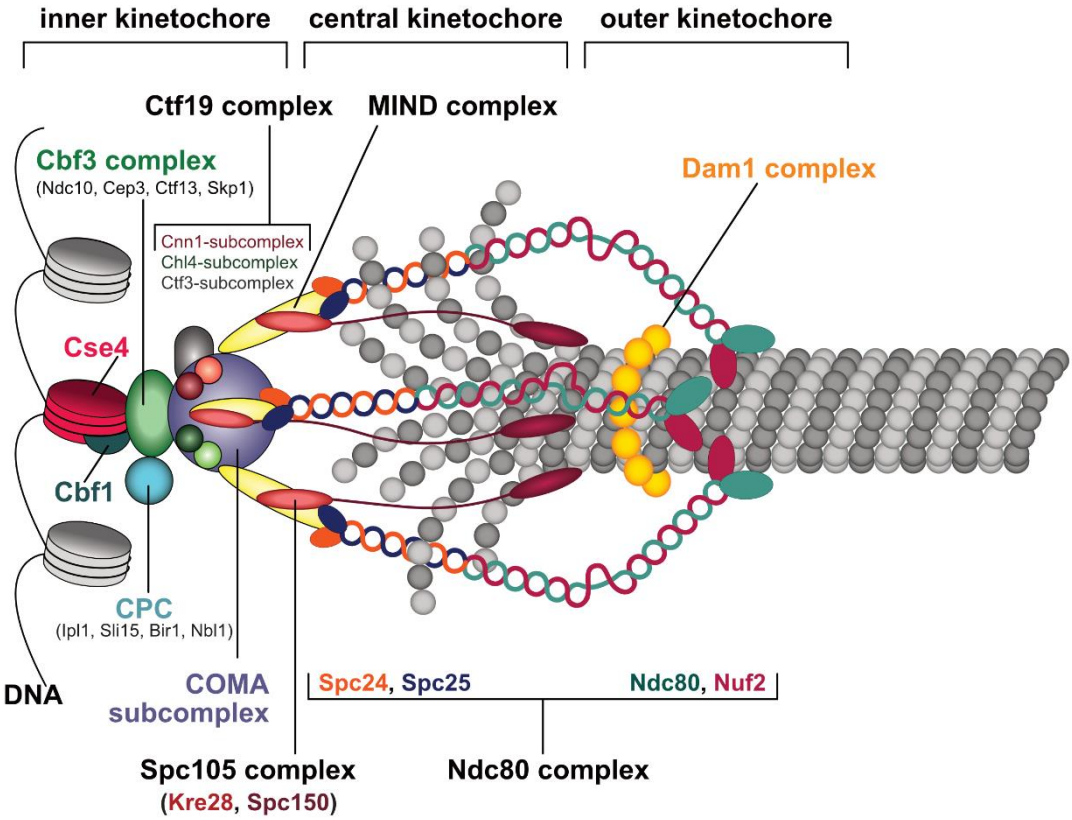

Figure I-6: The budding yeast kinetochore architecture. Figure is based on (A. Gupta et al., 2018). The illustration gives an overview over the KT architecture and is not true to scale. The inner KT consists of proteins that are associated or in proximity to the centromeric chromatin. The outer KT consists of proteins at the KT-MT interface. The central KT connects the inner and the outer KT. KT = kinetochore.

1.4.2 The kinetochore – a hub for checkpoint signaling

The KT constitutes a hub for multiple cell cycle checkpoints, including the spindle assembly checkpoint that monitors KT-MT attachments and the tension checkpoint that monitors the bipolar orientation of these attachments.

1.4.2.1 The spindle assembly checkpoint (SAC) is activated by uaKTs

In budding yeast, KTs are attached to MTs during the entire cell cycle, only during replication in S-Phase, MTs are transiently detached from KTs and the KTs must be recaptured in prometaphase (Kitamura et al., 2007). The SAC is activated in the presence of KTs that are detached from MTs (unattached KTs = uaKTs) and leads to inhibition of the APC. Thereby, anaphase onset is prevented until all chromosomes are properly attached to MTs. The regulatory network of the SAC consists of KT-bound components and soluble components (illustrated in Figure I-7). In budding yeast, the conserved key players of this checkpoint are the mitotic kinase Mps1, the proteins Mad1, Mad2, Mad3 (homolog of human BubR1) as well as Bub1 and Bub3. The outer KT proteins Ndc80 and Spc105 constitute binding platforms for the checkpoint proteins. The major checkpoint kinase, Mps1, binds to the N-terminal CH-domain of the outer KT protein Ndc80. When the KT detaches from its associated MT, the architecture at the KTs changes in a way that Mps1 gets in closer proximity to the inner KT and to its substrate Spc105. Mps1 can then phosphorylate Spc105 at its six consensus Mps1 phosphorylation sites, the Met-Glu-Leu-Thr (MELT) sites, to initiate the SAC signaling cascade (Aravamudhan et al., 2015).

Phosphorylation of these MELT sites activates the recruitment of the Bub1-Bub3 complex to Spc105. Phosphorylation of Bub1 by Mps1 leads to interaction with Mad1 and subsequently to the recruitment of Mad2 and to the formation of the Mad1-Mad2 complex at the KTs (London & Biggins, 2014). Mad2 binding to the KT leads to its conformational change from an “open” to a “closed” form (here called Mad2-O and Mad2-C respectively) (Luo et al., 2002).

The soluble Mad2 (Mad2-O) can again bind to Mad2-C, which is stably bound to the KT via Mad1. Thereby, Mad2-O is in turn also converted to Mad2-C (which is however soluble and distinct from KT-bound Mad2-C) (Figure I-7). This binding and conversion of Mad2-O at the KT is very dynamic. The converted, soluble Mad2-C can then bind the APC-activator, Cdc20, together with the SAC-proteins Bub3 and Mad3. Together, these proteins form a complex called the mitotic checkpoint complex (MCC) (London & Biggins, 2014). The MCC constitutes the main effector complex of the SAC and the main goal of the MCC is the binding of the APC-activator Cdc20 and thereby delaying anaphase onset.

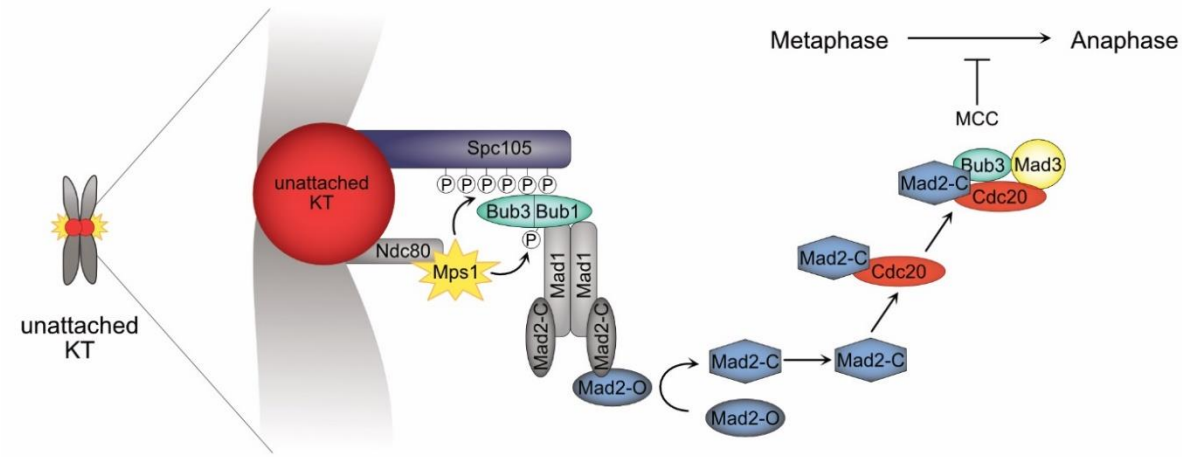

Figure I-7: The spindle assembly checkpoint. Figure is based on (Biggins, 2013) and (London & Biggins, 2014). The figure illustrates the spindle assembly checkpoint (SAC), which is activated upon KT detachment. The checkpoint kinase Mps1 phosphorylates the outer KT protein Spc105 at its conserved Met-Glu-Leu-Thr (MELT) sites. This recruits the Bub1-Bub3 complex to the KT. Phosphorylation of Bub1 by Mps1 leads to the recruitment of the Mad1-Mad2-C complex to the KTs. Soluble Mad2-O binds to KT-bound Mad2-C and is converted to soluble Mad2-C. Soluble Mad2-C and the SAC proteins Bub3 and Mad3 together form the mitotic checkpoint complex (MCC), which binds the APC activator Cdc20 and thus inhibits anaphase onset. APC = anaphase promoting complex, KT = kinetochore, Mad2-C = closed form of Mad2, Mad2-O = open form of Mad2.

The SAC is silenced after MT attachment and silencing additionally requires the phosphatase Glc7 (protein phosphatase 1 = PP1 in humans) that counteracts the phosphorylation of Mps1 (Pinsky et al., 2009). At anaphase onset, Glc7 localizes to Spc105 together with the Glc7-associating KT protein Fin1 in a FEAR-dependent manner and this is required to remove the SAC components Bub1 and Bub3 from KTs (Bokros et al., 2021),(Rosenberg et al., 2011), (Aravamudhan et al., 2015).

1.4.2.2 The tension checkpoint

Bipolar MT attachment (both sister chromatids attached to the two opposing SPBs) is a prerequisite for error-free chromosome segregation. Only after the establishment of correct bipolar MT attachments, tension is created at the KTs and the spindle. In contrast, incorrect attachments, such as syntelic attachments (both sister chromatids attached to same SPB) or monotelic attachments (only one sister chromatid attached to one SPB), lead to missing tension at KTs and must be corrected (Figure I-8). Therefore, tension-sensing checkpoints are optimal to ensure bipolar orientation of chromosomes prior to anaphase.

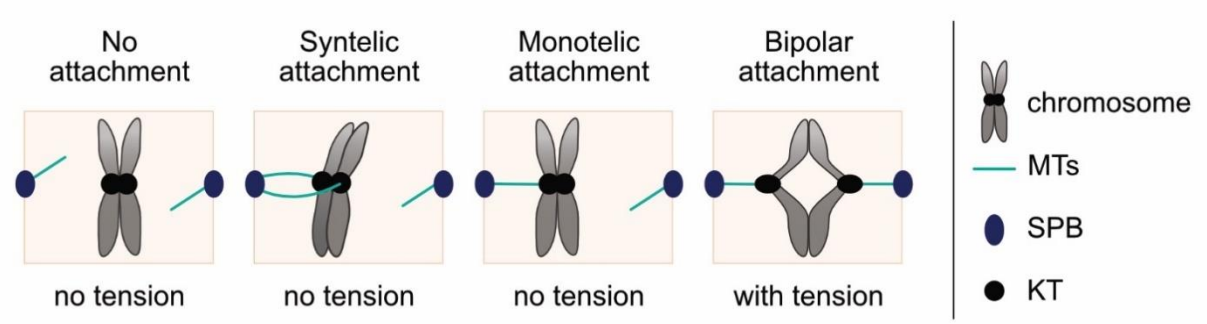

Figure I-8: Types of KT-MT attachments. Figure is based on (T. U. Tanaka et al., 2005). The figure illustrates the different types of KT-MT attachments and the resulting tension built on the KTs. Detached KTs experience no tension. Incorrect syntelic or monotelic attachments of sister chromatids also result in lacking tension at the KTs. Only bipolarly attached sister chromatids result in tension at the KTs. KT = kinetochore, MT = microtubule, SPB = spindle pole body.

Lacking tension at KTs with erroneous attachments is sensed by the chromosomal passenger complex (CPC). The CPC is comprised of Ipl1 (Aurora B kinase in humans), Sli15 (INCENP), Bir1 (Survivin) and Nbl1 (Borealin) and localizes at the centromeres in early mitosis (T. U. Tanaka, 2010),(Biggins & Murray, 2001).

At KTs with lacking tension, the effector kinase of this pathway, Ipl1, is in close proximity to its substrates and can destabilize erroneous MT attachments by phosphorylation of its targets at the KT and at the KT-MT interface. Thus, Ipl1 can increase the turnover rate of MT attachments and thereby increases the chance for bipolar KT-MT orientation (T. U. Tanaka, 2010),(Biggins & Murray, 2001) (illustrated in Figure I-9).

Important Ipl1 substrates at the KT-MT interface are Dam1 and Ndc80 (Cheeseman, Anderson, et al., 2002),(K. Zhang et al., 2005). Both the Dam1 complex (comprised of Dam1, Duo1, Ask1, Dad1–4, Spc19, Spc34, Hsk1) and the Ndc80 complex (comprised of Ndc80, Nuf2, Spc24, Spc25) are crucial for KT-MT attachment. Phosphorylation of Dam1 at its carboxyl-terminus (C-terminus) leads to reduced interaction with the Ndc80-complex (Tien et al., 2010). Phosphorylation of Ndc80 at the N-terminus reduces the affinity of the Ndc80 complex to MTs by interfering with electrostatic interactions (Cheeseman et al., 2006),(Ciferri et al., 2008).

If bipolar attachment of the chromosome is achieved, this leads to increased tension at the KTs (Salmon & Bloom, 2017) and to a physical separation of the Ipl1/Aurora B kinase from its substrates at the KT-MT interface (Liu et al., 2009) (illustrated in Figure I-9) (spatial separation model). Moreover, tension can also directly stabilize the KT-MT connections *in vitro* possibly by catch bond mechanisms (Akiyoshi et al., 2010),(Thomas et al., 2008). Furthermore, the XMAP215/Dis1 family member Stu2 (ch-TOG in humans) also plays a role in tension-sensing. Stu2 localizes to KTs via the Ndc80-complex and is required for

tension-dependent stabilization of KT-MT attachments (M. P. Miller et al., 2016),(Zahm et al., 2021). This tension-sensing function of Stu2 is also required for establishment of bipolar attachments together with Ipl1 (M. P. Miller et al., 2019).

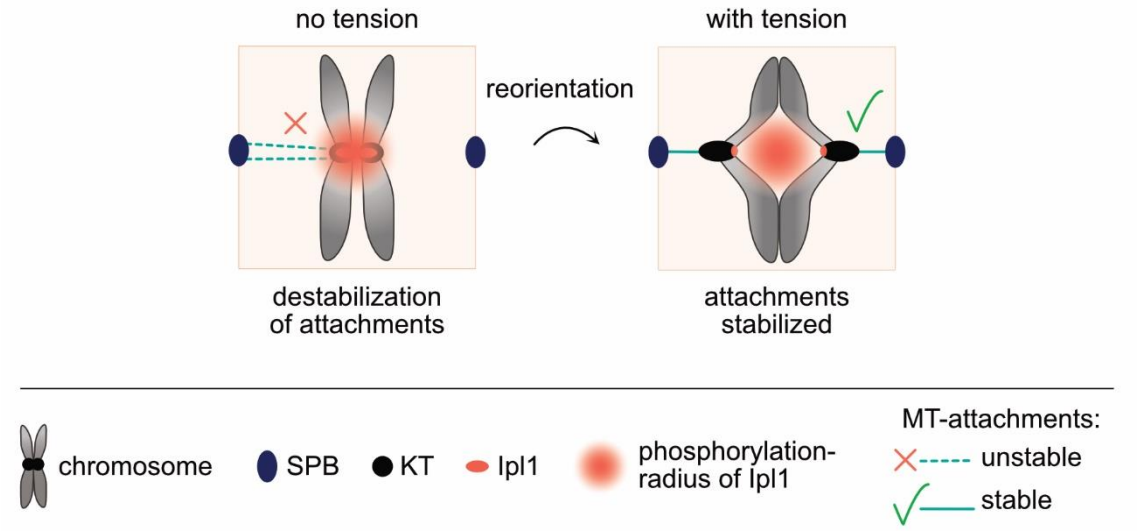

Figure I-9: Error correction of tensionless attachments by Ipl1. Figure is based on (T. U. Tanaka et al., 2005). The figure illustrates how erroneous KT-MT attachments are corrected by Ipl1 kinase activity according to the spatial separation model. Erroneous attachments of sister chromatids result in lacking tension at the KTs. At tensionless KTs, Ipl1 is in proximity to its substrates. Phosphorylation of Ipl1 substrates at the KT and KT-MT interface destabilizes tensionless MT attachments and increases their turnover rate. Bipolar attachment of sister chromatids leads to increased tension at the KTs and to a physical separation of Ipl1 from its substrates and thus to more stable MT attachments. MT = microtubule, SPB = spindle pole body, KT = kinetochore.

The CPC localizes to the inner KT complex CBF3 via interaction with Bir1. Bir1 and Sli15 link the CBF3 complex to MTs and are required for sensing the tension status at KTs (Sandall et al., 2006). The interaction of Ipl1 at the inner KT via Bir1 and Sli15 is required not only for its localization at tensionless KT-MT attachments, but also for its activation by Sli15 (Sandall et al., 2006). Moreover the CPC also localizes to the COMA complex via interaction with Sli15 (independently of Bir1) and this inner KT localization of Ipl1-Sli15 is required for bi-orientation (Fischböck-Halwachs et al., 2019),(Knockleby & Vogel, 2009),(García-Rodríguez et al., 2019).

Interestingly, the budding yeast shugosin Sgo1 is required to maintain centromeric localization of Ipl1 at tensionless KTs (Verzijlbergen et al., 2014),(Peplowska et al., 2014). The centromeric localization of Sgo1 depends on Bub1-dependent phosphorylation of histone H2A (Kawashima et al., 2010). Thus, both Bub1 and Sgo1 are required for the bipolar attachment of KTs (Fernius & Hardwick, 2007). Upon KT biorientation and tension

establishment in metaphase, Sgo1 dissociates from the centromeric region and this promotes Ipl1 dissociation from KTs (Nerusheva et al., 2014),(Shimogawa et al., 2009). This might be an additional mechanism to prevent phosphorylation of Ipl1 substrates besides the spatial separation between Ipl1 and its targets (illustrated in Figure I-9).

In budding yeast, KT detachment is also always accompanied with a decrease in tension since only one MT attaches to one KT (Winey et al., 1995). Therefore, the difference between the signaling pathways for checkpoint activation upon KT detachment or tension is not easy to dissect. In addition to the above-mentioned Bub1 function for the centromeric binding of Ipl1 (Verzijlbergen et al., 2014),(Peplowska et al., 2014), there are also indications that a subset of the SAC components (including Bub1) might mediate an additional parallel tension-dependent pathway: The two SAC components Bub1 and Bub3 can delay anaphase onset when tension at KTs is reduced although KTs are still attached to MTs. This tension-dependent delay of anaphase is not affected by *Δmad1*, *Δmad2* or *Δmad3*. Therefore, this described tension-dependent pathway must be distinct from the canonical SAC (described in chapter 1.4.2.1) (Proudfoot et al., 2019). Furthermore, also the SAC component Mad3 is phosphorylated by Ipl1 in response to low tension at KTs, which leads to an anaphase delay (E. M. J. King et al., 2007). These tension-dependent pathways may function in addition to the Ipl1-mediated error-correction pathway (Biggins & Murray, 2001),(T. U. Tanaka et al., 2002).

1.4.3 The mitotic spindle in budding yeast

1.4.3.1 Microtubules

The mitotic spindle is composed of MTs. MTs are filamentous polymers comprised of α- and β-tubulin heterodimers that assemble head-to-tail into protofilaments and 13 protofilaments assemble laterally in a pseudo-helical manner to form a hollow cylindrical shape with a diameter of 25 nm (Winey & Bloom, 2012),(Cooper, 2000a) (Figure I-10A a-c). The budding yeast tubulin genes are constitutively expressed: α-tubulin is encoded by TUB1 and TUB3, while β-tubulin is encoded by TUB2. The head-to-tail assembly of tubulin dimers gives rise to a polar MT structure with a minus end (α-tubulin) and a plus end (β-tubulin) (see Figure I-10B). This polarity is important for MT nucleation, growth and shrinkage as well as for directionality of transport processes via motor proteins (Winey & Bloom, 2012),(Cooper, 2000a). Both α- tubulin and β-tubulin are guanosine triphosphate (GTP)-binding proteins (Figure I-10A d) and GTP-bound tubulin is required for MT polymerization, which occurs specifically at the plus end of the MTs. During the process of polymerization, GTP bound to β-tubulin is hydrolyzed to guanosine diphosphate (GDP) and this, in turn, leads to destabilization of MTs due to reduced lateral affinity between neighboring tubulin dimers and subsequently to MT depolymerization (H. W. Wang & Nogales, 2005) (Figure I-10B). This dynamic character of MTs, with alternating cycles of

polymerization and depolymerization, is called dynamic instability (Mitchison & Kirschner, 1984). GDP-bound tubulin dimers can be dynamically exchanged by GTP-bound tubulin dimers at the plus ends. This leads to a stable "GTP cap" at the plus ends of MTs and allows MT growth (Figure I-10B). Thus, polymerization and depolymerization of MTs is determined by the ratio between the GTP-hydrolysis rate and the addition of GTP-bound tubulin at the MT plus end. Microtubule-associated proteins (MAPs) strongly influence MT dynamics and can control processes such as MT polymerization, depolymerization, stabilization, crosslinking and sliding (a subset of MAPs are described in more detail in chapter 1.5) (Winey & Bloom, 2012),(Cooper, 2000a).

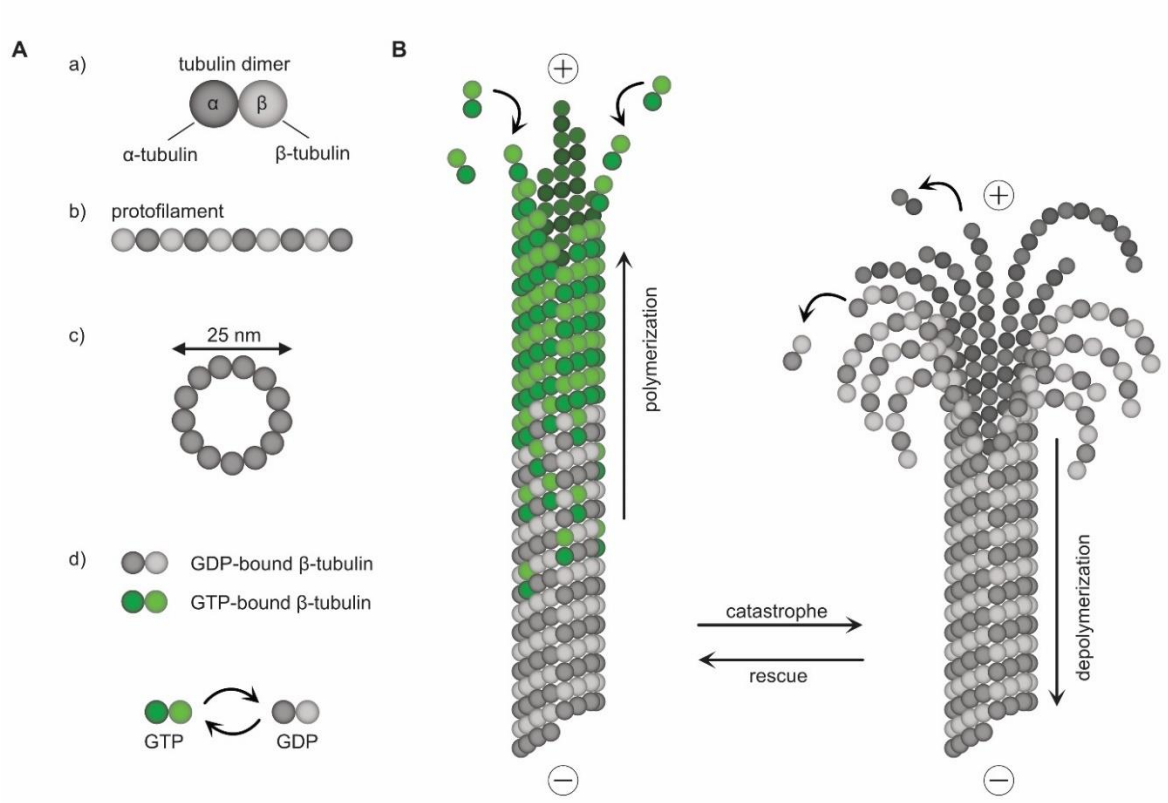

Figure I-10: Microtubules and their dynamics. Figure is based on (Al-Bassam & Chang, 2011). (A) Structural components of microtubules (MTs). (a) MTs are comprised of α- and β-tubulin heterodimers. (b) Tubulin dimers assemble head-to-tail into protofilaments creating a polar structure with minus end (α-tubulin) and a plus end (β-tubulin). (c) 13 protofilaments assemble laterally to form a hollow cylindrical shape with 25 nm diameter. (d) Tubulin dimer with GTP-bound β-tubulin is shown in green. Tubulin dimer with GDP-bound β-tubulin is shown in grey. (B) MTs polymerize specifically at their plus end. GTP-bound β-tubulin is required for MT polymerization. GTP bound to β-tubulin is hydrolyzed to GDP during polymerization, leading to destabilization and depolymerization of MTs. This results in a dynamic character of MTs with alternating cycles of polymerization (rescue) and depolymerization (catastrophe). GDP-bound tubulin dimers can be exchanged by GTP-bound tubulin dimers at the plus ends, leading to a stable "GTP cap" and MT growth.

1.4.3.2 Spindle pole bodies and MT nucleation

The initiation of MT polymerization (nucleation) starts from structures called microtubule organizing centers (MTOCs). In humans, the main MTOCs are the centrosomes: two centrioles surrounded by pericentriolar material. However, in animal cells, MTs can additionally nucleate from non-centrosomal MTOCs, e.g. from other cell organelles such as Golgi or mitochondria, pre-existing MTs, chromosomes and rarely also from KTs (Petry, 2016),(Sanchez & Feldman, 2017).

In *S. cerevisiae,* the functional equivalents of the centrosomes are called spindle pole bodies (SPBs), which constitute the main MTOCs in these cells. Also in budding yeast, short-lived KT-derived MTs can appear temporarily prior to KT capture (early mitosis) to facilitate lateral loading of KTs onto SPB-derived kMTs. However, those MTs play no role in formation of the mitotic spindle (Kitamura et al., 2010). Since *S. cerevisiae* has a closed mitosis, the SPBs are embedded within the nuclear envelope (Güttinger et al., 2009),(Boettcher & Barral, 2013),(Rose, 2007). SPBs are duplicated at the beginning of each cell cycle giving rise to two poles from which MTs can nucleate and this ensures bipolar spindle formation.

The SPB is comprised of an outer plaque at the cytoplasmic side of the nucleus, a central plaque spanning the nuclear envelope and an inner plaque at the inner side of the nucleus (Winey & Bloom, 2012). MTs can nucleate at the inner and outer plaque of the SPB and this requires a special tubulin variant, Tub4 (γ-tubulin humans), which is a common component of all MTOCs (reviewed in Jaspersen & Winey, 2004 and Cavanaugh & Jaspersen, 2017). In budding yeast, two molecules of Tub4, together with the SPB proteins Spc97 and Spc98 form a γ-tubulin small complex (γ-TuSC) that assembles into ring-like-structures and is stabilized by the SPB component Spc110. Binding of the γ-Tubulin complex to the SPB allows MT nucleation and forms a cap at the minus end of the MTs embedded in the SPB (Pereira & Schiebel, 1997),(Schiebel, 2000),(Vinh et al., 2002),(Kollman et al., 2010),(Winey & Bloom, 2012). Moreover, the microtubule-associated proteins Stu2, Bim1, Bik1, Kip3 as well as Vik1 (component of the heterodimeric motor Kar3-Vik1) are involved in the nucleation process (B. R. King et al., 2021).

The outer plaque of the SPB nucleates cytoplasmic MTs, also referred to as astral MTs (illustrated in Figure I-11). Astral MTs are required, together with cytoplasmic dynein, for movement and correct positioning of the nucleus to the bud neck throughout the cell cycle (Shaw et al., 1997),(D. S. Sullivan & Huffaker, 1992),(Jacobs et al., 1988),(Eshel et al., 1993),(R. E. Palmer et al., 1992),(Hildebrandt & Hoyt, 2000).

The inner plaque of the SPB nucleates the kinetochore MTs (kMTs) and the interpolar MTs (ipMTs) (Figure I-11) that together form the mitotic spindle apparatus within the nucleus (described in more detail below) (Byers & Goetsch, 1974),(Robinow & Marak, 1966),(reviewed in Fraschini, 2019). The ipMTs emerging from the two opposite poles interdigitate at the center of the spindle, forming antiparallel MT overlaps.

Another kind of nuclear MTs are the so called nuclear random MTs (nrMTs) (Figure I-11) that arise when the formation of the spindle is compromised or the antiparallel organization of ipMTs is disturbed. The nrMTs are highly dynamic and promote recapturing of uaKTs by scanning the nucleus for uaKTs (capturing process described in more detail below in chapter 1.5.3.2). Thus, nrMTs contribute to correct chromosome segregation. However, the appearance of nrMTs during mitosis is also indicative of a compromised spindle since any defects in spindle integrity also results in elevated levels of free nuclear tubulin (Kolenda et al., 2018).

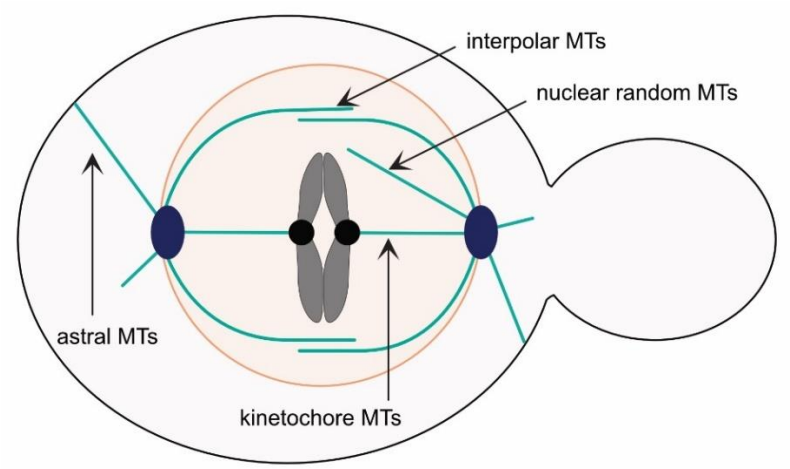

Figure I-11: Types of microtubules. Figure is based on (Biggins, 2013) and (Kolenda et al., 2018). The figure illustrates the different types of microtubules (MTs) in a budding yeast cell. Kinetochore MTs (kMTs) and interpolar MTs (ipMTs) nucleate at the inner plaque of the spindle pole body (within nucleus) and together form the mitotic spindle apparatus. Nuclear random MTs (nrMTs) arise when the mitotic spindle is compromised. Astral MTs nucleate at the outer plaque of the spindle pole body in the cytoplasm.

1.4.3.3 Formation of a bipolar spindle

SPBs are duplicated in late G1 and connected via a bridge structure (Jaspersen & Winey, 2004). The SPBs are located side by side and the emerging MTs form a monopolar spindle. Monopolar spindles have short MTs arranged in a high angle with less antiparallel MT overlaps compared to a bipolar spindle (Leary et al., 2019). The separation of the two duplicated SPBs in S-phase (described above in chapter 1.3.1) is the initial step of bipolar spindle formation (Jaspersen & Winey, 2004). This step requires Cdk1 phosphorylation of the bridge component, Sfi1 (Elserafy et al., 2014),(Avena et al., 2014). The transition of the monopolar spindle into a bipolar spindle is a very fast process in which the two SPBs “snap apart” (Leary et al., 2019). This transition is irreversible and is suggested to be the fastest step of spindle assembly with an average velocity of ~ 17 nm/s (according to Leary et al., 2019) . The budding yeast plus end-directed kinesin-5 motors, Cin8 and Kip1 (described in

more detail in chapter 1.5.1.1), accumulate during S-phase and are required for SPB separation by mediating this fast monopolar to bipolar transition step of the spindle (Roof et al., 1992),(Hildebrandt & Hoyt, 2001),(Crasta et al., 2006),(Leary et al., 2019). Notably, the fast step of monopolar to bipolar transition requires only the crosslinking but not the motor function of Cin8 and Kip1 (Crasta et al., 2006),(Leary et al., 2019). Cin8 seems to be especially important for this process since it is loaded onto the monopolar spindle prior to Kip1 and is present in higher intensities compared to Kip1 (Leary et al., 2019). In contrast, the MT-crosslinking protein Ase1 was not detected at the monopolar spindles prior to the transition step and thus does not seem to be required for this fast step (Leary et al., 2019). However, Ase1 becomes essential for SPB separation in cells lacking Cin8 (Kotwaliwale et al., 2007).

Only after the fast transition to a bipolar spindle when more ipMT overlaps are formed, the sliding function of the kinesin-5 motor proteins is required to generate an outward directed force, spindle length maintenance and spindle stabilization (M. A. Hoyt et al., 1992),(Leary et al., 2019). Moreover, several other MAPs are relevant for the integrity of the growing bipolar spindle by aligning, crosslinking, elongating and moving apart the interdigitating MTs. The MAPs that mediate these functions, such as the nuclear motor proteins Cin8, Kip1, Kar3 and Kip3 or the MT crosslinking and stabilizing proteins Ase1 and Stu1, are described in more detail below in chapter 1.5.

1.4.3.4 Mitotic spindle architecture

In budding yeast, the mitotic spindle is composed of eight interdigitating ipMTs (four from each SPB; as illustrated in Figure I-12) and 32 kMTs (16 from each SPB), each connected to one of the 16 duplicated sister chromatids (Winey et al., 1995),(O'Toole et al., 1999) (for simplicity only three exemplary kMTs are illustrated in Figure I-12). Thus, the budding yeast spindle is comprised of approximately 40 MTs in total. While kMTs are required for chromosome attachment, the ipMTs interdigitate in the spindle center and are required for spindle stability. Metaphase spindles have a length of approximately 1.5–2 µm, while anaphase spindles elongate to a length of 6–10 µm (Winey & Bloom, 2012). Besides the MT network, various MAPs and motor proteins are crucial for spindle biorientation, stability and spindle dynamics throughout the cell cycle. Especially the spindle dynamics in anaphase require a concerted action of MAPs and a highly organized region of ipMT overlaps, called "anaphase midzone" (Figure I-12).

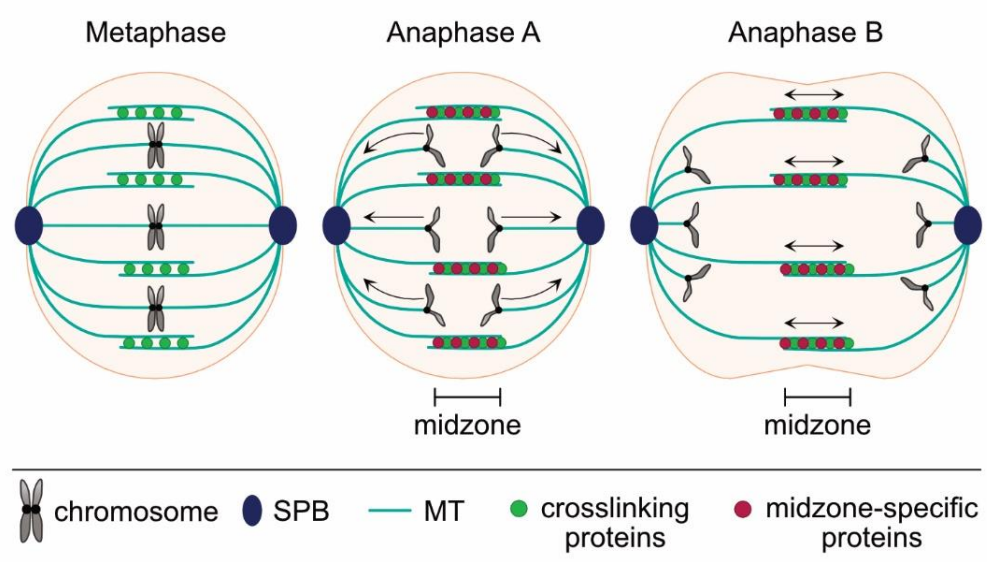

Figure I-12: Mitotic spindle architecture. Figure is based on (Singh et al., 2018). The figure illustrates the meta- and anaphase spindle in budding yeast. One kMT is connected to each sister chromatid of the 16 budding yeast chromosomes (for simplicity only three exemplary kMTs are shown). Eight ipMTs (four from each SPB) interdigitate at the center of the spindle. In anaphase, this overlap region is referred to as midzone. The overlaps are stabilized by crosslinking proteins (shown in green). In anaphase, kMTs shorten and sister chromatids separate to the opposing poles. Midzone specific proteins (shown in red) are recruited to the overlap zone allowing simultaneous MT sliding, polymerization and stabilization. SPB = spindle pole body, MT = microtubule, kMT = kinetochore MT, ipMT = interpolar MT.

1.4.3.5 The anaphase spindle midzone

The midzone is a spatially restricted region at the anaphase spindle center where ipMTs overlap (Figure I-12). The MT-crosslinking protein Ase1 functions as key midzone organizer by recruiting or focusing midzone proteins to the overlap region at anaphase onset (Ase1 functions described in detail in part 1.5.2) (Schuyler et al., 2003),(Khmelinskii et al., 2007). As measured by the Ase1 spread, the midzone has a length of approximately 2 µm (Khmelinskii et al., 2007). The proteins recruited to the anaphase midzone must fulfill several functions: 1) The anaphase spindle must be stabilized and crosslinked to promote MT alignment and prevent spindle breakage. 2) Antiparallel ipMTs must slide apart to allow spindle elongation and chromosome separation. 3) MTs must polymerize simultaneously with ipMT sliding to maintain ipMT overlaps. 4) Excessive growth of ipMTs is counteracted to regulate the length of the overlap zone.

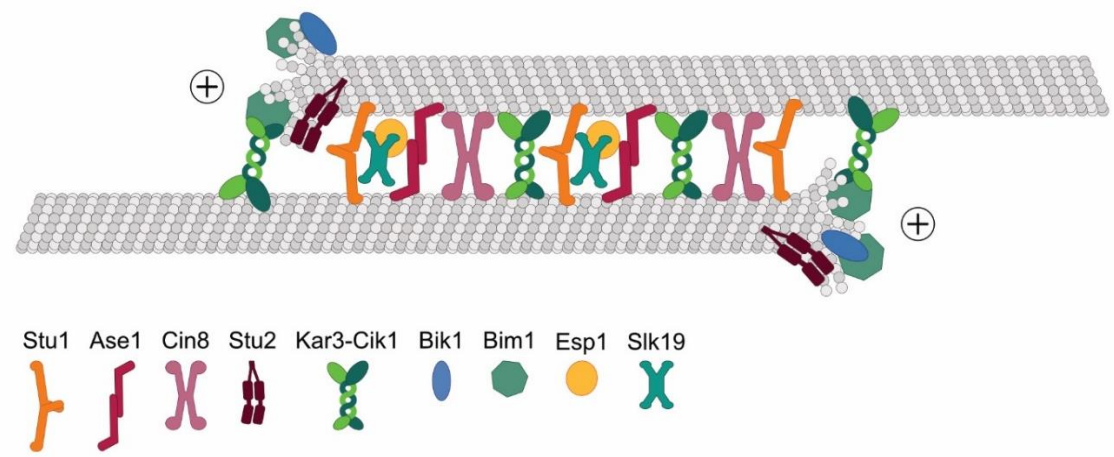

Figure I-13: Components of the anaphase spindle midzone. The figure gives an overview over midzone proteins in budding yeast. The shown midzone proteins are required for anaphase spindle stabilization and crosslinking (Stu1, Ase1, Kar3-Cik1), for ipMT sliding (motor protein Cin8) and regulated MT elongation (MT-polymerase Stu2, Bik1, Bim1). Moreover, Ase1 is the main midzone organizer and recruits other midzone specific proteins. Esp1 and Slk19 are required for a centered and restricted midzone assembly.

There are several proteins that mediate the above-mentioned functions (illustrated in Figure I-13): Stu2 localizes along the anaphase spindles and at MT plus ends and promotes spindle elongation due to its MT polymerase activity (P. J. Wang & Huffaker, 1997),(Severin et al., 2001),(Podolski et al., 2014). Also the plus end-binding protein Bik1 (CLIP-170 homolog) promotes the MT polymerization in anaphase (Gardner, Haase, et al., 2008) and requires Bim1 for its plus end binding (Blake-Hodek et al., 2010). The plus end-binding protein Bim1 (EB1 homolog) regulates spindle elongation and later on midzone disassembly (Zimniak et al., 2009). Together with the sliding function of the MT motor protein Cin8 (kinesin-5), this results in coordinated anaphase spindle elongation in anaphase B (Figure I-12) (Kahana et al., 1995),(Straight et al., 1998). The MT-destabilizing kinesin Kip3 counteracts the Stu2 activity and thereby prevents excessive spindle elongation (Severin et al., 2001). The midzone-binding proteins Slk19 and Esp1 localize to the midzone simultaneously at anaphase onset (possibly as a complex) and are required for a centered and restricted midzone assembly due to their FEAR function (described in chapter 1.3.3.3). Thus, Slk19 and Esp1 contribute to anaphase spindle stability and dynamics (Stegmeier et al., 2002). Moreover, Slk19 also has a second additional function for anaphase spindle stability (as described in more detail in chapter 1.5.4.3) (Jensen et al., 2001),(Khmelinskii et al., 2007), (Stegmeier et al., 2002). Also Stu1 binds to the midzone and ensures anaphase spindle integrity due to its rescue function (Yin et al., 2002).

The most important key players at the mitotic spindle and at the anaphase midzone are described in more detail in the following.

1.5 MAPs – key players at the mitotic spindle and KTs

1.5.1 Microtubule motors

MT motor proteins can bind and move along the lattice of MTs. They generate force by converting chemical energy (adenosine triphosphate (ATP) hydrolysis) into mechanical energy (motion). Thus, MT motors can fulfill various important functions such as cargo transport, MT alignment during spindle establishment, balanced inward and outward force generation at the mitotic spindle, controlled crosslinking and sliding of ipMTs in anaphase and chromosome movement. Budding yeast has six kinesin-like motors (Kar3, Cin8, Kip1, Kip2, Kip3 and Smy1) and one dynein (Winey & Bloom, 2012). The budding yeast dynein is a cytoplasmic minus end-directed motor protein and plays a key role in spindle positioning during mitosis (Li et al., 1993),(Eshel et al., 1993). Especially important for chromosome segregation are the nuclear kinesins Kar3, Cin8, Kip1, Kip3 since they facilitate bipolar spindle establishment and stability (Hildebrandt & Hoyt, 2000).

1.5.1.1 The kinesin-5 motors Kip1 and Cin8

The budding yeast kinesin-5 motors, Kip1 and Cin8, are bipolar homotetrameric complexes with two motor domains at each side of the molecule. The tetrameric structure of Kip1 and Cin8 allows their MT-crosslinking function (Hildebrandt & Hoyt, 2000),(D. M. Gordon & Roof, 1999),(Hildebrandt et al., 2006). Kip1 and Cin8 have overlapping functions in bipolar spindle assembly since they generate an outward force at the spindle by sliding antiparallel MTs apart via plus end-directed motility. Thus, Kip1 and Cin8 oppose the inward-directed force generated by the kinesin-14 Kar3 (described below in part 1.5.1.2) (Roof et al., 1992),(W. S. Saunders & Hoyt, 1992),(Straight et al., 1998). In budding yeast, either the kinesin-5 Kip1 or Cin8 is required for viability and deletion of both leads to mitotic arrest (Roof et al., 1992),(M. A. Hoyt et al., 1992). In metaphase, Kip3 and Cin8 additionally contribute to chromosome congression (positioning of chromosomes in the middle between the opposing spindle poles) by regulating the disassembly of long kMTs at their plus ends (Gardner, Bouck, et al., 2008). During anaphase B, Kip1 and Cin8 are required for spindle elongation in the slow phase and the fast phase respectively (Straight et al., 1998),(Winey & Bloom, 2012). Cin8 and Kip1 are phosphoregulated during the cell cycle. Clb/Cdc28-dependent phosphorylation of Cin8 and Kip1 promotes bipolar spindle formation (Chee & Haase, 2010) and dephosphorylation of Cin8 by Cdc14 at anaphase onset is required for anaphase spindle dynamics (Roccuzzo et al., 2015). The latter function is mediated by Cdc14-dependent dephosphorylation of the midzone organizing and MT-crosslinking protein Ase1, which in turn recruits Cin8 to the spindle midzone thereby promoting antiparallel MTs sliding (Khmelinskii et al., 2009). A common function of Ase1 with Cin8 (and other kinesin-5 motors) is the ability to crosslink MTs (Kapitein et al., 2005),(Shapira

et al., 2017). This common function might also explain the synthetic lethality of *Δase1* and *Δcin8* (Schuyler et al., 2003).

1.5.1.2 The kinesin-14 motor Kar3

The minus end-directed kinesin-14, Kar3 (Endow et al., 1994), forms heterodimers by associating with either of the paralogous proteins Vik1 or Cik1. The formation of heterodimeric Kar3-Vik1 or Kar3-Cik1 complexes results in distinct cellular localizations and functions of this MT motor protein (Page et al., 1994),(Manning et al., 1999),(Barrett et al., 2000). Kar3 possesses two MT-binding domains: the motor domain located at the C-terminus and a putative MT-binding domain at the N-terminus (Meluh & Rose, 1990). The interaction of Kar3 with Cik1 is required for functional MT binding via the Kar3 N-terminus (non-motor domain) and also Vik1 interaction promotes the localization of Kar3 to MTs (Allingham et al., 2007),(Page et al., 1994). The Kar3-Vik1 complex localizes to the SPBs in meta- and anaphase, while the Kar3-Cik1 complex localizes to the metaphase and anaphase spindle (Gardner, Haase, et al., 2008).

Kar3 is suggested to allow crosslinking and sliding of antiparallel MTs (Meluh & Rose, 1990) and to produce an inward-directed force at the spindle thereby opposing the outward-directed force generated by Cin8 and Kip1 (W. S. Saunders & Hoyt, 1992),(W. Saunders, Lengyel, et al., 1997). Supportingly, deletion of Kar3 can partially rescue the spindle collapse in cells with mutated *cin8* and *Δkip1* (W. S. Saunders & Hoyt, 1992),(M. A. Hoyt et al., 1993). Consequently, deletion of Kar3 should result in increased metaphase spindles since the outward force generated by Cin8 and Kip1 is not antagonized. However, deletion of Kar3 does not show an increased spindle length (W. Saunders, Lengyel, et al., 1997). In contrast, loss of Kar3 function leads to large-budded cells with short metaphase spindles, abnormal spindle morphology and reduced viability (Meluh & Rose, 1990),(W. Saunders, Hornack, et al., 1997),(W. Saunders, Lengyel, et al., 1997). Moreover, overexpression of Kar3 only leads to a slight reduction in metaphase spindle length compared to wild type (*WT*), but not to a metaphase spindle collapse (W. Saunders, Lengyel, et al., 1997). These partially conflicting data suggest that the generation of inward-directed force at the spindle is not the only function of Kar3 at the spindle.

The localization of Kar3-Cik1 to the metaphase spindle is additionally required for the alignment of ipMTs along the metaphase spindle axis. This is achieved by movement of Kar3-Cik1 towards the MT minus end and simultaneous tethering of the crosslinked MT from the opposite SPB towards the spindle axis (Figure I-14). Proper alignment of antiparallel MTs facilitates the binding of the kinesin-5 Cin8 and thus allows the generation of an outward force at the spindle and bipolar spindle establishment (Hepperla et al., 2014) (Figure I-14). This might be one explanation why deletion of Kar3 does not result in increased spindle length (mentioned above). In metaphase, the Kar3-Cik1 complex seems to be of greater importance for bipolar spindle formation and elongation compared to Kar3-

Vik1, since metaphase spindles in *Δcik1* cells are significantly shorter compared to *Δvik1* cells (Gardner, Haase, et al., 2008),(Hepperla et al., 2014).

In anaphase, the Kar3-Cik1 complex localizes specifically to the MT plus ends where it can be observed as dots at the anaphase spindle. Here, Kar3 and Cik1 are suggested to crosslink ipMTs thereby contributing to anaphase spindle stabilization (Gardner, Haase, et al., 2008),(Hepperla et al., 2014).

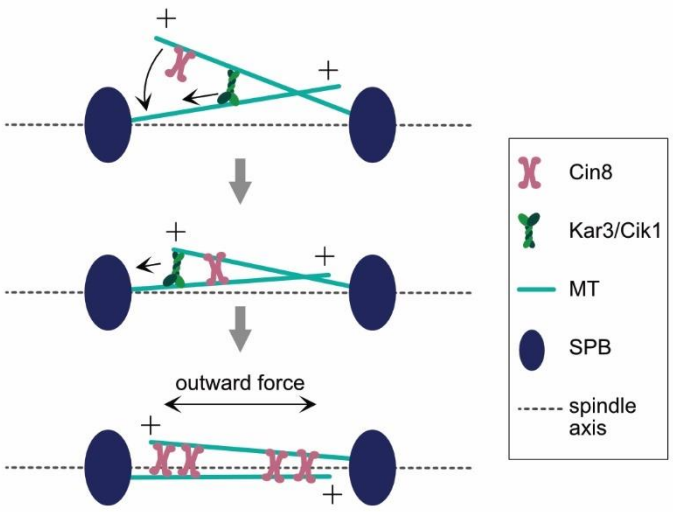

Figure I-14: MT alignment via MT motor proteins. Adapted from (Hepperla et al., 2014). Localization of the Kar3-Cik1 motor to the metaphase spindle aligns ipMTs along the metaphase spindle axis. The crosslinked MT from the opposite SPB is tethered towards the spindle axis by movement of Kar3-Cik1 towards the MT minus end. Alignment of antiparallel MTs facilitates the binding of the kinesin-5 Cin8. This allows the generation of outward force at the spindle and bipolar spindle establishment. MT = microtubule, ipMT = interpolar MT, SPB = spindle pole body.

In addition, Kar3 and Cik1 promote efficient bipolar spindle assembly and KT clustering also by bundling and aligning parallel MTs. This parallel MT-bundling functions via a trimeric complex of Kar3, Cik1 and the plus end-binding protein Bim1 (mentioned in chapter 1.4.3.4) (Kornakov et al., 2020).

Additionally, Kar3 localizes to uaKTs and is involved in the poleward movement of KTs once they are recaptured by the lateral surface of MTs (T. U. Tanaka et al., 2005). Moreover, Kar3 was also shown to have an intrinsic function to destabilize MTs (Endow et al., 1994),(Cottingham et al., 1999).

1.5.1.3 The kinesin-8 and MT depolymerase Kip3

The plus end-directed kinesin-8 motor, Kip3, moves to and accumulates at growing MT plus ends, where it specifically functions as MT depolymerase (M. L. Gupta et al., 2006),(Varga et al., 2006). The rate of Kip3-mediated depolymerization at MT plus ends is higher for longer MTs and decreases as MTs shorten (Varga et al., 2006). Furthermore, Kip3 functions cooperatively (Varga et al., 2009) as well as force-dependent (Bugiel et al., 2020) for driving MT depolymerization. At the anaphase midzone, Kip3 opposes the activity of the MT polymerase Stu2 and is required to restrict the length of the overlaps at the midzone (Rizk et al., 2014). Furthermore, Kip3 is needed for timely disassembly of the mitotic spindle (Straight et al., 1998).

1.5.2 Ase1 – a midzone organizing and crosslinking protein

The homodimer Ase1 (Schuyler et al., 2003) belongs to the conserved Ase1/PRC1/MAP65 family and is a major MT-bundling and midzone-organizing protein required for spindle stability (Jiang et al., 1998),(Loïodice et al., 2005),(Yamashita et al., 2005),(Chan et al., 1999),(Juang et al., 1997),(Mollinari et al., 2002). Budding yeast and fission yeast Ase1 as well as the human homolog PRC1 have the ability to efficiently crosslink MTs *in vivo* and *in vitro* and show an intrinsic preference for antiparallel MT crosslinking (Schuyler et al., 2003),(Janson et al., 2007),(Mollinari et al., 2002),(Bieling et al., 2010),(Khmelinskii et al., 2007). In contrast to the dimeric Ase1 in budding yeast, human PRC1 is kept in a monomeric state in early mitosis by Cdk-phosphorylation to prevent premature MT crosslinking. At anaphase onset, PCR1 is then dephosphorylated to induce dimerization and thus MT bundling (Mollinari et al., 2002),(C. Zhu et al., 2006).

Budding yeast Ase1 is a non-essential protein that shows similar expression patterns as the mitotic cyclin Clb2 and is targeted for degradation by APC^{Cdh1} in G1 (Juang et al., 1997),(Hildebrandt & Hoyt, 2001). Ase1 can bind to MTs via its C-terminus, while its dimerization domain is localized at the N-terminus (Khmelinskii et al., 2009). Ase1 can bind to metaphase and anaphase spindles (Schuyler et al., 2003) and its function during the cell cycle is phosphoregulated. Ase1 carries seven Cdk1 consensus sites and is phosphorylated in early mitosis by Cdc28-Clb5 (Ubersax et al., 2003),(Loog & Morgan, 2005),(Khmelinskii et al., 2007).

In metaphase, this phosphorylation is important for spindle stability since it prevents premature spindle elongation and ipMT sliding. Dephosphorylation of Ase1 in metaphase leads to premature recruitment of the kinesin-5 motor Cin8 and this causes ipMT sliding, increased speed of spindle elongation, spindle bending and eventually spindle breakage (Khmelinskii et al., 2009),(W. S. Saunders & Hoyt, 1992),(M. A. Hoyt et al., 1992).

In anaphase, Ase1 localizes specifically to the spindle midzone with a slow turnover rate and deletion of Ase1 leads to defective anaphase spindles (Schuyler et al., 2003),(Khmelinskii et al., 2007). Also in humans, depletion of PRC1 leads to severe spindle defects and defective midzone assembly (Mollinari et al., 2002). At anaphase onset, Ase1 is dephosphorylated by the phosphatase Cdc14 that is released by the FEAR pathway. Cdc14-dependent dephosphorylation of Ase1 at anaphase onset is required to recruit other midzone components that affect anaphase spindle integrity and dynamics. As mentioned above, the kinesin-5 Cin8 requires dephosphorylation of Ase1 for efficient midzone localization and ipMTs sliding (Khmelinskii et al., 2009). The presence of phosphorylated Ase1 in anaphase leads to an enlarged midzone (as assessed by Ase1 and Bim1 localization) probably due to defective spindle elongation and sliding (Stegmeier et al., 2002),(Khmelinskii et al., 2009). Since Ase1 is one of the first proteins that binds to the midzone at anaphase onset, also other midzone components, such as Esp1, Slk19, Bik1, Bim1, Kip3, Stu1 and the Sli15-Ipl1 complex, are dependent on Ase1 (or the correct midzone formation) for their efficient localization to the midzone (Khmelinskii et al., 2007),(Pereira & Schiebel, 2003). Taken together, Ase1 leads to the establishment of a matrix-like network at the anaphase midzone consisting of various MAPs with different functionalities (Schuyler et al., 2003).

1.5.3 Stu1 – a microtubule rescue factor

1.5.3.1 The MAP Stu1 stabilizes the mitotic spindle

The homodimer Stu1 is a member of the conserved **C**ytoplasmic **L**inker **A**ssociated **P**rotein (**CLAP**) family of MT rescue factors and is the functional homolog of human CLASP1 and *Schizosaccharomyces pombe* Cls1 (Yin et al., 2002),(Pasqualone & Huffaker, 1994),(Maiato et al., 2003),(Akhmanova et al., 2001),(Bratman & Chang, 2007),(Funk et al., 2014). CLASPs like Stu1 (as well as members of the XMAP215 protein family) contain conserved TOG domains (TOG = tumor overexpressed gene) that include six HEAT repeats (HEAT = **H**untington, **E**longation Factor 2, Phosphotase **A**2, **T**OR PI-3 kinase). Specific regions within the HEAT repeats, called intra-HEAT-repeat loops, are required for the binding of tubulin dimers (Al-Bassam et al., 2007),(Al-Bassam & Chang, 2011). This ability of CLASP TOG domains, to bind tubulin and recruit it to MTs, is essential for their function in promoting MT rescue and reducing MT catastrophe (Al-Bassam & Chang, 2011),(Majumdar et al., 2018).

Budding yeast Stu1 is an essential protein that localizes to KTs until anaphase, to the metaphase spindle and to the anaphase midzone. Stu1 is required for spindle stabilization and usage of a temperature sensitive (ts) Stu1 mutant (*stu1-ts)* leads to a collapsed mitotic spindle and SPBs (Yin et al., 2002). Stu1 contains two TOG-like (TOGL) domains at its N-terminus: TOGL1 (aa 1–260) and TOGL2 (aa 301–569) (Funk et al., 2014). These TOGL domains possess different functionalities. The TOGL2 domain mainly contributes to the

binding of α- and β-tubulin and is required for MT binding *in vivo* and *in vitro.* The TOGL2 domain constitutes a part of the microtubule-binding domain (MBD) of Stu1 that reaches from aa 461–716. The MBD also includes the serine-rich middle loop (ML) domain (aa 570–716) (Yin et al., 2002),(Funk et al., 2014). This MBD is required to localize Stu1 to the spindles in metaphase and thereby contributes to spindle stabilization by its rescue and crosslinking function. This ability of Stu1 to bind and crosslink MTs was shown *in vivo* and *in vitro* (Funk et al., 2014). The TOGL2 domain of Stu1 contains predicted intra-HEAT-repeat loops (in contrast to TOLG1) and mutations of 4 sites within these regions abolished its MT-binding ability (Funk et al., 2014). In contrast to TOGL2, TOGL1 only binds weakly to tubulin or MTs (Majumdar et al., 2018) but is required for localizing Stu1 to KTs in metaphase (Funk et al., 2014). In addition, Stu1 also requires dimerization via its domain 4 (D4) (aa 1182–1513) for efficient KT localization and for MT binding (Funk et al., 2014). In *stu1ΔTOGL1* cells, kMTs are significantly shorter compared to *WT* cells indicating that Stu1 localization at the KTs in metaphase is required for kMT stability (Funk et al., 2014).

Interestingly, the binding modes of Stu1 change at the meta-to-anaphase transition: Stu1 localization at KTs is lost and Stu1 localizes only to the anaphase spindle midzone dependent on Ase1 (Khmelinskii et al., 2007). Stu1 binding to the anaphase spindle midzone is not dependent on its MBD (as it is for metaphase spindle binding) but is only dependent on its D4 domain. Here, it is not differentiable whether dimerization is additionally required for anaphase spindle localization. The D4-dependent binding might indicate an indirect binding of Stu1 via other midzone proteins in anaphase (Funk et al., 2014).

Moreover, Stu1 together with the KT protein Slk19 facilitates the capturing of uaKTs. Interestingly, this process interferes with the spindle stabilizing function of Stu1, thus promoting KT capturing. The role of Stu1 and Slk19 in this process is described in more detail in the following (Ortiz et al., 2009),(Funk et al., 2014),(Kolenda et al., 2018).

1.5.3.2 Stu1-Slk19 sequestering facilitates KT recapturing by MT network reorganization

In *S. cerevisiae,* KTs are detached in S-phase of mitosis during replication of the centromeric region and also other environmental influences might induce the detachment of KTs during mitosis. In any case, the cell must ensure a timely recapturing of those KTs to allow the formation of a bipolar metaphase spindle and faithful chromosome segregation (Kitamura et al., 2007),(Kolenda et al., 2018).

Upon KT detachment, the two MAPs, Stu1 and Slk19, co-polymerize interdependently at uaKTs and form large clusters (referred to as sequestering, illustrated in Figure I-16) (the dynamic KT protein Slk19 is described in more detail in the next chapter 1.5.4) This sequestering process leads to withdrawal of Stu1 from the spindle, which leads to a spindle collapse and an increased pool of free tubulin. This promotes a reorganization of the MT network and the formation of highly dynamic nrMTs that facilitate capturing of uaKTs by KT attachment to the lateral MT lattice (Kolenda et al., 2018),(K. Tanaka et al., 2007) (process illustrated in Figure I-15). When more than one KT is detached, Stu1-Slk19 co-

polymerization is also required to group these uaKTs and this furthermore promotes their timely capturing (Kolenda et al., 2018),(Richmond et al., 2013),(Zhang et al., 2006).

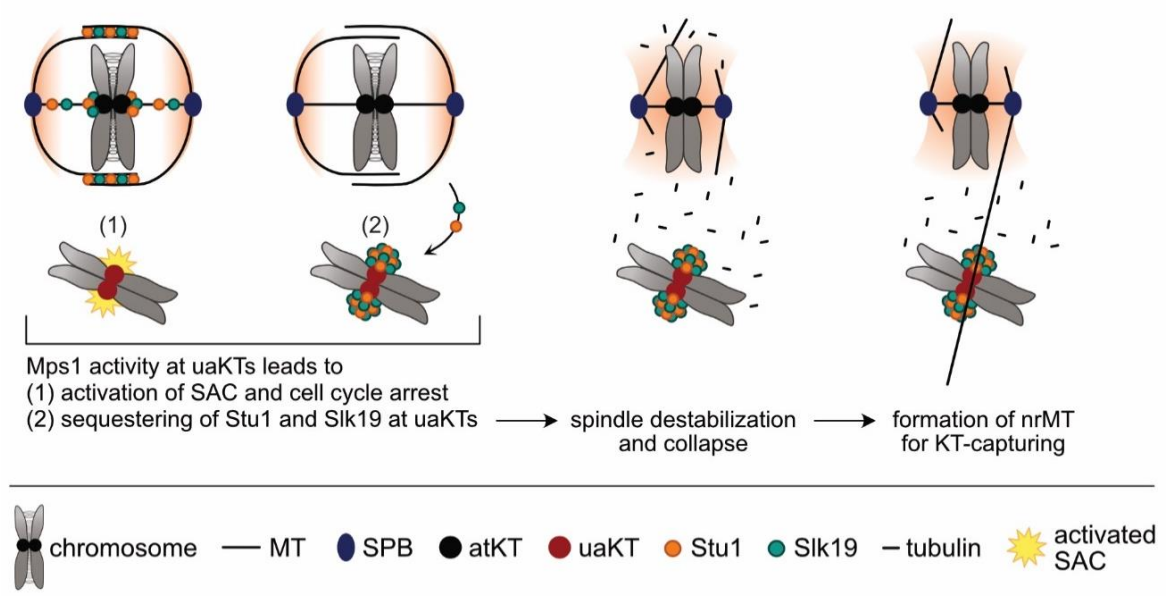

Figure I-15: Reorganization of the MT network promotes KT capturing. Figure is based on (Kolenda et al., 2018)**.** Unattached KTs (uaKTs) activate the spindle assembly checkpoint (SAC) and lead to Stu1-Slk19 co-polymerization (sequestering) at uaKTs. Withdrawal of Stu1 and Slk19 from the spindle due to the sequestering process results in spindle destabilization and collapse. Free tubulin is used for the formation of highly dynamic nuclear random MTs (nrMTs) that are ideal for capturing of uaKTs. KT = kinetochore, MT = microtubule, SPB = spindle pole body.

Three Stu1 domains are essential for the sequestering process: (1) the TOGL1 domain, which is the KT localization domain of Stu1 (Funk et al., 2014), (2) the D4 domain, which is the dimerization domain of Stu1 (Funk et al., 2014) and (3) the C-terminal loop (CL domain) (Funk et al., 2014), which is left as a potential Slk19 interaction domain. For Slk19, the domains required for sequestering are so far unknown.

According to the current model of the sequestering process (illustrated in Figure I-15 and I-16), the interaction between Stu1 and Slk19 is indispensable for their co-polymerization into large clusters (sequestering) at uaKTs (Kolenda et al., 2018). In nocodazole (Nz)-treated cells, depletion of Stu1 leads to a Slk19-sequestering defect and, *vice versa*, deletion of Slk19 leads to a Stu1-sequestering defect. In both cases, however, a basal amount of Slk19 or Stu1 is seen at uaKTs respectively that bind via other interaction partners at the KT (Kolenda et al. 2018).

Upon KT detachment, the SAC is activated and similar to the process of SAC-activation, also the Stu1-Slk19 sequestering process is dependent on Spc105 and its phosphorylation by

the Mps1 kinase (Kolenda et al., 2018) (Figure I-15 and I-16). Mps1 phosphorylates Spc105 at the six N-terminal MELT sites upon KT-MT detachment (London et al., 2012) and this is suggested to recruit Stu1 to the uaKT via the TOGL1 domain (Funk et al., 2014) (Figure I-16). Interfering with Spc105 phosphorylation by using the mutants *mps1-as1* or *spc105-6A* (constitutively dephosphorylated Spc105) abolished basal Stu1-binding to uaKTs while basal binding of Slk19 was still present (Kolenda et al. 2018). Thus, for Stu1 it seems evident that its basal localization at uaKTs depends on Spc105 and its phosphorylation status. For Slk19, however, basal binding at uaKTs is independent of the Spc105 phosphorylation status, and the question remains open which protein mediates its basal binding at uaKTs and whether this binding might as well be required to initialize the sequestering process.

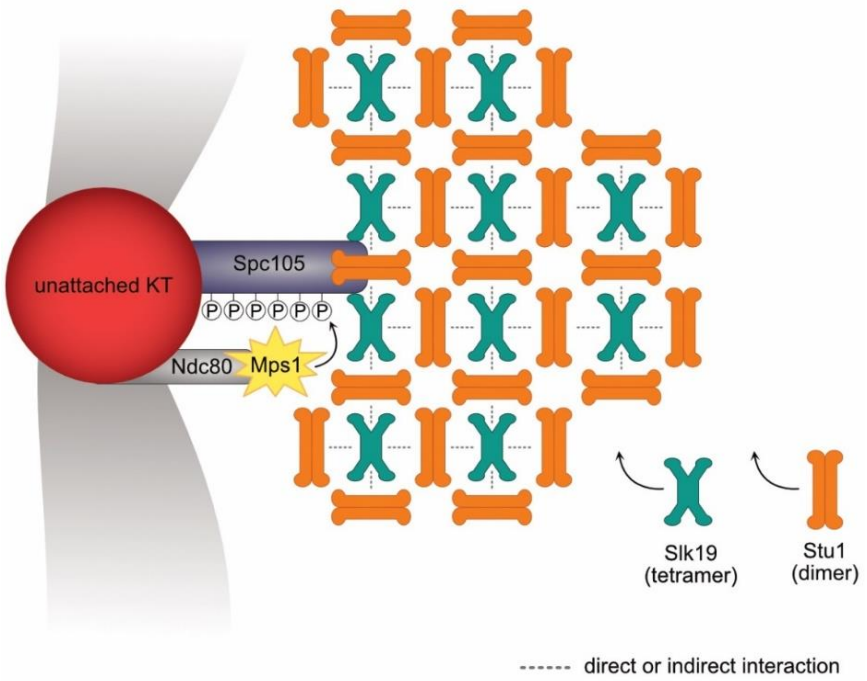

Figure I-16: Model of Stu1-Slk19 sequestering. Figure is based on (Kolenda et al., 2018). Upon KT detachment, the checkpoint kinase Mps1 phosphorylates Spc105 at its MELT-sites which recruits Stu1 to uaKTs. Stu1 dimers and Slk19 tetramers co-polymerize interdependently at uaKTs which results in the formation of large clusters (Stu1-Slk19 sequestering). KT = kinetochore, uaKT = unattached KT.

1.5.4 Slk19 – a dynamic kinetochore passenger

In budding yeast, Slk19 is a non-essential protein required for accurate chromosome segregation in mitosis (Pfiz et al., 2002). This importance of Slk19 in chromosome segregation is due to several functions during mitosis, that are summarized in the following.

1.5.4.1 Slk19 and its role at the KT

The homotetramer Slk19 (**S**ynthetically **l**ethal with *Δ**k**ar3*) (De Wulf et al., 2003),(Zeng et al., 1999) is a dynamic KT- and MT-associating protein. It localizes to attached KTs (atKTs) throughout mitosis and localizes to the spindle midzone in anaphase (Zeng et al., 1999), (Sullivan et al., 2001),(Khmelinskii & Schiebel, 2008).

The human protein most homologous to Slk19 is the KT passenger and MT-binding protein CENP-F (mitosin) (Kitagawa & Hieter, 2001),(Varis et al., 2006),(Richmond et al., 2013). Similar to Slk19, CENP-F localizes to the outer KT until anaphase onset and then localizes to the spindle midzone (Rattner et al., 1993). CENP-F is important for centromeric cohesion (Rattner et al., 1993), KT clustering (Holt et al., 2005), KT-MT attachments (J. Feng et al., 2006) and MT dynamics (Pfaltzgraff et al., 2016).

In fission yeast (*S. pombe*), the protein most homologous to Slk19 is Alp7/Mia1 (Sato et al., 2003). Alp7 co-localizes with the two KT clusters and localizes to the spindle and SPBs. Furthermore, Alp7 has the ability to bind and crosslink MTs (Sato et al., 2004). In comparison, whether Slk19 can bind to the spindle or crosslink MTs is so far unknown and elucidating this point is one part of this work.

As described above, budding yeast Slk19 is required for KT clustering of uaKTs by its ability to interdependently sequester with Stu1 at uaKTs (Kolenda et al., 2018),(Richmond et al., 2013). This process plays an important role for timely bipolar KT attachment after disturbances of the KT attachments (Zhang et al., 2006),(Kolenda et al., 2018). Also during an undisturbed budding yeast cell cycle (with attached KTs and no activation of the Stu1-Slk19 sequestering process), the KTs of the 16 chromosomes are held tightly together and can be observed as two KT clusters during chromosome segregation (Jin et al., 2000). Slk19 was shown to be also required for this described clustering of attached KTs (Richmond et al., 2013) similar to the function of its human homolog CENP-F (Holt et al., 2005). Slk19 seems to function together with Dam1 in clustering KTs. These two parallel pathways seem to influence each other, since depletion of Dam1 leads to disturbed Slk19 localization at the centromeres and, *vice versa*, *Δslk19* cells hinders efficient centromeric Dam1 localization (Mittal et al., 2019). The fact that Slk19 is suggested to form homotetramers (De Wulf et al., 2003) makes is especially suited for the function of holding several KTs together.

Upon bipolar KT attachment in metaphase, the sister chromatids are slightly separated from each other although still connected, as seen by the slight separation of the two KT clusters (an observation called “breathing”) (Winey & O’Toole, 2001). This separation is reversible

e.g. by treatment with the MT-depolymerizing agent nocodazole (Haering & Hasmyth, 2003). This observation is referred to as "centromeric elasticity" (Zhang et al., 2006). Apparently, Slk19 is required to maintain this elastic behavior since *Δslk19* cells show a loss of the observed centromeric elasticity (Zhang et al., 2006). The N-terminus seems to play a crucial role for this function (Zhang et al., 2006). Defects in chromosome cohesion could be one explanation for the lost elasticity in *Δslk19* cells. Although Slk19 was shown to physically interact with the cohesion complex subunit Scc1 (cohesion complex holds sister chromatids together until anaphase), it neither influenced the timing of its cleavage nor its binding to the centromeric region (Zhang et al., 2006). Thus, a defect in chromosome cohesion is not the explanation for the lost centromeric elasticity in *Δslk19* cells. However, Pds1-depleted *Δslk19* cells show premature Scc1 cleavage (as mentioned above in chapter 1.3.3.2) and premature loss of pericentric cohesion as measured by the signal intensity of the cohesion subunit Smc3 at the cohesion barrel. This might indicate a role of Slk19 at the chromatin (Lianga et al., 2018). This also reminds of the function of its human homolog CENP-F (Rattner et al., 1993) and might be in line with the described phenotype of "lost centromeric elasticity". Notably however, *Δslk19* alone does not lead to premature Scc1 degradation and therefore this phenotype should not be observable in cells with sole Slk19 depletion (Lianga et al., 2018). Clearly there is further research needed to illuminate the roles of Slk19 at the pericentromeric chromatin.

1.5.4.2 Slk19 plays a role for mitotic spindle stability

In budding yeast, Slk19 must play a role for spindle stability in metaphase, since *Δslk19* cells exhibit shorter metaphase spindles compared to *WT* cells (Zeng et al., 1999) and show an increased appearance of nrMTs (Kolenda et al., 2018). Both short spindles and the appearance of nrMTs are indications for a compromised mitotic spindle. Furthermore, deletion of Slk19 is synthetically lethal with *Δkar3* (as the name of Slk19 suggests: **S**ynthetically **l**ethal with *Δ**k**ar3*) and *Δslk19 kar3-ts* double mutants arrest with short spindles in metaphase (Zeng et al., 1999). The domains responsible for synthetic lethality with *Δkar3* have been identified and include the two middle coiled coil (cc) regions, reaching from aa 300–410 and aa 410–502, as well as the C-terminal region aa 709–821 (Havens et al., 2010). However, the exact functional roles of Slk19 at the metaphase spindle including the function of the above-mentioned domains remain largely uncertain so far. Moreover, Slk19 was also shown to influence the dynamics of MTs at the metaphase spindle: *Δslk19* cells show increased MT dynamics which leads to oscillations in metaphase spindle length, dynamic changes of the nuclear shape, premature nuclear movement through the mother-bud neck and partial chromatin division (while maintaining intact Scc1) (Zhang et al., 2006).

In anaphase, the presence of Slk19 at the anaphase spindle midzone was shown to be required for spindle stability (Sullivan et al., 2001). At anaphase onset, Esp1 cleaves Slk19 at aa 77, however this is not required for spindle stability since uncleavable Slk19 only shows mild effects on anaphase spindle stability and localizes comparable to *WT* at the spindle midzone

and at atKTs (Sullivan et al., 2001). As mentioned above (in chapter 1.3.3.3), Slk19 is a major component of the FEAR pathway at anaphase onset. The FEAR pathway contributes to the correct assembly of the midzone as well as anaphase spindle dynamics and stability (Pereira & Schiebel, 2003),(Woodbury & Morgan, 2006),(Khmelinskii et al., 2007), (Higuchi & Uhlmann, 2005). Thus, the FEAR function of Slk19 contributes to spindle stability. The Slk19 domains required for its FEAR function were determined and include the N-terminal globular domain (GD) reaching from aa 1–220 and the central coiled coil domain reaching from aa 300–410 (Havens et al., 2010). The exact functions of these domains are so far unknown.

Moreover, there are several indications that Slk19 influences the dynamics of spindle elongation in anaphase also independently of the FEAR pathway (described in the following chapter).

1.5.4.3 FEAR-independent function of Slk19 influences anaphase spindle dynamics

Esp1 and Slk19 (components of the FEAR pathway, described in detail in chapter 1.3.3.3) are interdependent for their midzone binding and both proteins are dependent on Ase1 dephosphorylation (FEAR pathway) for their localization to the anaphase midzone (Sullivan & Uhlmann, 2003). Thus, the FEAR pathway is required for the proper localization of its own effector proteins (Esp1 and Slk19). However, this specific localization at the anaphase midzone is, in turn, not required for a functional FEAR pathway: The C-terminal Slk19 deletion mutant, lacking aa 709–821, does not localize to the mitotic spindle or to KTs, however, cells carrying *slk19Δ709-821* maintain a functional FEAR pathway (Havens et al., 2010). Since a functional FEAR pathway can be maintained independently of the anaphase midzone localization of Slk19 (and consequently also of Esp1), this is a first indication that the localization of Slk19 together with Esp1 at the anaphase spindle midzone might have additional direct roles for anaphase spindle stability. Most importantly, although the FEAR pathway is functional in *slk19Δ709-821* cells, these cells show compromised anaphase spindles with less ipMT reaching the spindle center (Havens et al., 2010). This strongly suggests that Slk19 must play a role for spindle stability independently of its FEAR function.

In *WT* cells, there is a short intermediate pause during anaphase B in between the fast and the slow phase of spindle elongation (Kahana et al., 1995). This pause is lost in *Δslk19* cells as well as in the mutants *slk19ΔGD* (both with defective FEAR pathway) and in *slk19Δ709-821* (with functional FEAR). Moreover, the spindle elongation rate is increased in the fast phase in those cells. A common characteristic of FEAR-defective cells including *Δspo12*, *Δslk19* and *slk19ΔGD* cells is a longer residence time in anaphase and showing longer spindles at the end of anaphase compared to *WT*. However, in contrast to these Slk19 mutant cells, *Δspo12* cells did not show a loss of pause during anaphase B. Thus, this observation is probably due to an FEAR-independent function of Slk19 (Havens et al., 2010).

Thus, Slk19 clearly influences spindle dynamics not only in metaphase but also in anaphase by unknown mechanisms.

1.6 Objectives of this work

What is the role of Slk19 in the sequestering process?

In the presence of uaKTs, Stu1 and Slk19 co-polymerize to large clusters interdependently at uaKTs. This sequestering of Stu1 and Slk19 at uaKTs is of great importance for KT recapturing and thus for accurate chromosome segregation. So far, it is not known how the co-polymerization of the two proteins is initialized. Since Slk19 binds to uaKTs in a basal manner when sequestering was prohibited (Kolenda et al., 2018), this led to the question whether this constitutive Slk19-binding might be involved in the initiation of sequestering. Therefore, one aim of this study was to answer this question and to illuminate the role of Slk19 in the sequestering process. To answer this question, the aim was to identify all Slk19-domains required for the sequestering process at uaKTs as well as their functional relevance such as Stu1-interaction, KT binding and homotetramerization. To specifically interfere with Slk19 KT binding it was also aimed to identify the Slk19 interaction partner at the KTs.

What functional role does Slk19 play for metaphase spindle stabilization?

The withdrawal of the MT rescue factor Stu1 from the spindle by sequestering at uaKTs is presumably required to destabilize the mitotic spindle, which in turn allows the formation of nrMTs that facilitate capturing of uaKTs (Kolenda et al., 2018). Also for Slk19 there is clear evidence that it plays a role for metaphase spindle stability (Zeng et al., 1999). Thus, the withdrawal of Slk19 might work in concert with the withdrawal Stu1 (by the sequestering process at uaKTs) to destabilize the metaphase spindle in presence of uaKTs. However, it is so far unknown what functional role Slk19 performs at the spindle and whether it localizes to the metaphase spindle directly or indirectly. Here we wanted to shed light on the mechanistic functions of Slk19 for spindle stabilization and characterize specific Slk19 spindle localization defects. These questions were addressed by performing *in vivo* and *in vitro* experiments.

Can Slk19 confer MBD-independent Stu1 binding to the anaphase midzone?

Slk19 plays a role in the FEAR pathway (Stegmeier et al., 2002) and thus is required for the establishment of an organized midzone in anaphase (Khmelinskii et al., 2007). At anaphase onset, the binding mode of Stu1 to the spindle switches from a MBD-dependent binding in metaphase to a D4-dependent binding at the midzone in anaphase. This suggests an indirect binding of Stu1 via other midzone proteins (Funk et al., 2014). So far, it is not known how this altered binding mode is achieved. In this study, it is analyzed whether the FEAR function of Slk19 might regulate Stu1 binding to the midzone in anaphase or whether Slk19 might be the direct binding partner of Stu1 at the midzone.

2 Materials

2.1 *Saccharomyces cerevisiae* strains

Genotypes of all yeast strains used in this study are listed in the table below. All yeast strains that are used in this study are based on YPH499 (Sikorski & Hieter, 1989).

Strain	Genotype	Figure
YSN3095	*MATa ade2-101ochre trp1-Δ63 leu2-Δ1 ura3-52 his3-Δ200 lys2-801ambre bar1::loxP SPC72-ECFP-kanMX4 MTW1-3mcherry::hphNT1 SLK19-yeGFP::HIS3MX6*	Figure 1A
YSN3175	*MATa trp1-Δ63 leu2-Δ1 ura3-52 his3-Δ200 lys2-801ambre bar1::loxP SPC72-ECFP-kanMX4 MTW1-3mcherry::hphNT1 ade2Δ (pADE2 -321upstream start to aa1-68)::loxP-BleR-loxP-pADH1-OsTIR1-9Myc::ADE2 SLK19-yeGFP-klTRP1 STU2-IAA17::klURA3*	Figure 1A b
YJO2718[1]	*MATa bar1::loxP trp1-Δ63 leu2-Δ1 ura3-52 his3-Δ200 lys2-801ambre NUF2-3mcherry::natNT2 ade2-101ochre::PADH1-OsTIR1-9Myc::ADE2 STU1-IAA17::KanMX4 SPC72-eCFP::hphNT1 SLK19-yeGFP::HIS3MX6*	Figure 1A c
YSN3191	*MATa trp1-Δ63 leu2-Δ1 ura3-52 his3-Δ200 lys2-801ambre bar1::loxP SPC72-ECFP-kanMX4 MTW1-3mcherry::hphNT1 ade2Δ (pADE2 -321upstream start to aa1-68)::loxP-BleR-loxP-pADH1-OsTIR1-9Myc::ADE2 SLK19-yeGFP-klTRP1 STU2-IAA17::klURA3 STU1-IAA17::HIS3MX6*	Figure 1A d
YSN3209	*MATa trp1-Δ63 leu2-Δ1 ura3-52 his3-Δ200 lys2-801ambre bar1::loxP SPC72-ECFP-kanMX4 MTW1-3mcherry::hphNT1 ade2Δ (pADE2 -321upstream start to aa1-68)::loxP-BleR-loxP-pADH1-OsTIR1-9Myc::ADE2 SLK19-yeGFP-klTRP1 Ndc80-IAA17::klURA3*	Figure 1B
YSN2817	*MATa trp1-Δ63 leu2-Δ1 ura3-52 his3-Δ200 lys2-801ambre bar1::loxP ade2-101ochre::pADH1-OsTIR1-9Myc::ADE2 NUF2-3mcherry::natNT2 SPC72-yeCFP::hphNT1 SPC105-IAA17-3HA::HIS3 SLK19-yeGFP-klTRP1 cdc20::kanMX6-pGAL1-3HA-CDC20*	Figure 1C a
YSN3203	*MATa bar1::loxP trp1-Δ63 leu2-Δ1 ura3-52 his3-Δ200 lys2-801ambre NUF2-3mcherry::natNT2 ade2-101ochre::PADH1-OsTIR1-9Myc::ADE2 STU1-IAA17::KanMX4 SPC72-eCFP::hphNT1 SLK19-yeGFP::HIS3MX6 cdc20::klURA3-pGAL1-3HA-CDC20 SPC105-IAA17::klTRP1*	Figure 1C b
YSN2915[2]	*MATa ade2-101ochre trp1-Δ63 leu2-Δ1 ura3-52 his3-Δ200 lys2-801ambre bar1::loxP SPC72-ECFP-kanMX4 MTW1-3mcherry::hphNT1 Δslk19::HIS3MX6 lys2-801ambre:PrSLK19-FLAG-SLK19-NLS-EGFP-LYS2*	Figure 3A a, Figure 8C
YSN2826	*MATa ade2-101ochre trp1-Δ63 leu2-Δ1 ura3-52 his3-Δ200 lys2-801ambre bar1::loxP SPC72-ECFP-kanMX4 MTW1-3mcherry::hphNT1 Δslk19::HIS3MX6 lys2-801ambre:PrSLK19-FLAG-slk9Δ(1-77)-NLS-GFP-LYS2*	Figure 3A a
YSN2842[2]	*MATa ade2-101ochre trp1-Δ63 leu2-Δ1 ura3-52 his3-Δ200 lys2-801ambre bar1::loxP SPC72-ECFP-kanMX4 MTW1-3mcherry::hphNT1 Δslk19::HIS3MX6 lys2-801ambre:PrSLK19-FLAG-slk19Δ(aa1-220)-NLS-GFP-LYS2*	Figure 3A a, Figure 8C
YSN3044[2]	*MATa ade2-101ochre trp1-Δ63 leu2-Δ1 ura3-52 his3-Δ200 lys2-801ambre bar1::loxP SPC72-ECFP-kanMX4 MTW1-3mcherry::hphNT1 Δslk19::HIS3MX6 lys2-801ambre:PrSLK19-FLAG-slk19Δ(aa503-711)-NLS-GFP::LYS2*	Figure 3A a, Figure 8C
YSN2877	*MATa ade2-101ochre trp1-Δ63 leu2-Δ1 ura3-52 his3-Δ200 bar1::loxP SPC72-ECFP-kanMX4 MTW1-3mcherry::hphNT1 Δslk19::HIS3MX6 lys2-801ambre:PrSLK19-FLAG-slk19Δ(aa300-502)-NLS-EGFP-LYS2*	Figure 3A b
YSN2963[2]	*MATa ade2-101ochre trp1-Δ63 leu2-Δ1 ura3-52 his3-Δ200 lys2-801ambre bar1::loxP SPC72-ECFP-kanMX4 MTW1-3mcherry::hphNT1 Δslk19::HIS3MX6 lys2-801ambre:PrSLK19-FLAG-slk9Δ(aa300-410)-NLS-GFP-LYS2*	Figure 3A c, Figure 8C
YSN2879[2]	*MATa ade2-101ochre trp1-Δ63 leu2-Δ1 ura3-52 his3-Δ200 lys2-801ambre bar1::loxP SPC72-ECFP-kanMX4 MTW1-3mcherry::hphNT1 Δslk19::HIS3MX6 lys2-801ambre:PrSLK19-FLAG-slk19Δ(aa410-500)-NLS-EGFP-LYS2*	Figure 3A d, Figure 8C
YSN3126	*MATa ade2-101ochre trp1-Δ63 leu2-Δ1 ura3-52 his3-Δ200 lys2-801ambre bar1::loxP SPC72-ECFP-kanMX4 MTW1-3mcherry::hphNT1 Δslk19::HIS3MX6 lys2-801ambre:PrSLK19-FLAG-slk19Δ(aa711-758)-NLS-EGFP-LYS2*	Figure 3A e
YSN2964	*MATa ade2-101ochre trp1-Δ63 leu2-Δ1 ura3-52 his3-Δ200 lys2-801ambre bar1::loxP SPC72-ECFP-kanMX4 MTW1-3mcherry::hphNT1 Δslk19::HIS3MX6 lys2-801ambre:PrSLK19-FLAG-slk9Δ(760-821)-NLS-GFP-LYS2*	Figure 3A e

YSN2881[2]	*MATa ade2-101ochre trp1-Δ63 leu2-Δ1 ura3-52 his3-Δ200 lys2-801ambre bar1::loxP SPC72-ECFP-kanMX4 MTW1-3mcherry::hphNT1 Δslk19::HIS3MX6 lys2-801ambre:PrSLK19-FLAG-slk19Δ(aa709-821)-NLS-EGFP-LYS2*	Figure 3A e, Figure 8C
YSN3085[2]	*MATa ade2-101ochre trp1-Δ63 leu2-Δ1 ura3-52 his3-Δ200 lys2-801ambre bar1::loxP SPC72-ECFP-kanMX4 MTW1-3mcherry::hphNT1 Δslk19::HIS3MX6 lys2-801ambre:PrSLK19-FLAG-slk19Δ(aa1-708)-NLS-EGFP-LYS2*	Figure 3A f, Figure 8C
YSN3402	*MATa ade2-101ochre trp1-Δ63 leu2-Δ1 ura3-52 his3-Δ200 lys2-801ambre bar1::loxP SPC72-ECFP-kanMX4 MTW1-3mcherry::hphNT1 Δslk19::HIS3MX6 lys2-801ambre:PrSLK19-FLAG-slk19(aa300-502aa709-821)-NLS-GFP::LYS2*	Figure 3B a
YSN3403	*MATa ade2-101ochre trp1-Δ63 leu2-Δ1 ura3-52 his3-Δ200 lys2-801ambre bar1::loxP SPC72-ECFP-kanMX4 MTW1-3mcherry::hphNT1 Δslk19::HIS3MX6 STU1-yeGFP::klTRP1 lys2-801ambre:PrSLK19-FLAG-slk19(aa300-502aa709-821)-NLS::LYS2*	Figure 3B b
YSN2916	*MATa ade2-101ochre trp1-Δ63 leu2-Δ1 ura3-52 his3-Δ200 lys2-801ambre bar1::loxP SPC72-ECFP-kanMX4 MTW1-3mcherry::hphNT1 Δslk19::HIS3MX6 STU1-yeGFP::klTRP1 lys2-801ambre:PrSLK19-FLAG-SLK19-NLS-LYS2*	Figure 3C a
YSN2827	*MATa ade2-101ochre trp1-Δ63 leu2-Δ1 ura3-52 his3-Δ200 lys2-801ambre bar1::loxP SPC72-ECFP-kanMX4 MTW1-3mcherry::hphNT1 Δslk19::HIS3MX6 STU1-yeGFP::klTRP1 lys2-801ambre:PrSLK19-FLAG-slk19Δ(aa1-77)-NLS-LYS2*	Figure 3C a
YSN2843	*MATa ade2-101ochre trp1-Δ63 leu2-Δ1 ura3-52 his3-Δ200 lys2-801ambre bar1::loxP SPC72-ECFP-kanMX4 MTW1-3mcherry::hphNT1 Δslk19::HIS3MX6 STU1-yeGFP::klTRP1 lys2-801ambre:PrSLK19-FLAG-slk19Δ(aa1-220)-NLS-LYS2*	Figure 3C a
YSN3087	*MATa ade2-101ochre trp1-Δ63 leu2-Δ1 ura3-52 his3-Δ200 lys2-801ambre bar1::loxP SPC72-ECFP-kanMX4 MTW1-3mcherry::hphNT1 Δslk19::HIS3MX6 STU1-yeGFP::klTRP1 lys2-801ambre:PrSLK19-FLAG-slk19Δ(aa503-711)-NLS-LYS2*	Figure 3C a
YSN2880	*MATa ade2-101ochre trp1-Δ63 leu2-Δ1 ura3-52 his3-Δ200 lys2-801ambre bar1::loxP SPC72-ECFP-kanMX4 MTW1-3mcherry::hphNT1 Δslk19::HIS3MX6 STU1-yeGFP::klTRP1 lys2-801ambre:PrSLK19-FLAG-slk19Δ(aa410-500)-NLS-LYS2*	Figure 3C a
YSN2878	*MATa ade2-101ochre trp1-Δ63 leu2-Δ1 ura3-52 his3-Δ200 lys2-801ambre bar1::loxP SPC72-ECFP-kanMX4 MTW1-3mcherry::hphNT1 Δslk19::HIS3MX6 STU1-yeGFP::klTRP1 lys2-801ambre:PrSLK19-FLAG-slk19Δ(aa300-502)-NLS-LYS2*	Figure 3C b
YSN3005	*MATa ade2-101ochre trp1-Δ63 leu2-Δ1 ura3-52 his3-Δ200 lys2-801ambre bar1::loxP SPC72-ECFP-kanMX4 MTW1-3mcherry::hphNT1 Δslk19::HIS3MX6 STU1-yeGFP::klTRP1 lys2-801ambre:PrSLK19-FLAG-slk19Δ(aa300-410)-NLS-LYS2*	Figure 3C b
YSN2882	*MATa ade2-101ochre trp1-Δ63 leu2-Δ1 ura3-52 his3-Δ200 lys2-801ambre bar1::loxP SPC72-ECFP-kanMX4 MTW1-3mcherry::hphNT1 Δslk19::HIS3MX6 STU1-yeGFP::klTRP1 lys2-801ambre:PrSLK19-FLAG-slk19Δ(aa709-821)-NLS-LYS2*	Figure 3C b
YAW649	*MATa ade2-101ochre trp1-Δ63 leu2-Δ1 ura3-52 his3-Δ200 lys2-801ambre bar1::loxP SLK19-GFP::HIS3*	Figure 4
YSN2903	*MATa ade2-101ochre trp1-Δ63 leu2-Δ1 ura3-52 his3-Δ200 lys2-801ambre bar1::loxP SLK19-GFP::HIS3 lys2-801ambre:PrSLK19-FLAG-SLK19-NLS-LYS2*	Figure 4
YSN2884[2]	*MATa ade2-101ochre trp1-Δ63 leu2-Δ1 ura3-52 his3-Δ200 lys2-801ambre bar1::loxP SLK19-GFP::HIS3 lys2-801ambre:PrSLK19-FLAG-slk19Δ(aa410-500)-NLS-LYS2*	Figure 4
YSN2885[2]	*MATa ade2-101ochre trp1-Δ63 leu2-Δ1 ura3-52 his3-Δ200 lys2-801ambre bar1::loxP SLK19-GFP::HIS3 lys2-801ambre:PrSLK19-FLAG-slk19Δ(aa709-821)-NLS-LYS2*	Figure 4
YSN2883[2]	*MATa ade2-101ochre trp1-Δ63 leu2-Δ1 ura3-52 his3-Δ200 lys2-801ambre bar1::loxP SLK19-GFP::HIS3 lys2-801ambre:PrSLK19-FLAG-slk19Δ(aa300-502)-NLS-LYS2*	Figure 4
YSN2931[2]	*MATa ade2-101ochre trp1-Δ63 leu2-Δ1 ura3-52 his3-Δ200 lys2-801ambre bar1::loxP SLK19-GFP::HIS3 lys2-801ambre:PrSLK19-FLAG-slk19Δ(aa1-77)-NLS-LYS2*	Figure 4
YSN2932[2]	*MATa ade2-101ochre trp1-Δ63 leu2-Δ1 ura3-52 his3-Δ200 lys2-801ambre bar1::loxP SLK19-GFP::HIS3 lys2-801ambre:PrSLK19-FLAG-slk19Δ(aa1-220)-NLS-LYS2*	Figure 4
YSN2967[2]	*MATa ade2-101ochre trp1-Δ63 leu2-Δ1 ura3-52 his3-Δ200 lys2-801ambre bar1::loxP SLK19-GFP::HIS3 lys2-801ambre:PrSLK19-FLAG-slk19Δ(aa760-821)-NLS-LYS2*	Figure 4
YSN3098[2]	*MATa ade2-101ochre trp1-Δ63 leu2-Δ1 ura3-52 his3-Δ200 lys2-801ambre bar1::loxP SLK19-GFP::HIS3 lys2-801ambre:PrSLK19-FLAG-slk19Δ(aa1-708)-NLS-LYS2*	Figure 4
YSN3099[2]	*MATa ade2-101ochre trp1-Δ63 leu2-Δ1 ura3-52 his3-Δ200 lys2-801ambre bar1::loxP SLK19-GFP::HIS3 lys2-801ambre:PrSLK19-FLAG-slk19Δ(aa503-711)-NLS-LYS2*	Figure 4
YSN2904	*MATa ade2-101ochre trp1-Δ63 leu2-Δ1 ura3-52 his3-Δ200 bar1::loxP SPC72-ECFP-kanMX4 MTW1-3mcherry::hphNT1 Δslk19::HIS3MX6 lys2-801ambre:PrSLK19-FLAG-slk19Δ(aa709-800)-GCN4-Zipper-NLS-EGFP-LYS2*	Figure 5A a

YSN2905	*MATa ade2-101ochre trp1-Δ63 leu2-Δ1 ura3-52 his3-Δ200 bar1::loxP SPC72-ECFP-kanMX4 MTW1-3mcherry::hphNT1 Δslk19::HIS3MX6 STU1-yeGFP::klTRP1 lys2-801ambre:PrSLK19-FLAG-slk19Δ(aa709-800)-GCN4-Zipper-NLS-LYS2*	Figure 5A b
YSN2978	*MATa ade2-101ochre trp1-Δ63 leu2-Δ1 ura3-52 his3-Δ200 lys2-801ambre bar1::loxP SPC72-ECFP-kanMX4 MTW1-3mcherry::hphNT1 Δslk19::HIS3MX6 lys2-801ambre:PrSLK19-FLAG-slk19Δ(aa709-821)-CIN8-Tetramerization-domain-NLS-GFP-LYS2*	Figure 5B a
YSN2966	*MATa ade2-101ochre trp1-Δ63 leu2-Δ1 ura3-52 his3-Δ200 lys2-801ambre bar1::loxP SPC72-ECFP-kanMX4 MTW1-3mcherry::hphNT1 Δslk19::HIS3MX6 STU1-yeGFP::klTRP1 lys2-801ambre:PrSLK19-FLAG-slk19Δ(aa709-821)-CIN8-Tetramerization-domain-NLS-LYS2*	Figure 5B b
YJO1206[1]	*MATa ade2-101ochre trp1-Δ63 leu2-Δ1 ura3-52 his3-Δ200 lys2-801ambre bar1::loxP STU1-9MYC::KanMX6*	Figure 6
YSN3135	*MATa ade2-101ochre trp1-Δ63 leu2-Δ1 ura3-52 his3-Δ200 lys2-801ambre bar1::loxP STU1-9MYC::KanMX6 Δslk19::HAx3-HIS3MX6 lys2-801ambre:PrSLK19-FLAG-SLK19-NLS-LYS2*	Figure 6
YSN3138	*MATa ade2-101ochre trp1-Δ63 leu2-Δ1 ura3-52 his3-Δ200 lys2-801ambre bar1::loxP STU1-9MYC::KanMX6 Δslk19::HAx3-HIS3MX6 lys2-801ambre:PrSLK19-FLAG-slk19Δ(aa709-821)-NLS-LYS2*	Figure 6
YSN3137	*MATa ade2-101ochre trp1-Δ63 leu2-Δ1 ura3-52 his3-Δ200 lys2-801ambre bar1::loxP STU1-9MYC::KanMX6 Δslk19::HAx3-HIS3MX6 lys2-801ambre:PrSLK19-FLAG-slk19Δ(aa300-410)-NLS-LYS2*	Figure 6
YSN3163	*MATa ade2-101ochre trp1-Δ63 leu2-Δ1 ura3-52 his3-Δ200 lys2-801ambre bar1::loxP STU1-9MYC::KanMX6 Δslk19::HAx3-HIS3MX6 lys2-801ambre:PrSLK19-FLAG-slk19Δ(aa1-708)-NLS-LYS2*	Figure 6
YSN3136	*MATa ade2-101ochre trp1-Δ63 leu2-Δ1 ura3-52 his3-Δ200 lys2-801ambre bar1::loxP STU1-9MYC::KanMX6 Δslk19::HAx3-HIS3MX6 lys2-801ambre:PrSLK19-FLAG-slk19Δ(aa1-220)-NLS-LYS2*	Figure 6
YSN3161	*MATa ade2-101ochre trp1-Δ63 leu2-Δ1 ura3-52 his3-Δ200 lys2-801ambre bar1::loxP STU1-9MYC::KanMX6 Δslk19::HAx3-HIS3MX6 lys2-801ambre:PrSLK19-FLAG-slk19Δ(aa300-502)-NLS-LYS2*	Figure 6
YSN3226[2]	*MATa trp1-Δ63 leu2-Δ1 ura3-52 his3-Δ200 lys2-801ambre bar1::loxP SPC72-ECFP-kanMX4 MTW1-3mcherry::hphNT1 ade2Δ (pADE2 -321upstream start to aa1-68)::loxP-BleR-loxP-pADH1-OsTIR1-9Myc::ADE2 SLK19-yeGFP-klTRP1 SPC105-IAA17::klURA3 cdc20::HIS3MX6-pGAL1-3HA-CDC20*	Figure 7A and C, Figure 8A and B, Figure 10A, Figure 11B, Figure 24A
YSN3422[2]	*MATa bar1::loxP ade2-101ochre trp1-Δ63 leu2-Δ1 ura3-52 his3-Δ200 lys2-801ambre ade2Δ (pADE2 -321upstream start to aa1-68)::loxP-BleR-loxP-pADH1-OsTIR1-9Myc::ADE2 SLK19-yeGFP::natNT2 cdc20::LEU2-pMET25-CDC20*	Figure 7B, Figure 24E
YSN3426[2]	*MATa bar1::loxP ade2-101ochre trp1-Δ63 leu2-Δ1 ura3-52 his3-Δ200 lys2-801ambre ade2Δ (pADE2 -321upstream start to aa1-68)::loxP-BleR-loxP-pADH1-OsTIR1-9Myc::ADE2 SLK19-yeGFP::natNT2 SPC105-IAA17::klTRP1 cdc20::klURA3-pGAL-3HA-CDC20*	Figure 7B
YSN3483[2]	*MATa trp1-Δ63 leu2-Δ1 ura3-52 his3-Δ200 lys2-801ambre bar1::loxP SPC72-ECFP-kanMX4 MTW1-3mcherry::hphNT1 ade2Δ (pADE2 -321upstream start to aa1-68)::loxP-BleR-loxP-pADH1-OsTIR1-9Myc::ADE2 Δslk19::natNT2 SPC105-IAA17::klURA3 cdc20::HIS3MX6-pGAL1-3HA-CDC20 lys2-801ambre:PrSLK19-FLAG-slk19Δ(aa1-220)-NLS-GFP-LYS2*	Figure 8A and B
YSN3490[2]	*MATa trp1-Δ63 leu2-Δ1 ura3-52 his3-Δ200 lys2-801ambre bar1::loxP SPC72-ECFP-kanMX4 MTW1-3mcherry::hphNT1 ade2Δ (pADE2 -321upstream start to aa1-68)::loxP-BleR-loxP-pADH1-OsTIR1-9Myc::ADE2 Δslk19::natNT2 SPC105-IAA17::klURA3 cdc20::HIS3MX6-pGAL1-3HA-CDC20 lys2-801ambre:PrSLK19-FLAG-slk9Δ(aa503-711)-NLS-GFP::LYS2*	Figure 8A and B
YSN3482[2]	*MATa trp1-Δ63 leu2-Δ1 ura3-52 his3-Δ200 lys2-801ambre bar1::loxP SPC72-ECFP-kanMX4 MTW1-3mcherry::hphNT1 ade2Δ (pADE2 -321upstream start to aa1-68)::loxP-BleR-loxP-pADH1-OsTIR1-9Myc::ADE2 Δslk19::natNT2 SPC105-IAA17::klURA3 cdc20::HIS3MX6-pGAL1-3HA-CDC20 lys2-801ambre:PrSLK19-FLAG-slk19Δ(aa300-410)-NLS-EGFP-LYS2*	Figure 8A and B
YSN3487[2]	*MATa trp1-Δ63 leu2-Δ1 ura3-52 his3-Δ200 lys2-801ambre bar1::loxP SPC72-ECFP-kanMX4 MTW1-3mcherry::hphNT1 ade2Δ (pADE2 -321upstream start to aa1-68)::loxP-BleR-loxP-pADH1-OsTIR1-9Myc::ADE2 Δslk19::natNT2 SPC105-IAA17::klURA3 cdc20::HIS3MX6-pGAL1-3HA-CDC20 lys2-801ambre:PrSLK19-FLAG-slk19Δ(aa410-500)-NLS-EGFP-LYS2*	Figure 8A and B
YJO3534[2]	*MATa trp1-Δ63 leu2-Δ1 ura3-52 his3-Δ200 lys2-801ambre bar1::loxP SPC72-ECFP-kanMX4 MTW1-3mcherry::hphNT1 ade2Δ (pADE2 -321upstream start to aa1-68)::loxP-BleR-loxP-pADH1-OsTIR1-9Myc::ADE2 Δslk19::natNT2 SPC105-IAA17::klURA3 cdc20::HIS3MX6-pGAL1-3HA-CDC20 lys2-801ambre:PrSLK19-FLAG-slk19Δ(aa709-821)-NLS-EGFP-LYS2*	Figure 8A and B

YSN3489[2]	*MATa trp1-Δ63 leu2-Δ1 ura3-52 his3-Δ200 lys2-801ambre bar1::loxP SPC72-ECFP-kanMX4 MTW1-3mcherry::hphNT1 ade2Δ (pADE2 -321upstream start to aa1-68)::loxP-BleR-loxP-pADH1-OsTIR1-9Myc::ADE2 Δslk19::natNT2 SPC105-IAA17::klURA3 cdc20::HIS3MX6-pGAL1-3HA-CDC20 lys2-801ambre:PrSLK19-FLAG-slk19Δ(aa1-708)-NLS-EGFP-LYS2*	Figure 8A and B
YCF2601[1]	*MATa ade2-101ochre trp1-Δ63 leu2-Δ1 ura3-52 his3-Δ200 lys2-801ambre bar1::loxP STU1-3mCherry::natNT2 Δcen5::pGAL-CEN3-LEU2 ade1::pURA3-TetR-3XCFP-HPH1 1.4kb fromCEN5::CEN5-tetO2x112-HIS3 DAD1-yeGFP::klTRP1 cdc20::klURA3-pMET25-CDC20*	Figure 9
YME2719[1]	*MATa ade2-101ochre trp1-Δ63 leu2-Δ1 ura3-52 his3-Δ200 lys2-801ambre bar1::loxP STU1-3mCherry::natNT2 Δcen5::pGAL-CEN3-LEU2 ade1::pURA3-TetR-3XCFP-HPH1 1.4kb fromCEN5::CEN5-tetO2x112::HIS3 DAD1-yeGFP::klTRP1 Δslk19::KanMX6 cdc20::klURA3-pMET25-CDC20*	Figure 9
YSN3493[2]	*MATa ade2-101ochre trp1-Δ63 leu2-Δ1 ura3-52 his3-Δ200 lys2-801ambre bar1::loxP STU1-3mCherry::natNT2 Δcen5::pGAL-CEN3-LEU2 ade1::pURA3-TetR-3XCFP-HPH1 1.4kb fromCEN5::CEN5-tetO2x112::HIS3 DAD1-yeGFP::klTRP1 Δslk19::KanMX6 cdc20::klURA3-pMET25-CDC20 lys2-801ambre:PrSLK19-FLAG-slk19Δ(aa300-410)-NLS-LYS2*	Figure 9
YJO2792[2]	*MATa bar1::loxP trp1-Δ63 leu2-Δ1 ura3-52 his3-Δ200 lys2-801ambre NUF2-3mcherry::natNT2ade2-101ochre::PADH1-OsTIR1-9Myc::ADE2 STU1-IAA17::KanMX4 SPC72-eCFP::hphNT1 SLK19-yeGFP::HIS3MX6 cdc20::klURA3-pGAL1-3HA-CDC20*	Figure 10A
YSN3485	*MATa bar1::loxP trp1-Δ63 leu2-Δ1 ura3-52 his3-Δ200 lys2-801ambre NUF2-3mcherry::natNT2 ade2-101ochre::PADH1-OsTIR1-9Myc::ADE2 STU1-IAA17::KanMX4 SPC72-eCFP::hphNT1 SLK19-yeGFP::HIS3MX6 cdc20::klURA3-pGAL1-3HA-CDC20 SPC105-IAA17::klTRP1 lys2-801ambre::CFP-TUB1::LYS2*	Figure 10A
YSN3002	*MATa ade2-101ochre trp1-Δ63 leu2-Δ1 ura3-52 his3-Δ200 lys2-801ambre bar1::loxP STU1-9MYC::KanMX6 cdc20::klURA3-pMET25-CDC20*	Figure 10B and C
YSN3149	*MATa ade2-101ochre trp1-Δ63 leu2-Δ1 ura3-52 his3-Δ200 lys2-801ambre bar1::loxP STU1-9MYC::KanMX6 Δslk19::HAx3-HIS3MX6 lys2-801ambre:PrSLK19-FLAG-SLK19-NLS-LYS2 cdc20::klURA3-pMET25-CDC20*	Figure 10B and C
YSN3151	*MATa ade2-101ochre trp1-Δ63 leu2-Δ1 ura3-52 his3-Δ200 lys2-801ambre bar1::loxP STU1-9MYC::KanMX6 Δslk19::HAx3-HIS3MX6 lys2-801ambre:PrSLK19-FLAG-slk9Δ(300-410)-NLS-LYS2 dc20::klURA3-pMET25-CDC20*	Figure 10B and C
YJO2970[2]	*MATa bar1::loxP ade2-101ochre trp1-Δ63 leu2-Δ1 ura3-52 his3-Δ200 lys2-801ambre SLK19-9myc::klTRP1 cdc20::klURA3-pMET25-CDC20*	Figure 10E
YJO2969[2]	*MATa bar1::loxP ade2-101ochre trp1-Δ63 leu2-Δ1 ura3-52 his3-Δ200 lys2-801ambre SLK19-9myc::klTRP1 STU1-5xFLAG::hphNT1 cdc20::klURA3-pMET25-CDC20*	Figure 10E
YJO3090[2]	*MATa trp1-Δ63 leu2-Δ1 ura3-52 his3-Δ200 lys2-801ambre bar1::loxP stu1Δ(995-1180(ΔC-loop))-5xFLAG::hphNT1 SPC72-HAx3::HIS3MX6 ade2-101ochre::tetR-GFP::ADE2 ChrV-tetO2x112-URA3-ChrV SLK19-9myc-klTRP1 cdc20::natNT2-pMET25-CDC20*	Figure 10E
YSN3297[2]	*MATa ade2-101ochre trp1-Δ63 leu2-Δ1 ura3-52 his3-Δ200 lys2-801ambre bar1::loxP stu1::stu1Δ(995-1180(ΔC-loop))-CFP::KANMX6 SPC72-3mCherry::hphNT1 SLK19-GFP::klTRP1 cdc20::LEU2-pMET25-CDC20 MTW1-3mcherry::natNT2 SPC105-IAA17::klURA3 ade2::pADH1-OsTIR1-9Myc-ADE2*	Figure 11A and B
YSN3492[2]	*MATa ade2-101ochre trp1-Δ63 leu2-Δ1 ura3-52 his3-Δ200 lys2-801ambre bar1::loxP stu1::stu1Δ(995-1180(ΔC-loop))-CFP::KANMX6 SPC72-3mCherry::hphNT1 SLK19-GFP::klTRP1 cdc20::LEU2-pMET25-CDC20 MTW1-3mcherry::natNT2 SPC105-IAA17::klURA3 ade2::pADH1-OsTIR1-9Myc-ADE2 Δase1::HIS3MX6*	Figure 11A and B
YSN3491[2]	*MATa trp1-Δ63 leu2-Δ1 ura3-52 his3-Δ200 lys2-801ambre bar1::loxP SPC72-ECFP-kanMX4 MTW1-3mcherry::hphNT1 ade2Δ (pADE2 -321upstream start to aa1-68)::loxP-BleR-loxP-pADH1-OsTIR1-9Myc::ADE2 SLK19-yeGFP-klTRP1 SPC105-IAA17::klURA3 cdc20::HIS3MX6-pGAL1-3HA-CDC20 lys2-801ambre::CFP-TUB1::LYS2 Δase1::natNT2*	Figure 11A and B
YVS2313[2]	*MATa ade2-101ochre trp1-Δ63 leu2-Δ1 his3-Δ200 lys2-801ambre bar1::loxP Δstu1::His3MX6 STU1 promotor-Flag-stu1Δ(aa995-aa1180 (ΔC-loop))-NLS-GFP::LYS2 CDC20::LEU2-pMET25-CDC20 ura3-52::CFP-TUB1::URA3 ASE1-3mCherry::natNT2*	Figure 11A, Figure 15A and B
YSN3365	*Mata ade2-101ochre trp1-Δ63 leu2-Δ1 his3-Δ200 lys2-801ambre bar1::loxP Δstu1::His3MX6 STU1 promotor-Flag-stu1Δ(aa995-aa1180 (ΔC-loop))-NLS-GFP::LYS2 CDC20::LEU2-pMET25-CDC20 ura3-52::CFP-TUB1::URA3 ASE1-3mCherry::natNT2 Δslk19::hphNT1*	Figure 11A
YVS2151[1]	*Mata ade2-101ochre trp1-Δ63 leu2-Δ1 ura3-52 his3-Δ200 lys2-801ambre bar1::loxP stu1::stu1Δ(995-1180(ΔC-loop))-CFP::KANMX6 SPC72-3mCherry::hphNT1 SLK19-GFP::klTRP1*	Figure 11C

YVS2311[3]	*MATa ade2-101ochre trp1-Δ63 leu2-Δ1 his3-Δ200 lys2-801ambre bar1::loxP ura3-52:TUB1-CFP:URA3 STU1-GFP::HIS3MX6 ASE1-3mCherry:hphNT1 cdc20:LEU2-pMET25-CDC20*	Figure 12A and B, Figure 14A and B, Figure 15A and B
YSN3349[2]	*MATa ade2-101ochre trp1-Δ63 leu2-Δ1 his3-Δ200 lys2-801ambre bar1::loxP ura3-52:TUB1-CFP:URA3 STU1-GFP::HIS3MX6 ASE1-3mCherry:hphNT1 cdc20:LEU2-pMET25-CDC20 Δslk19::HAx3-kanMX6*	Figure 12A and B, Figure 14A and B, Figure 15A and B
YSN3476[2]	*MATa ade2-101ochre trp1-Δ63 leu2-Δ1 his3-Δ200 lys2-801ambre bar1::loxP ura3-52:TUB1-CFP:URA3 STU1-GFP::HIS3MX6 ASE1-3mCherry:hphNT1 cdc20:LEU2-pMET25-CDC20 Δslk19::HAx3-kanMX6 ys2-801ambre:PrSLK19-FLAG-slk19Δ(aa300-410)-NLS-LYS2*	Figure 12A and B, Figure 14A and B, Figure 15A and B
YSN3359[2]	*MATa ade2-101ochre trp1-Δ63 leu2-Δ1 his3-Δ200 lys2-801ambre bar1::loxP ura3-52:TUB1-CFP:URA3 STU1-GFP::HIS3MX6 ASE1-3mCherry:hphNT1 cdc20:LEU2-pMET25-CDC20 Δslk19::HAx3-kanMX6 lys2-801ambre:PrSLK19-FLAG-SLK19-NLS-LYS2*	Figure 12A and B, Figure 14A and B, Figure 15A and B
YSN3393[2]	*MATa bar1::loxP ade2-101ochre trp1-Δ63 leu2-Δ1 ura3-52 his3-Δ200 lys2-801ambre ASE1-9myc:hphNT1 cdc20::LEU2-pMET25-CDC20*	Figure 13A and B
YSN3404[2]	*MATa bar1::loxP ade2-101ochre trp1-Δ63 leu2-Δ1 ura3-52 his3-Δ200 lys2-801ambre ASE1-9Myc:hphNT1 cdc20::LEU2-pMET25-CDC20 Δslk19::KanMX6*	Figure 13A and B
YSN3471[2]	*MATa bar1::loxP ade2-101ochre trp1-Δ63 leu2-Δ1 ura3-52 his3-Δ200 lys2-801ambre ASE1-9Myc:hphNT1 cdc20::LEU2-pMET25-CDC20 Δslk19::KanMX6 lys2-801ambre:PrSLK19-FLAG-slk19Δ(aa300-410)-NLS-LYS2*	Figure 13A and B
YJO3002[2]	*MATa ade2-101ochre trp1-Δ63 leu2-Δ1 ura3-52 his3-Δ200 lys2-801ambre bar1::loxP STU1-9MYC::KanMX6 cdc20::klURA3-pMET25-CDC20*	Figure 13A and B
YSN3423[2]	*MATa ade2-101ochre trp1-Δ63 leu2-Δ1 ura3-52 his3-Δ200 lys2-801ambre bar1::loxP STU1-9MYC::KanMX6 cdc20::klURA3-pMET25-CDC20 Δslk19::HIS3MX6*	Figure 13A and B
YMS231	*MATa bar1::loxP ade2-101ochre trp1-Δ63 leu2-Δ1 ura3-52 his3-Δ200 lys2-801ambre*	Figure 13C
YJO2115	*MATa ade2-101ochre trp1-Δ63 leu2-Δ1 ura3-52 his3-Δ200 lys2-801ambre bar1::loxP SPC72-ECFP-kanMX4 MTW1-3mcherry::hphNT1 Δslk19::HIS3MX6*	Figure 13C
YVS2332	*MATa ade2-101ochre trp1-Δ63 leu2-Δ1 ura3-52 his3 lys2-801ambre bar1::loxP STU1-NLS-EGFP::klTRP1 lys2::CFP-TUB1::LYS2 AME1-Cherry::hphNT1 Δase1::HIS3MX6*	Figure 13C
YSN3389	*MATa ade2-101ochre trp1-Δ63 leu2-Δ1 ura3-52 his3 lys2-801ambre bar1::loxP STU1-NLS-EGFP::klTRP1 lys2::CFP-TUB1::LYS2 AME1-Cherry::hphNT1 Δase1::HIS3MX6 Δslk19::KanMX6*	Figure 13C
YSN3435[2]	*MATa ade2-101ochre trp1-Δ63 leu2-Δ1 ura3-52 his3-Δ200 lys2-801ambre bar1::loxP NUF2-GFP::HIS3 cdc20::LEU2-pMET25-CDC20 lys2-801ambre::pGal1-FLAG-ASE1-3mcherry-TermADH1::LYS2*	Figure 16A
YJO1938[2]	*MATa ade2-101ochre trp1-Δ63 leu2-Δ1 ura3-52 his3-Δ200 bar1::loxP lys2-801ambre::pGAL-FLAG-STU1-CFP::klTRP1-LYS2*	Figure 16A
YSN3027[2]	*MATa ade2-101ochre trp1-Δ63 leu2-Δ1 ura3-52 his3-Δ200 lys2-801ambre bar1::loxP SPC72-ECFP-kanMX4 MTW1-3mcherry::hphNT1 Δslk19::HIS3MX6 lys2-801ambre:PrSLK19-FLAG-SLK19-NLS-EGFP-LYS2 cdc20::klURA3-pMET25-CDC20*	Figure 16A
YSN3367[2]	*MATa ade2-101ochre trp1-Δ63 leu2-Δ1 ura3-52 his3-Δ200 lys2-801ambre bar1::loxP SPC72-ECFP-kanMX4 MTW1-3mcherry::hphNT1 Δslk19::HIS3MX6 lys2-801ambre:PrSLK19-FLAG-slk19Δ(aa300-410)-NLS-GFP-LYS2 cdc20::LEU2-pMET25-CDC20*	Figure 16A
YVS1718[3]	*MATa ade2-101ochre trp1-Δ63 leu2-Δ1 his3-Δ200 bar1::loxP ura3-52::CFP-TUB1::URA3 AME1-3mCherry::hphNT1 lys2-801ambre::pGAL-FLAG-STU1-NLS-GFP::LYS2*	Figure 21A a, B, C
YMP3288	*MATa ade2-101ochre trp1-Δ63 leu2-Δ1 his3-Δ200 bar1::loxP ura3-52::CFP-TUB1::URA3 AME1-3mCherry::hphNT1 lys2-801ambre::pGAL-FLAG-STU1-NLS-GFP::LYS2 Δslk19:HIS3MX6*	Figure 21A a, B, C
YSN3406	*MATa ade2-101ochre trp1-Δ63 leu2-Δ1 his3-Δ200 bar1::loxP ura3-52::CFP-TUB1::URA3 AME1-3mCherry::hphNT1 lys2-801ambre::pGAL-FLAG-STU1-NLS-GFP::LYS2 SPC72-3mcherry::HIS3MX6 leu2-Δ1::pGAL1-FLAG-SLK19::LEU2*	Figure 21A a, B, C
YSN3228	*MATa ade2-101ochre trp1-Δ63 leu2-Δ1 ura3-52 his3-Δ200 lys2-801ambre bar1::loxP SPC72-ECFP-kanMX4 MTW1-3mcherry::hphNT1 Δslk19::HIS3MX6 lys2-801ambre:pGAL1-FLAG-SLK19-NLS-GFP::LYS2*	Figure 21B, Figure 22 a
YSN3205	*MATa ade2-101ochre trp1-Δ63 leu2-Δ1 ura3-52 his3-Δ200 lys2-801ambre bar1::loxP SPC72-ECFP-kanMX4 MTW1-3mcherry::hphNT1 SLK19-yeGFP::HIS3MX6 cdc20::klURA3-pMET25-CDC20*	Figure 21B
YSN3284	*MATa bar1::loxP ade2-101ochre trp1-Δ63 leu2-Δ1 ura3-52 his3-Δ200 lys2-801ambre:pGAL1-FLAG-SLK19-NLS-GFP::LYS2 CDC14-3mcherry::hphNT1*	Figure 22 b
YSN3308	*MATa bar1::loxP ade2-101ochre trp1-Δ63 leu2-Δ1 ura3-52 his3-Δ200 lys2-801ambre:pGAL1-FLAG-SLK19-NLS-GFP::LYS2 STU1-3mcherry::hphNT1 Δbtn2::HIS3MX6*	Figure 22 c

YSN3285	*MATa bar1::loxP ade2-101ochre trp1-Δ63 leu2-Δ1 ura3-52 his3-Δ200 lys2-801ambre:pGAL1-FLAG-SLK19-NLS-GFP::LYS2 STU1-3mcherry::hphNT1*	Figure 22 d
YSN3275	*MATa bar1::loxP trp1-Δ63 leu2-Δ1 ura3-52 his3-Δ200 lys2-801ambre NUF2-3mcherry::natNT2 ade2-101ochre::PADH1-OsTIR1-9Myc::ADE2 STU1-IAA17::KanMX4 SPC72-eCFP::hphNT1 lys2-801ambre:pGAL1-FLAG-SLK19-NLS-GFP::LYS2*	Figure 22 e
YSN3278[2]	*MATa trp1-Δ63 leu2-Δ1 ura3-52 his3-Δ200 lys2-801ambre bar1::loxP SPC72-ECFP-kanMX4 MTW1-3mcherry::hphNT1 ade2Δ(pADE2 -321upstream start to aa1-68)::loxP-BleR-loxP-pADH1-OsTIR1-9Myc::ADE2 SLK19-yeGFP-klTRP1 cdc20::LEU2-pMET25-CDC20*	Figure 24 B-D, Figure 26 A and B
YSN3160[2]	*MATa trp1-Δ63 leu2-Δ1 ura3-52 his3-Δ200 lys2-801ambre bar1::loxP SPC72-ECFP-kanMX4 MTW1-3mcherry::hphNT1 ade2Δ (pADE2 -321upstream start to aa1-68)::loxP-BleR-loxP-pADH1-OsTIR1-9Myc::ADE2 SLK19-yeGFP-klTRP1 STU1-IAA17::klURA3 lys2::pSTU1-stu1Δ (TOG1)-NLS::LYS2 cdc20::LEU2-pMET25-CDC20*	Figure 24 B-D, Figure 26 A and B
YSN3429[2]	*MATa bar1::loxP ade2-101ochre trp1-Δ63 leu2-Δ1 ura3-52 his3-Δ200 lys2-801ambre ade2Δ (pADE2 -321upstream start to aa1-68)::loxP-BleR-loxP-pADH1-OsTIR1-9Myc::ADE2 SLK19-yeGFP::natNT2 STU1-IAA17::klURA3 cdc20::LEU2-pMET25-CDC20 lys2::pSTU1-stu1Δ (TOG1)-NLS::LYS2*	Figure 24E
YSN3309	*MATa trp1-Δ63 leu2-Δ1 ura3-52 his3-Δ200 lys2-801ambre bar1::loxP SPC72-ECFP-kanMX4 MTW1-3mcherry::hphNT1 ade2Δ (pADE2 -321upstream start to aa1-68)::loxP-BleR-loxP-pADH1-OsTIR1-9Myc::ADE2 SLK19-yeGFP-klTRP1 SCC1-IAA17::klURA3 lys2-801ambre::CFP-TUB1::LYS2*	Figure 25A
YSN3368	*MATa bar1::loxP trp1-Δ63 leu2-Δ1 ura3-52 his3-Δ200 lys2-801ambre NUF2-3mcherry::natNT2 ade2-101ochre::PADH1-OsTIR1-9Myc::ADE2 STU1-IAA17::KanMX4 SPC72-eCFP::hphNT1 SLK19-yeGFP::HIS3MX6 cdc20::klURA3-pGAL1-3HA-CDC20 lys2::pSTU1-stu1Δ (TOG1)-NLS::LYS2 SCC1-IAA17::klTRP1 leu2::CFP-TUB1::LEU2*	Figure 25B a, b
YSN3321	*MATa ade2-101ochre trp1-Δ63 leu2-Δ1 ura3-52 his3-Δ200 lys2-801ambre Δndc80::ndc80(Deletion AS 1-116)-3HA-KanMx6 Δbar1::loxP SPC72-eCFP::LEU2 MTW1-3mcherry::natNT2 SLK19-EGFP::klTRP1 cdc20::klURA3-pMET25-CDC20*	Figure 26 A and B
YJO2654[1]	*MATa ade2-101ochre trp1-Δ63 leu2-Δ1 ura3-52 his3-Δ200 lys2-801ambre bar1::loxP SPC72-ECFP-kanMX4 MTW1-3mcherry::hphNT1 Δslk19::HIS3MX6 STU1-yeGFP::klTRP1*	Figure 28 A b, B
YCF2404	*MATa bar1::loxP ade2-101ochre trp1-Δ63 leu2-Δ1 his3 lys2-801ambre STU1-NLS-EGFP::klTRP1 lys2::CFP-TUB1::LYS2 AME1-Cherry::hphNT1 Δase1::HIS3MX6 URA3::ase1-7D*	Figure 29 a
YCF2403	*MATa bar1::loxP ade2-101ochre trp1-Δ63 leu2-Δ1 his3 lys2-801ambre STU1-NLS-EGFP::klTRP1 lys2::CFP-TUB1::LYS2 AME1-Cherry::hphNT1 Δase1::HIS3MX6 ura3-52::ase1-7A-URA3*	Figure 29 b
YJO2868	*MATa bar1::loxP ade2-101ochre trp1-Δ63 leu2-Δ1 his3 STU1-NLS-EGFP::klTRP1 lys2-801ambre::CFP-TUB1::LYS2 AME1-Cherry::hphNT1 Δase1::HIS3MX6 ura3-52::ase1-7A-URA3 Δslk19::HAx3-kanMX6*	Figure 29 c
YSN2925	*MATa bar1::loxP trp1-Δ63 leu2-Δ1 ura3-52 his3-Δ200 NUF2-3mcherry::natNT2 ade2-101ochre::pADH1-OsTIR1-9Myc::ADE2 STU1-IAA17::KanMX4 SPC72-eCFP::hphNT1 lys2-801ambre::PSTU1-FLAG-stu1Δ(aa570-aa716(ΔM-loop))-NLS-GFP::LYS2 Δslk19::HAx3HIS3MX6 leu2-Δ1::PrSLK19-FLAG-SLK19-NLS::LEU2*	Figure 31A
YJO2617	*MATa bar1::loxP trp1-Δ63 leu2-Δ1 ura3-52 his3-Δ200 NUF2-3mcherry::natNT2 ade2-101ochre::pADH1-OsTIR1-9Myc::ADE2 STU1-IAA17::KanMX4 SPC72-eCFP::hphNT1 lys2-801ambre::PSTU1-FLAG-stu1Δ(aa570-aa716(ΔM-loop))-NLS-GFP::LYS2 Δslk19::HAx3HIS3MX6*	Figure 31A
YJO2926	*MATa bar1::loxP trp1-Δ63 leu2-Δ1 his3-Δ200 NUF2-3mcherry::natNT2 ade2-101ochre::PADH1-OsTIR1-9Myc::ADE2 STU1-IAA17::KanMX4 SPC72-eCFP::hphNT1 lys2-801ambre::PSTU1-FLAG-stu1Δ(aa570-aa716(ΔM-loop))-NLS-GFP::LYS2 Δase1::HIS3MX6 ura3-52::ase1-7A::URA3 Δslk19::loxP-pAgTEF-BleR-tAgTEF-loxP*	Figure 31A
YSN2955	*MATa bar1::loxP trp1-Δ63 leu2-Δ1 ura3-52 his3-Δ200 NUF2-3mcherry::natNT2 ade2-101ochre::ADH1-OsTIR1-9Myc::ADE2 STU1-IAA17::KanMX4 SPC72-eCFP::hphNT1 lys2-801ambre::PSTU1-FLAG-stu1Δ(aa570-aa716(ΔM-loop))-NLS-GFP::LYS2 Δspo12:HIS3MX6*	Figure 31A
YJO2873	*MATa bar1::loxP leu2-Δ1 ura3-52 his3-Δ200 NUF2-3mcherry::natNT2 STU1-IAA17::KanMX4 SPC72-eCFP::hphNT1 ade2-101ochre::pADH1-OsTIR1-9Myc::ADE2 lys2-801ambre::PSTU1-FLAG-stu1Δ(aa570-aa716(ΔM-loop))-NLS-GFP::LYS2 Δslk19::HAx3HIS3MX6 trp1-Δ63::pGal-CDC14-FLAG::klTRP1*	Figure 31A
YSN2924	*MATa bar1::loxP trp1-Δ63 leu2-Δ1 ura3-52 his3-Δ200 NUF2-3mcherry::natNT2 ade2-101ochre::pADH1-OsTIR1-9Myc::ADE2 STU1-IAA17::KanMX4 SPC72-eCFP::hphNT1 lys2-*	Figure 31A

	801ambre::PSTU1-FLAG-stu1Δ(aa570-aa716(ΔM-loop))-NLS-GFP::LYS2 Δslk19::HAx3HIS3MX6 leu2-Δ1::PrSLK19-FLAG-slk19Δ(aa709-821)-NLS::LEU2	
YSN2921	*MATa bar1::loxP trp1-Δ63 leu2-Δ1 ura3-52 his3-Δ200 NUF2-3mcherry::natNT2 ade2-101ochre::pADH1-OsTIR1-9Myc::ADE2 STU1-IAA17::KanMX4 SPC72-eCFP::hphNT1 lys2-801ambre::PSTU1-FLAG-stu1Δ(aa570-aa716(ΔM-loop))-NLS-GFP::LYS2 Δslk19::HAx3HIS3MX6 leu2-Δ1::PrSLK19-FLAG-slk19Δ(aa1-220)-NLS::LEU2*	Figure 31A
YSN2922	*MATa bar1::loxP trp1-Δ63 leu2-Δ1 ura3-52 his3-Δ200 NUF2-3mcherry::natNT2 ade2-101ochre::pADH1-OsTIR1-9Myc::ADE2 STU1-IAA17::KanMX4 SPC72-eCFP::hphNT1 lys2-801ambre::PSTU1-FLAG-stu1Δ(aa570-aa716(ΔM-loop))-NLS-GFP::LYS2 Δslk19::HAx3HIS3MX6 leu2-Δ1::PrSLK19-FLAG-slk19Δ(aa300-502)-NLS::LEU2*	Figure 31A
YCF2373	*MATa ade2-101ochre trp1-Δ63 leu2-Δ1 ura3-52 his3-Δ200 lys2-801ambre bar1::loxP Lys2::Stu1 promotor-stu1Δ(aa1-aa1181)-NLS-GFP (D4) STU1-ΔD4-Zipper-ECFP::KANMX4 ADE2::pGal-CDC14-FLAG cdc20::HIS3MX6-pMET25-CDC20*	Figure 32A a, b
YSN3159	*MATa ade2-101ochre trp1-Δ63 leu2-Δ1 ura3-52 his3-Δ200 lys2-801ambre bar1::loxP Lys2::Stu1 promotor-stu1Δ(aa1-aa1181)-NLS-GFP (D4) STU1-ΔD4-Zipper-ECFP::KANMX4 ADE2::pGal-CDC14-FLAG cdc20::HIS3MX6-pMET25-CDC20 Δslk19::hphNT1*	Figure 32 A c
YSN3473	*MATa ade2-101ochre trp1-Δ63 leu2-Δ1 ura3-52 his3-Δ200 lys2-801ambre bar1::loxP STU1-CFP::KANMX6 SPC72-3mCherry::hphNT1 ade2-101ochre::tetR-GFP::ADE2 ChrV-tetO2x112-URA3-ChrV Δase1::HIS3MX6 lys2-801ambre:pGAL1-FLAG-ase1-7A-3mcherry::LYS2*	Figure 32B
YSN3474	*MATa ade2-101ochre trp1-Δ63 leu2-Δ1 ura3-52 his3-Δ200 lys2-801ambre bar1::loxP STU1-CFP::KANMX6 SPC72-3mCherry::hphNT1 ade2-101ochre::tetR-GFP::ADE2 ChrV-tetO2x112-URA3-ChrV Δase1::HIS3MX6 lys2-801ambre:pGAL1-FLAG-ase1-7D-3mcherry::LYS2*	Figure 32B

[1](Kolenda et al. 2018), [2](Norell et al., 2021), [3](Funk et al., 2014)

2.2 Plasmids

The following plasmids were used to create the yeast strains in this study:

Plasmid	Features	Purpose
pYM1[1]	*HAx3-kanMX6*	Deletion cassette
pYM2[1]	*HAx3-HIS3MX6*	Deletion cassette
pYM28[2]	*EGFP-HIS3MX6*	Deletion cassette
pME1600	*yeGFP-natNT2*	Deletion cassette
pMK43[3]	*IAA17-KanMX4*	C-terminal tagging with *IAA17*
pME1595	*IAA17-klTRP1*	C-terminal tagging with *IAA17*
pJO1610	*IAA17-klURA3*	C-terminal tagging with *IAA17*
pFA6-Aid-3HA-HIS3MX6	*IAA17-3HA-HIS3MX6*	C-terminal tagging with *IAA17*
pME1624	*pADH1-OsTIR1-9Myc-ADE2*	Integration of *OsTIR1* for AID system
pVS1453	*pADH1-OsTIR1-9Myc-ADE2*	Integration of *OsTIR1* for AID system
pFA6a-HIS3MX6-pGAL1-3HA	*HIS3MX6-pGAL1-3HA*	promotor replacement for *CDC20*
pME1550	*klURA3-pGAL1-3HA*	promotor replacement for *CDC20*
pVS1488	*LEU2-pMET25-CDC20*	promotor replacement for *CDC20*
pCF1570	*klURA3-pMET25-CDC20*	promotor replacement for *CDC20*
pMK1169	*HIS3MX6-pMET25-CDC20*	promotor replacement for *CDC20*
pCF1571	*cdc20::natNT2-pMET25-CDC20*	promotor replacement for *CDC20*
pAK055	*PrASE1-ase1-7A-URA3 (mutated sites: T55, S64, S198, T675, S707, S803, S819)*	Integration of *ASE1* mutant
pAK069	*PrASE1-ase1-7D-URA3 (mutated sites: T55, S64, S198, T675, S707, S803, S819)*	Integration of *ASE1* mutant
pVS1346[4]	*PrSTU1-FLAG-stu1Δ(aa995-1180(ΔCL))-CFP-KANMX6*	Integration of *STU1* deletion construct
pCF1482[4]	*PrSTU1-FLAG-stu1Δ(aa1-260)-NLS-LYS2*	Integration of *STU1* deletion construct
pCF1498[4]	*PrSTU1-FLAG-stu1Δ(aa995-1180)-NLS-GFP-LYS2*	Integration of *STU1* deletion construct
pVS1499	*PrSTU1-FLAG-stu1Δ(aa570-716(ΔML))-NLS-GFP-LYS2*	Integration of *STU1* deletion construct

pCF1511[4]	*PrSTU1-FLAG-stu1Δ(aa1181-1513(ΔD4))-ZIPPER-NLS-ECFP-KANMX4*	Integration of *STU1* construct
pSN1621	*PrSLK19-FLAG-slk19Δ(aa1-77)-NLS-LYS2*	Integration of *SLK19* deletion construct
pSN1625	*PrSLK19-FLAG-slk19Δ(aa1-220)-NLS-LYS2*	Integration of *SLK19* deletion construct
pSN1626	*PrSLK19-FLAG-slk19Δ(aa1-220)-NLS-GFP-LYS2*	Integration of *SLK19* deletion construct
pSN1639	*PrSLK19-FLAG-slk19Δ(aa300-502)-NLS-GFP-LYS2*	Integration of *SLK19* deletion construct
pSN1640	*PrSLK19-FLAG-slk19Δ(aa300-502)-NLS-LYS2*	Integration of *SLK19* deletion construct
pSN1641	*PrSLK19-FLAG-slk19Δ(aa410-500)-NLS-GFP-LYS2*	Integration of *SLK19* deletion construct
pSN1642	*PrSLK19-FLAG-slk19Δ(aa709-821)-NLS-GFP-LYS2*	Integration of *SLK19* deletion construct
pSN1643	*PrSLK19-FLAG-slk19Δ(aa709-821)-NLS-LYS2*	Integration of *SLK19* deletion construct
pSN1644	*PrSLK19-FLAG-slk19Δ(aa410-500)-NLS-LYS2*	Integration of *SLK19* deletion construct
pSN1649	*PrSLK19-FLAG-SLK19-NLS-LYS2*	Integration of *SLK19* construct
pSN1652	*PrSLK19-FLAG-slk19Δ(aa709-821)-GCN4-Zipper-NLS-LYS2*	Integration of *SLK19* construct
pSN1653	*PrSLK19-FLAG-slk19Δ(aa709-821)-GCN4-Zipper-NLS-GFP-LYS2*	Integration of *SLK19* construct
pSN1657	*PrSLK19-FLAG-SLK19-NLS-GFP-LYS2*	Integration of *SLK19* construct
pSN1666	*PrSLK19-FLAG-slk19Δ(aa1-220)-NLS-LEU2*	Integration of *SLK19* deletion construct
pSN1667	*PrSLK19-FLAG-slk19Δ(aa300-502)-NLS-LEU2*	Integration of *SLK19* deletion construct
pSN1669	*PrSLK19-FLAG-slk19Δ(aa709-821)-NLS-LEU2*	Integration of *SLK19* deletion construct
pSN1670	*PrSLK19-FLAG-SLK19-NLS-LEU2*	Integration of *SLK19* construct
pSN1675	*PrSLK19-FLAG-slk19Δ(aa300-410)-NLS-GFP-LYS2*	Integration of *SLK19* deletion construct
pSN1676	*PrSLK19-FLAG-slk19Δ(aa760-821)-NLS-GFP-LYS2*	Integration of *SLK19* construct
pSN1677	*PrSLK19-FLAG-slk19Δ(aa760-821)-NLS-LYS2*	Integration of *SLK19* deletion construct
pMP1679	*PrSLK19-FLAG-slk19Δ(aa709-821)-CIN8-TD -NLS-LYS2*	Integration of *SLK19* construct
pMP1683	*PrSLK19-FLAG-slk19Δ(aa709-821)-CIN8-TD-NLS-eGFP-LYS2*	Integration of *SLK19* construct
pSN1686	*PrSLK19-FLAG-slk19Δ(aa300-410)-NLS-LYS2*	Integration of *SLK19* deletion construct
pSN1688	*PrSLK19-FLAG-slk19Δ(aa1-708)-NLS-GFP-LYS2*	Integration of *SLK19* deletion construct
pSN1689	*PrSLK19-FLAG-slk19Δ(aa503-711)-NLS-GFP-LYS2*	Integration of *SLK19* deletion construct
pSN1691	*PrSLK19-FLAG-slk19Δ(aa1-708)-NLS-LYS2*	Integration of *SLK19* deletion construct
pSN1692	*PrSLK19-FLAG-slk19Δ(aa503-711)-NLS-LYS2*	Integration of *SLK19* deletion construct
pSN1697	*PrSLK19-FLAG-slk19Δ(aa711-758)-NLS-GFP-LYS2*	Integration of *SLK19* construct
pSN1718	*PrSLK19-FLAG-slk19Δ(aa711-758)-NLS-LYS2*	Integration of *SLK19* construct
pSN1744	*PrSLK19-FLAG-slk19(aa300-502)-(aa709-821)-NLS-GFP-LYS2*	Integration of *SLK19* construct
pSN1745	*PrSLK19-FLAG-slk19(aa300-502)-(aa709-821)-NLS-LYS2*	Integration of *SLK19* construct
pVS1325	*pGal1-FLAG-STU1-GFP-LYS2*	Stu1 overexpression
pSN1722	*pGAL1-FLAG-SLK19-LYS2*	Slk19 overexpression
pSN1746	*pGAL1-FLAG-SLK19-LEU2*	Slk19 overexpression
pED999	*pGal-CDC14-flag; ADE2*	Cdc14 overexpression
pJO1645	*pGal-CDC14-FLAG-klTRP1*	Cdc14 overexpression
pSN1753	*pGal1-3HA-ASE1-3mcherry-LEU2*	Ase1 overexpression
pSN1761	*pGal1-FLAG-ASE1-3mcherry-LYS2*	Ase1 overexpression
pSN1778	*pGal1-FLAG-ase1-7A-3mcherry-LYS2*	Ase1-7A overexpression
pSN1779	*pGal1-FLAG-ase1-7D-3mcherry-LYS2*	Ase1-7D overexpression

[1](Knop et al., 1999), [2](Janke et al., 2004), [3](Nishimura et al., 2009) , [4](Funk et al., 2014), AID = auxin-induced degradation

2.3 Oligonucleotides

Oligonucleotides were obtained from Sigma-Aldrich or Thermo Fisher Scientific (HPLC purified). Oligonucleotides were resuspended in TE buffer (10 mM Tris/HCl pH 8.0, 1mM ethylenediaminetetraacetic acid (EDTA) pH 8.0) to a final concentration of 100 µM.

Name	**Sequence (5‘–3‘)**	**Purpose of usage**
AME1-S2-1	TATATATATATATATATATATATATACATCTTTTGAACCAA TTCCatcgatgaattcgagctcg	C-terminal tagging of Ame1

AME1-S3-2	GATAAATAAAATTAATGAAAATCTTTCTAACGAATTACAA CCAAGTCTAcgtacgctgcaggtcgac	C-terminal tagging of Ame1
ASE1-3/KAN-1	AGAATTCAAAGGTTTCATTTTGGATTCACTACTTTTGATGT TGAAccagcgacatggaggccca	Ase1-deletion
ASE1-S3	TGGAAAAATGAGCAAGTTTCGAAATTGAATGGATTCTCCTT TACAGATATTcgtacgctgcaggtcgac	C-terminal tagging of Ase1
ASE1-S2	TATTAATCCAGAGTCACGGTGCAATGGAAAAAGGAAAGGG AGAATGATAGatcgatgaattcgagctcg	C-terminal tagging of Ase1
ASE1-5	TATAACTGTAGTAGACCCAG	polymerase chain reaction (PCR) for clone verification
ASE1-6	GATGGAAGATGAAAATGATAAGGA	PCR for clone verification
BTN2-KAN-1	CAACAACCAAAAGAAAATAACTAATAGACCCCATTACAAT ATAGAACCAGCGACATGGAGGCCCA	Btn2-deletion
BTN2-S2	TCCGCCTTCTGCCGTGCCGATTTATATTCCTTTCATAAAGTC AGTGATCGATGAATTCGAGCTCG	Btn2-deletion
CDC14-S2	CACTGGAAAAATGGCATAAAACTTTTCAAGGTTATTATTAG Tatcgatgaattcgagctcg	C-terminal tagging
CDC14-S3	AGCGCCGCCGGTGGTATAAGAAAAATAAGTGGCTCCATCA AGAAAcgtacgctgcaggtcgac	C-terminal tagging
CDC15-S3	CCAAAGATAAAAGTGACGGCTTTTCCGTCCCCATTACAAC ATTTCAAACACGTACGCTGCAGGTCGAC	C-terminal tagging
CDC15-S2	ATGCTGTATTATTTCTCTATATATGTATGTATGCACATGCA ATTCCTACAATCGATGAATTCGAGCTCG	C-terminal tagging
CIN8-8-NotI	GAGAAATTGAAAgcggccgcTCGAAAAATGC	Amplification of CIN8-Stalk- and part of Tail-domain
CIN8-9-EagI	CAATTGCATGCcggccgGGCGATATTACAC	Amplification of CIN8-Stalk- and part of Tail-domain
DAD1-S2-1	CATAAATTTAGGATAATATTAGGAGAGACAGAGGGAACCG CAACTatcgatgaattcgagctcg	C-terminal tagging
DAD1-S3-2	GCGCCCATCGACGAGCAACCTACTTTATCTCAATCGAAAA CGAAGcgtacgctgcaggtcgac	C-terminal tagging
GCN4-1	TAGAAACAgcggccgcGGAGCAGGTGCTGGTGCTGGTGCTGG AGCAAGAATGAAACAACTTGAAG	Amplification of GCN4-domain
GCN4-2	AAAGGTAAgcggccggtGCGTTCGCCAACTAATTTCT	Amplification of GCN4-domain
S2-MTW1	TACATACATCATATCATAGCACATACTTTTTCCCACTTTAT ATTAatcgatgaattcgagctcg	C-terminal tagging
S3-MTW1	ATAGATATTGAAGAGCCTCAATTGGATTTACTTGATGATGT GTTAcgtacgctgcaggtcgac	C-terminal tagging
SCC1-S2	GCATCAGCTTATTGGGTCCACCAAGAAATCCCCTCGGCGT AACTAGGTTatcgatgaattcgagctcg	C-terminal tagging
SCC1-S3	TATTAAAATAGACGCCAAACCTGCACTATTTGAAAGGTTTA TCAATGCTcgtacgctgcaggtcgac	C-terminal tagging
SLK19-KAN-5	CAAGGGGCACCCAGTTAAAAAAGGTTTTGAGCACATATCG TAATTCccagcgacatggaggccca	Slk19-deletion
SLK19-S3	AAGAGAAGAAAAGCAGGAGTTACTCAAGTTGTTAGAAAAT GAAAAAAAAcgtacgctgcaggtcgac	C-terminal tagging
SLK19-S2	TGGCATGGACCGCAATGTCTTTGCTTGCTGGATTATTTATT TATATCTTGatcgatgaattcgagctcg	C-terminal tagging
SLK19-Not1-11	ACGATGACAAgcggccgcAAATGAACGAAGTTCCTACCACT	Cloning of Slk19 deletion construct
SLK19-28	CCTTCATTGAAtTcATTGTCCCATG	Cloning of Slk19 promoter
SLK19-29	CGATTGAgcggccgcaGTCATCAGCTCTT	Cloning of Slk19 deletion construct
SLK19-30	GtAtAtAgcggccgccTTTTTTTTCATTTTCTAACAAC	Cloning of Slk19 deletion construct
SLK19-31	GAAACGATAGTTTgcggccgcATACCGACAC	Cloning of Slk19 deletion construct
SLK19-NotI-32	ATCTCTATCCTTTTGATCATTGCggccgcTAACGCTATT	Cloning of Slk19 deletion construct
SLK19-33	TATAAGGTCAGAGTCGTTAAGTTGGTTGTCATCATC	Cloning of Slk19 deletion construct
SLK19-34	GATGATGACAACCAACTTAACGACTCTGACCTTATA	Cloning of Slk19 deletion construct
SLK19-35	GTCAGAGTCGTTGAAGTCATTTACTTCAGTAATTGA	Cloning of Slk19 deletion construct
SLK19-36	TCAATTACTGAAGTAAATGACTTCAACGACTCTGAC	Cloning of Slk19 deletion construct
SLK19-44	AATCACCGGATCCCtcaGACCTTTCTC	Cloning of Slk19 deletion construct
SLK19-45-NotI	CAAAATAATAATAACAAgcggccgcTTACTTTAAG	Cloning of Slk19 deletion construct

SLK19-46	gacagtattttcatgttcgccctttatAAGTTGGTTGTCATCATCGTAG	Cloning of Slk19 deletion construct
SLK19-47	aatgactacgatgatgacaaccaacttATAAAGGGCGAACATGAAAATAC	Cloning of Slk19 deletion construct
SLK19-48	ttcatcatctctatccttttgatcattGAAGTCCTTAGAAATCGATAAAG	Cloning of Slk19 deletion construct
SLK19-49	gaaactttatcgatttctaaggacttcAATGATCAAAAGGATAGAGATG	Cloning of Slk19 deletion construct
SLK19-50	tgacctttgttcgtgtttggatgaTAAAGTAACGCTATTATTGTTATT	Cloning of Slk19 deletion construct
SLK19-52-NotI	ACCTTTTGTTCgcggccgcATGAATACTGGATA	Cloning of Slk19 deletion construct
SLK19-62-NotI	GATGATGAGCGGCCGCAAGATATTAGACATGAC	Cloning of Slk19 deletion construct
SPC105-S2-2	gtcatgagatattactagtcatcgttgtcctattataaacactatcgatgaattcgagctcg	C-terminal tagging
SPC105-S3-1	TCTTCCTTCATTTACGAAAAGTAGAATACATTTAGAGTTTA CGcgtacgctgcaggtcgac	C-terminal tagging
SPC72-S2	TGACTGAGTGTTACATTAAATATATTTATATATAAACGTAT GATATatcgatgaattcgagctcg	C-terminal tagging
SPC72-S3	TGAGTCATTGAGATCGAAACTTTTCAACCTATCAATCAATC CCcgtacgctgcaggtcgac	C-terminal tagging
STU1-S3-1	CCTAAGAATGTCTTTAAAATGATCATGTTCATCGCCTCAAA CGAAcgtacgctgcaggtcgac	C-terminal tagging
STU1-S2-2	AAGAAACTCTGGTGAGACGCGTCACGGTAAAAAAAAATTA CGCGTatcgatgaattcgagctcg	C-terminal tagging
SPO12-S2	CGTTTGCTTATTGGTTTAGTGTAGCATTTGGCTATTTTTGGA TGAatcgatgaattcgagctcg	Spo1-deletion
SPO12-KAN/HIS-1	GAAAACAAAATAACATATACAGTAAGAACAATAGAAAAC GTATTTccagcgacatggaggccca	Spo1-deletion
Pho5-forward	GAATAGGCAATCTCTAAATGAATCGA	RT-PCR, quantitative chromatin immunoprecipitation (ChIP)
Pho5-reverse	GAAAACAGGGACCAGAATCATAAATT	RT-PCR, quantitative ChIP
Cen3-forward	CCTTCCGCTTATAGTACAGTACCTA	RT-PCR, quantitative ChIP
Cen3-reverse	TTCAATGAATAGCTTTCTGTGGA	RT-PCR, quantitative ChIP

TaqMan® probes used in this study:

Name	Sequence (5‘–3‘)	5’ reporter	3‘ quencher	Purpose of usage
Pho5-probe	ACCTTGGCACTCACACGTGGGACTAGC	6FAM	TAMRA	RT-PCR, quantitative ChIP
Cen3-probe	CGATCAGCGCCAAACAATATGGAA	6FAM	TAMRA	RT-PCR, quantitative ChIP

2.4 Antibodies

Name	Company	Description	Figure
rabbit anti-GFP antibody	in-house	Primary antibody, for Western blot: usage 1:2000, for ChIP: 7µL per sample	Figure 4
mouse anti-FLAG-horseradish peroxidase (HRP) monoclonal antibody	Sigma-Aldrich	Primary antibody, usage 1:2000	Figure 4, Figure 6A, Figure 10E
mouse anti-FLAG monoclonal antibody	Sigma-Aldrich	Primary antibody, usage 1:2000	Figure 10B
mouse anti-Myc monoclonal antibody	Sigma-Aldrich	Primary antibody, usage 1:1500	Figure 6A, Figure 10B and E, Figure 13A
rabbit anti-Arc1 antibody	in-house	Primary antibody, usage 1:100000	Figure 13A
goat α-rabbit-HRP antibody	Sigma-Aldrich	Secondary antibody, usage 1:10000	Figure 4
goat anti-mouse-HRP antibody	Sigma-Aldrich	Secondary antibody, usage 1:10000	Figure 6A, Figure 10E
Alexa-Fluor® 680 goat α-mouse polyclonal antibody	Invitrogen	Secondary antibody, usage 1:10000	Figure 13A
Alexa-Fluor® 680 goat α-rabbit polyclonal antibody	Invitrogen	Secondary antibody, usage 1:10000	Figure 13A

2.5 Media for culturing and imaging

Media used for *S. cerevisiae* culturing:

Media	Composition
YP medium	10 g/L yeast extract, 20 g/L peptone, adjusted to pH 5.5 with HCl
YPD+2 medium	YP medium (pH 5.5), 30 mg/L adenine, 30 mg/mL uracil, 2 % glucose as carbon source
YPD+3 medium	YP medium (pH 5.5) supplemented with 100 mg/L adenine, 30 mg/L uracil, 50 mg/L tryptophan and 2 % sterile filtered glucose as carbon source (culturing medium for yeast strains used for microscopy)
YPR+2 medium	YP medium (pH 5.5), 2 % raffinose, 30 mg/L adenine, 30 mg/mL uracil
YPRG+3 medium	YP medium (pH 5.5) supplemented with 100 mg/L adenine, 30 mg/L uracil, 50 mg/L tryptophan, 2 % sterile filtered raffinose and 1 % sterile filtered galactose as carbon source (culturing medium for yeast strains used for microscopy)
SC -Met medium	6.7 g/L yeast nitrogen base without amino acids, 0.7 g/L complete supplement mixture (CSM) double drop-out -methionine (Met) -tryptophan (Formedium), 100 mg/L adenine, 50 mg/L tryptophan
SDC -Met medium	SC-Met medium, 2 % glucose, 100 mg/L adenine
SRC -Met medium	SC-Met medium, 2 % raffinose, 100 mg/L adenine

For the preparation of agarose plates, the different media were supplemented and heated with 2 % (w/v) agarose. Plates were stored sealed at 4°C until usage.

Non-fluorescent media (NFM) used for *S. cerevisiae* imaging:

Media	Composition
NFM (with glucose or galactose)	0.9 g/L KH_2PO_4, 0.23 g/L K_2HPO_4, 0.5 g/L $MgSO_4$, 3.5 g/L $(NH_4)_2SO_4$, 20 g/L glucose or galactose as carbon source, 0.79 g/L CSM (Qbiogene), 0.5 mg/L β-alanine, 0.2 mg/L thiamine HCl, 3.0 mg/L D-pantothenic acid calcium salt, 2.0 mg/L inositol, 0.4 mg/L biotin, pH adjusted to 5.5–6 with KOH

Escherichia coli (*E. coli*) culturing media:

Media	Composition
LB medium	10 g/L tryptone, 5 g/L yeast extract, 10 g/L NaCl, pH 7.0
SOC-medium	20 g/L tryptone, 5 g/L yeast extract, 0,5 g/L NaCl, 2.5 mM KCl, 0.4 % (w/v) glucose, 10 mM $MgCl_2$, pH 7.0

For the preparation of agarose plates, LB medium was supplemented and heated with 2 % (w/v) agarose. Plates were stored sealed at 4°C until usage.

2.6 Chemicals, media components, enzymes and consumables

Chemicals, media components, enzymes and consumables used in this study were obtained from the following companies:

AppliChem GmbH; Becton, Dickinson and Company Corporation; Berkel AHK Alkoholhandel GmbH & Co. KG; Bernd Kraft GmbH; Biological Industries Ltd.; Bio-Rad Laboratories Inc.; Carl Roth GmbH & Co. KG; Caslo ApS; Cayman Chemical Company Inc.; Cole-Parmer GmbH; Cytiva - Global Life Sciences Solutions GmbH; Cytoskeleton Inc.; Enzo Life Sciences Inc.; EURx GmbH; Fermentas GmbH; Focus Biomolecules LLC; Formedium Ltd.; Honeywell International Inc.; Invitrogen AG; Iris Biotech GmbH; Merck KGaA; neoFroxx GmbH; neoLab Migge GmbH; New England Biolabs GmbH; Olympus K.K.; Pharmacia Biotech Inc.; Promega GmbH; Serva Electrophoresis GmbH; Sigma-Aldrich Corporation; Sigmund Lindner GmbH; Starlab International GmbH; Thermo Fisher Scientific Inc.; VWR International, LLC.

2.7 Equipment

Devices:

Description	Company
Real-Time PCR Thermocycler, StepOnePlus™ Real-Time PCR System, operated by the StepOne™ Software	Thermo Fisher Scientific Inc.
PCR Thermal Cycler, Techne Techgene	Techne Ltd.
LI-COR Odyssey® CLx Imaging System, operated by the Image Studio™ Software Version 5.0	LI-COR Biosciences GmbH
Sonicator, SONOPULS Ultrasonic homogenizers HD 2070, used with Microtip, MS 72, dia. 2 mm	BANDELIN electronic GmbH & Co. KG
Photometer, Spectronic GENESYS™ 10 Bio Spectrophotometer	Thermo Fisher Scientific Inc.
Benchtop centrifuges, Eppendorf 5417R Refrigerated Centrifuge and Eppendorf Centrifuge 5417C with fan cooling, Rotor: 45-30-11 30 x3,75 g 30 x1.5/2.0 ml	Eppendorf AG
Hettich® ROTINA 46R centrifuge and Hettich® ROTINA 38R centrifuge	Andreas Hettich GmbH & Co. KG
Eppendorf 5415C Microcentrifuge Rotor F-45-18-11 18	Eppendorf AG
Eppendorf® Thermomixer Compact with 1.5 mL block	Eppendorf AG
Trans-Blot® SD Semi-Dry Transfer Cell	Bio-Rad
Mini-PROTEAN® Tetra cell	Bio-Rad Laboratories, Inc.
WTC Binder incubator	BINDER GmbH
Infors HT Shaking incubator	Infors Gmbh
Electrophoresis power supply 600/250	H. Hölzel GmbH
PowerPac™ HC High-Current Power Supply	Bio-Rad Laboratories, Inc.
Eppendorf Thermomixer 5355 Comfort Mixer shaker	Eppendorf AG

Imaging Station:

Description	Company
Olympus IX 81 Motorized inverted fluorescence microscope (Plan-Apochromat objective, numerical aperture of 1.4, 100x magnification)	Olympus K.K.
Olympus MT20 illumination device with a 150 W Xenon arc burner	Olympus Soft Imaging Solutions GmbH
Charge-coupled device camera; ORCA-ER model C4742-80-12AG, operated by the Olymus xCellence software	Hamamatsu Photonics Olympus K.K.
Olympus Microscope System controller IX2-UCB	Olympus K.K.
Fujitsu CELSIUS W520 Power PC	FUJITSU Technology Solutions GmbH
Hamamatsu C4742-80-12AG ORCA-ER Camera Controller	Hamamatsu Photonics K.K.
ControllerE-665.XR LVPZT Piezo Amplifier / Servo-Controller Module	Physik Instrumente (PI) GmbH & Co. KG
Corvus high resolution positioning controller	ITK Dr. Kassen GmbH

3 Methods

3.1 Cell biological methods – *Escherichia coli*

E. coli DH5α cells were used for plasmid transformation, amplification and extraction. The exact compositions of *E. coli* culturing media are listed above in chapter 2.5.

3.1.1 *E. coli* cell culturing

E. coli cells were cultured at 37°C either in liquid LB medium at 180 rpm or on solid LB agarose plates. Culturing media were supplemented with 100 µg/ml ampicillin for selection of plasmid-containing cells.

3.1.2 Generation of competent cells

Chemically competent cells were prepared as described (Inoue et al., 1990). Cells had a transformation efficiency of $1x10^8$ colonies/µg DNA (tested with 0.1 ng pUC18). Competent cells were quick frozen in 60 µL aliquots (OD_{600} = 0.55) and stored at -80°C until usage.

3.1.3 *E. coli* transformation

For *E. coli* cell transformation, 60 µL of competent DH5α cells were mixed with 3 µL of the ligation reaction (ligation described in chapter 3.3.1 Plasmid construction), incubated on ice for 30 min and heat-shocked for 1 min at 42°C. DH5α cells were supplemented with 500 µL SOC-medium, recovered for 1h at 37°C at 180 rpm and plated out on ampicillin containing selection plates. After overnight (o/n) incubation at 37°C, single *E. coli* clones were tested for successful transformation by colony polymerase chain reaction (PCR) (described in chapter 3.3.4).

3.1.4 Preparation of glycerol stocks

For preparation of glycerol stocks, 800 µL o/n culture was mixed with 200 µL of 99 % glycerol, quick frozen in liquid nitrogen and stored at -80°C.

3.2 Cell biological methods – *Saccharomyces cerevisiae*

3.2.1 Culturing of yeast cells

Description of yeast strain culturing is adapted from Norell et al., 2021 (copyright: ©2021 Norell et al., CC BY-NC-SA 3.0, http://creativecommons.org/licenses/by-nc-sa/3.0). Compositions of used culturing and imaging media are listed in chapter 2.5 above.

Cycling cell growth

Yeast cells were streaked out from the glycerol stock on agarose plates with the appropriate medium and grown exponentially at 25°C for 2–3 days before inoculation of a liquid culture. Liquid yeast cultures of cycling cells were grown exponentially at 180 rpm at 25°C in a shaking incubator in the appropriate culturing medium.

Nocodazole treatment

To provoke uaKTs, yeast cells were treated with the MT-depolymerizing drug nocodazole (Nz) (Figure 1, Figure 3, Figure 5, Figure 6). For this, yeast cultures were incubated for 2.5–3 h with α-factor, released from α-factor arrest into media containing 15 µg/mL Nz and incubated for another 3.5 h.

Cell cycle synchronization by G1 arrest

For cell cycle synchronization, the yeast cells were incubated for 1.5–2 h with 200 ng/ml α-factor to induce a G1 arrest. For the release from this α-factor arrest, cells were washed in three consecutive steps with sterile millipore water (mp$H_2$0). For synchronized growth, cells were resuspended in YPD+3 medium and observed at the indicated timepoints (Figure 8C, Figure 11C).

Metaphase arrest by Cdc20 depletion

CDC20 was placed either under the control of the *GAL1* or the *MET25* promoter in the respective yeast strains. Cells carrying *pGAL1-CDC20* were grown exponentially in YPRG+3 medium and were then shifted to YPD+3 medium for 3.5 h for metaphase arrest (Figure 1C, Figure 7, Figure 8A-B, Figure 10, Figure 11A-B, Figure 24A). For analysis of the cells by fluorescence microscopy, they were washed and resuspended in non-fluorescent media (NFM) supplemented with 2 % glucose. Cells carrying *pMET25-CDC20* were grown exponentially in synthetic dextrose complete (SDC) medium lacking methionine (SDC -Met medium) and were then shifted to YPD+3 medium supplemented with 2 mM methionine. The arrest time for these cells was 3.5 h (Figure 9, Figure 10, Figure 11A-B, Figure 25, Figure 26, Figure 32A) or 4.5 h (Figure12, Figure 24B-E). For analysis of the cells by fluorescence microscopy, they were washed and resuspended in NFM supplemented with 2 % glucose and 2 mM methionine.

Conditional protein depletion

Proteins were conditionally depleted with the auxin-induced degradation (AID) system based on (Nishimura et al., 2009) in cells expressing *OsTIR1*. The proteins of interest (for degradation) were tagged with the degron *IAA17*. For inducing protein depletion, these cells were shifted to YPD+3 medium containing 1 mM indole acetic acid (IAA) and were observed by microscopy after 2 h (Figure 25A and B, b) or after 3.5 h (Figure 1, Figure 7, Figure 8B, Figure 10A, Figure 11A-B, Figure 22, Figure 24). For protein depletion in G1 phase (Figure 31A, Figure 25B, a), cells were arrested for 2 h with α-factor and 1 h with additionally added 1 mM IAA (total 3h G1 arrest). Cells were released into YPD+3 medium containing 1 mM IAA and were observed after 2 h (Figure 25B, a) or 2.5 h (Figure 31A).

For analysis of the cells by fluorescence microscopy, they were washed and resuspended in NFM supplemented with 2 % glucose and 1mM IAA.

Induced protein overexpression

Proteins of interest were overexpressed by replacing the endogenous promotor by the *GAL1* promoter. The respective yeast strains were grown exponentially in YPR+2 or SRC -Met medium and overexpression was induced by adding a final concentration of 2 % galactose to the culturing medium. Strains were incubated for 4 h (Figure 21, Figure 22, Figure 32).

3.2.2 Yeast cell transformation

The yeast cell transformation protocol was adapted from Schiestl & Gietz, 1989. 10 OD_{578} of exponentially cycling cells were harvested at 1560 rcf for 3 min at room temperature (RT). The washed cell pellet was resuspended in LiSorb (composition listed in table below) to a final concentration of 0.1 OD_{578}/µL to make cells competent. For DNA integration, either 0.5–1 µg of linearized plasmid DNA or a PCR-sample (see chapter 3.3.2 Yeast strain construction) was used. 100 µL of competent cells were mixed with 25 µL of denatured single stranded salmon testes DNA (ssSTD) (Sigma-Aldrich, stock 5 µg/µL), 600 µL LiPEG (composition listed in table below) and with the DNA used for integration. The mixture was placed on a shaker at 2000 rpm for 30 min at RT. Subsequently, 70 µL DMSO was added to make cells more permeable. Cells were heat-shocked for 20 min at 37°C for DNA uptake. For recovery, cells were resuspended in their respective growth medium (without selection pressure) and incubated at 25°C and 180 rpm for 3 h. Recovered cells were plated out on appropriate selection plates. Successful yeast cell transformation was verified by clone check PCR as described in chapter 3.3.4.

Solution	Composition
LiSORB	100 mM lithium acetate, 10 mM Tris/HCl pH 8.0, 1 mM EDTA pH 8.0, 1 M sorbitol (SORB), filter sterilized
LiPEG	100 mM lithium acetate, 10 mM Tris/HCl pH 8.0, 1 mM EDTA pH 8.0, 400 mg/mL polyethylene glycol (PEG)-4000, filter sterilized

3.2.3 Preparation of yeast glycerol stocks

Yeast cells were exponentially grown on agarose plates with the appropriate medium at 25°C for 2–3 days. Cells were collected from the plates, resuspended in 800 µL 15 % glycerol, quick frozen in liquid nitrogen and stored at -80°C.

3.2.4 Spot test analysis

For the yeast growth spot test, the used yeast strains (Figure 13) were grown exponentially to a $OD_{578} = 1$ and counted in a Neubauer chamber (hemocytometer). Five serial dilutions in steps of 1:10 were prepared and 5 µL of each dilution were dropped on YPD+3 agarose plates. Serial dilutions started with $4x10^6$ cells/mL (20000 cells in 5µL) and ended up with a dilution of $4x10^2$ cells/mL (2 cells in 5µL).

3.3 Molecular biology techniques

3.3.1 Plasmid construction and isolation from *E. coli* cells

PCR for insert amplification

Insert DNA sequences used for plasmid construction were amplified with the Q5® High-Fidelity DNA Polymerase (New England Biolabs) in a total reaction volume of 50 µL. The PCR reactions contained, 1 U Q5-polymerase, 1x Q5 reaction buffer, max. 1 µg template DNA, 200 µM of each deoxynucleotide triphosphate (dNTP) and 0.5 µM of each primer.

PCR reaction steps	Temperature	Time	Cycle number
Initial denaturation	95°C	3 min	1
Denaturation	98°C	15 sec	30
Annealing	Tm* (+/- 5°C)	30 sec	
Extension	72°C	30 sec per kb	
Final extension	72°C	7 min	1

* The melting temperature (Tm) of each primer was calculated based on the number of cytosine/guanine (n_G+n_c) and adenine/thymine (n_A+n_T) by the following equation: $Tm = 3*(n_G+n_c) + 2*(n_A+n_T)$.

The PCR reaction was checked by agarose gel electrophoresis. For isopropanol precipitation of PCR products, 45 µL of the PCR reaction was supplemented with 45 µL TE buffer, 10 µL of 10 M sodium acetate and 110 µL isopropanol. After 15 min incubation at RT, precipitated DNA was pelleted at 20817 rcf for 30 min at RT, washed with 70 % ethanol and dried at RT. The dried DNA pellet was resuspended in 20 µL TE buffer and used for restriction enzyme digest (see below).

SLK19 deletion constructs

All *SLK19* constructs used in this study were either created by PCR or overlap-PCR and were constructed with a FLAG-tag at the N-terminus, a C-terminal SV40 nuclear localization signal (NLS) and (where indicated) a C-terminal tag with green fluorescent protein (GFP). The different *SLK19* constructs created in this study were integrated into the yeast genome either into the *LEU2* or the *LYS2* locus and are all under the control of the endogenous promoter of *SLK19* (see table in chapter 2.2).

Restriction enzyme (RE) digest

For plasmid construction, vector and insert DNA were cut with compatible REs (obtained from Fermentas or New England Biolabs). RE digests were performed in a total volume of 10–20 µL using 1 U RE per 1 µg DNA. REs were used with the reagents and instructions provided by the manufacturer.

Modifications of DNA fragments

Where necessary, blunt ends were created by filling up 5' overhangs by using Klenow fragment (Thermo Fisher Scientific) or by trimming 3' overhangs by using T4 DNA polymerase (Thermo Fisher Scientific). Prior to ligation, linearized vector DNA was treated with calf intestinal alkaline phosphatase (CIAP) (Invitrogen) for dephosphorylation of 5' ends to prevent re-ligation of vector DNA. Where necessary, 5' ends of insert DNA were phosphorylated by T4 polynucleotide kinase (PNK) (Promega). DNA modifying enzymes were used with the reagents and instructions provided by the manufacturer. After enzymatic treatment, vector and insert DNA were purified by agarose gel extraction.

Agarose gel electrophoresis

DNA samples were mixed with loading dye (6x: 60 mM Tris pH 7.5, 0.06 % (w/v) bromophenol blue, 0.06 % (w/v) xylene cyanol, 60 % (v/v) glycerol, 1 mM EDTA) and loaded onto a 1 % agarose gel with 0.5 µg/µL ethidium bromide (Sigma-Aldrich) in electrophoresis chambers filled with TAE buffer (0.04 M Tris acetate, 1 mM EDTA pH 8.0). Agarose gels were run constantly at 80–120 V for approximately 30–40 min before detecting the bands with UV-light.

Agarose gel extraction

For agarose gel purification the GeneJET Gel Extraction Kit (Thermo Fisher Scientific) was used according to the manufacturer's instructions.

Plasmid ligation

100 ng of the linearized and purified vector was used for ligation together with the 3-fold molar amount of purified insert with sticky ends or with equal molar amounts of insert with blunt ends. Ligation reactions were performed in a total volume of 10 µL containing 1 U T4 DNA ligase (Thermo Fisher Scientific), 1x T4 DNA ligase buffer, 1 mM ATP and 5 % polyethylene glycol (PEG)-4000. Ligation samples were incubated at 22°C for 3 h. Ligated plasmids were used for *E. coli* transformation (as described in chapter 3.1.3).

Plasmid isolation from *E. coli* cells

10 mL *E. coli* o/n culture was harvested at 1840 rcf at 4°C for 10 min. Cells were resuspended in 500 µL P1 buffer supplemented with 0.1 mg/mL RNAse. For cell lysis, 500 µL P2 buffer was added, and cells were inverted gently for 5 min at room temperature (RT). Cell lysis was stopped by adding 500 µL of cold P3 buffer leading to neutralization, and precipitation of cell debris and genomic DNA. The latter components were removed by three consecutive centrifugation steps at 20817 rcf at 4°C each for 30 min. For plasmid precipitation, 800 µL

of clarified supernatant was mixed with 600 µL isopropanol and incubated for 15 min at RT. Plasmid DNA was pelleted at 20817 rcf at 4°C for 30 min, washed with 70 % ethanol, dried at RT and was finally resuspended in 70–100 µL TE buffer. Verification of the plasmid DNA was performed by RE digest (described above) and by sequencing.

Buffer	Composition
P1 buffer	50 mM Tris/HCl pH 8.8, 10 mM EDTA pH 8.0
P2 buffer	0.2 M NaOH, 1 % sodium dodecyl sulfate (SDS)
P3 buffer	2.6 M potassium acetate pH 5.2
TE buffer	10 mM Tris/HCl pH 8.0, 1mM EDTA pH 8.0

3.3.2 Yeast strain construction

Description of yeast strain construction is adapted from Norell et al., 2021 (copyright: ©2021 Norell et al., CC BY-NC-SA 3.0, http://creativecommons.org/licenses/by-nc-sa/3.0). The genotypes of all used yeast strains are listed in chapter 2.1. All plasmids that were used for yeast cell construction are listed in chapter 2.2.

Vector based sequence integration

Integration vectors carrying the desired gene and an appropriate selection marker were linearized by RE digest (described in chapter 3.3.1) to allow sequence integration into the yeast genome by homologous recombination.

PCR-mediated sequence integration

PCR-mediated sequence integration was used for gene deletions, promoter replacements and tagging of endogenous genes e.g. with the *IAA17*-degron or different fluorophores (adapted from Knop et al., 1999). A plasmid, containing the desired integration sequence including the appropriate selection marker, was used as template together with S2-/S3 primers that contained gene specific regions allowing homologous recombination into the yeast genome.

Sequences for gene tagging were amplified by PCR using the OptiTaq DNA polymerase (obtained from EUR_X) in a total reaction volume of 50 µL. The reactions contained 2.5 U OptiTaq polymerase, 1x buffer A (provided by the manufacturer), 2.75 mM $MgCl_2$, 500 µM of each dNTP, 1 µM of each primer and max. 0.5 µg template DNA.

OptiTaq-PCR program:

PCR reaction steps	Temperature	Time	Cycle number
Initial denaturation	95°C	3 min	1
Denaturation	95°C	15 sec	10
Annealing	54°C	30 sec	
Extension	68°C	2.5 min	
Denaturation	95°C	15 sec	15
Annealing	54°C	30 sec	
Extension	68°C	2.5 min + 20 sec/cycle	
Final extension	60°C	10 min	1

The PCR reaction was checked by agarose gel electrophoresis. For ethanol precipitation, the PCR reaction was supplemented with 50 µL H_2O and final 1 M LiCl. 300 µL of 95% ice cold ethanol was added to the sample and incubated for 1 h at -20°C. The precipitated DNA was pelleted at 20817 rcf for 20 min at 4°C. The dried DNA pellet was resuspended in 10 µL sterile mpH_2O before usage for transformation (described in chapter 3.2.2).

3.3.3 Yeast genomic DNA extracts

Single yeast clones were resuspended in 50 µL NTES buffer (10 mM Tris/HCl pH 8.0, 100 mM NaCl, 1mM EDTA pH 8.0, 1 % SDS) and incubated for 10 min. Subsequently, 50 µL phenol/chloroform/isoamyl alcohol (ratio 25:24:1; Sigma Aldrich) was added to each sample. For cell lysis, glass beads were added to the mixture and samples were placed on a shaker for 40 min at 1800 rpm and 4°C. Samples were centrifuged at 20817 rcf for 3 min and 30 µL of the upper aqueous phase (containing the genomic DNA) was transferred into a fresh tube. 20 µL chloroform was added, samples were mixed thoroughly for 1 min and centrifuged at 20817 rcf for 3 min. 10 µL of the upper aqueous phase was transferred to a new tube. This yeast extract was used as template with the respective primers for clone check PCR (see chapter 3.3.4 below).

3.3.4 Clone verification by PCR

For verification of *S. cerevisiae* strains, 0.5 µL of yeast cell extract (preparation described in chapter above) was added to 4.5 µL mpH_2O, denatured for 3 min at 95°C and used as PCR template. For verification of *E. coli* strains, single colonies were picked, resuspended in 5 µL mpH_2O and boiled for 3 min at 95°C and used as PCR template. Clone check PCRs were performed in a total volume of 25 µL. The reaction contained 1x PCR buffer (10 mM Tris pH 8.3, 1.5 mM $MgCl_2$, 50 mM KCl), 1 µL homemade Taq, 200 µM of each dNTP, 1 µM of each primer and the 5 µL template premix (mentioned above).

Clone check PCR program:

PCR reaction steps	Temperature	Time	Cycle number
Initial denaturation	95°C	3 min	1
Denaturation	95°C	20 sec	30
Annealing	Tm* (+/- 5°C)	45 sec	
Extension	72°C	1 min per kb	
Final extension	72°C	7 min	1

* The melting temperature (Tm) of each primer was calculated based on the number of cytosine/guanine (n_G+n_c) and adenine/thymine (n_A+n_T) by the following equation: $Tm = 3*(n_G+n_c) + 2*(n_A+n_T)$.

3.3.5 Whole cell extracts (WCE) of yeast cells

The description of WCE preparation is adapted from Norell et al., 2021 (copyright: ©2021 Norell et al., CC BY-NC-SA 3.0, http://creativecommons.org/licenses/by-nc-sa/3.0).

Metaphase-arrested yeast cells were used to prepare WCE (Figure 13A). The protocol for WCE preparation was based on (Hecht & Grunstein, 1999). 25 OD_{578} of cells were harvested, resuspended in 80 µL breaking buffer (100 mM Tris HCL pH 8.0, 20 % glycerol, 1 mM dithiothreitol (DTT), 10 mM NaF and 3 mM phenylmethylsulfonyl fluoride (PMSF)) and lysed with glass beads at 4°C. The lysate was clarified at 20817 rcf for 30 min at 4°C. The protein concentration of the WCE was quantified by a Bradford assay: 1 µL WCE was mixed with 99 µL H_2O and 900 µL Bradford solution (100 mg/L Coomassie® Brilliant Blue G-250 (Serva), 5 % ethanol, 8.5 % phosphoric acid) and measured with the photometer at a wavelength of 595 nm. The standard curve for comparison was generated with bovine γ-globulin (Serva) with concentrations of 0, 5, 10, 15, 20 and 25 mg/mL (diluted in H_2O).

3.3.6 SDS-PAGE and Western blot analysis

The sodium dodecyl sulfate polyacrylamide gel electrophoresis (SDS-PAGE) protocol is based on (Laemmli, 1970). Protein samples were mixed with SDS loading dye (62.5 mM Tris/HCl pH 6.8, 2 % (w/v) SDS, 5 % (v/v) β-mercaptoethanol, 0.0025 % (w/v) bromophenol blue, 20 % glycerol), boiled for 3 min at 95°C and were loaded on a precast SDS-PAGE gradient gel (4–20 % Mini-PROTEAN® TGX™, Bio-Rad Laboratories) (Figure 13A, Figure 16A) or on an 8 % SDS-PAGE gel (Figure 4, Figure 6). PageRuler™ unstained protein ladder (Thermo Fisher Scientific) was used as protein marker. SDS-PAGE gels were run in electrophoresis champers with 1x SDS running buffer (25 mM Tris, 192 mM glycine, 0.1 % (w/v) SDS) at 135 V for approximately 1.5 h.

Preparation of SDS-Page gels:

	Composition
4 % stacking gel	125 mM Tris/HCl pH 6.8, 4 % (v/v) bis-acrylamide (37.5:1 mix), 0.1 % (w/v) SDS, 0.065 % (w/v) ammonium persulfate (APS), 0.15 % (v/v) N,N,N′,N′-tetramethylethylene-diamine (TEMED)
8 % separating gel	377 mM Tris/HCl pH 8.8, 8 % (v/v) bis-acrylamide (37.5:1 mix), 0.1 % (w/v) SDS, 0.075 % (w/v) APS, 0.075 % (v/v) TEMED

For Western blot analyses, proteins were transferred on a polyvinylidene fluoride (PVDF) membrane (Amersham™ Hybond™ 0,45 µm pore size, Cytiva) by semi-dry electroblotting at 11 V for 1.5 h using a Trans-Blot® SD Semi-Dry Transfer Cell (Bio-Rad). Blotting buffer (48.3 mM Tris, 39 mM glycine, 0.037 % (w/v) SDS, 10 % methanol) was used for equilibration of membrane and blotting paper (Whatman™ medium thickness Grade 3MM, Cytiva). Blocking of the membrane was performed with 5 % milk powder (blotting-grade, Carl Roth) in phosphate buffered saline (PBS). The primary and secondary antibodies used in this study are listed in chapter 2.4 and were used with the indicated dilutions. Blocking and antibody incubation was performed each for 1 h. Washing between the steps was performed with PBS/Tween® (PBST) (three times for 10 min). Signals were detected by chemiluminescence, using an enhanced chemiluminescence (ECL) detection kit (obtained from Biological Industries) (Figure 4, Figure 6A, Figure 10E) or by the LI-COR Odyssey® CLx Imaging System (LI-COR Biosciences; operated by the Image Studio™ Software) (Figure 13A). The signals obtained from the latter detection method were quantified with the Fiji software.

3.3.7 Chromatin immunoprecipitation (ChIP) and quantitative PCR (qPCR)

ChIP and qPCR methods are adapted from Norell et al., 2021 (copyright: ©2021 Norell et al., CC BY-NC-SA 3.0, http://creativecommons.org/licenses/by-nc-sa/3.0) and were performed according to the protocol described in Funk et al., 2014.

For the qPCR reactions, the TaqMan® Gene Expression Master Mix (Thermo Fisher Scientific) was used. The PCR reactions were performed according to the instructions provided by the manufacturer (Thermo Fisher Scientific). An amplification temperature of 60°C was used. The ChIP samples were diluted 1:5. The input samples were used as control and were diluted 1:100. The qPCR reactions were carried out in the StepOnePlus™ Real-Time PCR System (Applied Biosystems; thermal cycler operated by the StepOne™ Software). The primers and probes used for quantitative ChIP analyses are listed in chapter 2.3. For quantification of the qPCR results, the mean enrichment of centromeric DNA (*CEN3)* was calculated in relation to the non-centromeric DNA (*PHO5*) and the values were normalized (with *WT* representing the highest value of 100%) (Figure 7B, Figure 24E).

3.3.8 Co-immunoprecipitation (CoIP)

The CoIP method is adapted from Norell et al., 2021 (copyright: ©2021 Norell et al., CC BY-NC-SA 3.0, http://creativecommons.org/licenses/by-nc-sa/3.0). The CoIP experiments (Figure 4 and Figure 6, Figure 10B and E) were performed with anti-FLAG® M2 magnetic beads (Sigma-Aldrich). The Slk19-Slk19 CoIPs shown in Figure 4 were performed according to the protocol described in Funk et al., 2014. For the pulldown of Stu1-9Myc by FLAG-tagged Slk19 constructs (Figure 6, Figure10B) and the pulldown of Slk19-9Myc by 5xFLAG-tagged Stu1 or Stu1ΔCL (Figure 10E), 500 OD_{578} of cells were harvested at 1560 rcf for 3 min at 4°C. After the last wash step, the supernatant was completely removed to obtain a dry pellet and cells were resuspended in 4 µL/OD_{578} lysis buffer (see buffer list below). The resuspended cells were slowly dripped into liquid nitrogen to create small frozen droplets. For cell lysis, the frozen droplets were placed into a precooled mortar and crushed with a pestle until approximately 65% of the cells were lysed (cell lysis was checked under a light microscope). During this procedure, the cells and equipment were continuously cooled by the addition of small amounts of liquid nitrogen. The collected cell lysate was thawed on ice and clarified in two consecutive centrifugation steps (each for 30 min at 20817 g and 4°C). The procedure after the clarification steps was performed analogously to the procedure described in Funk et al., 2014. 250 µg/mL FLAG-peptide (Caslo ApS) in BH0.10$^+$ was used to elute the FLAG-tagged proteins from the anti-FLAG® M2 magnetic beads. For protein elution, the samples were incubated for 25 min on a shaker at 25°C and 900 rpm.

CoIP buffers	**Composition**
BH0.10	25 mM 4-(2-hydroxyethyl)-1-piperazineethanesulfonic acid (HEPES) pH 8.0, 2 mM $MgCl_2$, 150 mM KCl, 10 % glycerol, 0.1 mM EDTA pH 8.0, 0.5 mM ethylene glycol-bis(β-aminoethyl ether)-N,N,N′,N′-tetraacetic acid (EGTA) pH 8.0, 0.1 % NP.40
BH0.10$^+$	BH0.10 supplemented with 2 mM DTT, 0.4 mM PMSF, 20 µg/mL chymostatin, 20 µg/mL leupeptin, 20 µg/mL pepstatin
Lysis buffer	BH0.10$^+$ supplemented with 2 mM β-glycerol phosphate disodium salt, 1 mM sodium pyrophosphate, 5 mM sodium fluoride, 0.1 mM vanadate, 0.1 µM microcystin

3.3.9 Protein purifications for *in vitro* assays

The method for protein purification and for the MT binding assay is adapted from Norell et al., 2021 (copyright: ©2021 Norell et al., CC BY-NC-SA 3.0, http://creativecommons.org/licenses/by-nc-sa/3.0).

All proteins used for the *in vitro* experiments were purified via FLAG tag from S. *cerevisiae*. Except for Slk19 and Slk19Δcc1, which were expressed from the endogenous promoter of *SLK19*, all purified proteins were overexpressed under the control of the *GAL1* promoter

(Figure 16A and Figure 32B). For the induced overexpression, cells were cultured for 4–5 h in medium containing 2 % galactose. Slk19, Slk19Δcc1 and Ase1 were purified from cells that were additionally metaphase arrested by Cdc20 depletion (*CDC20* under the control of the *MET25* promoter). Overexpression of Stu1 itself led to a metaphase arrest of the respective cells.

The yeast cells used for protein purification, were washed, harvested and a dry cell pellet was frozen in liquid nitrogen. Cryogenic cell lysis was performed with a Cryomill (two rounds of cell lysis, each for 1 min and with a frequency of 30 sec^{-1}). The lysed cells were resuspended in 1 µL/OD_{578} lysis buffer (see buffer list above in chapter 3.3.8). Cells were clarified from cell debris by two consecutive centrifugation steps (each for 30 min at 20817 g and 4°C).

α-FLAG antibody (Sigma-Aldrich) was bound to protein G Dynabeads (Invitrogen), which were used to pull down FLAG-tagged proteins from the lysate. For this, the clarified lysate was incubated together with the beads for 3 h at 4°C with a constant rotation of 8 rpm. After the incubation, the beads were washed six times with BH0.10 buffer supplemented with 200 mM PMSF and 2 mM DTT to remove unbound or unspecifically bound proteins.

The proteins that bound specifically to the beads via their FLAG-tag were eluted by using 250 µg/ml FLAG-Peptide (Caslo ApS) (added to the respective elution buffer as described in the following). A volume of 0.075 µL/OD of the respective elution buffer was added to the beads and the sample was incubated on a shaker: Stu1 and Slk19Δcc1 were eluted at 25°C at 900 rpm for 25 min in $BH0.10^{+}$ (see buffer list above in chapter 3.3.8). The elution of Slk19 was performed analogously, however, the KCl concentration in the elution buffer was increased to 250 mM. The elution of Ase1, Ase1-7A and Ase1-7D was performed in 20 mM glycine buffer (prepared like $BH0.10^{+}$ but without HEPES and adjusted to pH 2.5) containing 250 µg/ml FLAG-Peptide (Caslo ApS). The elution was performed at 25°C at 900 rpm for 10 min. After elution, the sample was immediately neutralized with 25 mM HEPES to pH 7.

Eluted proteins were quick-frozen in liquid nitrogen. Samples of the purified proteins were checked and quantified by colloidal Coomassie staining of SDS-PAGE gels.

Colloidal Coomassie staining of SDS-PAGE gels

After SDS-PAGE, gels were fixed for 1 h in fixing solution (40 % (v/v) methanol, 2 % (v/v) acetic acid) and subsequently incubated for approximately 8–12 h in colloidal Coomassie staining solution (20 % (v/v) ROTI®Blue Colloidal Coomassie® (Carl Roth), 20 % (v/v) methanol). Gels were detained in mpH_2O for approximately 5 h before the quantification of bands was performed (described in chapter 3.5).

3.3.10 *In vitro* MT binding assay and MT crosslinking assay

The described *in vitro* MT binding and MT crosslinking methods are adapted from Norell et al., 2021 (copyright: ©2021 Norell et al., CC BY-NC-SA 3.0, http://creativecommons.org/licenses/by-nc-sa/3.0).

Preparation of glass slides for in vitro MT assays

The procedure for cleaning, hydroxylation, amino-silanization and PEGylation of the glass slides is based on the "Slide Cleaning and Preparation Protocol 2.5" from the Hoskins laboratory (University of Wisconsin-Madison, last modified 2016, accessed 2022, https://hoskins.biochem.wisc.edu/files/Data_Upload/2017-03-29_1413_Slide%20Prep%202_5.pdf).

Cleaning of glass slides and hydroxylation:

Cover slips of the sizes of 24 mm x 24 mm and 24 mm x 60 mm (Th. Geyer GmbH & Co. KG) were cleaned for 1 h with a 2 % Micro-90® detergent solution (Cole-Parmer GmbH), washed with water and subsequently cleaned for 1 h with ethanol (p.a. grade) in a sonicator water bath (Ultrasonic bath USR 9, VWR International). For activation of the reactive hydroxyl groups on the glass surface (before amino-silanization), the cover slips were treated with 1 M potassium hydroxide (KOH) solution. Cover slips were blown dry with nitrogen.

Amino-silanization:

A hydrophobic surface area of the glass slides was generated by amino-silanization to reduce unspecific binding of polar protein groups to polar groups of the glass surface (SiO_2). The glass slides were incubated with 1.5 % 3-aminopropyltriethoxysilane (APTES) diluted in acetone (p.a. grade) for 10 min at RT and were subsequently washed with ethanol (p.a. grade). Cover slips were blown dry with nitrogen and stored in a desiccator.

Preparation of flow champers:

The flow chamber was assembled by fixing three parallel stripes of double-sided tape on the larger (24 x 60 mm) cover slip. The smaller cover slip (24 x 24 mm) was placed on top, to create two closed flow chamber spaces.

PEGylation:

PEGylation prevents unspecific binding of proteins and allows binding of neutravidin (added in the next step). PEGylation was performed using alpha-Biotin-omega-carboxy succinimidyl ester polyethylene glycol (Biotin-PEG-NHS) (5000 Da, Iris Biotech) and alpha-Methoxy-omega-carboxylic acid succinimidyl ester polyethylene glycol (MeO-PEG-NHS) (5000 Da, Iris Biotech). A 1:1 mixture of 5 mg/mL Biotin-PEG-NHS and 500 mg/mL MeO-PEG-NHS (both dissolved in 0.1 M sodium hydrogen carbonate ($NaHCO_3$), pH 7.5) were mixed and added to the flow chambers. Slides were incubated for 1 h in a humid chamber to prevent desiccation. Each flow chamber was washed consecutively with 200 µL mpH_2O and 200 µL PBS before neutravidin coating.

Neutravidin coating:
Neutravidin has a high affinity for biotin and is required for the immobilization of biotinylated MTs. 30 µL of 5 mg/mL neutravidin (Invitrogen) dissolved in PBS was infused into each flow chamber and incubated for 20 min (protocol based on Mieck et al., 2015). Unbound neutravidin was removed by washing each flow chamber with 50 µL PBS.

Blocking:
Passivation of the glass surface was achieved by blocking unspecific binding sites at the glass surface with 1 % Pluronic® F-127 solution (Invitrogen) dissolved in PBS. The flow chamber was incubated for 5 min and then washed with 40 µL BRB80$^+$ buffer (see buffer list below).

Buffers used for MT binding and crosslinking assays

Assay buffers	Composition
BRB80	80 mM PIPES pH 6.8/KOH, 1 mM $MgCl_2$, 1mM EGTA pH 6.8/KOH
BRB80$^+$	BRB80 supplemented with 2 mM DTT, 50 mM KCl and 20 µM taxol
MC/C buffer	BRB80$^+$ buffer containing 0.13% methylcellulose and 0.7 mg/mL β-casein
Imaging buffer	MC/C buffer supplemented with 0.4 mg/mL glucose oxidase (Sigma-Aldrich), 0.07 mg/mL catalase (Sigma-Aldrich) and 45 mM glucose

MT polymerization and pelleting

For MT polymerization, unlabeled bovine tubulin, biotinylated porcine brain tubulin and fluorophore labeled porcine tubulin was used (obtained from Cytosceleton, Inc.). MTs labeled with the fluorophore rhodamine (Rho) or aminomethylcoumarin acetate (AMCA) (Figure 16B and C, Figure 17A, Figure 19A, Figure 32B) were polymerized according to the protocol described in Funk et al., 2014. Polymerized MTs were centrifuged through a BH0.40 cushion (as described in Funk et al., 2014), to remove unpolymerized tubulin and small MT fragments. The cushion was carefully removed with a pipette tip and the MT pellet was resuspended in BRB80$^+$ buffer (see buffer list above).

Preparation of polarity marked MTs

The protocol for the preparation of polarity marked MTs was adapted from the Mitchinson Lab (Harvard University; protocol obtained from Mitchinson Lab homepage, accessed 2022, https://mitchison.hms.harvard.edu/files/mitchisonlab/files/preparation_of_segmented_and_polarity_marked_microtubules.pdf). For the production of polarity marked MTs (Figure 23), with a bright MT seed at the minus end and a fainting signal towards the plus end, the minus end polymerization of MTs was selectively blocked by using N-ethylmaleimide (NEM)-treated tubulin. NEM-tubulin was prepared by treating unlabeled tubulin (10 mg/mL resuspended in BRB80 supplemented with 0.5 mM GTP) with final 1mM NEM at 0°C for 10 min. NEM was quenched with 8 mM β-mercaptoethanol for 10 min at 0°C. For the polymerization of bright MT seeds, a 5 mg/ml tubulin mix was used, consisting of 1:3 Rho-

or AMCA-labeled tubulin and 2:3 unlabeled tubulin and supplemented with 0.5 mM GMPCPP. The GMPCPP seeds were polymerized at 37°C for 15–20 min. For polymerization of immobile Rho-MTs, the tubulin mix consisted of 0.5 µl of 5 mg/ml Rho-labeled tubulin, 3.83 µl of 5 mg/ml unlabeled tubulin, 1.86 µl of 5 mg/ml biotinylated tubulin and 2.05 µl of the NEM-treated tubulin in a final volume of 25 µl (in BRB80 supplemented with 1 mM GTP, 1mM DTT). For polymerization of mobile AMCA-MTs, the tubulin mix consisted of 0.65 µl of 5 mg/ml AMCA-labeled tubulin, 6.04 µl of 5 mg/ml unlabeled tubulin and 2.05 µl of the NEM-treated tubulin in a final volume of 25.54 µl (in BRB80 supplemented with 1 mM GTP and 1 mM DTT). The mix was polymerized at 37°C for 25 min, then supplemented with 1/10 volume of GMPCPP seeds and incubated for 20 min. Taxol was added stepwise up to a concentration of 20 µM. The polarity marked MTs were pelleted and resuspended in taxol-containing BRB80^{+} buffer as described (Funk et al., 2014).

MT immobilization

For MT immobilization, 10 µL of polymerized MTs were added to each flow chamber and incubated for 15 min in the dark at RT. To remove unbound MTs, the chamber was washed with 30 µL methylcellulose/β-casein buffer (MC/C buffer; see buffer list above). The MC/C buffer was incubated for 5 min to block unspecific binding sites. Subsequently, the purified proteins of interest were infused into the chamber for binding analysis.

Protein binding analysis

The purified proteins (Figure 16A) were clarified from possible protein aggregations by centrifugation at 20817 g for 10 min at 4°C. Purified proteins were diluted in MC/C buffer to the respective final protein concentration as indicated below (the final volume was 20 µL; the final KCl concentration was kept constant at 60 mM for all analyzed samples). The final protein concentrations used for the experiments shown in Figure 16B and C, were 14.5 nM for Ase1, 10 nM for Stu1 and 20 nM for Slk19. The final protein concentrations used for the experiments shown in Figure 17A, were 2.5 nM for Ase, 1.5 nM for Stu1 and 20 nM for Slk19. The indicated protein or protein premix was infused to the flow chamber (containing immobilized MTs) and incubated for 15 min in the dark at RT. Unbound proteins were removed by a subsequent wash step with 30 µL Imaging buffer (listed in buffer table above) and were analyzed by microscopy.

MT crosslinking analysis

The final protein concentrations used for the MT crosslinking assays (shown in Figure 19 and Figure 23), was 10 nM for Slk19, 7.2 nM for Ase1 and 5 nM for Stu1 (the final volume was 20 µL; the final KCl concentration was kept constant at 60 mM for all analyzed samples). 20 µL of MC/C buffer (final 60 mM KCl) was used as negative control containing none of the purified proteins. The proteins of interest were infused to the flow chamber (containing immobilized MTs) and incubated for 15 min in the dark at RT. Protein mixtures were either incubated as premix (Figure 19B, Figure 23) or successively (Figure 19C). Unbound protein was washed off with 30 µL Imaging buffer. Subsequently, 10 µL of mobile

unbiotinylated AMCA-MTs were added to the flow chambers and incubated for 10 min. MTs that were not crosslinked, were washed off by perfusion of the flow chamber with 60 µL Imaging buffer. The efficiency of MT crosslinking was then analyzed by microscopy.

3.4 Fluorescence microscopy

The fluorescence microscopy method is adapted from in Norell et al., 2021 (copyright: ©2021 Norell et al., CC BY-NC-SA 3.0, http://creativecommons.org/licenses/by-nc-sa/3.0).

For fluorescence microscopy, an Olympus CellR life science imaging station was used, including the devices listed in chapter 2.7 and the Olymus xCellence software (Olympus K.K.). Imaging was performed with a Plan-Apochromat objective 100X/1.4 (Olympus). IMMOIL-F30CC low autofluorescence immersion oil (Olympus) was used as immersion liquid. The acquired images had a 16-bit depth, a specification of 1344 x 1024 pixels (width x height) and a scale of 15.625 pixels per µm. Proteins analyzed in this study via fluorescence microscopy were tagged with the following fluorophores: green fluorescent protein (GFP), cyan fluorescent protein (CFP) and mCherry (for proteins expressed in *S. cerevisiae*) as well as Rho and AMCA (for labeling of MTs).

For live-cell imaging, yeast cells were washed in three consecutive steps with sterile mpH_2O, and the washed cell pellet was resuspended in NFM (composition of NFM listed above in chapter 2.5). Images with seven z-stacks were acquired (distance of z-stacks = 0.43 µm) that were subsequently projected using the Fiji software (ImageJ).

The fluorescence microscopy analyses of the *in vitro* MT binding and MT crosslinking assays were performed in Imaging buffer (composition of Imaging buffer listed of above in chapter 3.3.10). Only one z-stack was acquired for the imaging of MTs.

3.5 Image processing, analysis and quantifications

The method of image processing, analysis and quantification is adapted from Norell et al., 2021 (copyright: ©2021 Norell et al., CC BY-NC-SA 3.0, http://creativecommons.org/licenses/by-nc-sa/3.0).

Image adjustment (brightness and contrast), image analysis (signal intensities, distances, areas) as well as projection of acquired z-stacks was performed with the Fiji software (ImageJ) and the included tools.

Longitudinal RGB-plots were created to depict signal intensities of different proteins (indicated in the respective Figure) along the metaphase spindle axis (Figure 7C, Figure 14A, Figure 15A, Figure 24D, Figure 26B). RGB-plots were obtained by measuring the metaphase spindle length (line tool of Fiji), which was defined as distance between two opposing SPBs (Figure 7C, Figure 24D, Figure 26B) or by the spread of the Tub1-CFP signal (Figure 14A, Figure 15A). This measured length was extended by 0.4 µm on each side (start and end

points of the measurement are not part of the spindle). The respective gray values (y-axis) were plotted against the measured distance in microns (x-axis) by using the "Plot Profile" feature of Fiji for each color channel. The plots contain one measuring point per pixel, resulting in 45–60 measuring points, depending on the measured spindle lengths (2 µm spindles in Figure 7C; 2.4 µm spindles in Figure 14A, Figure 15A; 3 µm spindles in Figure 24D, Figure 26B). The lowest signal intensity value (not located within metaphase spindle) of each curve was defined as background signal and was subtracted from all other values of this curve (resulting in a minimum value of 0). Where indicated, mean values were calculated from several measured cells ($n \geq 10$) to obtain a mean value curve for each experiment. The exact number of measurements for each experiment is listed in the appendix (chapter 6). For each shown RGB-plot, two individual experiments were performed. The average curve and the standard deviations (S.D.; shown as error bars) calculated from the two experiments are shown in the respective Figure. In Figure 15A and Figure 26B, the RGB-curves were normalized to values ranging from 0–1 (minimum–maximum value).

Cross-section RGB-plots were created to depict the Tub1 signal intensities at the metaphase spindle center in the indicated cell types (Figure 14B). The metaphase spindle length was measured (defined as Tub1-CFP signal spread) and the center of the spindle was determined. Metaphase spindles with a length of 1.6–2.6 µm were included in the cross-section measurements. For this, a line with a length of 2.5 µm was placed at the metaphase spindle center orthogonally to the spindle axis (as illustrated in Figure 14B) and the plot profile was obtained from this measurement (containing 40 measuring points). The lowest signal intensity value of each curve (not part of the spindle) was defined as background signal and was subtracted from all other values of this curve (resulting in a minimum value of 0). Mean values were calculated from several measured cells ($n > 80$) to obtain a mean value curve of Tub1-CFP for each experiment. The exact number of measurements for each experiment is listed in the appendix (chapter 6). For each cross-section RGB-plot (Figure 14B), two individual experiments were performed. The average curves and the standard deviations (S.D.; shown as error bars) calculated from these two experiments are shown in Figure 14B.

Signal intensities were quantified by measuring the mean signal intensity within a defined area by using the "rectangle", "oval" or "polygon" tool of Fiji. The background signal was measured at an appropriate site (not within the measuring area) and subtracted from the measured value for the mean signal intensity. In Figure 11B, the measured signal was normalized to the respective spindle length and in Figure 17B the measurements were normalized to the respective MT length. For the quantitative Western blot analysis (Figure 13B), the measured signal was normalized to the Arc1-signal (used as loading control). A mean value was calculated from three stepwise increasing protein amounts (as indicated in Figure 13B), which at the same time was a control for signal linearity.

Purified proteins used for the *in vitro* MT binding and crosslinking assays (Figure 16A) were quantified by colloidal Coomassie staining of SDS-PAGE gels and by comparison with a defined protein standard.

The binding efficiency of Stu1 and Ase1 to MTs *in vitro* (Figure 17B) was quantified by measuring the signal intensity at MTs with a length of approximately 10 µm (number of measurements: n>100). The measured MTs were obtained from 4–8 different micrographs.

The efficiency of MT crosslinking (Figure 19B and C) was quantified by measuring the sum of all overlap lengths between immobilized Rho-MTs and mobile AMCA-MTs. This cumulative overlap length (indicated in µm) was then divided by the cumulative length of all immobilized Rho-MTs (indicated in cm) (measurements obtained from ≥ 5 micrographs).

In the experiments shown in Figure 24A and B, the spindle length was measured as distance between the opposite spindle poles from one cell. The KT-KT distance was measured as distance between the two KT-clusters of one metaphase cell. The kMT lengths were measured as distance from one KT-cluster to its connected SPB.

3.6 Statistical analyses

The methods of statistical analyses are also described in Norell et al., 2021 (copyright: ©2021 Norell et al., CC BY-NC-SA 3.0, http://creativecommons.org/licenses/by-nc-sa/3.0).

For all statistical analyses in this study, the significance level (α) was set to $\alpha = .05$. For the analyses of metric data, a two-tailed unpaired t-test was performed to evaluate whether the means of two independent groups are significantly different from each other. The software used for the two-tailed unpaired t-test was accessed via the following homepage: https://www.socscistatistics.com/tests/studentttest/default2.aspx (Social Science Statistics homepage, by Jeremy Stangroom, last accessed 2022). For the analyses of categorical data, such as different yeast phenotypes, either a two-tailed Fisher's exact test or a χ^2-test was used to evaluate whether phenotype frequencies of two independent groups are significantly different from each other. The two-tailed Fisher's exact test was used to compare two independent phenotype categories. The software used for the two-tailed Fisher's exact test was accessed via the following homepage: https://www.socscistatistics.com/tests/fisher/default2.aspx (Social Science Statistics homepage, by Jeremy Stangroom, last accessed 2022). The χ^2-test was used when there were more than two distinct phenotype categories. The software used for the χ^2-test was accessed via the following homepage: https://www.socscistatistics.com/tests/chisquare2/default2.aspx (Social Science Statistics homepage, by Jeremy Stangroom, last accessed 2022).

4 Results

4.1 Slk19 domains and protein interactions required for sequestering at uaKTs

4.1.1 Spc105, a major mitotic regulation hub, is the platform for basal Slk19 binding at uaKTs

Slk19 and Stu1 are interdependent for their sequestering ability at uaKTs: Stu1-depleted cells show a sequestering defect of Slk19 and deletion of Slk19 leads to a sequestering defect of Stu1 (Kolenda et al. 2018). However, in both cases a residual amount of Slk19/Stu1 is seen at the uaKTs, which must bind via other KT proteins. The basal Stu1 binding was shown to be dependent on Spc105 and its phosphorylation status (Kolenda et al. 2018). For Slk19, however, the question remains open so far, which protein mediates the basal binding at uaKTs. Therefore, it was aimed to determine the interaction partner of Slk19 at uaKTs and furthermore, to find out whether this basal binding of Slk19 is required to initialize the sequestering process.

Several possible KT proteins came into consideration as Slk19-interactors at the uaKT. Stu2 came into account as a potential interaction partner of Slk19 at uaKTs, since the protein most homologous to Slk19 in *S. pombe*, Alp7/ Mia1 (Sato et al., 2003), was shown to interact with Alp14 (Sato et al., 2004), the homologue of Stu2 (Garcia et al., 2001). Ndc80 and Spc105 were also likely candidates for Slk19 interaction partners at the uaKTs, since it was shown by ChIP analysis, that centromeric binding of Slk19 is strongly reduced in temperature sensitive *ndc80* and *spc105* mutants (Pagliuca et al., 2009). Thus, it was analyzed whether the basal binding of Slk19 at uaKTs shows a dependency on either of these proteins: Ndc80, Stu2 or Spc105. The localization of GFP-tagged Slk19 at uaKTs was analyzed in Nz-treated cells. Nz functions as inhibitor of MT polymerization and thus provokes uaKTs within the cells.

When Stu2 was depleted in Nz-treated cells, the sequestering of Slk19 was still functional (comparable to *WT* cells Figure 1A, a). This hindered the observation of basal binding of Slk19 at uaKTs (Figure 1A, b). To prevent sequestering, Stu1 was depleted additionally to Stu2 in those cells. This co-depletion, however, did not abolish the basal binding of Slk19 at uaKTs (Figure 1A, c-d). Conclusively, Slk19 shows neither dependency on Stu2 for its sequestering at uaKTs nor for its basal KT localization at uaKTs.

Depletion of Ndc80 leads to uaKTs, even in the absence of Nz, since Ndc80 is required for MT attachment at the KT-MT interface (Cheeseman et al., 2006),(Ciferri et al., 2008),(Powers et al., 2009),(Foley & Kapoor, 2013). Furthermore, sequestering in Ndc80-depleted cells is not possible, since the Ndc80/Nuf2-complex constitutes the binding site for the Mps1 kinase (Kemmler et al., 2009), which initiates sequestering by Spc105 phosphorylation upon KT detachment (Kolenda et al., 2018). As a consequence of defective

sequestering, the uaKTs are declustered in Ndc80-depleted cells, which makes the observation of proteins at uaKTs more difficult. Nevertheless, Slk19 was observed at those uaKTs at basal levels (basal Slk19 amount at uaKTs = comparable to Stu1-depleted cells) (Figure 1B). This indicates that Ndc80 is also not required for the basal Slk19 localization at uaKTs.

Spc105-depleted cells (*'Δspc105'*) are deficient in important checkpoint functions (Rosenberg et al., 2011),(London et al., 2012),(Aravamudhan et al., 2016) and therefore *'Δspc105'* cells were arrested in metaphase by Cdc20 depletion, in addition to the Nz-treatment. When Spc105 was depleted, the basal Slk19 binding to uaKTs was completely abolished and Slk19 was only observed as a dot-like signal at the collapsed spindle (Figure 1 C, a). This indicates that Slk19 is dependent on Spc105 for its localization at uaKTs. Notably however, as mentioned in introduction chapter 1.5.3.2, the KT localization of Slk19 is independent of the phosphorylation status of Spc105 (Kolenda et al., 2018).

Spc105-depleted Nz-treated cells still show Slk19 in vicinity to the collapsed SPBs (Figure 1C, a). Since Slk19 does not bind to SPBs themselves (as seen in Figure 1B), this signal could derive either from binding to atKTs or from short residual MTs of the collapsed spindle. As will be shown later (in chapter 4.2.4), Slk19 is dependent on Stu1 for its binding to the spindle. Thus, co-depletion of Stu1 and Spc105 in Nz-treated cells completely eliminated the Slk19 binding at the collapsed spindle and at uaKTs (Figure 1C, b). Since the Slk19 signal at atKTs is also abolished in these co-depleted cells, this result suggests that Slk19 localization at atKTs might also be dependent on Spc105 (as will be shown later in chapter 4.2.1). Moreover, the finding that basal Slk19 localization at uaKTs is Mps1-independent strongly supports this assumption (Kolenda et al. 2018).

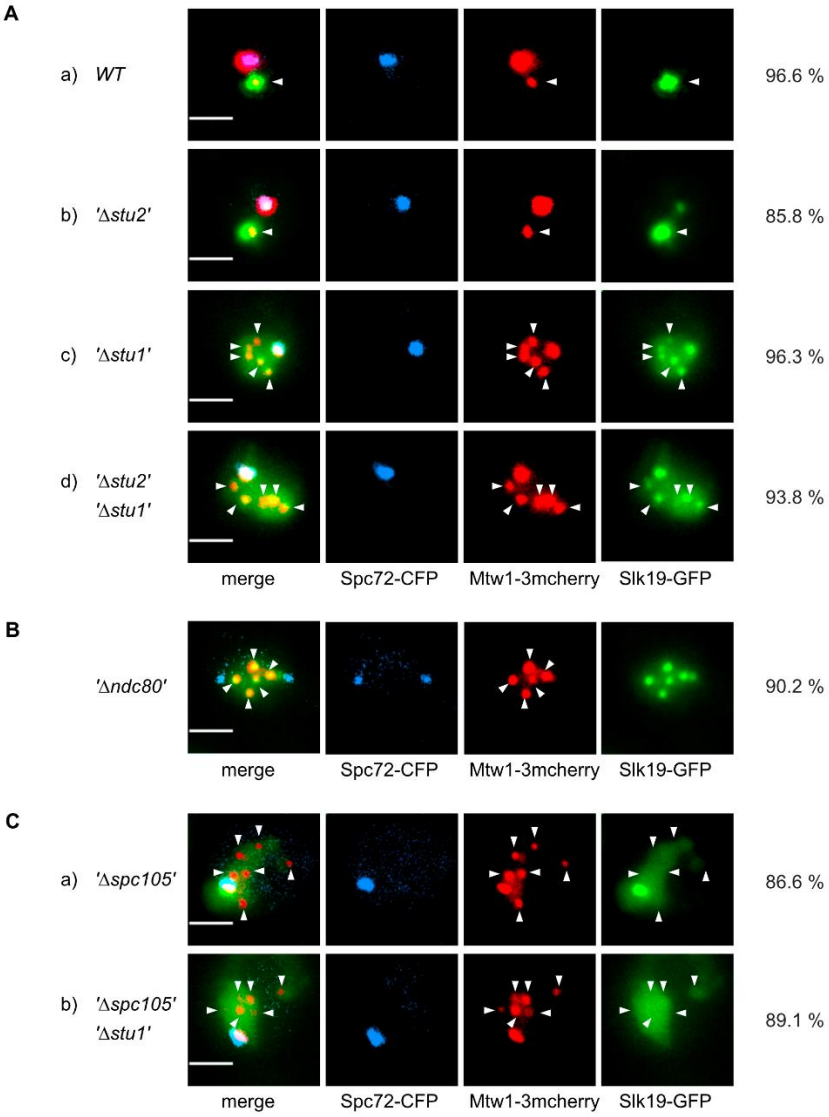

Figure 1: Slk19 depends on Spc105 for its basal binding at uaKTs and on Stu1 for its localization to atKTs and/or MTs.

(A-C) Cells were treated with nocodazole (Nz) after G1 release to provoke uaKTs. Indicated proteins were conditionally depleted by IAA-treatment (AID) (described in Methods chapter). White arrowheads indicate uaKTs (not colocalizing with SPBs). Spc72-CFP marks spindle pole bodies, Mtw1-3mcherry marks kinetochores. Genotypes of used strains are listed in Materials chapter. Phenotypes with the exact numbers of counted cells are listed in the appendix. Scale bar = 2 µm. (A) (a-b) Stu2-depleted cells (*'Δstu2'*) showed functional sequestering comparable to *WT* cells. (c) Stu1-depleted cells (*'Δstu1'*) showed defective sequestering with basal Slk19 binding at uaKTs and (d) additional depletion of Stu2 (*'Δstu1' 'Δstu2'*) did not resolve basal Slk19 binding at uaKTs. (B) Ndc80-depleted (*'Δndc80'*) cells showed a sequestering defect but basal binding of Slk19 at uaKTs is still possible. (C) Cells with Spc105 depletion (*'Δspc105'*) were arrested in metaphase by Cdc20-depletion (*GAL1*-promoter shut-off) during Nz-treatment to prevent cell cycle progression due to checkpoint defects. (a) Spc105-depleted cells (*'Δspc105'*) showed loss of Slk19 localization at uaKTs. (b) Spc105 and Stu1 co-depleted (*'Δspc105', 'Δstu1'*) cells showed a loss of Slk19 localizations at uaKTs and at the collapsed spindle.

4.1.2 The C-terminus and the cc1 domain of Slk19 are essential for sequestering and the C-terminus incorporates the KT localization domain of Slk19

Different Slk19 domain deletions were analyzed with the aim to interfere more specifically with the Slk19-KT interaction. It was attempted to find a specific Slk19 domain deletion, interfering with basal binding at the uaKTs while leaving the Slk19 sequestering function intact. Slk19 constructs that showed functional sequestering should then be analyzed for defective basal binding at uaKTs in Nz-treated *'Δstu1'* cells in a second step.

For secondary structure predictions of Slk19, the protein structure prediction server PSIPRED was used. The predicted secondary structure of Slk19 is indicated in more detail with the SOPMA tool in Figure 2A. Slk19 is composed of an N-terminal globular domain (GD) reaching from amino acid (aa) 1–220 and seven predicted coiled coil domains, in the following named cc1-cc7 (Figure 2B). For the Slk19 domain analyses, several Slk19 deletion constructs were created by PCR or overlap-PCR on the basis of the PSIPRED structure predictions and based on previous studies from Havens et al. 2010 (Figure 2C). The constructs are listed below in Table 1 with a short description about what is known about the different Slk19 domains in the literature.

WT-like sequestering at uaKTs (induced by Nz-treatment) was observed with the constructs Slk19Δ1-77, Slk19ΔGD and Slk19Δcc3-5 (Figure 3A, a). The constructs Slk19Δcc1+2 and Slk19Δcc1 showed a sequestering defect with residual binding at uaKTs (reflecting basal Slk19 binding) and residual binding in proximity to the collapsed spindle (Figure 3A, b-c). In contrast, Slk19Δcc2 showed functional sequestering comparable to *WT* (Figure 3A, d). Thus, deletion of the cc1 domain of Slk19 led to sequestering defects, while basal KT localization was still intact.

The C-terminal deletion constructs Slk19Δcc6+7, Slk19Δcc6 and Slk19Δcc7 showed sequestering defects with no remaining binding to uaKTs and did not localize at the collapsed spindle (atKTs or MTs) leading to a diffuse nuclear GFP signal (Figure 3A, e). The C-terminus alone, Slk19Δ1-708 (cc6+7), was not sufficient for sequestering, but localized at basal levels to uaKTs and in proximity to the collapsed spindle (latter turned out to be binding to atKTs, as shown later in chapter 4.2.1 and 4.2.2) (Figure 3A, f). This indicates that the C-terminus most probably contains the KT-binding domain of Slk19 required for basal localization to uaKTs.

Taken together, the microscopy results showed that the cc1 domain and the C-terminus are required for sequestering. To support that the C-terminus and the cc1 domain are not only essential but sufficient for sequestering, a Slk19 "minimal construct" was created consisting only of Slk19-cc1+2-cc6+7. Intriguingly, the minimal construct was able to restore the Slk19 sequestering to a large extend (Figure 3B, a).

Analogously to the Slk19 analysis, sequestering of GFP-tagged Stu1 was analyzed in cells carrying the different Slk19 deletion constructs. In all cases, Stu1 and Slk19 behaved alike in terms of their sequestering ability at uaKTs. Functional Stu1 sequestering was observed

with Slk19Δ1-77, Slk19ΔGD, Slk19Δcc3-5 and Slk19Δcc2 (Figure 3B, a). Defective sequestering was observed with Slk19Δcc1+2, Slk19Δcc1 and Slk19Δcc6+7 (Figure 3B, b). Also for Stu1, the sequestering could be largely restored by using the minimal Slk19 construct Slk19-cc1+2-cc6+7 (Figure 3B, b).

The observed defects with the deletion constructs Slk19Δcc1 and Slk19Δcc6+7 might be due to deletion of its tetramerization domain. This possibility was analyzed in the following.

Table 1: Created Slk19 deletion constructs with short description.

Slk19 construct	**Description**
Slk19Δ1-77	deletion of aa 1–77; equivalent to the Esp1 cleavage product
Slk19ΔGD	deletion of the complete globular domain (aa 1–220); required for FEAR pathway (Havens et al., 2010)
Slk19Δcc1+2	combined deletion of cc1 and cc2 (aa 300–502); required for FEAR pathway and synthetically lethal with *Δkar3* (Havens et al., 2010)
Slk19Δcc1	deletion of cc1 (aa 300–410); required for FEAR pathway and synthetically lethal with *Δkar3* (Havens et al., 2010)
Slk19Δcc2	deletion of cc2 (aa 410–500); synthetically lethal with *Δkar3* (Havens et al., 2010)
Slk19Δcc3-5	deletion of cc3-cc5 (aa 503–711); function unknown
Slk19Δcc6, Slk19Δcc7, Slk19Δcc6+7	C-terminal deletion constructs with individual deletion of cc6 (aa 711-758), individual deletion of cc7 (aa 760–821) or combined deletion of cc6 and cc7 (aa 709–821); Slk19Δcc6+7 and Slk19Δcc7: synthetically lethal with *Δkar3* (Havens et al., 2010)
Slk19Δ1-708	deletion construct consisting only of the C-terminus (cc6+7, aa 709–821)
Slk19-cc1+2-cc6+7	Slk19 minimal construct consisting of cc1+2 and cc6+7 (aa 300–502 and aa 709–821)

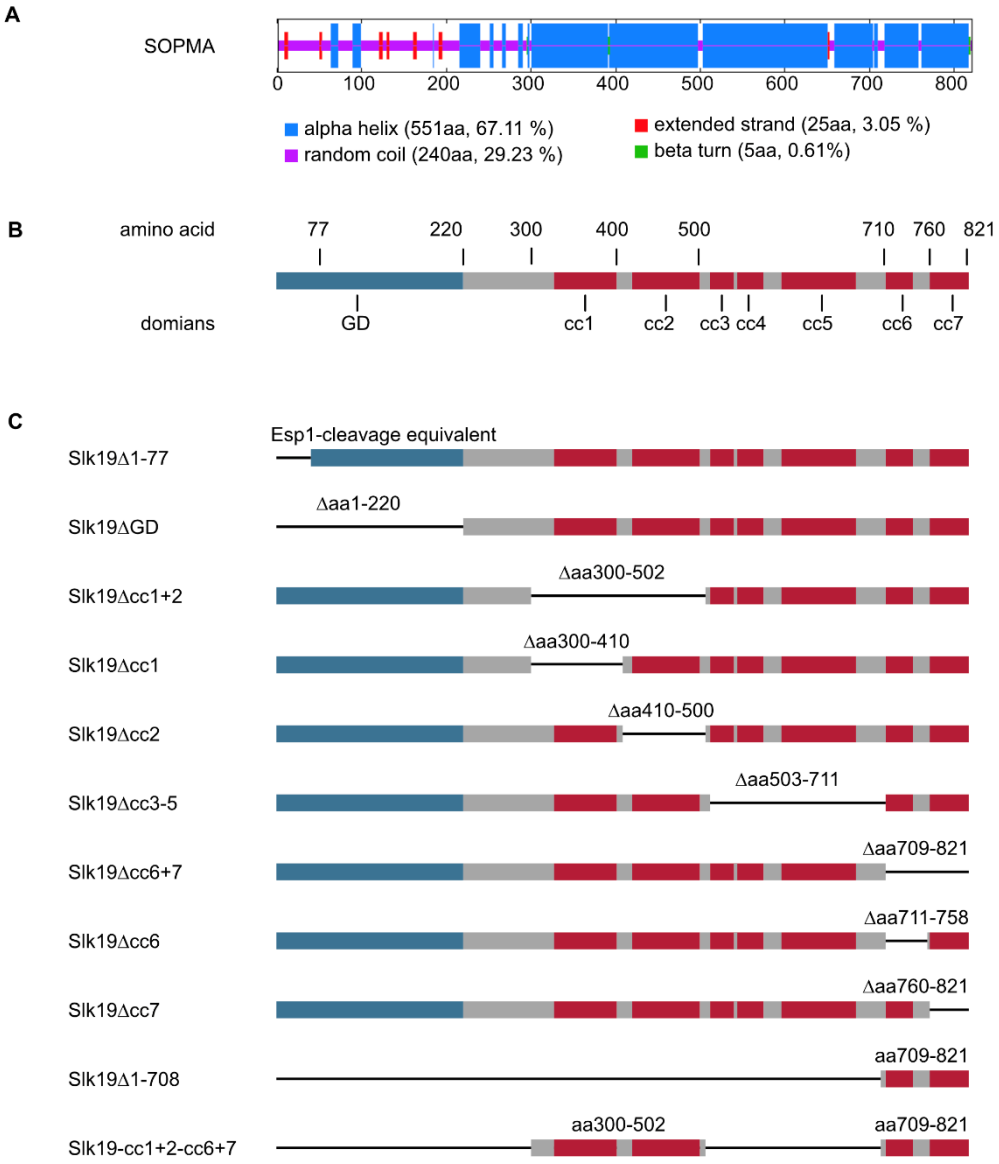

Figure 2: Schematic illustration of Slk19 protein domains and overview of the different Slk19 deletion constructs.

(A) Predicted secondary structure of Slk19 analyzed by the SOPMA tool. (B) Schematic illustration of Slk19 protein domains. GD = globular domain, cc = coiled coil domain. (C) Slk19 deletion constructs used for analysis in this study. Constructs were created on the basis of secondary structure predictions using PSIPRED and based on previous studies from Havens et al. 2010.

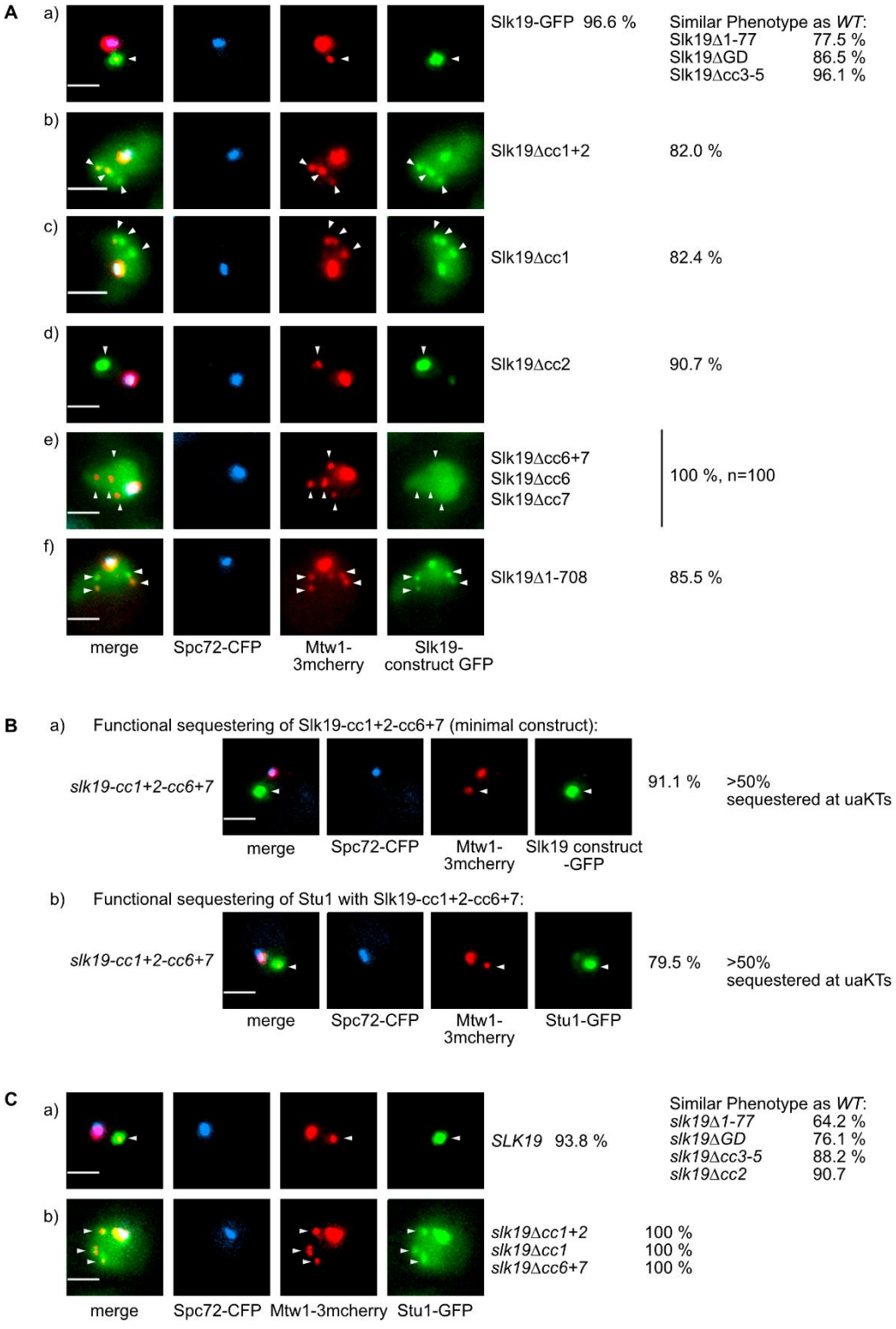

Figure 3: The C-terminus and the cc1 domain of Slk19 are essential for sequestering and the C-terminus incorporates the KT localization domain of Slk19.

(A-C) Cells were treated with nocodazole (Nz) after G1 release to provoke uaKTs as described in Methods chapter. Spc72-CFP marks spindle pole bodies, Mtw1-3mcherry marks kinetochores. Genotypes of used strains are listed in Materials chapter. All Slk19 constructs were expressed from

the endogenous promoter of *SLK19*. The indicated percentages represent the frequency of the shown phenotype among all counted cells. Phenotypes with the exact numbers of counted cells are listed in the appendix. White arrowheads indicate uaKTs (not colocalizing with SPBs). GD = globular domain, cc = coiled coil domain. (A) (a) Slk19 sequesters at uaKTs. Slk19Δ1-77, Slk19ΔGD, Slk19Δcc3-5 showed functional sequestering comparable to *WT*. (b) Slk19Δcc1+2 and (c) Slk19Δcc1 showed defective sequestering at uaKTs. (d) Slk19Δcc2 showed functional sequestering. (e) Slk19Δcc6+7, Slk19Δcc6 and Slk19Δcc7 showed a sequestering defect. (f) Slk19Δ1-708 (C-terminus only) could not restore sequestering but showed basal binding to KTs and localization in proximity to the collapsed SPBs. (B) (a) The minimal construct Slk19Δcc1+2-cc6+7-GFP was sufficient to restore functional sequestering. (b) Stu1-GFP showed functional sequestering at uaKTs in cells carrying the minimal construct *slk19Δcc1+2-cc6+7*. (C) (a) *slk19Δ1-77, slk19ΔGD, slk19Δcc3-5* and *slk19Δcc2* cells showed functional Stu1 sequestering comparable to *WT*. (b) Defective Stu1 sequestering was seen in *slk19Δcc1+2*, *slk19Δcc1* and *slk19Δcc6+7* cells.

4.1.3 The C-terminus is the oligomerization domain of Slk19

Slk19 is suggested to form homotetramers (De Wulf et al., 2003). To analyze which domain is required for oligomerization/tetramerizetaion, the Slk19-Slk19 interaction was studied in cycling cells by co-immunoprecipitation (CoIP) with FLAG-tagged Slk19 deletion constructs as bait to pull down full-length Slk19-GFP. The results presented in this chapter (Figure 4) are also published in Norell et al., 2021 (copyright: ©2021 Norell et al., CC BY-NC-SA 3.0, http://creativecommons.org/licenses/by-nc-sa/3.0).

The Slk19 deletion constructs Slk19Δcc6+7 as well as Slk19Δcc7 were not able to pull down Slk19-GFP, while all other deletion constructs could (Figure 4). Furthermore, the C-terminal region alone, Slk19Δ1-708 (cc6+7), could very efficiently co-immunoprecipitate Slk19-GFP. Conclusively, the CoIP results showed that the C-terminus of Slk19, but not the cc1 domain, is required for Slk19 tetramerization.

Obviously, the tetramerization is required for all localizations of Slk19 observed in the Nz-treated cells: at uaKTs, atKTs and MTs (see chapter 4.1.2, Figure 3A, e). Since also the C-terminal deletion construct Slk19Δcc6 shows the same cellular phenotype observed with fluorescence microscopy, the results indicate that both of the last two coiled coil domains (cc6 and cc7) are probably needed for tetramerization. Since the C-terminus (cc6+7) has been shown to bind to KTs independently (Figure 3A, f), it has a dual function of oligomerization (tetramerization) and KT localization.

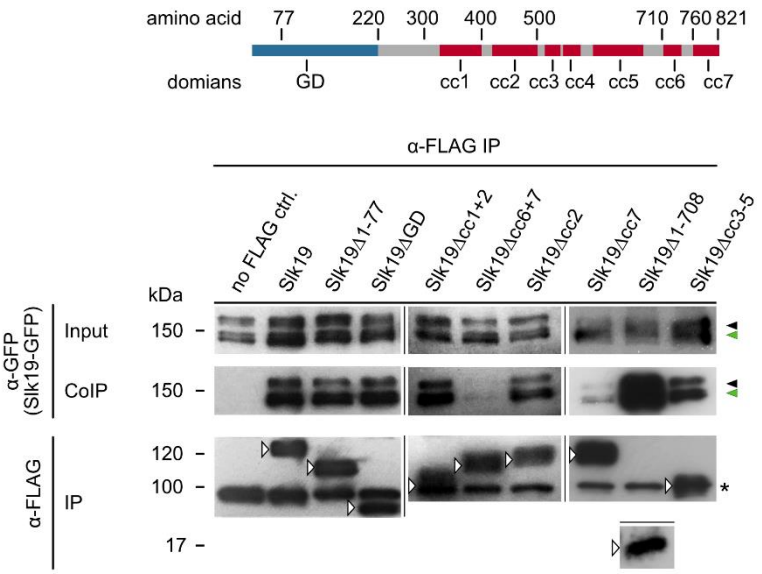

Figure 4: The C-terminus constitutes the tetramerization domain of Slk19.

Cycling cells carrying different Slk19 constructs were used for Slk19-Slk19 CoIP analyses as described in the Methods chapter. Schematic illustration of Slk19 is depicted for overview of protein domains. GD = globular domain, cc = coiled coil domain. FLAG-tagged Slk19 deletion constructs were used as bait (marked with white arrow heads) to pull down Slk19-GFP as prey. Black arrowheads indicate full length Slk19, green arrowheads indicate the cleavage product of Slk19 (Sullivan et al., 2001). Unspecific background bands are marked with asterisks. The genotypes of used strains are described in Materials chapter. All Slk19 constructs were expressed from the endogenous promoter of *SLK19*.

4.1.4 Replacement of the Slk19 C-terminus with *GCN4-Zipper or CIN8-TD* could not rescue sequestering

To dissect, whether oligomerization of Slk19 alone can restore sequestering, without the need of functional KT binding, it was aimed to oligomerize Slk19 by replacing the C-terminus by an *GLC4*-dimerization domain (*slk19Δcc6+7-GCN4-Zipper*). However, this replacement did not rescue the sequestering of Slk19 and Stu1 (Figure 5A, a-b). This might indicate that the binding of Slk19 to uaKTs is required for functional sequestering. On the other hand, replacement of the C-terminus by the *GLC4-Zipper* did also not restore other localizations of Slk19 (e.g. at MTs of the collapsed spindle) (Figure 5A, a) indicating that the artificial construct might not possess the right folding required for oligomerization or for interaction with other proteins. Furthermore, the *GLC4-Zipper* resembles a dimerization domain and not a tetramerization domain. Thus, an incorrect tertiary and/or quaternary structure is most likely the cause for the defective Slk19 localizations. The replacement of the Slk19 C-terminus with the tetramerization domain (TD) of Cin8 (aa 549–973; named in the following *CIN8-TD*) (Hildebrandt et al., 2006), could also not restore the *WT*

localizations and the sequestering of Slk19. Replacement by the *CIN8-TD* led to artifacts with ectopic localizations of the recombinant Slk19 construct making a reliable conclusion not possible (Figure 5B, a). Moreover, Stu1 showed a clear sequestering defect in the cells carrying the *slk19Δcc6+7-CIN8-TD* construct and did not localize ectopically together with Slk19, as would be expected if both proteins showed functional interaction (Figure 5B, b).

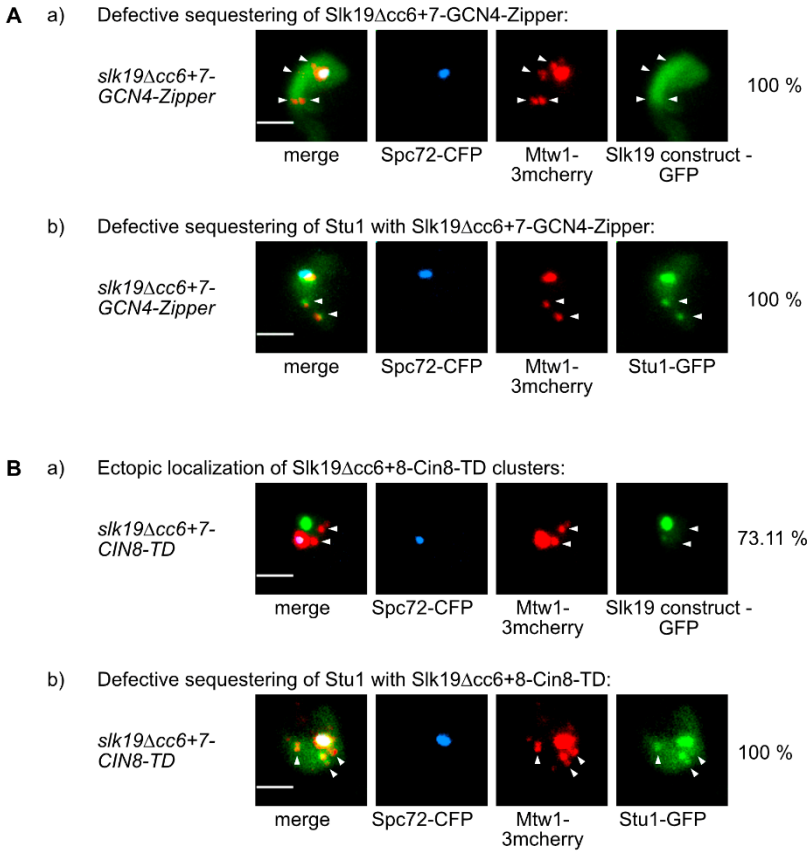

Figure 5: Replacement of the C-terminus with the *GLC4-Zipper* or *CIN8-TD* could not rescue sequestering ability of Slk19 and Stu1.

(A-B) Cells were treated with nocodazole (Nz) after G1 release to provoke uaKTs as described in Methods chapter. Spc72-CFP marks spindle pole bodies, Mtw1-3mcherry marks kinetochores. Genotypes of used strains are described in Materials chapter. All Slk19 constructs were expressed from the endogenous promoter of *SLK19*. The indicated percentages represent the frequency of the shown phenotype among all counted cells. Phenotypes with the exact numbers of counted cells are listed in the appendix. White arrowheads indicate uaKTs (not colocalizing with SPBs). (A) (a) Slk19Δcc6+7-GCN4-Zipper-GFP showed defective sequestering. (b) Stu1-GFP showed defective sequestering in cells carrying *slk19Δcc6+7-GCN4-Zipper*. (B) (a) Slk19Δcc6+7-Cin8-TD-GFP showed defective sequestering. (b) Stu1-GFP showed defective sequestering in cells carrying *slk19Δcc6+7-CIN8-TD*.

Outcome: The KT localization domain as well as the tetramerization domain of Slk19 was determined. Slk19 requires tetramerization for its localizations at the uaKTs, atKTs, MTs and for sequestering. Since both domains (KT localization and tetramerization domain) are located within the C-terminus, the initial attempt to create a Slk19 mutant with a specific defect in KT localization, while leaving sequestering function intact, was not possible. Thus, the question whether Slk19 basal binding at the uaKT is required for initiation of the sequestering process could not be answered. It was shown that cc1-deletion leads to a specific sequestering defect and thus remains as a potential Stu1-interaction domain facilitating co-polymerization. This interaction was analyzed in the following chapter.

4.1.5 The cc1 domain and the C-terminus of Slk19 both contribute to Stu1 interaction at uaKTs

The interaction of Slk19 tetramers and Stu1 dimers is a prerequisite for co-polymerization and sequestering at uaKTs according to the current sequestering model (Kolenda et al., 2018). For Stu1, there are three domains that are essential for sequestering: TOGL1, D4 and CL. Stu1ΔTOGL1 shows a sequestering defect because of the loss of the KT localization domain and Stu1ΔD4 shows a sequestering defect because of the loss of the dimerization domain (Funk et al., 2014). This leaves the CL domain of Stu1 as likely candidate for a Slk19 interaction domain (Funk et al., 2014). For Slk19, the cc1 domain and the C-terminus (cc6+7) are essential for sequestering and thus likely candidates for Stu1 interaction domains at uaKTs. To analyze this, Nz-treated cells were used for CoIP analyses: FLAG-tagged Slk19 deletion constructs showing a defective sequestering in microscopy data (see part 4.1.2) were analyzed for their ability to pull down Stu1-9Myc.

Compared to *WT* Slk19, the constructs Slk19Δcc1, Slk19Δcc1+2 and Slk19Δcc6+7 show a strongly reduced, but not completely abolished, Stu1 interaction (Figure 6A). In comparison, the construct Slk19ΔGD (functional sequestering) showed Stu1-interaction comparable to *WT*. As shown in part 4.1.2, deletion of the C-terminus led to a sequestering defect, which could be the cause for the strongly reduced interaction ability with Stu1 at uaKTs. However, CoIP analysis of Stu1 with only the C-terminus of Slk19, Slk19Δ1-708 (cc6+7), showed a direct interaction with Stu1 (Figure 6A). The constructs Slk19Δcc1, Slk19Δcc1+2 and Slk19Δ1-708 (cc6+7) show a similar interaction with Stu1, when compared with the amount of bait protein (Figure 6B).

Taken together, the results suggest that Slk19 has at least two domains that contribute to Stu1 interaction during the sequestering process at uaKTs: the C-terminus (cc6+7, aa 709–821) and the cc1 domain (aa 300–410).

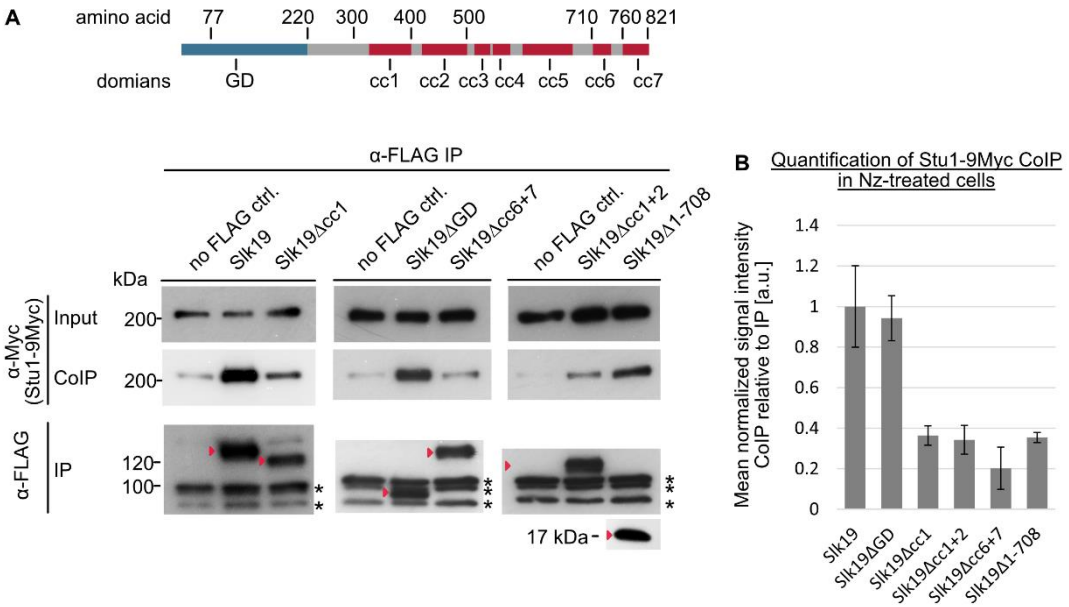

Figure 6: The C-terminus and the middle region of Slk19 are required for Stu1 interaction in Nz-treated cells.

(A-B) Genotypes of used strains are described in Materials chapter. Slk19 constructs were expressed from the endogenous promoter of *SLK19*. (A) Cells carrying different Slk19 constructs were treated with nocodazole (Nz) after G1 release to provoke uaKTs and used for Slk19-Stu1 CoIP analysis as described in Methods chapter. Schematic illustration of Slk19 is depicted for overview of protein domains. GD = globular domain, cc = coiled coil domain. FLAG-tagged Slk19 deletion constructs were used as bait (marked with red arrow heads) to pull down Stu1-9Myc as prey. Unspecific background bands are marked with asterisks. (B) Quantification of Slk19-Stu1 CoIP in Nz-treated cells. Pulled-down Stu1-9Myc protein amounts were normalized to respective bait protein amounts. Standard deviations calculated from two technical replicates. Exact values of quantification are listed in the appendix.

Interestingly, all Slk19 domains required for sequestering were also involved in Stu1 interaction as assessed by the *in vivo* observations and by the *in vitro* CoIP experiments. As shown in chapter 4.1.2, the minimal construct consisting only of those domains was sufficient rescue sequestering to a large extend. This again emphasizes the importance of the Stu1-Slk19 interplay in this cellular process.

Stu1 is an essential component for spindle stability during an undisturbed cell cycle and the withdrawal of Stu1 from the spindle by the Stu1-Slk19 sequestering process at uaKTs leads to a restructuring of the MT network (Kolenda et al., 2018). This leads to the formation of nuclear random microtubules (nrMTs) (Kolenda et al., 2018) that are unaligned with the spindle and scan the nucleus for uaKTs and assure an efficient recapturing of the lost chromosomes. The question now arose, whether Slk19 might also play a role for spindle integrity during an undisturbed cell cycle in metaphase. This analysis would not only shed light on the Slk19 functions at the metaphase spindle but also on the overriding importance of Slk19 to sequester together with Stu1 in the presence of an uaKT.

4.2 Slk19 functions at the metaphase spindle to stabilize ipMTs via Stu1 and Ase1 *in vivo* and enhances MT crosslinking *in vitro*

4.2.1 Slk19 localizes at the spindle in metaphase cells and binds to attached kinetochores via Spc105

Slk19 must clearly play a role in metaphase, since deletion of Slk19 leads to shortened metaphase spindles and *Δslk19 kar3-ts* double mutants arrested with short spindles in metaphase (Zeng et al., 1999). However, the exact function of Slk19 in metaphase is so far unknown. The aim here was to find out which function Slk19 has at the metaphase spindle and whether it can directly localize to MTs (ktMTs and/or ipMTs) by itself. The results presented in this chapter (Figure 7A and C) are in part also published in Norell et al., 2021 (copyright: ©2021 Norell et al., CC BY-NC-SA 3.0, http://creativecommons.org/licenses/by-nc-sa/3.0).

In metaphase-arrested cells, Slk19 could be observed between the two KT clusters in many of the *WT* cells (75.31 %) in addition to its localization at the KTs (Figure 7A, a). The question arose whether this detected signal between the KTs was derived from a spindle localization of Slk19. Due to the spatial proximity of the two KT clusters within the relatively short metaphase spindles, the Slk19 signals at the atKTs and between the KTs are not clearly delimitable from each other. To clarify if Slk19 localizes to the spindle, it was attempted to specifically interfere with the KT localization of Slk19.

The KT protein Spc105 appears to be a likely candidate for a Slk19 interaction partner at atKTs in metaphase, since Spc105 was shown to be required for basal binding at uaKTs in Nz-treated cells (*in vivo* data, mentioned in part 4.1.1). In addition, centromeric Slk19 binding was strongly reduced in *spc105-ts* mutants shown by ChIP analysis using cycling cells (Pagliuca et al., 2009). Here, a quantitative ChIP analysis, performed exclusively with metaphase-arrested cells, also showed a strong reduction of Slk19 at atKTs in '*Δspc105'* comparted to *WT* cells (90% reduction) (Figure 7B). Indeed, when Spc105 was depleted ('*Δspc105*') *in vivo* in metaphase-arrested cells, Slk19 localization at the atKTs was abolished, however, a strong Slk19 signal at the spindle center was observed (Figure 7A, a). The signal intensities along the metaphase spindle were measured and depicted in RGB-plots (Figure 7C, a-b). In *WT* cells, the plot profile showed a Slk19-GFP intensity distribution with <u>two</u> peaks that are close to the KT signal peaks (Figure 7C, a). In contrast, the plot profile in Spc105-depleted cells showed only <u>one</u> peak for Slk19-GFP between the two KT signal intensity peaks (Figure 7C, b).

Taken together, Slk19 did not localize to atKTs in metaphase-arrested '*Δspc105*' cells, as shown by the quantitative ChIP and the microscopy analyses. Thus, Slk19 seems to be not only dependent on Spc105 for its basal binding at uaKTs but also for its binding to atKTs in metaphase cells.

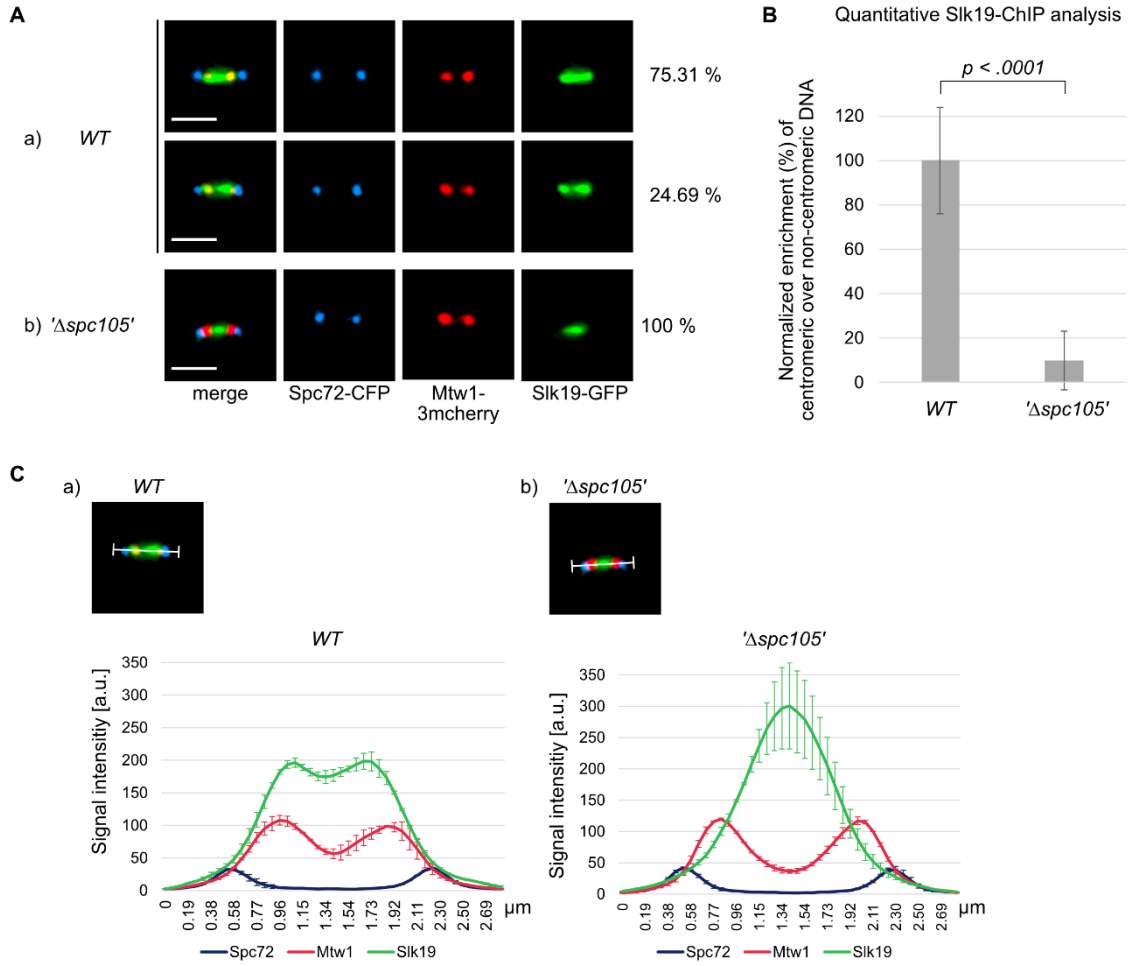

Figure 7: Slk19 is dependent on Spc105 for its localization at attached KTs (atKTs) and binds strongly to the metaphase spindle center in Spc105-depleted cells.

(A-C) Cells were arrested in metaphase by depletion of Cdc20 (*GAL1*-promoter shut-off). Spc105 was conditionally depleted (*'Δspc105'*) by IAA-treatment (AID) during metaphase arrest as described in Methods chapter. Genotypes of used strains are described in Materials chapter. (A and C) Spc72-CFP marks spindle pole bodies, Mtw1-3mcherry marks KTs. (A) Indicated percentages represent the frequency of the shown phenotype among all counted cells. (a) Slk19-GFP localized to atKTs and between the two KT clusters in the majority of metaphase-arrested cells. Upper row shows cells with Slk19 at atKTs and the spindle. Lower row shows Slk19 mainly at the two KT clusters. (b) Slk19 localized at the spindle center in metaphase-arrested *'Δspc105'* cells. (B) Quantitative PCR analysis of Slk19-ChIP showed significantly reduced centromeric enrichment of Slk19 in *'Δspc105'* cells compared to *WT* cells. The mean enrichment of centromeric DNA (*CEN3*) was calculated in relation to the non-centromeric DNA (*PHO5*) and the values were normalized (WT represents 100%). Standard deviations were calculated from two biological replicates of the ChIP assays, each with three technical replicates for the qPCR reactions. The p-value was calculated using a two-tailed unpaired t-test. (C) RGB-plots were measured as described in Methods chapter. Longitudinal RGB-plots of metaphase spindles measured in (a) *WT* cells and (b) *'Δspc105'* cells showing the mean distribution and signal intensity of indicated proteins. RGB-plots show the average of n>16 cells per experiment; 2 µm spindles were measured. Exact numbers of measured cells are listed in the appendix. Error bars show the standard deviations calculated from two independent experiments.

Most interestingly, Slk19 was not distributed evenly along the metaphase spindle in '*Δspc105*' cells but instead concentrated at the center of the spindle. This localization might represent specific binding to the spindle overlaps rather than to the kMTs or the rest of the ipMTs. Furthermore, an increase of Slk19 signal intensity (exceeding the *WT* levels) was observed at the spindle center (in between the two KT clusters). A possible explanation might be that the elimination of the Slk19 binding site at atKTs in *'Δspc105'* cells leads to an increased free pool of Slk19 that can bind to the alternative Slk19 binding site: the spindle overlaps. However, also other (possibly additional) explanations are conceivable here, which are further explored in chapter 4.3.

4.2.2 The cc1 domain and the C-terminus of Slk19 are required for its spindle localization

Slk19 can be clearly seen at the center of the spindle in Spc105-depleted cells, a localization that coincides with the overlaps of ipMTs (see chapter 4.2.1). The question arose which role Slk19 has at this spindle localization. Deletion of Slk19 leads to both spindle defects and defects caused by lacking Slk19 localization at KTs. To better understand the specific function of Slk19 at the metaphase spindle, the aim was to find a Slk19 mutant with a specific localization defect at the spindle but intact localization at atKTs. Therefore, the spindle localization of different GFP-tagged Slk19 deletion constructs was analyzed in metaphase-arrested cells with and without Spc105 depletion (Figure 8A and B). The results presented in this chapter (Figure 8A-C) are also published in Norell et al., 2021 (copyright: ©2021 Norell et al., CC BY-NC-SA 3.0, http://creativecommons.org/licenses/by-nc-sa/3.0).

In metaphase-arrested cells, the Slk19 deletion constructs Slk19Δ1-77, Slk19ΔGD, Slk19Δcc2 and Slk19Δcc3-5 showed similar cellular localizations as *WT* Slk19 (Figure 8A). All of those constructs localized to the spindle in Spc105-depleted cells (Figure 8B). These constructs also localized at the atKTs and the midzone in anaphase cells (Figure 8C). The C-terminal deletion construct Slk19Δcc6+7 failed to localize to the metaphase spindle (Figure 8A and B), to atKTs in metaphase (Figure 8A) and in anaphase (Figure 8C) and to the anaphase midzone (Figure 8C). Only a diffuse nuclear Slk19-GFP signal was visible. However, the C-terminus alone, consisting only of the domains cc6+7 (Slk19Δ1-708), localized to atKTs in metaphase-arrested cells (Figure 8A) and in anaphase cells (Figure 8C) but not to the metaphase spindle (Figure 8B) or the anaphase midzone (Figure 8C). Similar to the observations in Nz-treated cells, this again indicates that the C-terminus includes the KT-binding domain of Slk19. The homotetramerization of Slk19 via the C-terminus (shown in chapter 4.1.3) might or might not be additionally required for KT binding. Nevertheless, as shown by the mentioned results, Slk19Δ1-708 (cc6+7) is required but apparently not sufficient to localize to the metaphase spindle efficiently by itself (Figure 8B). Thus, it is likely that tetramerization is needed for Slk19 binding to the metaphase spindle and to the anaphase midzone.

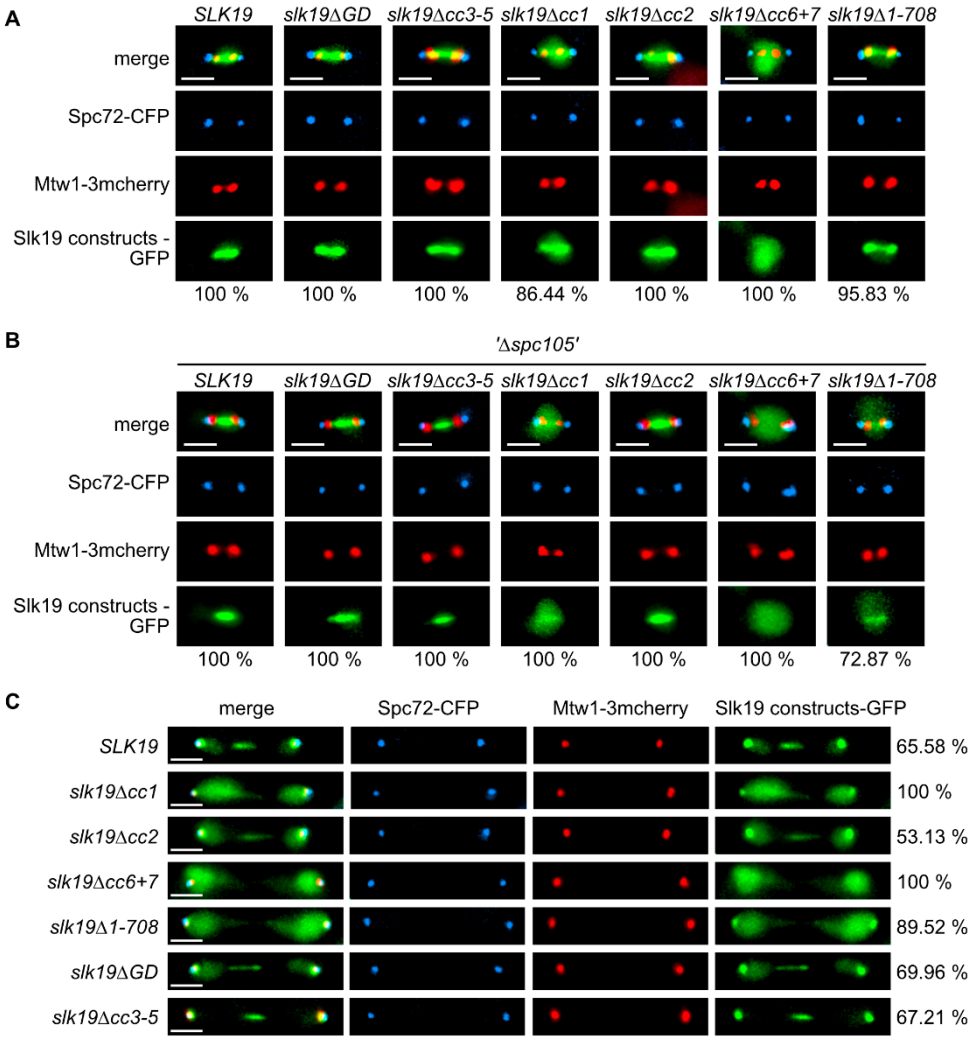

Figure 8: Deletion of the cc1 of Slk19 leads to a specific defect in spindle localization while leaving the KT localization intact.

(A-C) Spc72-CFP marks spindle pole bodies, Mtw1-3mcherry marks kinetochores. Genotypes of used strains are described in Materials chapter. Phenotypes with the exact numbers of counted cells are listed in the appendix. GD = globular domain, cc = coiled coil domain. Slk19 constructs were expressed from the endogenous promoter of *SLK19*. (A-B) Cells carrying GFP-tagged Slk19 constructs were arrested in metaphase by Cdc20-depletion (*GAL1*-promoter shut-off). (A) Slk19Δcc6+7 showed no *WT* localizations. All other analyzed Slk19 constructs localized at atKTs or at the spindle and atKTs. (B) Spc105 was depleted (*'Δspc105'*) by IAA-treatment (AID) during metaphase arrest (described in Methods chapter). Slk19 localized between the two KT clusters in most of metaphase-arrested *'Δspc105'* cells. Slk19Δcc6+7, Slk19Δ1-708 and Slk19Δcc1 showed no efficient localization at the spindle in *'Δspc105'*cells. All other analyzed Slk19 constructs were observed at the center of metaphase spindles similar to *SLK19 'Δspc105'* cells. (C) Synchronized cycling cells carrying GFP-tagged Slk19 constructs were analyzed 2–2.5 h after the release from a G1 arrest, when most of the cells appeared in anaphase. Slk19 localized to the anaphase spindle midzone and to KTs. Slk19Δcc6+7 showed no *WT* localizations in anaphase cells. Slk19Δ1-708 and Slk19Δcc1 showed a specific defect in midzone binding, while KT localizations were still observable. All other analyzed Slk19 constructs showed localizations comparable to *WT SLK19* cells.

The construct Slk19Δcc1 localized to the KTs in metaphase-arrested cells and in anaphase cells (Figure 8B and C). In metaphase-arrested cells with Spc105 depletion, Slk19Δcc1 could not (or only very weakly) localize to the metaphase spindle (Figure 8B). In anaphase cells Slk19Δcc1 showed a strong defect in midzone binding (Figure 8C) (anaphase functions discussed in more detail in chapter 4.4).

Since Slk19Δcc1 shows a specific defect in spindle localization, but not in KT binding, this Slk19 mutant was chosen for further analysis of the Slk19 spindle function in metaphase.

4.2.3 Slk19Δcc1 shows an increased number of cells with nrMTs

The deletion of Slk19 was shown to lead to several spindle defects in metaphase, such as short spindle length (Zeng et al., 1999) and increased number of nrMTs as observed via Dad1-labeling (nrMTs = nuclear MTs that are unaligned with the spindle) (Kolenda et al., 2018). To analyze whether these defects shown in *Δslk19* cells can be solely attributed to missing spindle localization of Slk19, the spindle lengths and the number of nrMTs were observed and quantified in *slk19Δcc1* cells. The results presented in this chapter (Figure 9) are also published in Norell et al., 2021 (copyright: ©2021 Norell et al., CC BY-NC-SA 3.0, http://creativecommons.org/licenses/by-nc-sa/3.0).

Indeed, the phenotypes of *Δslk19* and *slk19Δcc1* cells were very similar. Both *Δslk19* and *slk19Δcc1* cells showed a large proportion of cells with short spindles and increased number of nrMTs (Figure 9). Interestingly, cells with short spindles showed a correlation with the appearance of nrMTs. The nrMTs are polymerized from a free pool of tubulin in the nucleus and are not aligned with the spindle (Kolenda et al., 2018), thus, the appearance of nrMTs is indicative of a compromised spindle. These findings suggest, that Slk19 spindle localization via its cc1 domain might be important to maintain a stable metaphase spindle with aligned ipMTs.

Taken together, it was shown that these defects (short spindles and increased number of nrMTs) are not due to KT localization defects of Slk19 but clearly due to spindle localization defects.

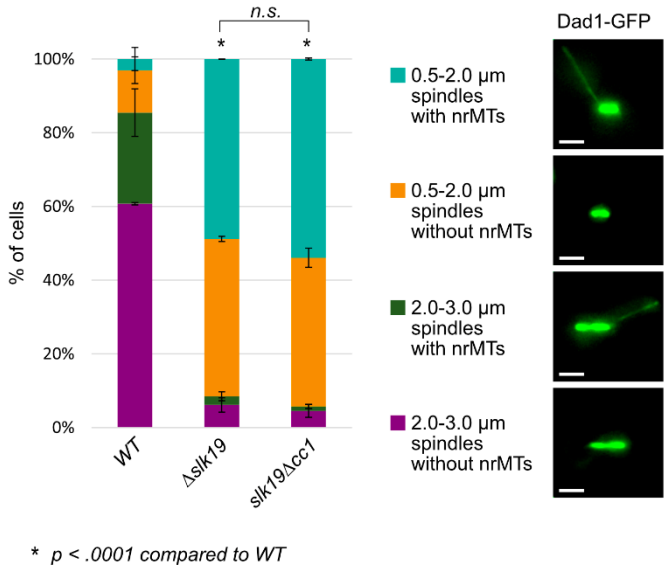

Figure 9: *Δslk19* and *slk19Δcc1* cells show a large proportion of cells with short spindles correlating with an increased appearance of nrMTs.

Cells were arrested in metaphase by depletion of Cdc20 (by shutting off the expression from the *MET25* promoter). Dad1-GFP was used to analyze the spindle length and to specifically observe the appearance of nuclear random MTs (nrMTs). Slk19Δcc1 was expressed from the endogenous promoter of *SLK19*. Cells were categorized according to the metaphase spindle length (short spindles: 0.5–2.0 µm; long spindles: 2.0–3.0 µm) and according to the appearance of nrMTs. Most *WT* cells showed long spindles without nrMTs. The large majority of *Δslk19* and *slk19Δcc1* cells showed short spindles correlating with a significant increase in the appearance of nrMTs. Genotypes of used strains are described in Materials chapter. Phenotypes with the exact numbers of counted cells are listed in the appendix. The p-values were calculated using chi-square tests. Scale bar = 2 µm. cc = coiled coil domain. n.s. = not significant.

4.2.4 Spindle localization of Slk19 depends on the CL domain of Stu1 and on Ase1

To find out whether Slk19 binds directly or indirectly to the metaphase spindle, it was aimed to identify interaction partners of Slk19, to analyze if Slk19 binding to the metaphase spindle is dependent on these interaction partners. Stu1 is a potential Slk19 interaction partner since it also binds to the metaphase spindle and interacts with the cc1 domain of Slk19 at uaKTs in Nz-treated cells (shown in chapter 4.1.5). Furthermore, it was shown in chapter 4.1.1 that Slk19 is dependent on Stu1 for its localization at the collapsed spindle in Nz-treated *'Δspc105'* cells. For this reason, it was analyzed whether Slk19 is dependent on Stu1 at the spindle in metaphase-arrested cells. The results presented in this chapter (Figure 10A, E and Figure 11A, B) are also published in Norell et al., 2021 (copyright: ©2021 Norell et al., CC BY-NC-SA 3.0, http://creativecommons.org/licenses/by-nc-sa/3.0).

In Stu1-depleted cells, Slk19 localized as a dot-like signal at the collapsed metaphase spindle (*'Δstu1'* cells, Figure 10A). This Slk19 localization was abolished in metaphase-arrested cells with Stu1 and Spc105 co-depletion (*'Δspc105' 'Δstu1'* cells) (Figure 10A). However, because Stu1 is a spindle stabilizing protein, it is uncertain whether those cells have intact metaphase spindles (with intact ipMT overlaps). Possibly, Stu1 is only indirectly required to maintain metaphase spindle overlaps to which Slk19 can bind but does not directly mediate Slk19 spindle localization. To analyze whether Slk19 directly interacts with Stu1 in metaphase, a CoIP analysis was performed in metaphase-arrested cells. The results showed a direct interaction of Stu1 and Slk19 (Figure 10B). In *slk19Δcc1* cells, this interaction was reduced, however, not completely abolished (Figure 10B and C). Nevertheless, the results indicate that Stu1 and Slk19 seem to exist as complex in metaphase and the cc1 domain might be involved in its formation.

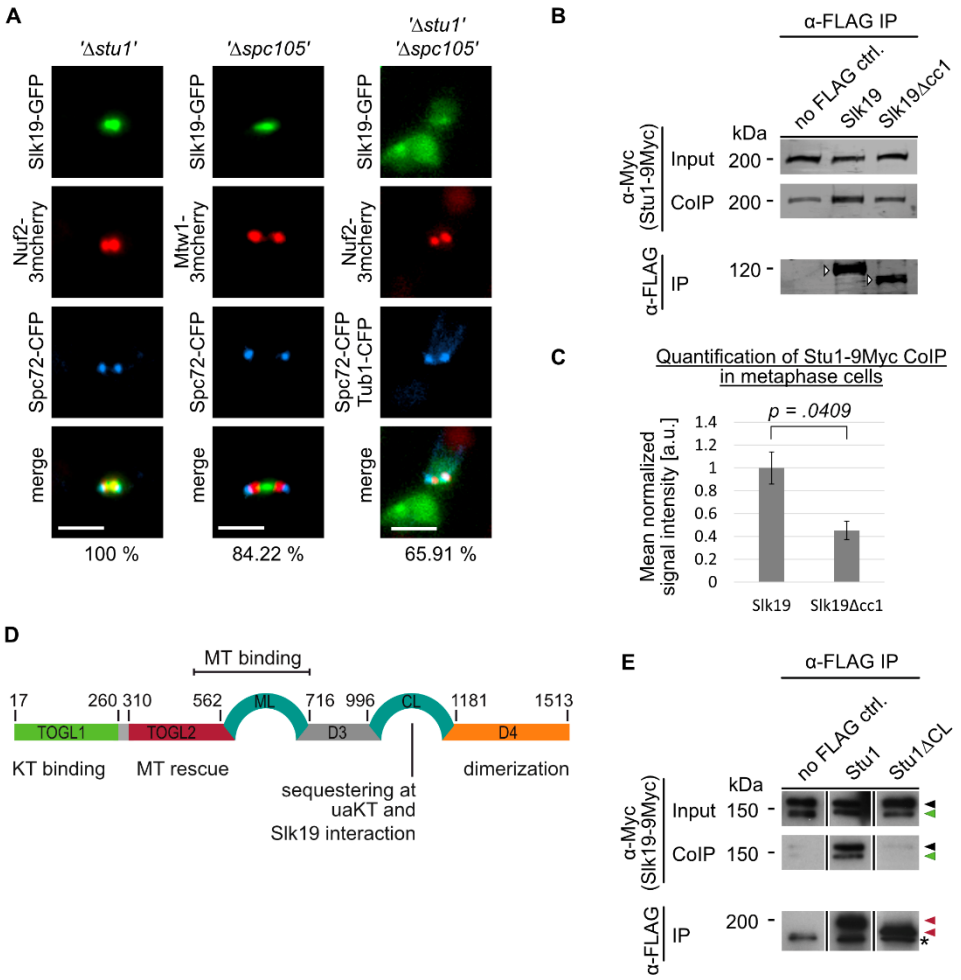

Figure 10: Slk19 localization at the metaphase spindle is dependent on Stu1 and Slk19 interacts with Stu1 via the CL domain in metaphase cells.

(A-E) Genotypes of used strains are described in Materials chapter. Cells were arrested in metaphase by depletion of Cdc20 (by shutting off the expression from the *GAL1* or *MET25* promoter). (A) Conditional depletion of Stu1 (*'Δstu1'*), Spc105 (*'Δspc105'*), or both proteins (*'Δstu1' 'Δspc105'*) was

performed by IAA-treatment (AID) during metaphase arrest (described in Methods chapter). Spc72-CFP marks spindle pole bodies, Tub1-CFP marks microtubules, Mtw1-3mcherry or Nuf2-3mcherry marks kinetochores. The indicated percentages represent the frequency of the shown phenotype among all counted cells. Phenotypes with exact numbers of counted cells are listed in the appendix. (B) Cells carrying *SLK19* or *slk19Δcc1* were used for Slk19-Stu1 CoIP analysis as described in Methods chapter. FLAG-tagged Slk19 constructs were used as bait (marked with white arrow heads) to pull down Stu1-9Myc as prey. Slk19 constructs were expressed from the endogenous promoter of *SLK19*. Proteins were detected by the LI-COR imaging system. (C) Quantification of Slk19-Stu1 CoIP in metaphase-arrested cells. Pulled-down Stu1-9Myc protein amounts were normalized to respective bait protein amounts. The p-value was calculated using a two-tailed unpaired t-test. Standard deviations calculated from two technical replicates. Exact values of quantification are listed in the appendix. cc = coiled coil domain. (D) Schematic illustration of Stu1 for overview of protein domains and domain functions. (E) Cells carrying 5xFLAG-tagged *STU1* or *stu1ΔCL* were used for Slk19-Stu1 CoIP analyses as described in Methods chapter. 5xFLAG-tagged Stu1 constructs were used as bait (marked with red arrow heads) to pull down Slk19-9Myc as prey. Black arrowheads indicate full length Slk19, green arrowheads indicate the cleavage product of Slk19 (Sullivan et al., 2001). Unspecific background bands are marked with asterisks. CL = C-terminal loop.

To exclude the above-mentioned possibility, that Stu1 is only required for Slk19 spindle localization due to its role in maintaining spindle integrity, it was aimed to find a Stu1 mutant with intact spindles but defective Slk19 interaction. The CL domain of Stu1 is a potential Slk19 interaction domain since it was also required for Stu1-Slk19 sequestering at uaKTs (Funk et al., 2014) (Stu1 domains illustrated in Figure 10D). Since *stu1ΔCL* cells are viable and show intact metaphase spindles (Funk et al., 2014), this mutant was especially suitable to analyze Slk19 localizations. Indeed, CoIP analysis revealed the CL domain of Stu1 as the Slk19 interaction domain also in metaphase-arrested cells (Figure 10E).

In metaphase-arrested *stu1ΔCL* cells, Slk19 was strongly reduced at the spindle in comparison to *WT* but still localized at the atKTs (Figure 11A, a, for *WT* localization of Slk19 at the metaphase spindle see Figure 7A or Figure 8A). In *stu1ΔCL 'Δspc105'* cells, Slk19 localization at the atKTs was prevented and thus the spindle localization of Slk19 could be better analyzed. Also in these *stu1ΔCL 'Δspc105'* cells, only a weak Slk19 signal at the spindle was observed (Figure 11A, b and B). Since a weak spindle binding of Slk19 remained in those cells, other proteins at the spindle might be additionally needed for efficient Slk19 spindle binding.

Intriguingly, although Slk19 was strongly reduced at the spindle in *stu1ΔCL* cells in metaphase (Figure 11A, a and C, a), in anaphase, Slk19 localized to the spindle midzone in *stu1ΔCL* cells comparable to *WT* (Figure 11D, for *WT* localization of Slk19 at the anaphase spindle see Figure 8C). This indicates that either a second Stu1 interaction domain becomes relevant for Slk19 interaction in anaphase, or another protein confers the localization of Slk19 to the spindle midzone after anaphase onset (discussed in more detail in chapter 4.4).

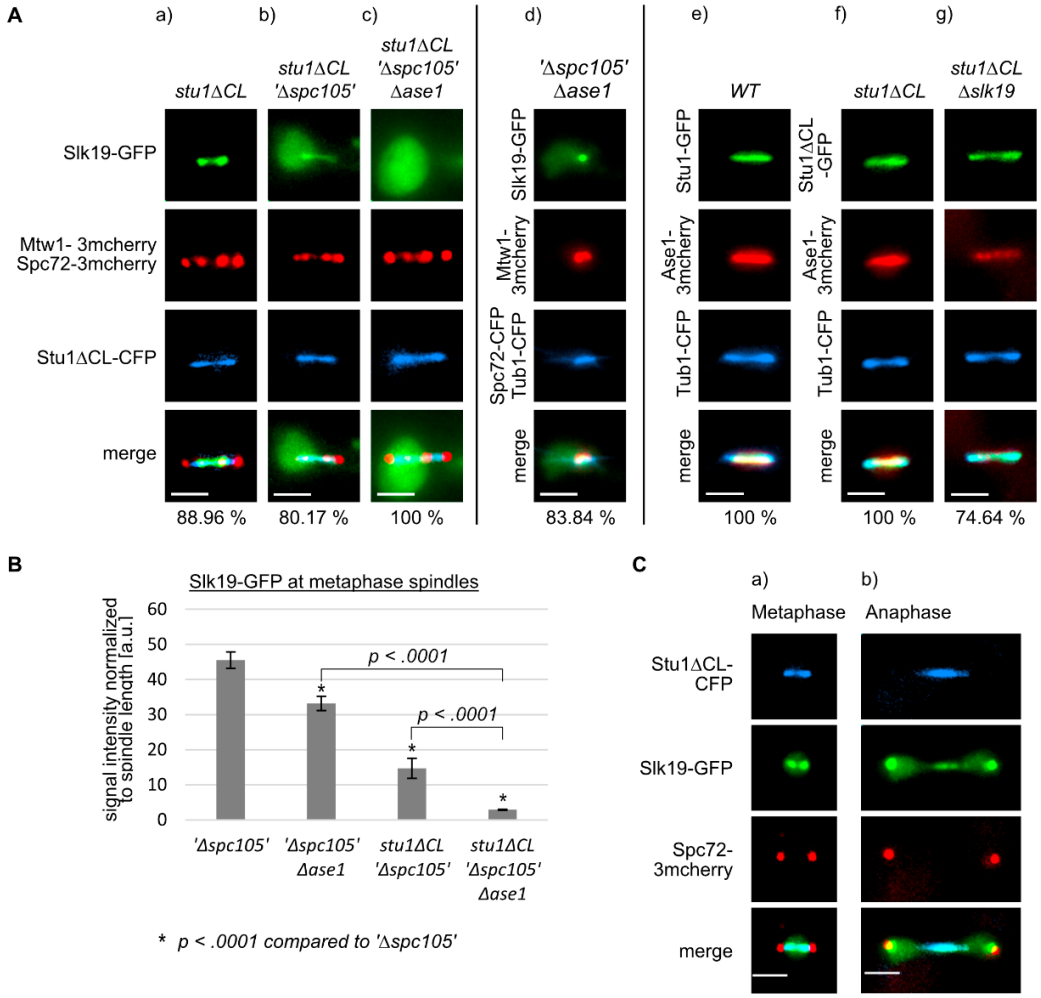

Figure 11: Ase1 and the Stu1 CL domain play a synergistic role in localizing Slk19 to the metaphase spindle.

(A-C) Spc72-CFP or -3mcherry marks spindle pole bodies, Tub1-CFP marks microtubules, Mtw1-3mcherry marks kinetochores. Genotypes of used strains are listed in Materials chapter. CL = C-terminal loop. (A-B) Dependency of Slk19 metaphase spindle localization on Stu1 CL domain and on Ase1. (A) Cells were arrested in metaphase by depletion of Cdc20 (*GAL1* or *MET25* promoter shut-off). Conditional Spc105 depletion (*'Δspc105'*) was performed by IAA-treatment (AID) during metaphase arrest. Indicated percentages represent the frequency of the shown phenotype among all counted cells. Phenotypes with exact numbers of counted cells are listed in the appendix. (a) Slk19 localized mainly at KTs in *stu1ΔCL* cells. (b) *stu1ΔCL 'Δspc105'* cells showed reduced Slk19 levels at spindle. (c) Slk19 spindle localization was abolished in *stu1ΔCL 'Δspc105' Δase1* cells. (d) Slk19 localized at collapsed spindle in *'Δspc105' Δase1* cells. (e) Ase1 bound to metaphase spindles in *WT* cells. (f) Ase1 bound to metaphase spindles in *stu1ΔCL* cells. (g) *stu1ΔCL Δslk19* cells showed long metaphase spindles. (B) Quantification of Slk19-GFP at metaphase spindle (normalized to spindle length). Cells were cultured as described for (A). Measured Slk19 intensities normalized to respective spindle lengths. The p-values were calculated using two-tailed unpaired t-tests. Standard deviations were calculated from two individual experiments. Exact values of quantification are listed in the appendix. (C) Synchronized cycling cells were analyzed after release from G1 arrest after (a) 1.5 h for metaphase cells or (b) 2–2.5 h for anaphase cells. Slk19 was not dependent on the Stu1 CL domain for its localization to the anaphase midzone.

Ase1, a MAP with MT-crosslinking function, also localizes to the spindle overlaps in metaphase cells. Therefore, it was analyzed whether binding of Slk19 to the spindle might also be dependent on Ase1. In '*Δspc105*' *Δase1* cells, Slk19 still localized to the metaphase spindle, however, this localization was reduced compared to '*Δspc105*' cells (Figure 11A, b and B). This raised the question whether Ase1 might also be reduced at the spindles in *stu1ΔCL* cells and whether this further reduces Slk19 amounts at the spindle as secondary effect. For this reason, the Ase1 localization in *stu1ΔCL* cells was analyzed and it was shown that Ase1 binding to the spindle is not reduced in *stu1ΔCL* cells compared to *WT* cells (Figure 11A, e and f). In *stu1*ΔCL '*Δspc105*' *Δase1* cells, the Slk19 localization at the metaphase spindle was completely abolished (Figure 11A, c compared to b; Figure 11B). Thus, the results indicate that both Ase1 and the CL domain of Stu1 might contribute to Slk19 spindle localization. Unfortunately, a direct interaction between Slk19 and Ase1 could not be shown by CoIP analysis, unlike the Stu1-Slk19 interaction. This indicates that the Ase1-Slk19 interaction might be less stable or more transient than the Stu1-Slk19 interaction.

Interestingly, *stu1*ΔCL *Δslk19* cells did not show a reduced spindle length (74.64 % of cells had a spindle length of ≥ 2 µm; listed in the appendix in table for Figure 11A), although Slk19 does not localize to the metaphase spindles in these cells (Figure 11A, g). Furthermore, also *stu1*ΔCL '*Δspc105*' *Δase1* cells show no reduced spindle length (Figure 11A, c). The absence of each Ase1 or Slk19 individually would be sufficient to cause a spindle defect. This shows that Stu1ΔCL can compensate all spindle defects caused by the absence of Ase1 and Slk19. It was shown in previous studies that *stu1ΔCL* cells have comparable spindle lengths to *WT* cells but show increased kMT lengths and decreased inter-KT distances (Funk et al., 2014). This suggests a decreased tension at the KTs and thus the spindle must resist less force. This might be one possible explanation for sustained spindle integrity in *stu1*ΔCL '*Δspc105*' *Δase1* cells and *stu1ΔCL Δslk19* cells.

4.2.5 Deletion of Slk19 leads to a strong reduction of Ase1 protein levels and to a moderate reduction of Stu1 levels at the metaphase spindle

Slk19 does not localize to MTs by itself but is dependent on Stu1 and Ase1 for its spindle localization (see part 4.2.4). Thus, it seems obvious that these MAPs are required for Slk19 to accomplish its spindle function. *Vice vera*, the question arose whether other MAPs, such as Stu1 and Ase1, are influenced by Slk19 in their localization and/or functionality. Slk19 is a tetramer with multiple binding sites, optimal for multiple protein interactions (as during the sequestering together with Stu1). Thus, Slk19 might also affect Stu1 and/or Ase1 amounts at the metaphase spindle. The results presented in this chapter (Figure 12 and Figure 13A-B) are also published in Norell et al., 2021 (copyright: ©2021 Norell et al., CC BY-NC-SA 3.0, http://creativecommons.org/licenses/by-nc-sa/3.0).

To analyze the effects of Slk19 on Stu1 and Ase1, signal intensities of Ase1-3mcherry and Stu1-GFP were measured over the complete metaphase spindles in *WT*, *Δslk19* and *slk19Δcc1* cells (Figure 12A and B). For comparison, short metaphase spindles of 1.8 µm and longer metaphase spindles of 2.4 µm were measured (Figure 12B). In metaphase-arrested *Δslk19* and *slk19Δcc1* cells, the Stu1 levels were reduced compared to *WT* (1.5-fold and 1.8-fold reduction in *Δslk19* and *slk19Δcc1* cells respectively). Ase1 levels were even more drastically reduced in *Δslk19* and *slk19Δcc1* cells (7.8-fold and 5.4-fold reduction in *Δslk19* and *slk19Δcc1* cells respectively) (Figure 12A and B).

Re-integration of *SLK19* into the *LYS2*-locus of *Δslk19* cells rescued Ase1 as well as Stu1 levels at the spindle showing that this phenotype is indeed dependent on Slk19 (Figure 12A and B).

The results show that Slk19 affects Ase1 and Stu1 levels at the spindle. Could this effect be the result of altered protein levels in the cell? Western blot analyses using whole cell extracts of metaphase-arrested cells showed that Stu1 protein levels were not significantly reduced in *Δslk19* cells compared to *WT* (Figure 13A and B). In contrast, Ase1 protein levels were reduced 2.0-fold in *Δslk19* cells compared to *WT* cells. Also in *slk19Δcc1* cells, Ase1 protein levels were similarly reduced (Figure 13A and B). This indicates that Ase1 might need Slk19 interaction at the spindle for higher protein stability e.g. for correct folding or prevention of premature protein degradation. Possibly, Ase1 might need Slk19 even for more effective protein expression, however, Slk19 has never been characterized as transcription factor so far. The exact reason why Ase1 levels are reduced in *Δslk19* cells (and Stu1 levels are not) is so far unknown.

Notably, Ase1 total protein levels in the cell are reduced 2.0-fold while Ase1 levels bound to the metaphase spindle are reduced 7.8-fold compared to *WT* cells (Figure 12B). This indicates that *Δslk19* not only alters Ase1 protein levels but probably also the effectiveness of Ase1 binding to the spindle directly.

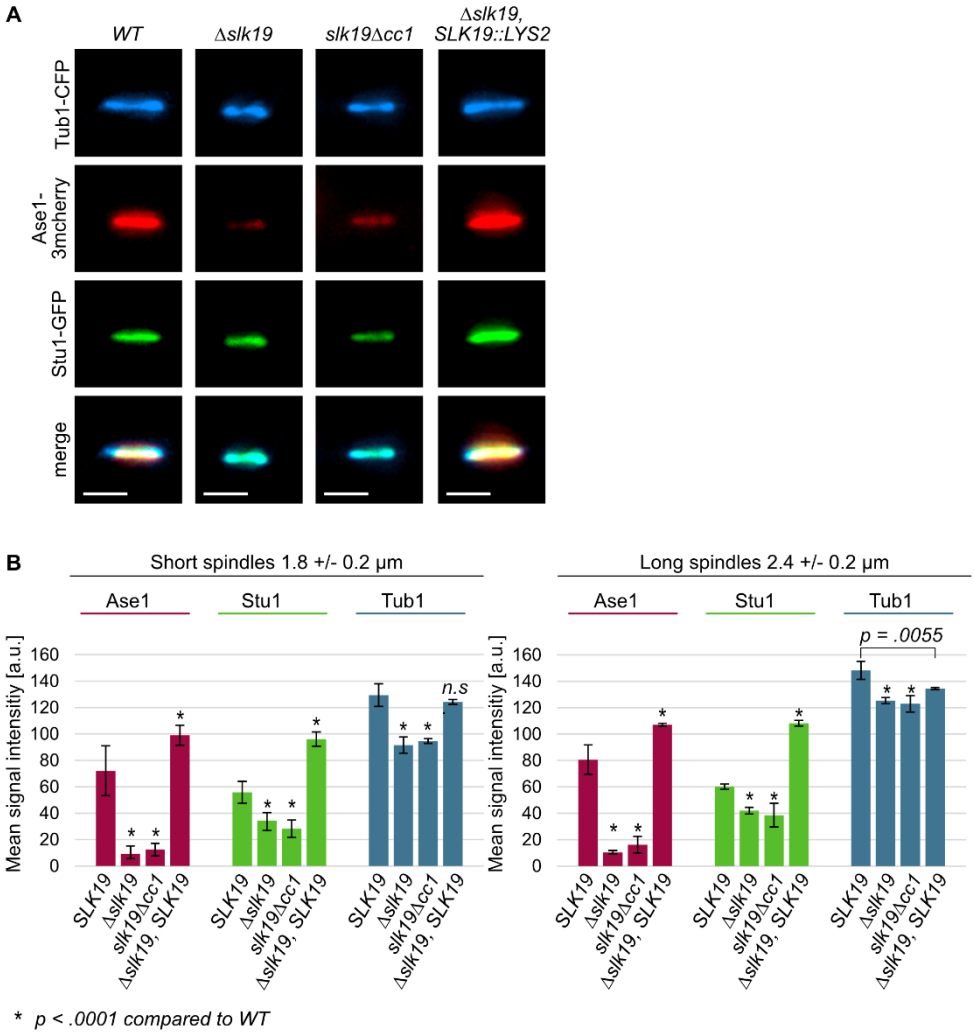

Figure 12: Deletion of Slk19 leads to a strong reduction of Ase1 and moderate reduction of Stu1 at the metaphase spindle and deletion of the cc1 domain shows a similar phenotype.

(A-B) Cells were arrested in metaphase by depletion of Cdc20 (by shutting off the expression from the *MET25* promoter). Genotypes of used strains are described in Materials chapter. Slk19 constructs were expressed from the endogenous promoter of *SLK19*. Where indicated, *WT SLK19* was re-integrated into the *LYS2*-locus in *Δslk19* cells (*Δslk19, SLK19::LYS2).* (A) Micrographs of indicated cell types. Tub1-CFP marks microtubules and was used to analyze the spindle length. Scale bar = 2 µm. (B) The total protein amounts of Ase1-3mcherry, Stu1-GFP and Tub1-CFP were analyzed by measuring signal intensities of the proteins at the metaphase spindle. Short metaphase spindles (1.6–2.0 µm) and long metaphase spindles (2.2–2.6 µm) were analyzed. Exact values of quantification and number of measured cells are listed in the appendix. The p-values were calculated using two-tailed unpaired t-tests. Standard deviations were calculated from two individual experiments. n.s. = not significant.

Since both Ase1 and Slk19 are non-essential proteins and both have a role for metaphase spindle stability, one could assume that those proteins are synthetically lethal. However, *Δslk19, Δase1* cells are viable (Figure 13C), supporting that the two proteins might work in the same pathway for stabilizing the mitotic spindle.

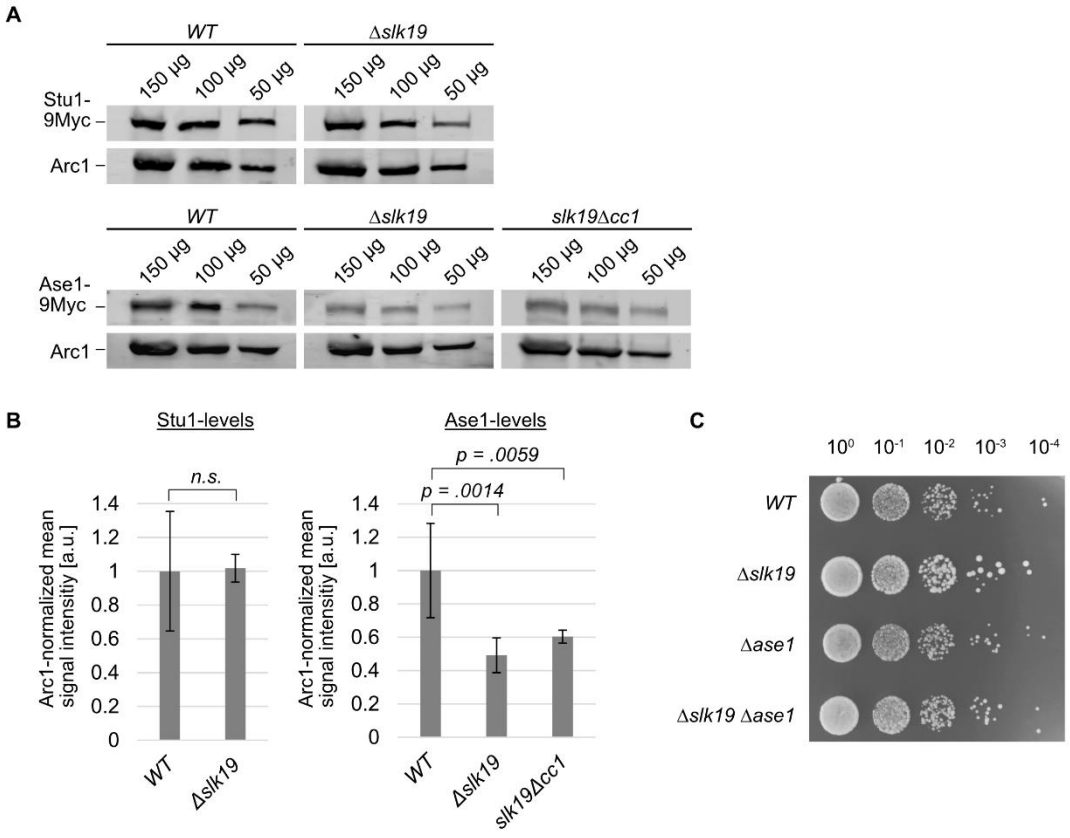

Figure 13: *Δslk19* and *slk19Δcc1* cells show reduced protein levels of Ase1 while Stu1 protein levels are not influenced by Slk19 deletion.

(A-C) Genotypes of used strains are described in Materials chapter. (A-B) Slk19Δcc1 was expressed from the endogenous promoter of *SLK19*. (A) Protein amounts of Stu1-9Myc or Ase1-9Myc in the indicated cell types were analyzed by Western blot analysis using whole cell extracts. Protein amounts were loaded in stepwise decreasing quantities to assure linearity (150 µg, 100 µg, 50 µg). Arc1 was detected as internal loading control. Proteins were detected by the LI-COR imaging system. (B) Quantification of protein levels showed unchanged Stu1-9Myc levels in *Δslk19* cells compared to *WT* cells. Ase1-9Myc levels were similarly reduced in *Δslk19* and *slk19Δcc1* cells. The p-values were calculated using two-tailed unpaired t-tests. Standard deviations were calculated from two individual experiments. Exact values of quantification are listed in the appendix. n.s. = not significant. (C) Slk19 and Ase1 are not synthetically lethal. Dot growth test with serial dilutions of respective yeast strains grown on YPD+3 plates, incubated for 2 days at 25°C.

4.2.6 Deletion of Slk19 or its cc1 domain leads to reduced Tub1 levels at the spindle center and altered binding of Stu1 and Ase1

The previous data suggest that Slk19 plays a role at the metaphase spindle overlaps via Ase1 and Stu1. *Δslk19* and *slk19Δcc1* cells showed short metaphase spindles and an increased number of unaligned nrMTs. Thus, the influence of Slk19 on the metaphase spindle integrity was further analyzed. For this, the Tub1-CFP signal intensity was measured along the metaphase spindle axis of *WT*, *Δslk19* and *slk19Δcc1* cells (Figure 14A, spindles with an average *WT* metaphase spindle length of 2.4 µm were measured). Furthermore, cross-section measurements of the Tub1-CFP signal were analyzed at the center of the metaphase spindle representing the region of ipMT overlaps (Figure 14B). The mean signal intensities are depicted as longitudinal or cross-section plots and show the average signal distributions of several measured spindles of the respective cell types (Figure 14A and B). The results presented in this chapter (Figure 14) are also published in Norell et al., 2021 (copyright:).

The results show that Tub1 signals are reduced in the spindle center in *Δslk19* cells (Figure 14A and B). Here, the mean maximum Tub1 value in the spindle center at the site of ipMT overlaps is significantly lower compared to *WT* (Figure 14B). The same effect could be observed in *slk19Δcc1* cells. This suggests that less MTs reach the middle of the spindle in *Δslk19* and *slk19Δcc1* cells and consequently less MT overlaps can be formed. Supportingly, re-integration of *SLK19* into the *LYS2*-locus of *Δslk19* cells could rescue the Tub1 signal intensity at the spindle center (Figure 14A and B) showing that this effect is indeed Slk19-dependent.

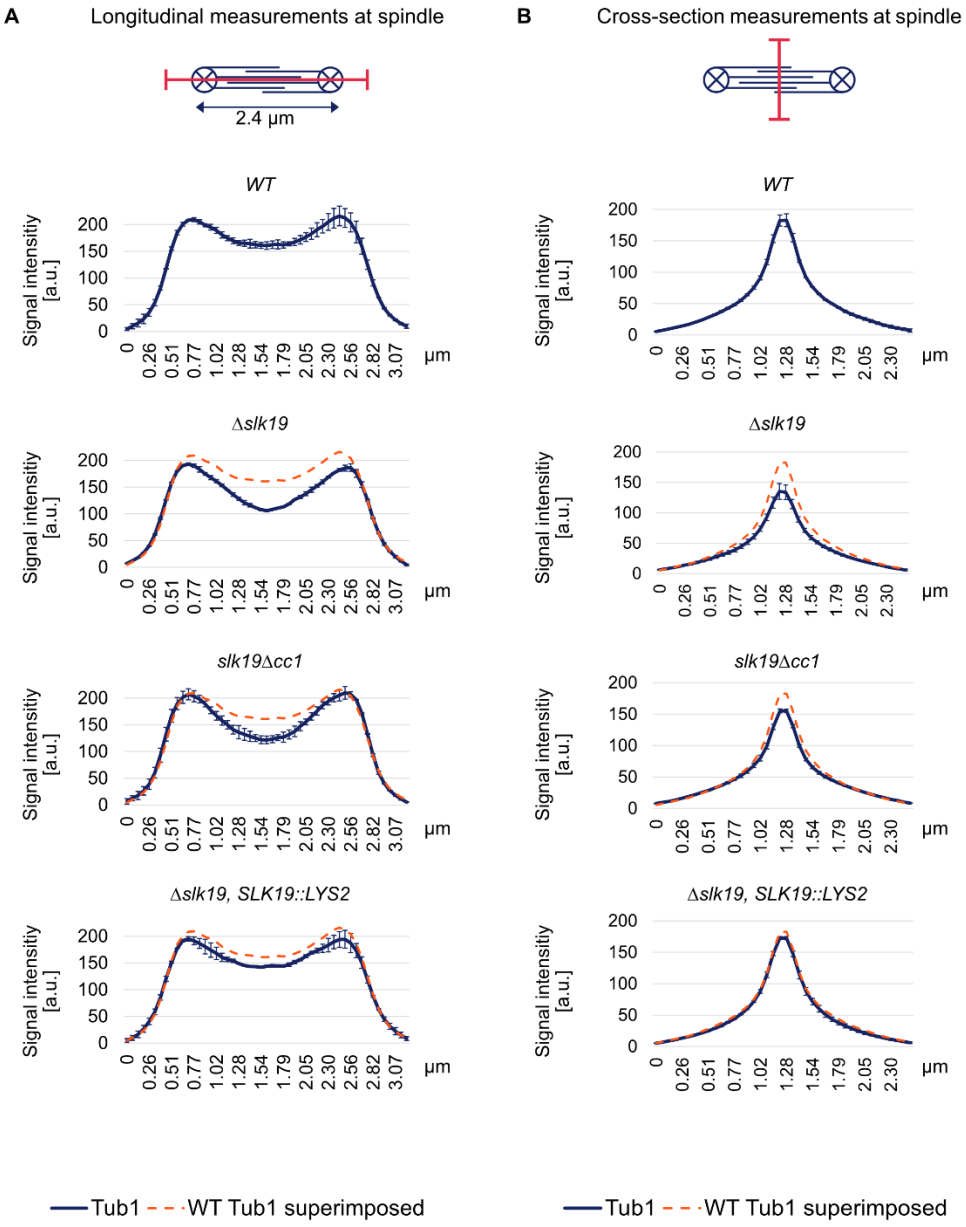

Figure 14: *Δslk19* and *slk19Δcc1* cells show reduced tubulin levels at the metaphase spindle center and re-integration of *SLK19* into the *LYS2*-locus can rescue this phenotype.

(A-B) RGB-plots were measured as described in Methods chapter. Genotypes of used strains are listed in Materials chapter. Slk19 constructs were expressed from the endogenous promoter of *SLK19*. Where indicated, *WT SLK19* was re-integrated into the *LYS2*-locus in *Δslk19* cells (*Δslk19, SLK19::LYS2)*. Standard deviations were calculated from two individual experiments. The *WT* Tub1 distribution (orange line) is superimposed in the respective RGB-plots for better comparison. (A) Longitudinal RGB-plots of metaphase spindles were measured in the indicated cell types showing the mean distribution and signal intensity of Tub1-CFP. RGB-plots shows the average of n>16 cells per experiment; 2.4 µm spindles were measured. (B) Cross-section RGB-plots were measured orthogonally to the spindle axis showing the mean Tub1-CFP signal at the metaphase spindle center. Mean Tub1-CFP curves were calculated for each experiment (n>80); 1.6–2.6 µm spindles were measured. Exact values of quantification and number of measured cells are listed in the appendix.

4.2.7 Slk19 might be required for an organized and synchronized MT overlap zone in metaphase and confers overlap-specificity of Stu1

Since Slk19 shows reduced Tub1 at the spindle center, the question arose whether the disturbed formation of ipMTs is also reflected in the distribution of Ase1 and Stu1. To analyze this, the distribution patterns of Ase1 and Stu1 along the metaphase spindle were observed. For better visualization, signal intensities were measured along the metaphase spindle axis of individual cells and normalized to values ranging from 0–1 (example cells with the most frequently observed phenotypes are shown in Figure 15A; spindles with a length of 2.4 µm were measured). The results presented in this chapter (Figure 15) are in part also published in Norell et al., 2021 (copyright: ©2021 Norell et al., CC BY-NC-SA 3.0, http://creativecommons.org/licenses/by-nc-sa/3.0).

In *WT* cells, both the Ase1 and the Stu1 signals showed a signal intensity maximum in the center of the spindles (centered peaks in *WT* cells, Figure 15A). Intriguingly, metaphase-arrested *Δslk19* cells showed an increased percentage of cells with an acentric signal intensity maximum for Ase1. Based on the assumption that Ase1 represents the localization of ipMT overlaps (with four ipMTs emerging from each SPB), the results suggests that *Δslk19* cells more often have acentric MT overlaps compared to *WT* cells (46.5 % of *Δslk19* cells show an acentric Ase1 maximum *versus* (*vs.*) 10,7 % in *WT* cells) (Figure 15B). Also for Stu1, an altered localization pattern along the metaphase spindles was observed in *Δslk19* cells compared to *WT* cells. In *WT* cells, Stu1 localized to the central part of the spindle, very close to the central localization of Ase1, which most probably indicates MT overlaps. In *Δslk19* cells, however, Stu1 was not restricted to the central part of the spindle anymore but was spread over the complete spindle with no defined maximum (Stu1 signal width almost as long as tubulin signal) (Figure 15B). Interestingly, a similar phenotype was observed in *stu1ΔCL* cells. Also here, Stu1ΔCL was spread out over the complete spindle, possibly because deletion of the CL domain leads to a loss of Slk19 interaction (Figure 15A and B). As mentioned above (chapter 4.2.4), Ase1 levels at the spindle were not reduced in *stu1ΔCL* cells meaning that the observed Stu1 mislocalization is probably not a secondary effect of decreased Ase1 levels but rather of lost Slk19 interaction.

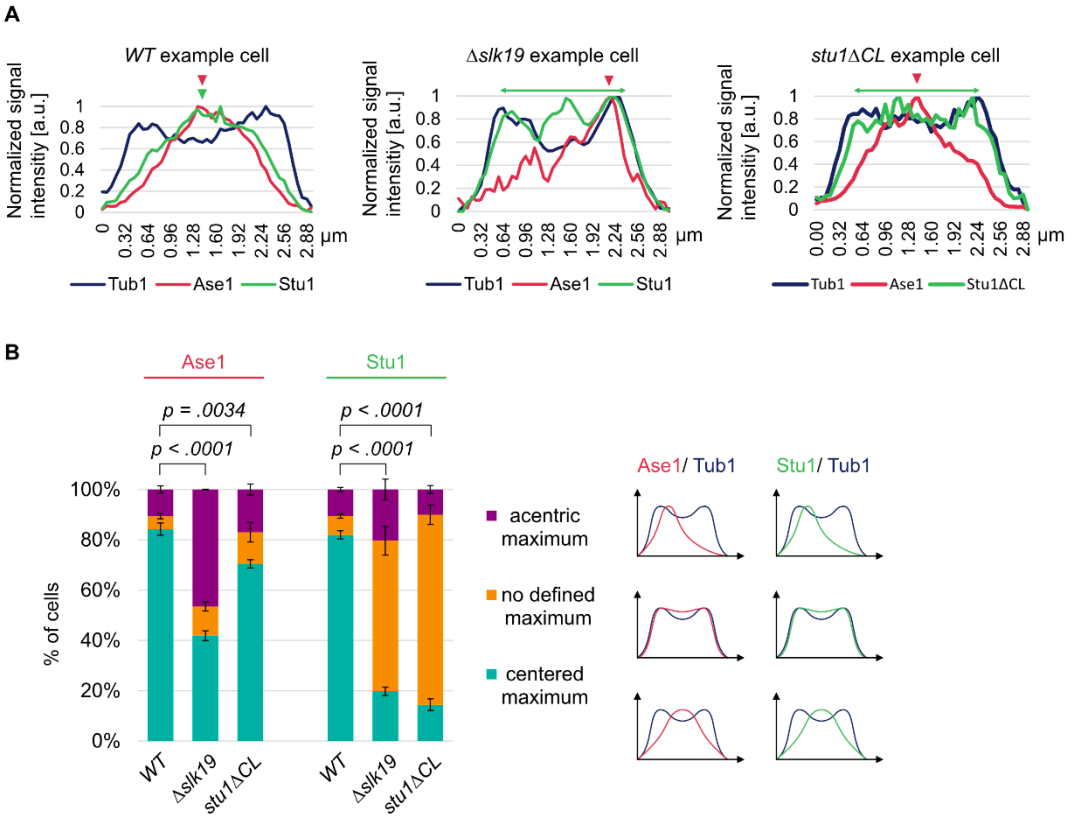

Figure 15: Slk19 deletion leads to more irregular overlaps as defined by Ase1 distribution and Stu1-Slk19 interaction is required for Stu1 overlap specificity at the metaphase spindle.

(A-B) Genotypes of used strains are described in Materials chapter. CL = C-terminal loop. (A) RGB-plots were measured as described in Methods chapter. Longitudinal RGB-plots of single cells are shown as examples for the most frequent phenotype of the respective cell type. Signal intensities of indicated proteins were measured and normalized to values ranging from 0–1; 2.4 µm spindles were measured. Arrowheads indicate a signal maximum; double-sided arrow indicates a broadened signal with no defined maximum. (B) Quantification of observed phenotypes regarding Ase1 and Stu1 distribution along the metaphase spindles in the indicated cell types. Phenotypes were categorized as illustrated. The p-values were calculated using chi-square tests. Standard deviations were calculated from two individual experiments. Exact values of quantification and number of measured cells are listed in the appendix.

Taken together, the results indicate that loss of Slk19 leads to more acentric MT overlaps as defined by the Ase1 signal intensity maximum. Furthermore, Slk19-Stu1 interaction seems to be required to focus Stu1 (directly or indirectly) at the overlap regions of the metaphase spindle. Without Slk19, Stu1 was still able to bind along the spindle MTs but its specificity for overlaps seemed diminished. The findings of increased acentric MT overlaps in *Δslk19* cells and decreased Tub1 signals at the spindle center (shown in previous chapter 4.2.6) might be the cause or consequence of reduced Ase1 and Stu1 levels or altered distribution patterns of these proteins at the spindle.

4.2.8 Slk19 binding to MTs is dependent on Stu1 or Ase1 *in vitro*, whereas Slk19Δcc1 is deficient in this binding

The obtained *in vivo* data (chapter 4.2.1 - 4.2.7) reveal interdependencies between Slk19 and the MAPs, Ase1 and Stu1, at the metaphase spindle. Slk19 is needed to enrich protein levels of Ase1 and Stu1 at the spindle and for a synchronized ipMT overlap organization. These findings give Slk19 an important role for spindle stability. To confirm these *in vivo* data, the interplay between Slk19 together with Stu1 and Ase1 was analyzed *in vitro* in the following. The proteins Stu1-CFP, Ase1-3mcherry, Slk19-GFP as well as Slk19Δcc1-GFP were purified from *S. cerevisiae* (Figure 16A) and used for MT binding assays. For this, the purified proteins were incubated with taxol stabilized immobilized MTs within perfusion chambers and binding was analyzed by fluorescence microscopy. The results presented in this chapter (Figure 16) are also published in Norell et al., 2021 (copyright: ©2021 Norell et al., CC BY-NC-SA 3.0, http://creativecommons.org/licenses/by-nc-sa/3.0).

As was shown before (Funk et al., 2014),(Schuyler et al., 2003),(Kapitein et al., 2008), Stu1 and Ase1 bound to MTs individually in the *in vitro* MT binding assay (Figure 16B). In contrast to Stu1 and Ase1, Slk19 was not able to bind to MTs individually under the used conditions (Figure 16B). However, when Slk19 was added to MTs with prebound Stu1 or Ase1, Slk19 efficiently bound to MTs and colocalized with Stu1 or Ase1 (Figure 16C). In contrast, Slk19Δcc1 could neither bind to MTs via Stu1 nor via Ase1 (Figure 16C). These result support the *in vivo* observations that the cc1 domain of Slk19 as well as the interaction with Stu1 and Ase1 is required for efficient Slk19 spindle binding (chapter 4.2.2 and 4.2.4).

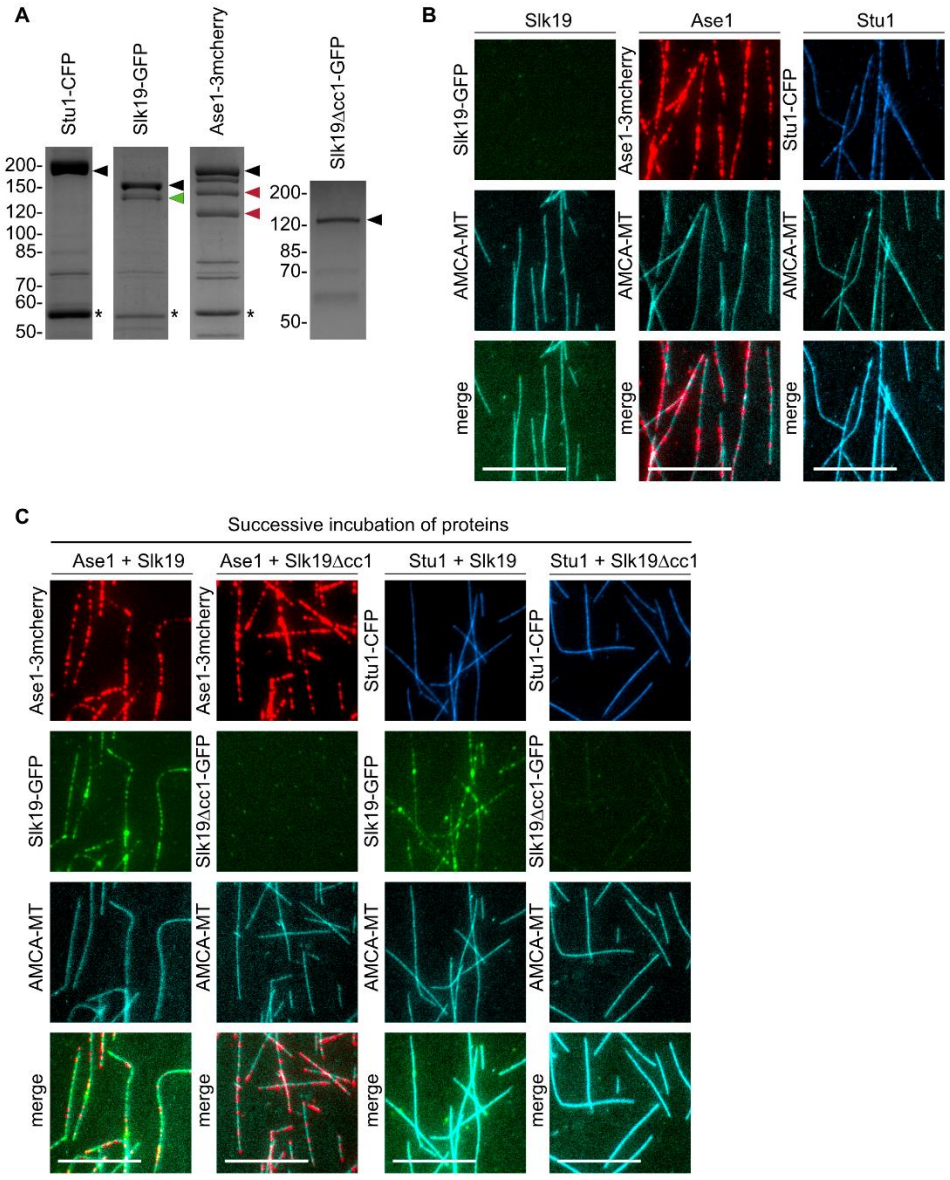

Figure 16: Slk19 binds to MTs via Ase1 and Stu1, while Slk19Δcc1 is deficient in this binding.

(A) Coomassie stained SDS-PAGE gels showing purified proteins used for MT binding and cross-linking assays. Proteins were purified via FLAG-tag. Stu1-CFP was overexpressed from the *GAL1*-promoter (cells arrest in metaphase due to overexpression). Ase1-3mcherry was overexpressed from the *GAL1*-promoter in metaphase-arrested cells. Slk19-GFP and Slk19Δcc1-GFP were expressed from the endogenous promoter of *SLK19* in metaphase-arrested cells. Genotypes of used strains are listed in Materials chapter. Black arrowheads indicate full-length proteins. Green arrowhead indicates the cleavage product of Slk19 (Sullivan et al., 2001). Red arrowheads indicate Ase1-2mcherry and Ase1-mcherry. Background bands are marked with asterisks and show eluted IgG antibodies. (B-C) MT polymerization and protein incubation was performed as described in Methods chapter. (B) Ase1 and Stu1 bound to MTs *in vitro* while Slk19 did not. Individual incubation of Slk19-GFP, Ase1-3mcherry, Stu1-CFP with immobilized AMCA-MTs. Scale bar = 10 µm. (C) Slk19 bound to MTs preincubated with Ase1 or Stu1, while Slk19Δcc1 did not. Immobilized AMCA-MTs were incubated with Ase1 or Stu1 and subsequently Slk19 or Slk19Δcc1 was added. Scale bar = 10 µm.

4.2.9 Slk19 can enhance MT binding of Stu1 and Ase1 *in vitro*

Since Ase1 was strongly and Stu1 moderately reduced in *Δslk19* cells *in vivo* (chapter 4.2.5), the question arose whether Slk19 has an effect on the binding efficiency of Ase1 and/or Stu1. This was analyzed *in vitro* by incubating equal quantities of Ase1 or Stu1 alone or with premixed Slk19. The latter resulted in enriched binding at the MTs compared to the single proteins (Figure 17A and B). Thereby, Ase1 showed a more dramatic increase with Slk19 (3.57-fold) compared to Stu1 (1.66-fold) reflecting the situation *in vivo* (also here Ase1 amounts at the spindle are more drastically increased by Slk19 compared to Stu1).

Taken together, the presence of Slk19 seems to increase the amount of Stu1 and Ase1 at MTs not only *in vivo* but also *in vitro*. The results presented in this chapter (Figure 17) are also published in Norell et al., 2021 (copyright: ©2021 Norell et al., CC BY-NC-SA 3.0, http://creativecommons.org/licenses/by-nc-sa/3.0).

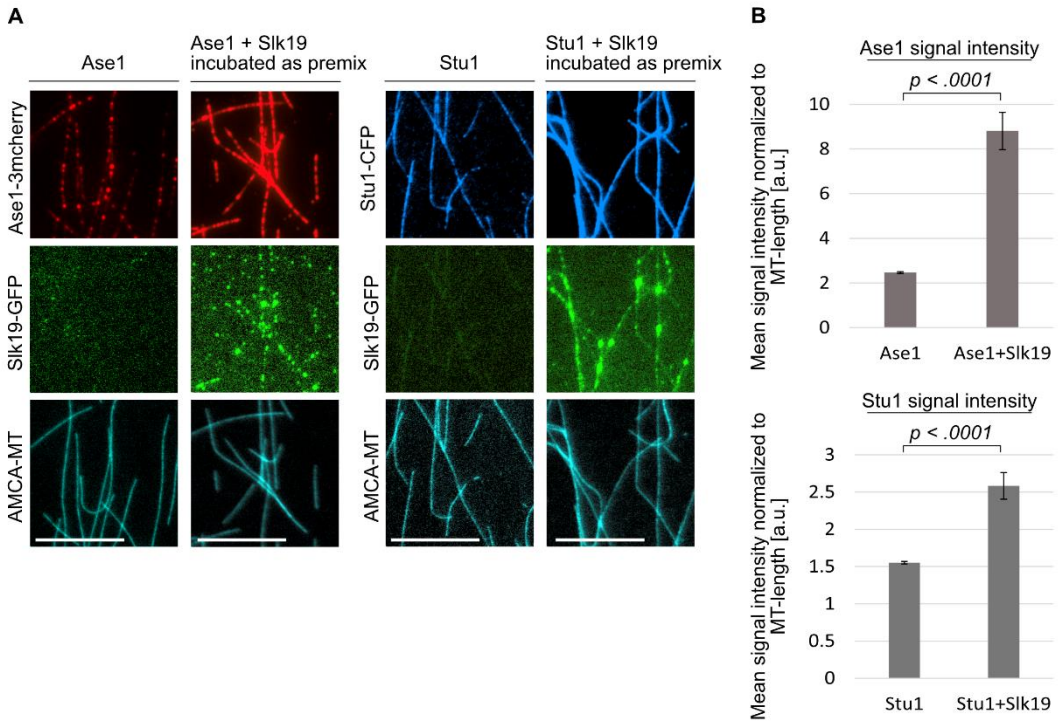

Figure 17: Slk19 amplifies Ase1 and Stu1 binding to MTs *in vitro*.

(A) MT polymerization and protein incubation was performed as described in Methods chapter. Equal amounts of Ase1-3mcherry and Stu1-CFP were incubated with immobilized AMCA-MTs individually or as premix with Slk19. Scale bar = 10 µm. (B) Quantification of Ase1-3mcherry and Stu1-CFP protein amounts based on signal intensity measurements at the MTs (background subtracted). Slk19 amplified the binding of Ase1 and Stu1 to MTs *in vitro*. Exact values of quantifications and number of measurements are listed in the appendix. The p-values were calculated using two-tailed unpaired t-tests. Standard deviations were calculated from two individual experiments.

4.2.10 Slk19 can enhance MT crosslinking via Stu1 and Ase1 *in vitro*, while Slk19Δcc1 can not

The *in vivo* data (chapter 4.2.1 - 4.2.7) strongly indicate that Slk19 plays a role for ipMT overlap integrity and organization. These results raised the question, whether Slk19 might enhance the crosslinking of ipMTs, e.g. by enriching the MT-crosslinking proteins Ase1 and Stu1 at the spindle overlaps. To analyze the MT crosslinking efficiency, *in vitro* MT crosslinking assays were performed using immobilized biotinylated Rho-labeled MTs (Rho-MTs) and mobile unbiotinylated AMCA-MTs (illustrated in Figure 18).

For the MT crosslinking assays, the purified proteins Ase1-3mcherry, Stu1-CFP, Slk19-GFP and Slk19Δcc1-GFP were used (see Figure 16A). Crosslinking efficiency was measured as sum of all overlap-lengths between mobile AMCA-MTs and Rho-MTs, divided by the sum of all length of Rho-MTs. The crosslinking efficiency of each individual protein itself and in combination with Slk19 or Slk19Δcc1 was measured. The contents presented in this chapter (Figure 18, Figure 19A-B, Figure 20) are in part also published in Norell et al., 2021 (copyright: ©2021 Norell et al., CC BY-NC-SA 3.0, http://creativecommons.org/licenses/by-nc-sa/3.0).

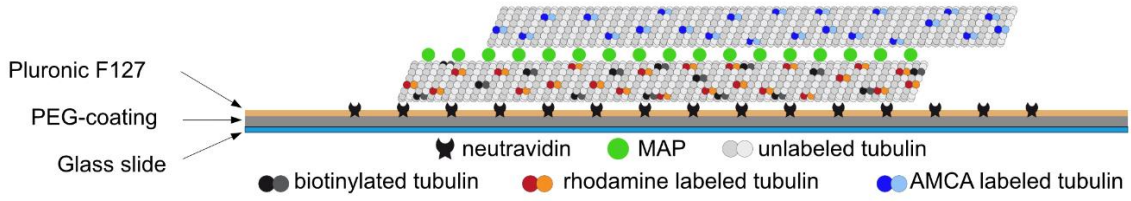

Figure 18: Schematic illustration of experimental design for *in vitro* MT crosslinking assay.

Image adapted from (Funk et al., 2014),(Norell et al., 2021). Glass slides were cleaned, PEGylated, neutravidin coated and passivated with Pluronic® F-127. Biotinylated Rho-MTs were immobilized on a coverslip by binding to neutravidin. Microtubule-associated proteins were bound to immobilized Rho-MTs and the ability of crosslinking mobile, unbiotinylated AMCA-MTs was analyzed.

Ase1 and Stu1 were shown to have crosslinking functions by themselves (Figure 19A and B) (Schuyler et al., 2003),(Funk et al., 2014). In contrast, Slk19 alone cannot bind to MTs by itself and thus is also not sufficient for crosslinking (Figure 19A and B). When incubating Stu1 together with Slk19, a 2.7-fold increase in crosslinking was observed, while Ase1 together with Slk19 showed a 3.0-fold increase in crosslinking. In accordance with the *in vivo* data, Slk19Δcc1 did not show an increase in crosslinking for Ase1 or for Stu1. This again supports the idea that the cc1 domain of Slk19 is especially important for its spindle function. The incubation of all three proteins together (Slk19+Stu1+Ase1) resulted in a 2.3-fold increase in crosslinking efficiency (compared to Ase1+Stu1). This result confirms that Slk19 increases crosslinking efficiency of Ase1 and Stu1, but also indicates that there is no

further/additional boost in crosslinking by the potential formation of a trimeric complex (Ase1-Slk19-Stu1). However, a possibly limited Slk19 protein amount might have been a limiting factor for such an observation.

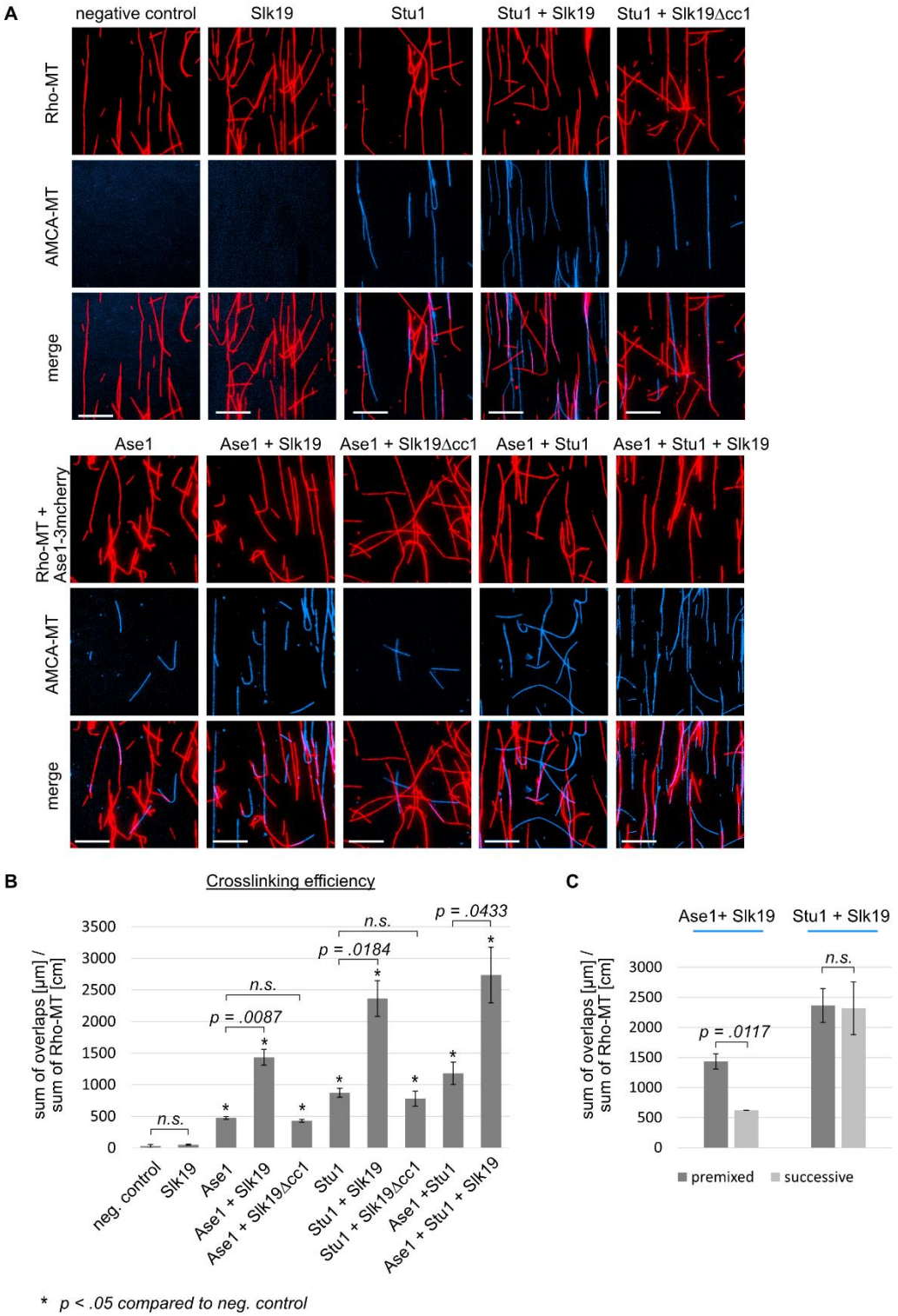

Figure 19: Slk19 enhances crosslinking efficiency of Ase1 and Stu1, while Slk19Δcc1 did not.

(A) Immobilized Rho-MTs were incubated with indicated proteins or premixed protein combinations for analysis of crosslinking efficiency of mobile AMCA-MTs. MT polymerization and protein incubation was performed as described in Methods chapter. Micrographs show representative images of crosslinking assays. Scale bar = 10 µm. (B-C) The p-values were calculated using two-tailed unpaired t-tests. Standard deviations were calculated from two individual experiments. Exact values of quantifications are listed in the appendix. n.s. = not significant. (B) Quantification of crosslinking efficiency as defined by the sum of all overlap lengths with mobile AMCA-MTs divided by the sum of all lengths of immobilized Rho-MTs. (C) Enhanced crosslinking ability of Ase1 via Slk19 was only observed when the proteins were incubated as premix before adding mobile AMCA-MTs. For Stu1 both incubation methods (premixed or successive incubation of Stu1 and Slk19) showed equally strong enhancement of crosslinking.

Interestingly, when incubating the proteins successively (e.g. Stu1 was first incubated with the MTs, then the excess protein was washed off and then Slk19 was added), Stu1 still showed the same increase in crosslinking as when premixed, while Ase1 did not (Figure 19B). This could indicate that the mode of operandi by which Slk19 might enhance crosslinking is different for Ase1 and Stu1. For Ase1, a preincubation with Slk19 might be the prerequisite to enhance its binding to the MTs. This Ase1 enrichment, in turn, might constitute the basis for increased crosslinking efficiency.

In the case of Stu1, the increased crosslinking efficiency could (additionally) be based on a different method: Slk19 might interact with the prebound Stu1 and thus might induce a Stu1 conformation more favorable for MT crosslinking. In accordance with this hypothesis is the finding that a premix of Ase1+Slk19 resulted in a stronger effect for protein enrichment at MTs than Stu1+Slk19 (compared to the binding of the individual protein: Ase1 or Stu1 respectively) (Figure17A and B). Although Slk19 also increased Stu1 amounts at MTs when incubated as premix (Figure17A and B), an additional increase in crosslinking was not observed compared to successive protein incubation (Figure 19C). Possibly this effect was already fully titrated by high Stu1 amounts.

Taken together, the combined *in vivo* and *in vitro* data suggest a current model where Slk19 leads to increased binding of Ase1 and Stu1 to the overlaps of ipMTs. The putative tetrameric structure of Slk19 gives it the optimal requirements for multiple interactions at the overlaps and thus, to interact with several Ase1 and/or Stu1 molecules at the same time. The idea of how this might look like on a molecular level is depicted in the model shown in Figure 20.

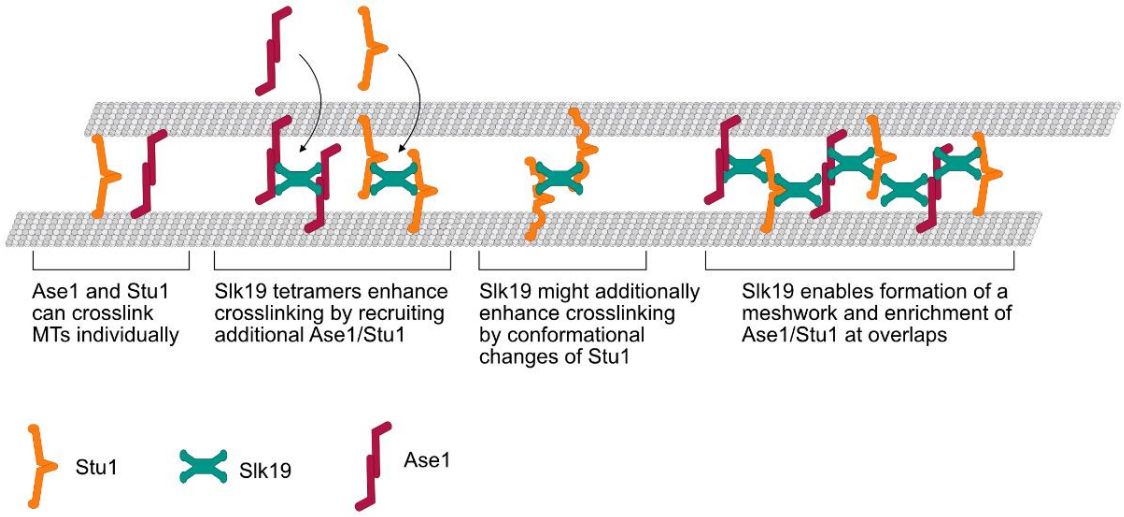

Figure 20: Model how Slk19 might enhance crosslinking and stabilize ipMTs overlaps by enriching Ase1 and Stu1 at spindle overlaps.

The model schematically illustrates how Slk19 might enhance crosslinking and metaphase spindle stabilization. Ase1 and Stu1 can crosslink MTs individually, however, the Slk19 tetramer might enhance the binding of Ase1 and Stu1 at the MT overlaps. Thus, a meshwork of interacting proteins might be generated at the metaphase spindle overlaps that increases crosslinking efficiency and spindle stabilization. Additionally, Slk19 might induce conformational changes of Stu1 that further support its crosslinking function. Adapted from (Norell et al., 2021).

4.2.11 A delicate equilibrium of Stu1 and Slk19 might be required for the formation of bipolar spindles

To find out whether Stu1 and Slk19 are required in defined quantities to fulfil their function in the protein meshwork at the overlaps (see model Figure 20), it was analyzed which effect an overexpression of these proteins has on the spindle.

Stu1 overexpression (Stu1-OE) led to a metaphase arrest with shorter spindles compared to *WT* cells probably due to increased MT crosslinking (shown in Funk et al., 2014) (phenotype of Stu1-OE cells shown in Figure 21A, a). In addition to that, Stu1-OE led to more cells with monopolar oriented spindles compared to *WT* cells (Figure 21A, a-b, Figure 21B). Slk19 deletion in Stu1-overexpressing cells further increased the proportion of cells with monopolar spindles (Figure 21B). These results might indicate that Stu1-Slk19 interaction at the overlaps (Stu1-Slk19 meshwork indicated in model depicted in Figure 20) might facilitate the Stu1 function of antiparallel MT bundling. Excess of Stu1 at the spindle might thus lead to bundling of parallel instead of antiparallel MTs due to unbalanced Stu1-Slk19 levels. Deletion of Slk19 alone was not sufficient to increase the formation of monopolar spindles (Figure 21B). However, *Δslk19* led to an increased number of unaligned nuclear MTs (shown in chapter 4.2.3) and lost overlap specificity of Stu1 in metaphase-arrested cells

(see chapter 4.2.7). Thus, additional Stu1-OE in these *Δslk19* cells (with compromised spindles) might further drive the formation of monopolar spindles leading to the observed phenotype.

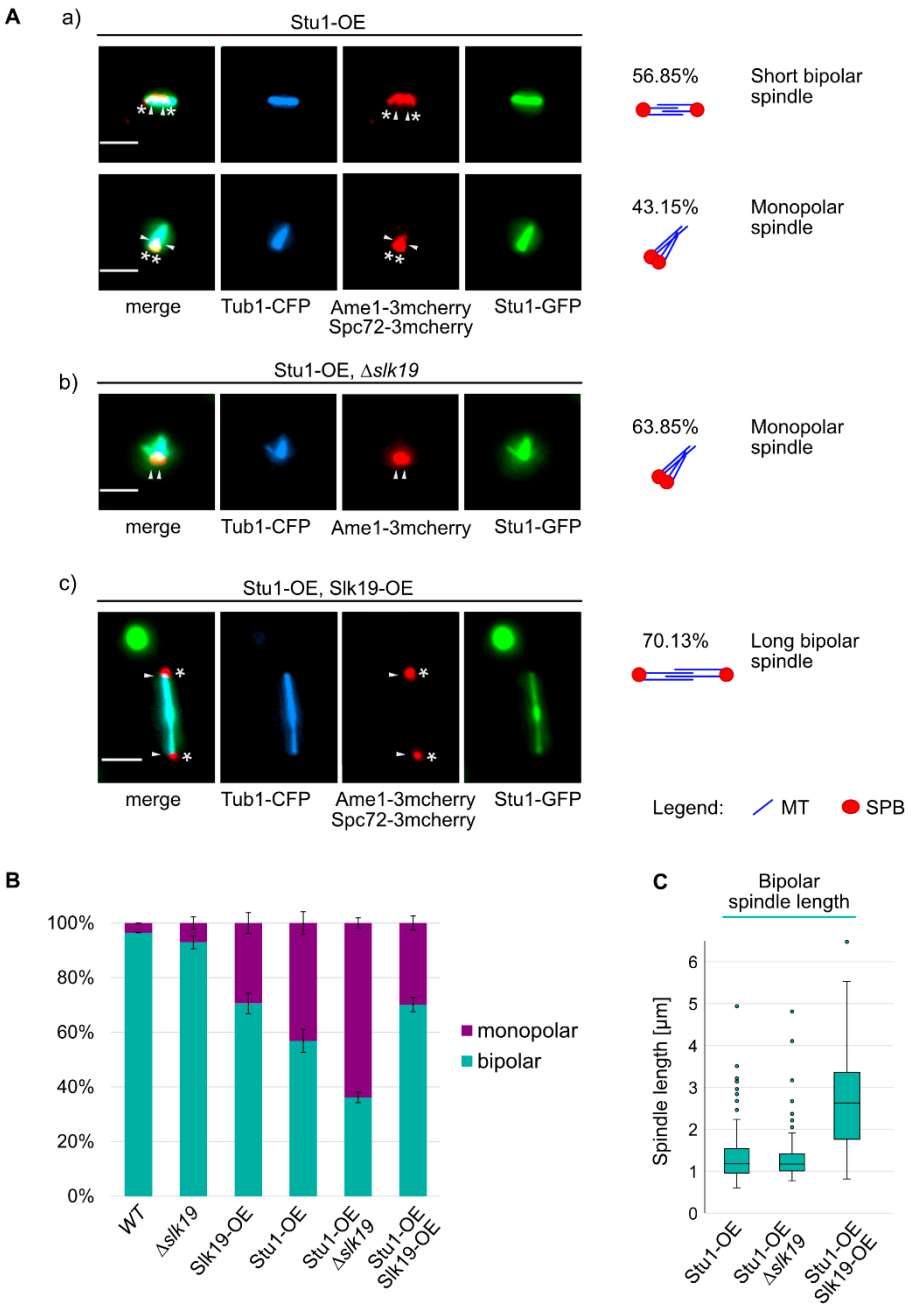

Figure 21: Slk19-OE partially rescues monopolar spindle formation in Stu1-OE cells, while Δ*slk19* aggravates the phenotype.

(A-C) G1-arrested cells were released into galactose containing medium for induced overexpression of Stu1, Slk19 or both (*GAL1*-promoter) for 4 h. Only large-budded cells were analyzed. Genotypes of used strains are listed in Materials chapter. (A-B) Phenotypes with exact numbers of counted cells are listed in the appendix. (A) White arrowheads indicate position of KTs, asterisks indicate position

of spindle pole bodies (SPBs). Spc72-CFP marks SPBs, Tub1-CFP marks microtubules, Ame1-3mcherry marks kinetochores. The indicated percentages represent the frequency of the shown phenotype among all counted cells. (a) Increased formation of monopolar spindles in cells with Stu1 overexpression (Stu1-OE). Phenotype was (b) aggravated by simultaneous Slk19 deletion (Δ*slk19*) and (c) partially rescued by Slk19 overexpression (Slk19-OE). (B) Quantification of phenotypes of indicated cell types. Standard deviations were calculated from two individual experiments. (C) Monopolar and bipolar spindle lengths were measured in the indicated cell types. Exact values of quantification and number of measured cells are listed in the appendix.

To analyze whether balanced Stu1-Slk19 amounts are required for bipolar spindle assembly, it was attempted to restore the balance in Stu1-OE cells by Slk19-overexpression (Slk19-OE). Interestingly, this simultaneous overexpression could partially rescue the formation of bipolar spindles to some extent in comparison to Stu1-OE (Figure 21A, c and Figure 21B). Also, simultaneous overexpression of Slk19 and Stu1 could rescue the short spindle phenotype of Stu1-OE cells (Figure 21C). Surprisingly, these spindles were often even longer than average *WT* spindles (Figure 21A and C, for *WT* see chapter 4.3.1).

Notably, overexpression of Slk19 led to large clusters of Slk19 within the nucleus (Figure 22, a). Intriguingly, these Slk19 clusters were functional for the recruitment and binding of Stu1 as seen by colocalization at the clusters in Figure 22, d and by the Stu1 localization in Figure 11A, c. The perinucleolar localization of these clusters (as assessed by its localization relative to Cdc14; see Figure 22, b) might reflect an intranuclear quality control compartment that is dependent on the protein Btn2 (S. B. Miller et al., 2015). In this case, deletion of Btn2 should resolve these clusters (S. B. Miller et al., 2015). However, the Slk19 clusters were still present in *Δbtn2* cells (Figure 22, c). Moreover, the cluster formation was also not dependent on Stu1 as seen in *'Δstu1'* cells (Figure 22, e). The exact mechanisms behind the cluster formation and the increase in bipolar spindle length, when overexpressing Stu1 and Slk19 simultaneously, is so far unknown and is discussed later (see Discussion chapter).

Taken together, it can be concluded that balanced Stu1 and Slk19 protein levels are critical for the formation of a bipolar spindle.

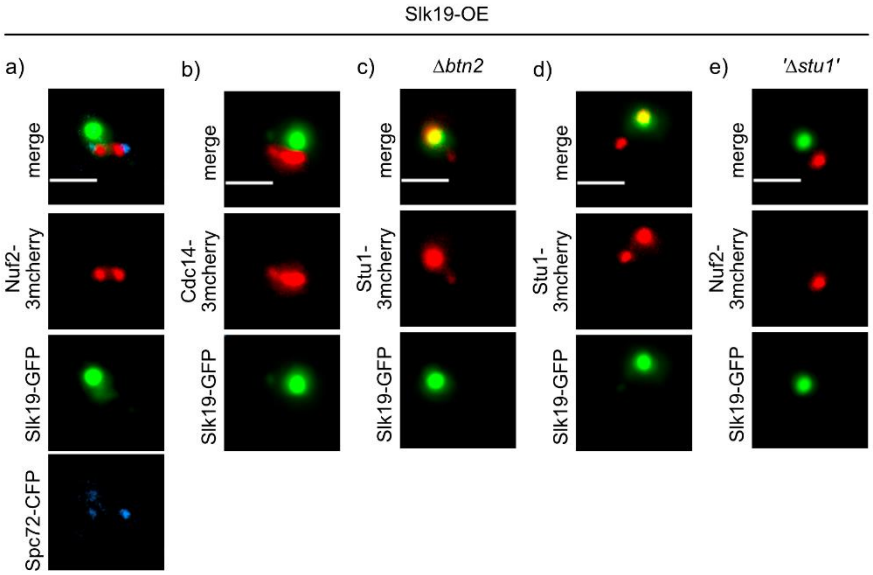

Figure 22: Slk19-OE leads to peri-nucleolar accumulations functional for Stu1 recruitment.

Cells were arrested in G1 and released into galactose-containing medium for induced overexpression of Slk19-GFP (*GAL1*-promoter) for 4h. Spc72-CFP marks spindle pole bodies, Nuf2-3mcherry marks kinetochores. Genotypes of used strains are described in Materials chapter. OE = overexpression. (a) Slk19-OE leads to accumulations within the nucleus. (b) In cells with Slk19-OE, Slk19-GFP clusters are positioned close to the nucleolus visualized by Cdc14-3mcherry. (c) Slk19-GFP clusters are still present in *Δbtn2* cells. (d) Stu1-3mcherry colocalizes with Slk19-GFP clusters in Slk19-OE cells. (e) Conditional depletion of Stu1 (*'Δstu1'*) was performed by IAA-treatment (AID). The formation of Slk19-GFP clusters was still possible in Slk19-OE *'Δstu1' cells.*

4.2.12 Slk19 did not change preference of Ase1 and Stu1 for antiparallel MT crosslinking

The previous *in vivo* data indicate that Slk19 might not only play a role in enhancing crosslinking but might also change the preference for antiparallel *vs.* parallel MT crosslinking (Figure 21B, chapter 4.2.11). For this reason, the directionality of crosslinked MTs was analyzed *in vitro* by using polarity marked MTs. It was shown that Ase1 (and its homologues) already possesses an intrinsic preference for antiparallel MT crosslinking (Schuyler et al., 2003), (Loïodice et al., 2005),(Janson et al., 2007),(Subramanian et al., 2010). This could be verified, and antiparallel crosslinking was observed in 71.2 % of the counted crosslinked MT pairs (Figure 23). The preferred directionality of MT crosslinking was also analyzed for Stu1. Unlike Ase1, Stu1 did not show a preference for antiparallel crosslinking by itself (antiparallel and parallel MT crosslinking occurred in approximately 50% of the cases; see Figure 23). When Ase1 or Stu1 were incubated together with Slk19, no increase in antiparallel MT crosslinking was observed (Figure 23). However, the experiments could be possibly optimized by varying the protein amounts of the used proteins e.g. increasing the used Slk19 amount.

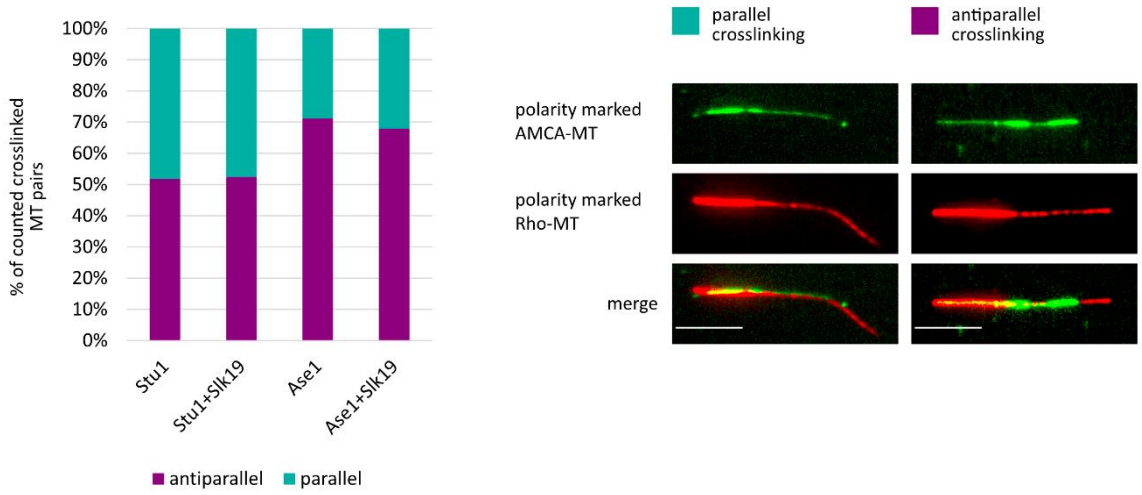

Figure 23: Slk19 did not increase the preference of Ase1 or Stu1 for antiparallel compared to parallel crosslinking.

Polarity marked AMCA- and Rho-MTs were created as described in Methods chapter. Immobilized polarity marked Rho-MTs were incubated with the indicated protein(s) and mobile polarity marked AMCA-MTs were added for crosslinking analysis. The directionality of crosslinked AMCA- and Rho-MT pairs were evaluated for the individual proteins, Stu1 or Ase1, compared to the respective premixed proteins, Slk19+Stu1 or Slk19+Ase1. Exact values of quantification and number of counted crosslinked MT pairs are listed in the appendix. Scale bar = 5 µm. Rho = rhodamine. MT = microtubule. Proteins were purified and incubated as described in Methods chapter.

4.3 Slk19 localization at the metaphase spindle might be tension regulated

4.3.1 Enhanced Slk19 localization to the spindle overlaps correlates with high tension at the KTs

It was shown (in chapter 4.2.1, Figure 7) that Slk19 localization is lost at the KTs in Spc105-depleted cells and that the Slk19 signal at the spindle center was increased compared to *WT* cells. One possible mentioned explanation for this observation might be that an increased free pool of Slk19 is available (upon elimination of its binding site at the KT) that can then bind to the alternative Slk19 binding site at the spindle overlaps.

Intriguingly, however, it was observed that in '*Δspc105*' cells the mean kMT length was significantly shorter, while the mean inter-KT distance was increased compared to *WT* cells (Figure 24A). The mean spindle length was only slightly reduced in '*Δspc105*' cells compared to *WT* cells (Figure 24A). Hence, the KTs most likely experience more tension in '*Δspc105*' compared to *WT* cells. The question arose whether increased tension at the KTs in metaphase might trigger a regulatory pathway to recruit Slk19 to the spindle e.g. to

provide the higher spindle stability that is needed under conditions with increased tension. To explore this hypothesis and to exclude the possibility that the increased signal at the spindle is only due to an increased pool of free Slk19, a yeast strain was used that exhibited increased tension at the KTs without disturbing the Slk19 localization at the KTs.

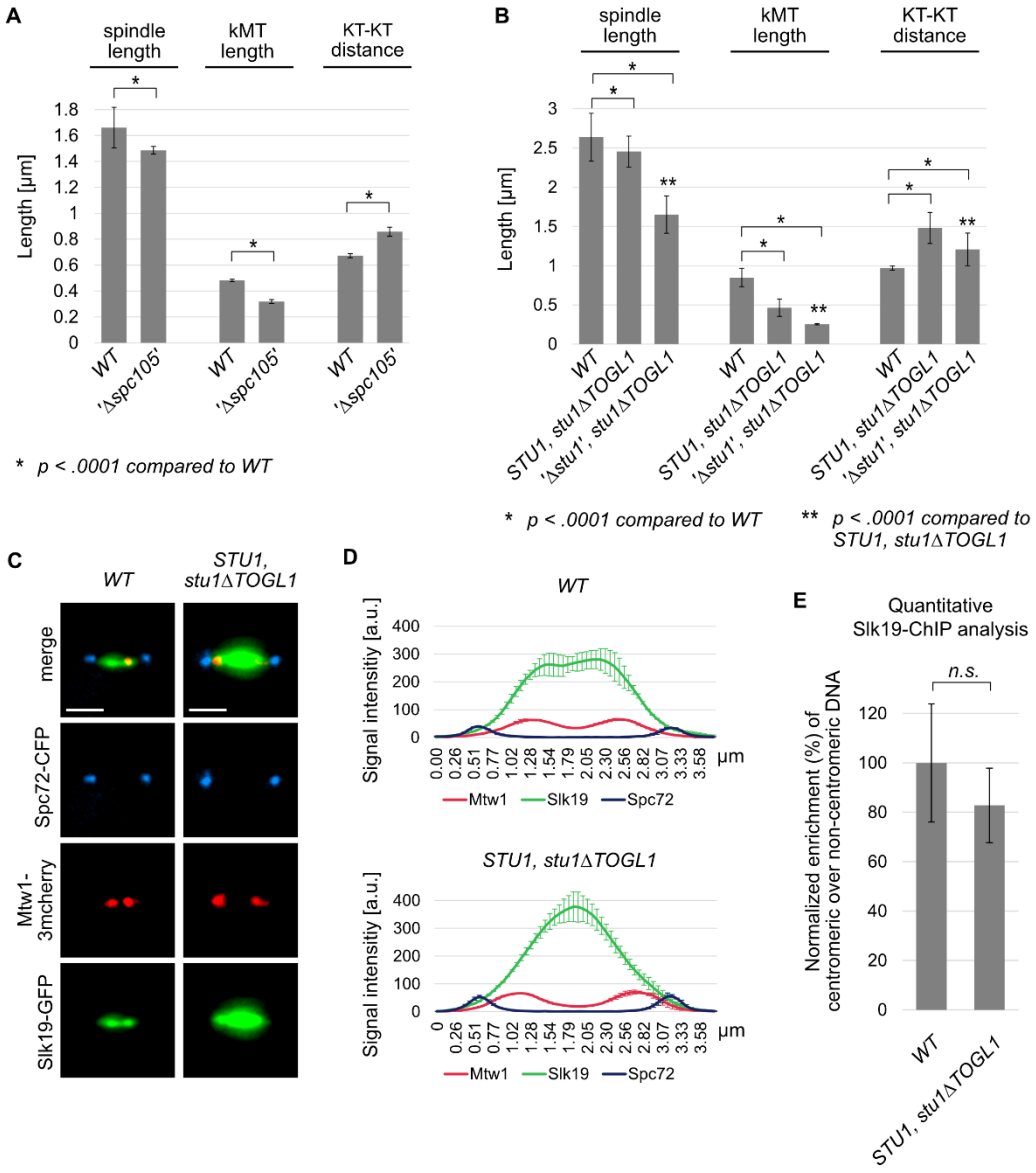

Figure 24: High tension at KTs correlates with increased Slk19 signal at the spindle center.

(A-E) Cells were metaphase-arrested by Cdc20-depletion (*GAL1*- or *MET25*-promoter shut-off). Depletion of Spc105 (*'Δspc105'*) or Stu1 (*'Δstu1'*) was performed by IAA-treatment (AID) during metaphase arrest. Genotypes of used strains are described in Materials chapter. Shortened kMTs and increased KT-KT distances were interpreted as indication for increased tension at KTs. (A-B and D-E) Exact values of quantifications and number of measured cells are listed in the appendix. (A-B) Spindle length: distance between two opposing SPBs. KT-KT distance: distance between the two KT-clusters of one cell. kMT length: distance from one KT-cluster to its connected SPB. The p-values were calculated using two-tailed unpaired t-tests. (A) Metaphase-arrested *'Δspc105'* cells

showed slightly shortened spindle lengths, shorter kMTs and increased KT-KT distances compared to *WT*. (B) Metaphase-arrested *STU1, stu1ΔTOGL1* cells showed slightly shortened spindle lengths, while *'Δstu1', stu1ΔTOGL1* cells showed a strong reduction in spindle length compared to *WT*. Both *STU1, stu1ΔTOGL1* and *'Δstu1', stu1ΔTOGL1* cells showed shorter kMTs and increased KT-KT distances compared to *WT*. (C-D) Slk19 localized strongly to the spindle center in *STU1, stu1ΔTOGL1* cells. Spc72-CFP marks spindle pole bodies, Mtw1-3mcherry marks kinetochores. (C) Scale bar = 2 µm. (D) RGB-plots were measured as described in Methods. Longitudinal RGB-plots of metaphase spindles measured in *WT* and *STU1, stu1ΔTOGL1* cells showing the mean distribution and signal intensity of indicated proteins. RGB-plots show the average of several cells per experiment; 3 µm spindles were measured. Exact numbers of measured cells are listed in the appendix. Error bars show standard deviations calculated from two independent experiments. (E) qPCR analysis of Slk19-ChIP showed no significant difference in centromeric Slk19 enrichment in *STU1, stu1ΔTOGL1* cells compared to *WT*. The mean enrichment of centromeric DNA (*CEN3*) was calculated in relation to the non-centromeric DNA (*PHO5*) and the values were normalized (WT represents 100%). The p-value was calculated using a two-tailed unpaired t-test. Standard deviations were calculated from two biological replicates of the ChIP assays, each with three technical replicates for the qPCR.

The TOGL1 domain is the KT localization domain of Stu1 (Funk et al., 2014). Since Stu1 binding to the KTs stabilizes kMTs, *stu1ΔTOGL1* cells possess significantly reduced kMT lengths compared to *WT* cells (Funk et al., 2014). Despite that, the spindles are shorter in those cells and the inter-KT distances are increased compared to *WT* cells (Funk et al., 2014). This indicates that *stu1ΔTOGL1* cells most likely have higher tension at the KTs compared to *WT* cells. Interestingly, metaphase-arrested *stu1ΔTOGL1* cells that additionally carry *WT STU1* in the background show a dominant *stu1ΔTOGL1* phenotype in regard to shortened KT-MTs and increased inter-KT distances (compared to *WT)*. However, those cells have longer metaphase spindles than *stu1ΔTOGL1* cells (almost as long as *WT* spindles) (Figure 24B and D). This most likely leads to an even higher increase in tension at the KTs and spindles than in *stu1ΔTOGL1* cells. Therefore, this strain was used to analyze the Slk19 localizations. Slk19 localizes strongly to the middle region of the spindle in those cells (Figure 24C) reminiscent of the Slk19 localization in Spc105-depleted cells (for comparison see chapter 4.2.1, Figure 7).

Importantly, the KT localization of Slk19 in *STU1*, *stu1ΔTOGL1* cells was very similar to *WT* cells. This could not be deduced from the micrographs due to the strong spindle signal, however, the quantitative ChIP analysis (by qPCR) clearly proved that point. This showed that the centromeric enrichment of Slk19 does not significantly differ between *STU1*, *stu1ΔTOGL1* and *WT* cells (Figure 24E).

Taken together, these results again show a correlation of high tension and increased Slk19 signal at the metaphase spindle center. Since the KT localization of Slk19 was still intact in *STU1*, *stu1ΔTOGL1* cells, the increased Slk19 spindle localization was not caused by abolished KT interaction as questioned in the Spc105-depleted cells.

4.3.2 Slk19 might translocate to the metaphase spindle when tension is produced after bipolar spindle establishment

The previous results (chapter 4.3.1) showed a correlation of increased Slk19 spindle binding in cells with increased KT tension. If this spindle localization is regulated by tension at KTs and spindles, then low or no tension at the KTs should lead to diminished Slk19 localization at the spindle. There are two ways to eliminate/reduce tension: (1) Conditional depletion of the cohesion subunit Scc1 (*'Δscc1'*): Sister-KTs are not hold together anymore and no tension can be established at the KTs and the spindles. (2) Deletion of the N-terminal tail of Ndc80 (*ndc80Δ1-116*): Mutants lacking the Ndc80 N-terminal tail have strongly reduced tension at the KTs (Suzuki et al., 2016).

To test the first condition, Slk19 localization was analyzed in cells where Scc1 was depleted in G1 phase of the cell cycle. Subsequently cells were arrested in metaphase (by Cdc20 depletion) without tension at the KTs. In metaphase-arrested '*Δscc1*' cells, the spindles were longer than in *WT* and the KTs were observed in proximity to the SPBs (atKTs close to SPB are marked with asterisks in Figure 25A): Both of these observations result from the depletion of the cohesion subunit and the consequential relief in tension.

In 60 % of the cells, Slk19 was sequestered at uaKTs (in 8 % of those cells, Slk19 sequestering was observed but the uaKTs could not be visualized). The uaKTs were most probably produced due to the lack of tension as described in introduction chapter 1.4.2.2 (Biggins et al., 1999),(Cheeseman, Drubin, et al., 2002),(T. U. Tanaka et al., 2002),(Akiyoshi et al., 2010). Since the sequestering at uaKTs interferes with the binding of Slk19 to the spindle and with the spindle integrity, these cells were not usable for the purpose of analyzing the Slk19 spindle localization. Interestingly, the other 40% of the '*Δscc1*' cells showed no uaKTs and thus, only these cells were important for the analysis of Slk19 localization. These cells showed Slk19 mainly at the atKTs but barely at the metaphase spindle (Figure 25A).

In addition to this, Slk19 localization was analyzed in a *stu1ΔTOGL1, 'Δscc1'* strain to prevent sequestering. In this strain, the increased tension at the KTs (as proposed for *stu1ΔTOGL1* cells) was resolved by Scc1 depletion. Here, two distinct situations were compared with each other: (1) Scc1 was depleted in G1 and cells were arrested in metaphase (by Cdc20 depletion) under a no tension situation; (2) Cells were arrested in metaphase (by Cdc20 depletion) with bi-oriented KTs and established tension and then Scc1 was depleted. In the first condition, when Scc1 was depleted in G1 and cells arrested in metaphase without tension at the KTs, Slk19 was seen only at KTs in the majority of the cells (72 %). Intriguingly, in the second condition, Slk19 was seen weakly at the center of the metaphase spindles in cells where tension was established prior to Scc1 depletion (in over 73 % of the cells) (Figure 25B, b). This might indicate that Slk19 stays at the overlaps after tension is

lost or that Slk19 spindle localization is not immediately resolved but only over a certain time (further possible explanations see also Discussion chapter).

In conclusion, these results indicate that Slk19 localizes to the metaphase spindle overlaps after bi-orientation and after establishment of tension at the KTs has occurred.

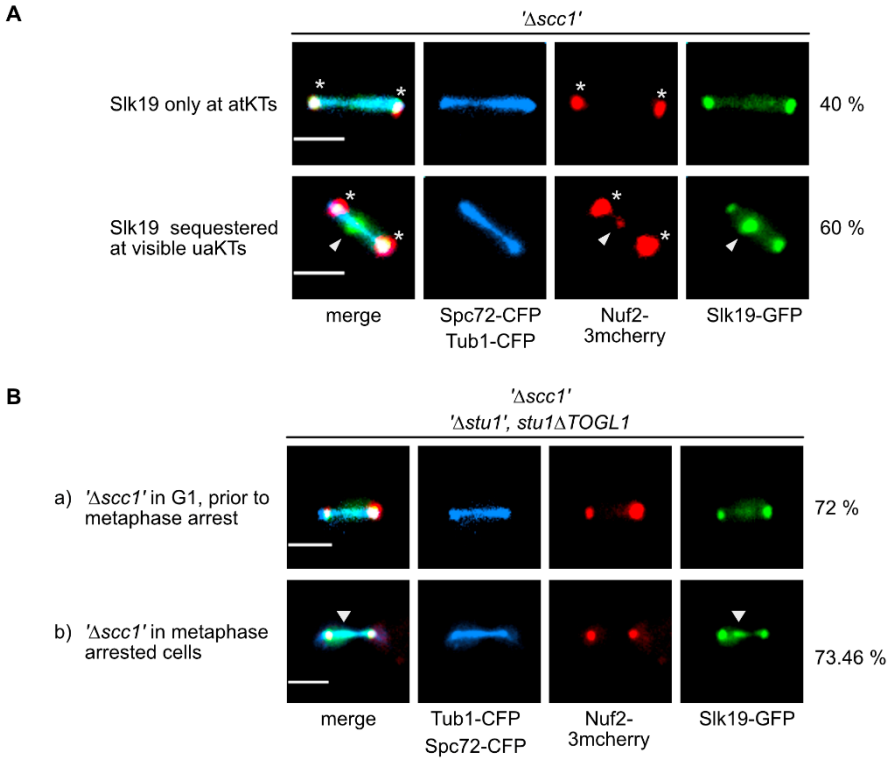

Figure 25: Slk19 localizes to atKTs without tension and only binds at the metaphase spindle after KTs experienced tension during the establishment of a bipolar spindle.

(A-B) Cells were arrested in metaphase by depletion of Cdc20 (by shutting off the expression from the *MET25* promoter). Depletion of Scc1 (*'Δscc1'*) or Stu1 (*'Δstu1'*) was performed by IAA-treatment (AID) during metaphase arrest. Spc72-CFP marks spindle pole bodies, Tub1-CFP marks microtubules, Nuf2-3mcherry marks kinetochores. Genotypes of used strains are listed in Materials chapter. The indicated percentages represent the frequency of the shown phenotype among all counted cells. Phenotypes with exact numbers of counted cells are listed in the appendix. (A) Scc1 was depleted in G1. Subsequently, cells were arrested in metaphase. *'Δscc1'* cells often show uaKTs with sequestered Slk19-GFP. White arrowhead indicates uaKT. Asterisks indicate atKTs close to the SPBs. (B) Slk19 localization to the spindle might occur after bipolar spindle orientation. To prevent Slk19-sequestering, Scc1 was depleted in *'Δstu1', stu1ΔTOGL1* cells. (a) Scc1 was depleted in G1 in *'Δstu1', stu1ΔTOGL1* cells, with a subsequent arrested in metaphase. Slk19 localized mainly to atKTs. (b) Scc1 was depleted after *'Δstu1', stu1ΔTOGL1* cells arrested in metaphase. Slk19 localized to spindles and atKTs. White arrowhead indicates Slk19 spindle localization.

The second way to reduce tension at atKTs (but leaving the cohesion complex intact) was the deletion of the Ndc80 N-terminal tail (*ndc80Δ1-116*) (Suzuki et al., 2016). The N-terminus of Ndc80 contains the MT attachment site as well as regulatory phosphorylation sites (Akiyoshi et al., 2009),(Wei et al., 2007), however, the Ndc80 N-terminal tail is not essential in budding yeast. Slk19 localization was analyzed in *ndc80Δ1-116* cells (low tension) and compared to *WT* (normal tension) and to *STU1*, *stu1ΔTOGL1* cells (increased tension) (Figure 26A-C). The signal intensities of the indicated proteins were measured along the metaphase spindle axis and are depicted as normalized RGB-plots for comparison of the relative Slk19-distribution (Figure 26B). The results clearly show a correlation between spindle localization of Slk19 and tension: In *ndc80Δ1-116* cells with low tension, the two maxima of the KT clusters (indicated by the Mtw1-signal) coincide with the Slk19 signal peaks. In *WT* cells (normal tension), the Slk19 signal at the spindle center slightly increases relative to its KT localization. In *STU1*, *stu1ΔTOGL1* cells with increased tension, the Slk19 signal strongly increases at the spindle center relative to its KT localization (Figure 26B).

Taken together, the Slk19 signal shows an increase at the spindle center (relative to its KT localization) as tension increases. The results are summarized and illustrated in Figure 26C.

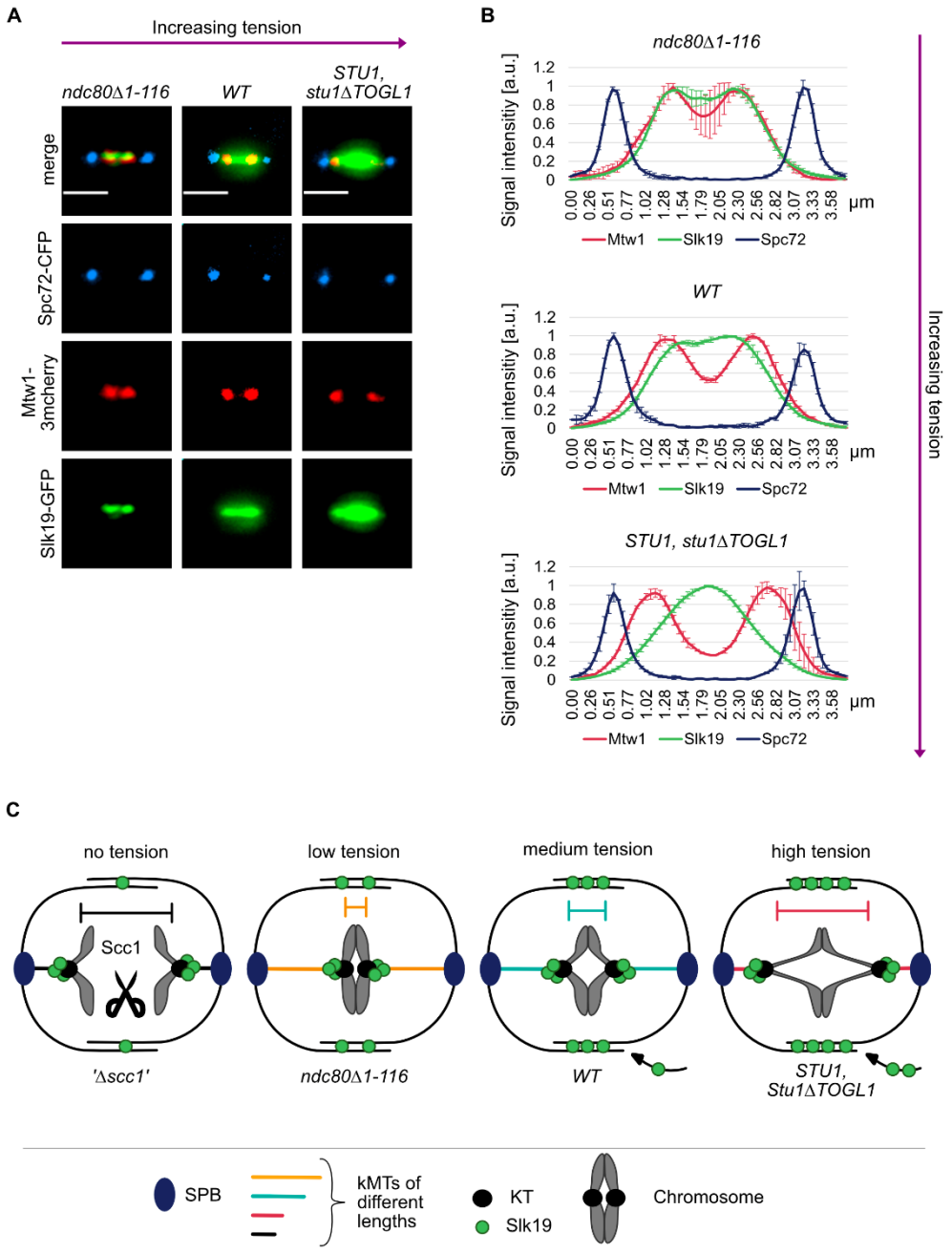

Figure 26: Summary how Slk19 spindle localization might be regulated by increasing tension.

(A-B) Cells were arrested in metaphase by depletion of Cdc20 (by shutting off the expression from the *MET25* promoter). Spc72-CFP marks spindle pole bodies, Mtw1-3mcherry marks kinetochores. (A) Increased Slk19 localization at the metaphase spindle center correlated with increasing tension at KTs (*ndc80Δ1-116:* low tension; *WT:* "medium" tension; *STU1, stu1ΔTOGL1:* high tension). Scale bar = 2 µm. (B) RGB-plots were measured as described in Methods chapter. Longitudinal RGB-plots of metaphase spindles measured in *WT*, in *STU1, stu1ΔTOGL1* and in *ndc80Δ1-116* cells. Signal intensities of indicated proteins were measured and normalized to values ranging from 0–1; 3 µm spindles were measured. Exact numbers of measured cells are listed in the appendix. Error bars show the standard deviations calculated from two independent experiments. (C) Model how tension at the KTs might regulate Slk19 localization to the metaphase spindle overlaps.

4.4 Slk19 stabilizes the anaphase spindle by recruiting Stu1 to the midzone by FEAR-dependent and -independent mechanisms

4.4.1 Slk19 is required for centered Stu1 midzone localization by FEAR-dependent mechanisms

As shown before (chapter 4.2.5 and 4.2.7), deletion of Slk19 influenced the protein abundance of Stu1 at the metaphase spindle and had strong impacts on the Stu1 distribution at the metaphase spindle. In metaphase-arrested *Δslk19* cells, Stu1 was not concentrated at the overlaps anymore, but bound along the complete spindle (chapter 4.2.7). Similar to the situation in metaphase, in anaphase the deletion of Slk19 also leads to an altered localization of Stu1: In *WT* cells, Stu1 is concentrated at the midzone (Figure 28A, a), the region of ipMT overlaps, while in *Δslk19* cells Stu1 is distributed along the entire spindle and its specificity for midzone binding is lost or a midzone per definition is lost (Figure 28A, b) (Stu1 localization at anaphase spindle in *Δslk19* cells is also shown in Khmelinskii et al., 2007).

However, it must be considered that there are major differences between the situation in meta- and anaphase. In metaphase, Stu1 binds to the spindle and to atKTs. Here, Stu1 spindle binding is mediated by its microtubule-binding domain (MBD) (includes the ML and part of TOGL2-domain) (Funk et al., 2014), while the CL domain appears to confer its overlap-specificity via Slk19 interaction (shown in chapter 4.2.7).

In anaphase, however, the interaction modes of Stu1 become changed (see illustration in Figure 27): Stu1 does not localize to KTs anymore but only localizes specifically to the spindle midzone. This localization was shown to be dependent on its D4 domain (dimerization domain of Stu1) (Funk et al., 2014). The D4-dependent binding suggests an indirect binding of Stu1 via other midzone proteins upon anaphase onset. So far, it is not known whether the MBD can additionally bind to MTs once the D4 binds to its putative target at the midzone (see Figure 27B).

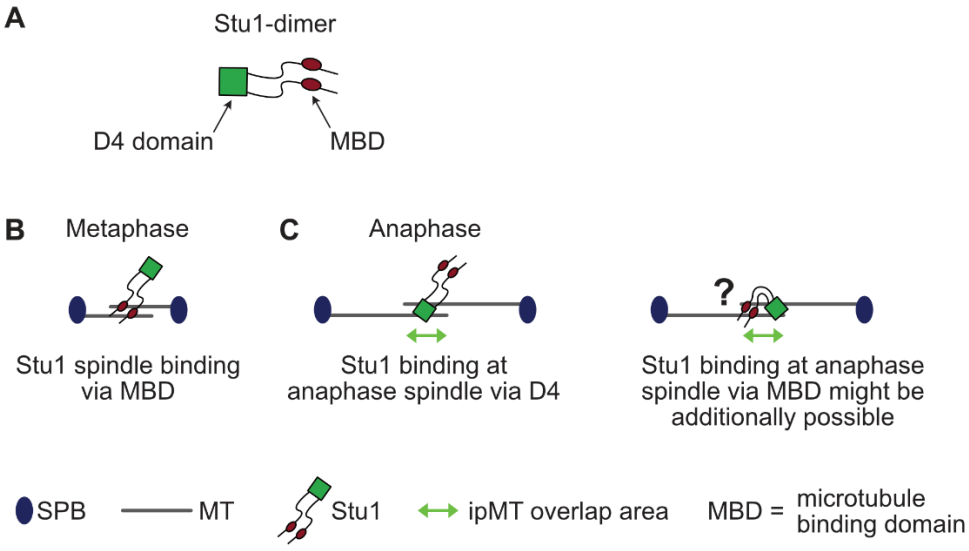

Figure 27: Overview over Stu1 binding modes in metaphase compared to anaphase in *WT* cells.

(A) Schematic illustration of Stu1. (B) Illustration of Stu1 binding mode to the spindle in metaphase. (C) Illustration of possible Stu1 binding modes at the anaphase spindle.

Like *WT* cells (Figure 28A, a), *slk19Δcc2* and *slk19Δcc6+7* cells (Figure 28A, f and g respectively) show a defined and centered Stu1 localization at the anaphase spindle. These cell types also possess a functional FEAR pathway (Havens et al., 2010).

In contrast, the anaphase spindle localization of Stu1 is broadened in *Δslk19* cells but also in *slk19ΔGD, slk19Δcc1* and *slk19Δcc1+2* cells (as shown in Figure 28A, c-e). These cell types all show a defective FEAR pathway (Havens et al., 2010). Thus, the Stu1 localization at the anaphase spindle is clearly dependent on the FEAR pathway.

Figure 28B gives an overview of the Slk19 regions required for FEAR and the lengths of Stu1 spread at the anaphase spindle in the respective cell types. Table 2 (below) summarizes the correlation between Slk19 FEAR function and Stu1 localization at the anaphase spindle.

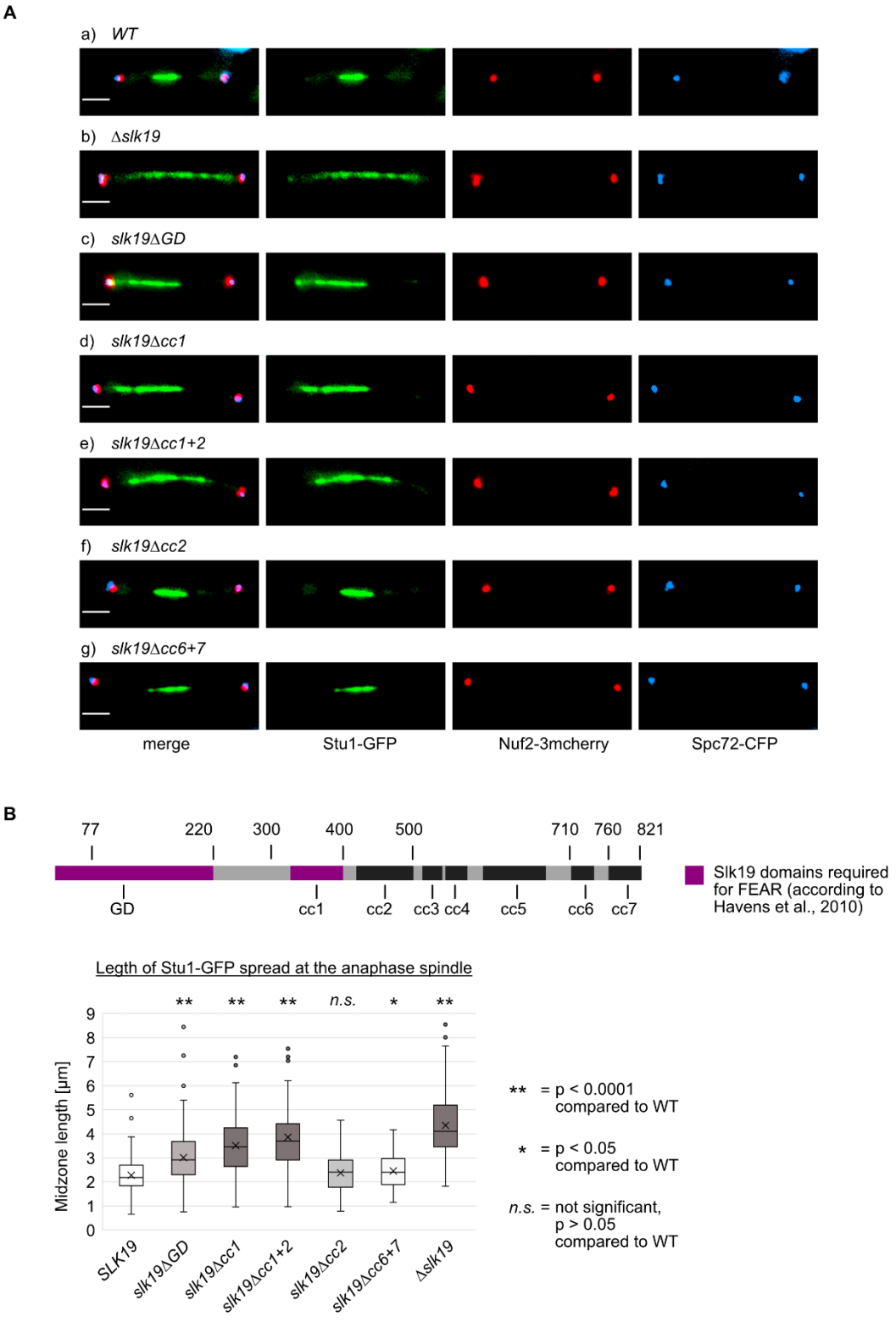

Figure 28: Deletion of Slk19 or different Slk19 domains influences Stu1 localization to the anaphase spindle.

(A-B) Cells were analyzed 2–2.5 h after release from G1 arrest, when most cells were in anaphase. Slk19 constructs were expressed from the endogenous promoter of *SLK19*. Genotypes of used strains are listeded in Materials chapter. Exact values of quantification and number of measured cells are

listed in the appendix. (A) Stu1 anaphase spindle localization was analyzed in indicated cell types (a-f). Spc72-CFP marks spindle pole bodies, Nuf2-3mcherry marks kinetochores. Scale bar = 2 µm. (B) Schematic illustration of Slk19 domains required for FEAR function. Length of Stu1-GFP spread at the anaphase spindle was measured in different cell types carrying the different Slk19 constructs. The p-values were calculated using two-tailed unpaired t-tests. n.s. = not significant.

Table 2: Correlations between the FEAR function of Slk19 and Stu1 localization at the anaphase spindle.

Cell type	**FEAR pathway**	**Stu1 localization at anaphase spindles**
SLK19	Functional*	Centered & restricted
Δslk19 and *slk19Δcc1* and *slk19Δcc1+2*	Defective*	Significantly broadened**
slk19ΔGD	Defective*	Significantly broadened**
slk19Δcc6+7	Functional*	Centered & restricted
Δslk19, ase1-7A	Mimics only a part of the FEAR pathway (Ase1-7A)	Centered & restricted

* According to analyses from Havens et al., 2010. ** $p < 0.0001$ compared to *WT*; broadened ipMT overlap region probably due to inefficient Cin8 localization at overlaps (Khmelinskii et al., 2009).

One main FEAR function is the Cdc14-dependent dephosphorylation of Ase1, the key midzone organizer (Khmelinskii et al., 2007). Defects in Ase1 dephosphorylation, e.g. by defective FEAR pathway, lead to an increased length of this ipMT overlap region probably due to inefficient Cin8 midzone localization and thus insufficient MT sliding (Khmelinskii et al., 2009). Consequently, this also leads to a broadened localization of other midzone proteins.

In accordance with this, integration of phosphomimetic Ase1, Ase1-7D, also led to a broadened Stu1 localization at the anaphase spindle (Figure 29, a), while Ase1-7A (permanently dephosphorylated version of Ase1) did not (Figure 29, b) (in accordance with the findings shown in Khmelinskii et al., 2007). To test whether the broadened Stu1 spindle localization in Δ*slk19* cells can be rescued by Ase1-7A (mimics a part of the FEAR pathway), I here analyzed the Stu1-GFP localization in Δ*slk19 ase1-7A* cells (Figure 29, c). I found that in these cells, the presence of Ase1-7A was apparently sufficient to rescue centered and restricted Stu1-GFP spindle localization (Figure 29, c) (see also Table 2 above: *Δslk19, ase1-7A*).

Thus, the physical presence of Slk19 is not required for the formation of a defined overlap zone. Defective Ase1 dephosphorylation, caused by a defective FEAR pathway due to the deletion of Slk19, is sufficient to explain the broadened Stu1 localization to the anaphase spindle in these cells.

However, this does not exclude the possibility that Stu1 binds along the entire anaphase spindle via its MBD domain (not midzone-specific), because D4-dependent binding might not be enabled in Δ*slk19* (or FEAR-defective) cells. Hence, the broadened Stu1 signal might be reflective of an altered binding mode of Stu1 to the anaphase spindle.

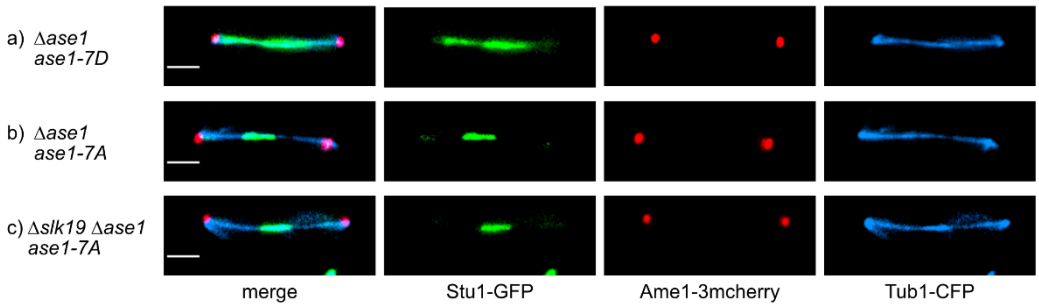

Figure 29: Ase1-7A can rescue a defined Stu1 localization at anaphase spindles in *Δslk19* cells.

Cells were analyzed 2–2.5 h after release from G1 arrest when most cells were in anaphase. Genotypes of used strains are described in Materials chapter. Stu1 anaphase spindle localization was analyzed in indicated cell types (a-c). Tub1-CFP marks microtubules, Ame1-3mcherry marks kinetochores. Scale bar = 2 µm. (a) *ase1-7D* cells showed a broadened Stu1 localization at the anaphase spindle. (b) *ase1-7A* cells showed a centered and restricted Stu1 localization at the anaphase spindle center. (c) Integration of *ase1-7A* in *Δslk19* cells could rescue the broadened Stu1-GFP localization to a centered and restricted anaphase spindle localization.

4.4.2 Slk19 is required for D4-mediated Stu1 binding by FEAR-independent mechanisms

So far it is unknown if or how the MBD- *vs.* D4-mediated binding of Stu1 at the meta-to-anaphase transition is regulated. Here, it was attempted to find out whether the D4-mediated midzone binding of Stu1 might be dependent on Slk19 or the FEAR function of Slk19. FEAR might regulate "a switch" that enables D4-mediated Stu1 binding upon anaphase onset and this might even attenuate MBD-mediated Stu1 binding to promote more flexibility at the midzone (as proposed in the model discussed in Funk et al., 2014). However, it is likewise conceivable that Slk19 might be directly required to recruit Stu1 via its D4 domain to the anaphase spindle midzone.

To analyze the MBD- *vs.* D4-mediated binding in anaphase, a Stu1 mutant with defective MBD (Stu1ΔML) was used that can still bind to the midzone via its D4 domain (Funk et al., 2014) (principle illustrated in Figure 30 below). The *stu1ΔML* cells can proceed to anaphase and clearly show a midzone localization of Stu1ΔML-GFP in most anaphase cells (Figure 31A). Is this D4-mediated Stu1 binding still possible in FEAR-defective *Δslk19* cells?

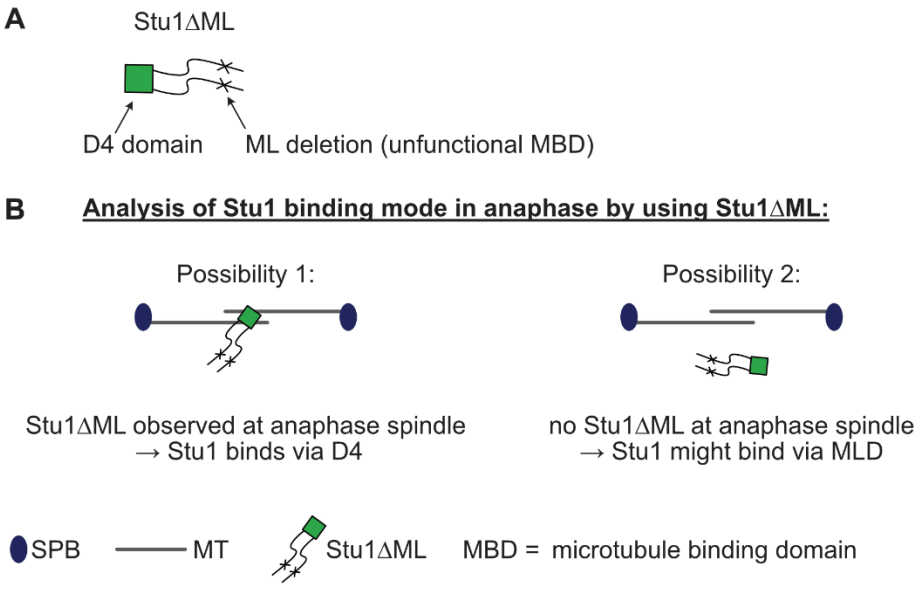

Figure 30: Principle of testing Stu1 binding mode in different cell types by using Stu1ΔML as a control for functional D4 binding.

(A) Schematic illustration of Stu1ΔML. (B) Possible outcomes and conclusions for Stu1-binding from experiments using Stu1ΔML.

In *stu1ΔML* cells, the majority of the cells (53,9 %) were in anaphase at the observed timepoint (2.5 h after release from G1 arrest). In contrast, 85.3% of the *stu1ΔML Δslk19* cells were observed still in metaphase at this timepoint (Figure 31A). Also in *stu1ΔML slk19Δcc1+2* cells (Slk19Δcc1+2: no spindle binding and no FEAR function), an increased proportion of cells were still in metaphase at the observed timepoint (Figure 31A). The reason for this could be a defective regulation of D4-mediated binding in *Δslk19 or slk19Δcc1+2* cells, which in turn might lead to an insufficient stabilization of anaphase spindles. Consequently, a larger proportion of cells might remain in metaphase (quasi metaphase arrest). This would implicate that D4-dependent binding (enabled by Slk19) becomes close to essential when MBD-dependent binding of Stu1 to the anaphase spindle is not possible (as in *stu1ΔML Δslk19* cells).

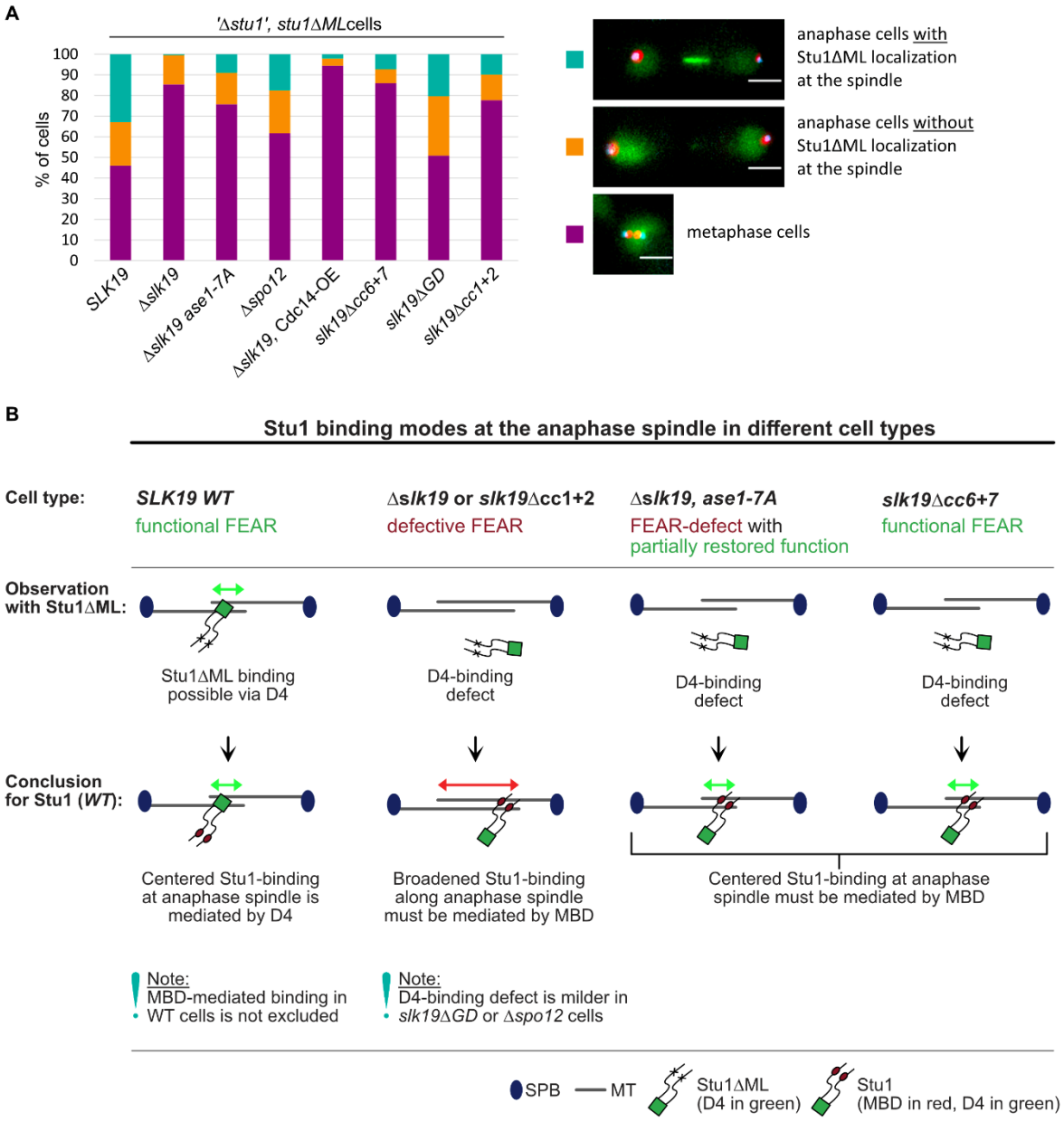

Figure 31: Slk19 it might have a direct role in D4-mediated Stu1 anaphase spindle binding additionally to its the FEAR function.

(A) Conditional depletion of *WT* Stu1 (*'Δstu1'*) in *stu1ΔML* cells was performed by IAA-treatment (AID). Phenotypes of *'Δstu1'*, *stu1ΔML* cells with different genetic backgrounds were analyzed (as indicated). Cells were analyzed 2.5 h after release from G1 arrest when most of the cells were in anaphase. Exact values of quantifications and number of measured cells are listed in the appendix. Slk19 constructs were expressed from the endogenous promoter of *SLK19*. Genotypes of used strains are described in Materials chapter. Scale bar = 2 µm. ML = middle loop. GD = globular domain. cc = coiled coil domain. (B) Summary of results using different *stu1ΔML* strains and the conclusion for the Stu1 binding mode in the respective cell types.

A complete D4 binding defect should result in no binding of Stu1 at the anaphase spindle. Indeed, in *stu1ΔML Δslk19* cells, almost none of the few cells that proceeded to anaphase showed Stu1ΔML binding at the anaphase spindle (Figure 31A). This indicates that either Slk19 itself or the FEAR function of Slk19 is required for D4-mediated Stu1 midzone binding.

The results furthermore suggests that the broadened Stu1 (*WT*) signal at the anaphase spindle in Δ*slk19* cells (see Figure 28A, b) might reflect mainly MBD-mediated Stu1 binding.

As shown above in chapter 1.4.1, integration of *ase1-7A* (rescues a part of the FEAR defects) was sufficient to allow a defined and centered Stu1 (*WT*) localization at anaphase spindles (Khmelinskii et al., 2007) even in absence of Slk19 (Figure 29C). Is this centered Stu1 binding mediated by D4? In *Δslk19 stu1ΔML* cells (defective MBD binding) with *ase1-7A*, the localization of Stu1ΔML at the anaphase spindle could not be fully rescued and a large proportion of cells remained in metaphase (Figure 31A). Even overexpression of Cdc14 in Δ*slk19* cells (should revert all FEAR defects) did not rescue the midzone localization of Stu1ΔML (Figure 31A). Taken together, the result indicates that Stu1 (*WT*) localizes to spindles via its MBD in the above-mentioned cells and this binding still confers overlap specificity. Moreover, the result shows that FEAR alone is not sufficient to induce D4-mediated Stu1 binding in absence of Slk19.

Vice versa, cells with defective FEAR pathway but functional Slk19 binding at the anaphase spindle were analyzed. A FEAR defect alone, generated by a Spo12 deletion (*Δspo12*), resulted in a much milder phenotype compared to *Δslk19* cells (see Figure 31A). Cells carrying the Slk19 deletion construct *slk19ΔGD* were also shown to have a defective FEAR pathway (Havens et al., 2010), however, the construct itself is still physically present at the anaphase spindle (see chapter 4.2.2, Figure 7C). Interestingly, *stu1ΔML slk19ΔGD* cells showed a similar proportion of cells proceeding to anaphase (compared to *stu1ΔML*, *SLK19* cells) but a slightly reduced proportion of anaphase cells with Stu1ΔML localization at the anaphase spindle (Figure 31A).

Taken together, reconstitution of the FEAR function (described above) was not sufficient to rescue localization of Stu1ΔML at anaphase spindles in *Δslk19* cells. In contrast to the *Δslk19* defects, FEAR defects alone caused milder defects in D4-dependent Stu1 binding (Figure 31A: *slk19ΔGD* and *Δspo12* cells). A possible reason for this is discussed later (Discussion chapter 5.4.2).

Analyzed mutants with a sole FEAR defect included *slk19ΔGD* or *Δspo12* cells, in which Slk19 (or Slk19ΔGD) still localizes to the spindle. Thus, the question arose how important the physical presence of Slk19 at the anaphase spindle might be for the D4-mediated Stu1 binding. Therefore, the deletion construct *slk19Δcc6+7* was analyzed, which itself shows no *WT* localizations anymore (chapter 4.2.2, Figure 7C), but was shown to maintain a functional FEAR network (Havens et al., 2010). In those *slk19Δcc6+7* cells, Stu1 localizes strongly

and centered to the anaphase spindle (Figure 28A, g). However, analysis of *stu1ΔML* localization in *slk19Δcc6+7* cells showed most of the cells remaining in metaphase and only very few cells proceeded to anaphase with Stu1ΔML spindle localization (Figure 31A). This again suggests that the physical presence of Slk19 at the spindle is strongly required for D4-mediated Stu1 binding and that Stu1 might localize to the anaphase midzone via its D4 domain and via Slk19 (probably by direct or indirect Slk19-D4 interaction).

The result also suggests that the centered Stu1 (*WT*) signal at the anaphase spindle in *slk19Δcc6+7* cells (see Figure 28A, g) is not a D4-dependent binding but might reflect MBD-mediated Stu1 binding. Thus, if formation of an overlap zone in anaphase is possible, then Stu1 preferentially binds to this (via D4 or via MBD).

Figure 31B summarizes and illustrates the results using different *stu1ΔML* strains and shows the conclusions for the Stu1 binding mode in the respective cell types. Table 3 (below) summarizes the correlation between physical presence of Slk19 at the spindle and D4-dependent Stu1 anaphase spindle binding in *stu1ΔML* cells.

Table 3: Correlation between physical presence of Slk19 at the spindle and D4-dependent midzone binding of Stu1ΔML.

Cell type	**Slk19**	**Stu1ΔML phenotype**
SLK19	Physically present at midzone (FEAR-functional)	- Cells proceed to anaphase * - Stu1ΔML binds to midzone
Δslk19 and slk19Δcc1+2	Not present at anaphase spindle (FEAR-defective)	- prolonged time in metaphase ** - Stu1ΔML binding less efficient
Δslk19, ase1-7A	Not present at anaphase spindle (FEAR only partially restored)	- prolonged time in metaphase ** - Stu1ΔML binding less efficient
slk19ΔGD	Physically present at midzone (FEAR-defective)	- Cells proceed to anaphase * - Stu1ΔML binding less efficient
slk19Δcc6+7	Not present at anaphase spindle (FEAR-functional)	- prolonged time in metaphase ** - Stu1ΔML binding less efficient

* Anaphase spindle stabilization possible. ** Probably metaphase arrest due to D4 binding defect and thus insufficient anaphase spindle stabilization.

To support the finding that spindle bound Slk19 is required for D4-mediated Stu1 binding, it was aimed to confirm these results in metaphase cells. In metaphase, Cdc14 is normally bound to its inhibitor Cfi1/Net1 in the nucleolus (described in introduction chapter 1.3.3.3). Therefore, Cdc14 was overexpressed (Cdc14-OE) in metaphase-arrested cells, which leads to the presence of free active Cdc14 in the nucleus. The Cdc14-OE should induce the formation of an artificial midzone in the observed cells due to premature Ase1 dephosphorylation (Khmelinskii et al., 2007),(Khmelinskii et al., 2009). To discriminate between changes in Stu1 MBD- or D4-dependent binding, a Stu1ΔD4-Zipper-CFP (only MBD-dependent binding possible) and the D4 domain alone (D4-GFP) was used. Upon Cdc14-OE, the D4-GFP domain got recruited to the metaphase spindles in the majority of cells (Figure 32A, a-b). Interestingly, in Cdc14-OE Δ*slk19* cells, D4 domain recruitment to the artificially induced midzone was not possible anymore (Figure 32A, c). Thus, also here the results indicate that both Slk19 as well as Cdc14 are required for D4-mediated Stu1 midzone binding.

Moreover, the localization of Stu1ΔD4-Zipper did not substantially change in those Cdc14-OE cells. This indicates that there is no Cdc14-regulated mechanism that simultaneously attenuates the MBD-dependent Stu1 binding while promoting the D4-dependent binding. This is in accordance with or finding in *slk19Δcc6+7* cells that still showed efficient MBD-dependent Stu1 binding despite functional Cdc14-release (Havens et al., 2010). If there is an attenuation of MBD-dependent Stu1 binding, then this attenuation must depend on D4-Slk19 interaction, which might result in conformational changes (discussed in more detail in Discussion chapter 5.4.4)

How Slk19 promotes D4-mediated binding of Stu1 to the midzone is still unknown so far (see also Discussion chapter). One possibility might be, that Slk19 directly interacts with D4 of Stu1 in anaphase (as already indicated) and thus might mediate interaction between Stu1 and another midzone protein, e.g. dephosphorylated Ase1 (illustrated in Figure 32C).

Here it was shown that Slk19 binds to metaphase spindles via Ase1 *in vivo* (chapter 4.2.4). Supportingly, Slk19 also binds to MTs *in vitro* via Ase1 purified from metaphase-arrested cells (chapter 4.2.8) and via Ase1-7D (mimics metaphase situation) (Figure 32B, a). However, Slk19 also efficiently binds to MTs *in vitro* via Ase1-7A (mimics anaphase situation) (Figure 32B, b). Therefore, Slk19 might bind to the spindle also *in vivo* via dephosphorylated Ase1 in anaphase and could thereby recruit D4 specifically to the overlap zone (as suggested in the section above).

However, since the Ase1 phosphorylation status does not influence its interaction with Slk19 (no change at the meta-to-anaphase transition), this is probably not the regulatory step controlling the recruitment of Stu1 via the D4 domain. Consequently, other regulatory factors must be involved in this process (e.g. additional phosphoregulation of Slk19 or the D4 domain itself). Clearly more research is needed to clarify these points.

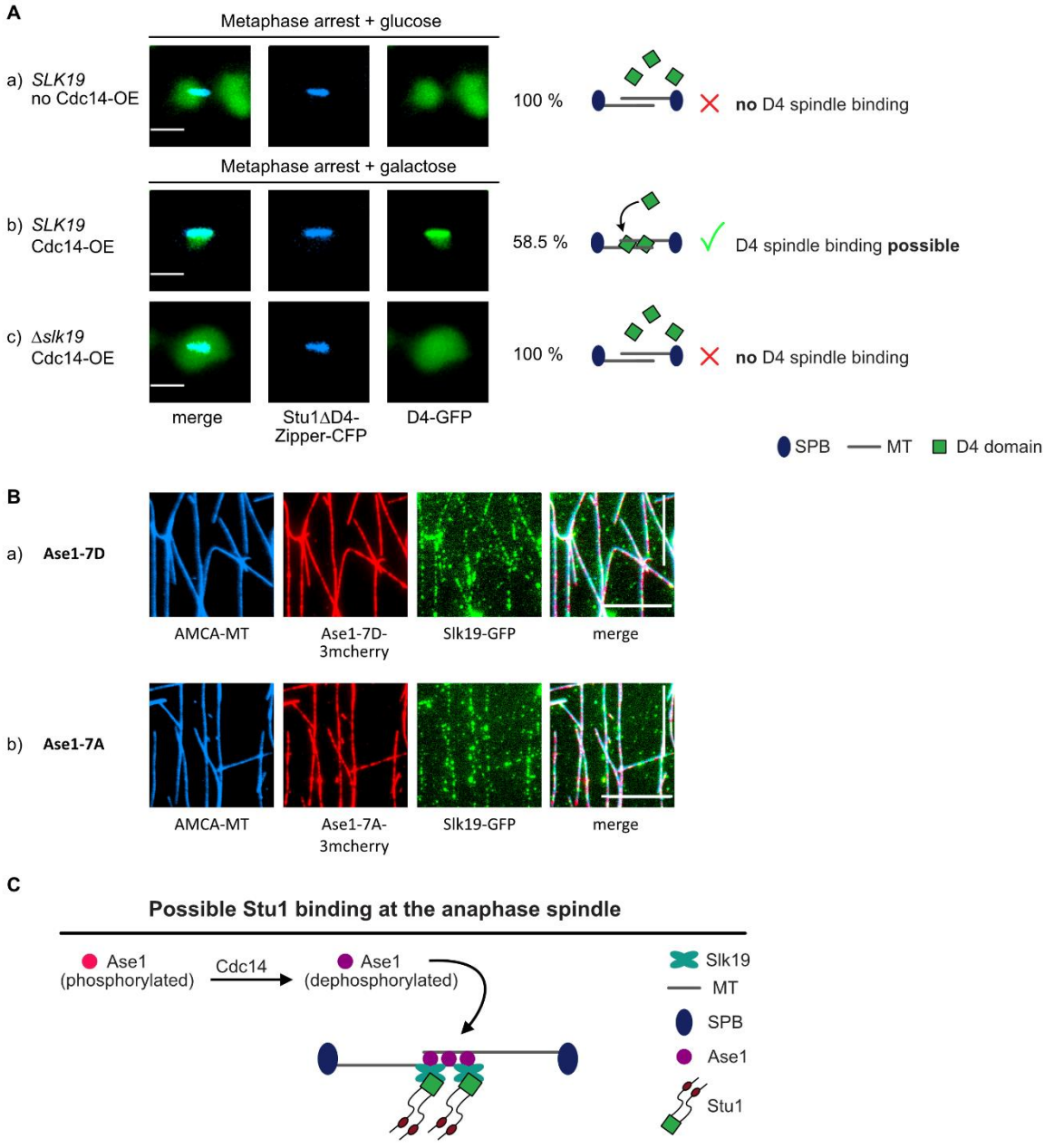

Figure 32: Cdc14 and Slk19 itself are required for D4-mediated Stu1 midzone binding.

(A) Cells were arrested in metaphase by depletion of Cdc20 (by shutting off the expression from the *MET25* promoter). Where indicated, Cdc14 was overexpressed upon galactose induction (*GAL1*-promoter) as described in Methods chapter. Genotypes of used strains are listed in Materials chapter. The indicated percentages represent the frequency of the shown phenotype among all counted cells. OE = overexpression. Scale bar = 2 µm. Illustration of D4 binding mode included. (a) D4-GFP was not recruited to the metaphase spindle without Cdc14-OE. (b) D4-GFP was recruited to the artificially induced midzone by Cdc14-OE in metaphase cells. (c) D4-GFP recruitment to the artificially induced midzone was not possible in *Δslk19* cells. (a-c) Localization of Stu1ΔD4-Zipper-CFP did not substantially change in the different conditions. (B) Protein purification and incubation was performed as described in Methods chapter. Slk19 could bind to both Ase1-7D and Ase1-7A *in vitro*. Scale bar = 10 µm. (C) Possible indirect Stu1 binding via D4 at the anaphase spindle midzone.

Taken together, the results suggest that Slk19 promotes the midzone localization of Stu1 by two distinct mechanisms:

1) The FEAR function of Slk19 (Cdc14 release) is required for the formation of a defined overlap zone to which Stu1 preferentially binds (Table 2, chapter 4.4.1). Cdc14-dependent dephosphorylation of Ase1 (and thus Cin8 recruitment) is sufficient for this and the physical presence of Slk19 is not required. Moreover, Cdc14 is needed to promote D4-dependent Stu1 binding at the anaphase spindle.
2) Spindle-localized Slk19 is required in a direct manner and in addition to the Cdc14 release, for the D4-mediated Stu1 binding to the anaphase midzone (see Table 3, correlation between spindle bound Slk19 and D4-dependent Stu1 binding in *stu1ΔML* cells).

5 Discussion

5.1 Slk19 and its role in initiating the sequestering process at uaKTs

In *S. cerevisiae,* the KT protein Slk19 and the MT rescue factor Stu1 sequester specifically at uaKTs with high efficiency (Funk et al., 2014),(Ortiz et al., 2009). This sequestering facilitates capturing of uaKTs and thus is crucial for faithful chromosome segregation (Kolenda et al., 2018) (described in detail in introduction chapter 1.5.3.2). In sequestering defective *spc105-6A* cells and *'Δstu1'* cells, a basal amount of Slk19 remains bound to the uaKTs (Kolenda et al., 2018). One aim of this study was to figure out whether this basal binding of Slk19 at uaKTs is required for initiation of the sequestering process and thereby better understand the sequestering process at uaKTs.

5.1.1 Slk19 cc6+7 is required for multiple functions including basal KT binding

To analyze the importance of basal Slk19 binding at uaKTs for the sequestering process, the aim was to identify a Slk19 deletion mutant with a specific defect that removes basal KT binding while leaving sequestering intact.

In this study, it was found that deletion of the Slk19 C-terminus (containing cc6+7, aa 709-821) leads to defective Stu1-Slk19 sequestering at uaKTs (Figure 3A, e). Moreover, the C-terminus (cc6+7) was found to be required and sufficient for the basal Slk19 binding to uaKT (Figure 3A, e-f). This C-terminal domain also conferred KT binding of Slk19 at attached KTs in metaphase and anaphase cells (Figure 8). Interestingly, the fission yeast protein most homologous to Slk19, Alp7, also binds to KTs via its C-terminal transforming acid coiled coil (TACC) domain (Tang et al., 2013),(Tang et al., 2014). The database "Pfam" (Protein families; categorizes proteins according to aa sequence similarities) also categorized Slk19 as TACC containing protein (ID: PF12709) and placed the TACC domain of Slk19 at its C-terminus (aa 742–818). Thus, similar domains target Slk19 and Alp7 to KTs.

Moreover, it was shown here that the C-terminus (cc6+7) of Slk19 also constitutes its homotetramerization domain (Figure 4). Slk19 tetramerization is one prerequisite for functional sequestering according to the current sequestering model (Kolenda et al., 2018). Since the KT-binding domain also facilitates Slk19 tetramerization, it was not possible to show conclusively that defective sequestering is a consequence of defective KT binding.

Replacement of the C-terminus (cc6+7) by other oligomerization domains (*GLC4-Zipper* or *CIN8-TD)* did not restore KT binding and it also did not restore sequestering (Figure 5A and B). Whether tetramerization or dimerization was restored was not checked. However, no other Slk19 function was restored (Figure 5A and B) (except FEAR, that is anyway functional in *slk19Δcc6+7* cells (Havens et al., 2010)). Thus, it is very likely that oligomerization was not restored by the C-terminal replacements with these artificial oligomerization domains. One explanation might be, that the chimeric proteins do not resemble the *WT* structure of Slk19 tetramers. For example, the *GLC4-Zipper* forms parallel

dimers (O'Shea et al., 1991) that might not be suited to drive the tetramerization of Slk19. Thus, the attempts to rescue sequestering by reconstituting Slk19 oligomerization by replacement of the C-terminus were not successful. However, other tetramerization domains that were not included within this study might be able to reconstitute functional Stu1-Slk19 sequestering at uaKTs.

Taken together, the C-terminus of Slk19 contains both its tetramerization and its KT localization domain and is required for functional sequestering at uaKTs. Whether the basal Slk19 binding at KTs is required for the initiation of sequestering process could not be clarified with this mutant.

5.1.2 Deletion of cc1 leads to a sequestering defect although KT binding is intact

Besides Slk19Δcc6+7, I also found that Slk19Δcc1 is defective in sequestering. A second prerequisite for sequestering (besides Slk19 tetramerization that is mediated by the C-terminus (cc6+7, aa 791-821) as I showed in chapter 4.1.3), is the interaction between Slk19 tetramers and Stu1 dimers (Kolenda et al., 2018),

Here, I found that cc1 mediates the interaction with Stu1. Surprisingly however, also the C-terminus does (Figure 6). Furthermore, a minimal Slk19 construct consisting only of the C-terminus and the cc1+2 domain was sufficient to restore the sequestering process at uaKTs (Figure 3B), while the C-terminus alone was not (Figure 3A, f). Thus, the two domains (the C-terminus and the cc1+2 domain) are essential and sufficient for sequestering, and both contribute to Stu1-Slk19 interaction at uaKTs (Figure 3A, c,e,f, B). Unlike the C-terminus, cc1 however is not required for Slk19-Slk19 interaction (Figure 4).

Taken together, all Slk19 domains that were shown to be required for functional sequestering (C-terminus and cc1) (Figure 3A, c, e, f) also contribute to Stu1 interaction at uaKTs (Figure 6). This again emphasizes the importance of the Stu1-Slk19 protein interaction. Moreover, this finding gives the C-terminus of Slk19 another essential function for sequestering besides its tetramerization and possibly its KT-binding functions.

5.1.3 Role of Spc105-mediated basal Slk19 KT binding for sequestering

In sequestering defective *'Δstu1'* cells, a basal amount of Slk19 remains bound at uaKTs (Kolenda et al., 2018). This indicates that Slk19 interacts with KT core proteins directly. Since interfering with the Slk19 KT-binding domain could not clarify the importance of basal Slk19 localization (discussed above), it was attempted to prevent Slk19 KT localization by identifying and manipulating the KT protein that confers Slk19 KT localization.

Several possible KT proteins came into consideration as Slk19 interactors at the KT. Firstly, the *S. pombe* Slk19 homolog Alp7 (mentioned above in chapter 5.1.1) localizes at KTs in

dependence of Alp14 (Sato et al., 2004), the homologue of budding yeast Stu2. However, depletion of Stu2 did not affect basal binding of Slk19 (Figure 1A, d). Nevertheless, these results do not exclude a possible functional link between Stu2 and Slk19 at atKTs or the spindle (not part of this study).

Secondly, ChIP analyses showed that KT localization of Slk19 is strongly reduced in temperature sensitive *ndc80* and *spc105* mutants (Pagliuca et al., 2009). Ndc80 depletion did not affect the basal binding of Slk19 at uaKTs (Figure 1B). However, depletion of Spc105 abolished basal Slk19 binding at uaKTs (Figure 1C, a) and at atKTs (Figure 7A-C). So far it is not known whether Slk19 binds to KTs via Spc105 directly, or indirectly e.g. by interaction with Kre28, which forms a KT subcomplex together with Spc105. However, a yeast two-hybrid assay demonstrated interaction between Spc105 (aa 584–639) and Slk19 (Y. Wang et al., 2012). Therefore, a direct interaction between Slk19 and Spc105 seems likely. Two Spc105 deletion mutants were analyzed in respect to sequestering and basal KT localization of Slk19: *spc105Δ1-339* and *spc105Δ584-639* (data not shown). For the *spc105Δ1-339* mutant, sequestering was defective, while the basal Slk19 binding at uaKTs and KT localization of Spc105 was unaffected. Thus, Slk19 must bind to the remaining part of Spc105. The *spc105Δ584-639* mutant was defective in sequestering and Slk19 localization. Thus, the absence of basal binding of Slk19 at KTs again correlated with defective sequestering. However, this deletion also abolished Spc105 KT localization.

Phosphorylation of Spc105 (at the six MELT sites within the N-terminus at aa T149, T172, T211, T235, T284, T313 (London et al., 2012)) also plays a crucial role for the initiation of sequestering (described in introduction chapter 1.5.3.2), but not for basal Slk19 localization at uaKTs (Kolenda et al., 2018). Thus, if KT-localized phosphorylated Spc105 is the trigger for sequestering, then the defective KT localization of Spc105Δ584-639, is sufficient to explain the sequestering defect. The results therefore neither prove nor exclude an essential function of basal Slk19 KT localization for the initiation of the sequestering process.

5.2 Slk19 stabilizes metaphase spindle overlaps via Ase1 and Stu1

Withdrawal of the rescue factor Stu1 from the spindle during the sequestering process results in a destabilization and reorganization of the MT network, which facilitates recapturing of the KT (Kolenda et al., 2018),(Ortiz et al., 2009) (described in introduction chapter 1.5.3.2). This observation raised the questions which functions Slk19 might have at the mitotic spindle during an undisturbed cell cycle and furthermore, which consequences the Slk19-withdrawal might have during the sequestering process at uaKTs. There have been several indications that Slk19 must play a role for spindle stability in metaphase cells (Zeng et al., 1999),(Ye et al., 2005),(T. Zhang et al., 2006),(Richmond et al., 2013). However, the exact spindle function of Slk19 was so far unknown. Therefore, it was aimed to identify the Slk19 spindle functions in more detail by *in vivo* and *in vitro* studies.

5.2.1 Slk19 might enhance MT crosslinking via protein network formation

Theoretically, Slk19 could contribute to spindle stabilization by several possible mechanisms: by a MT rescue activity, by controlling MT polymerization, by crosslinking of antiparallel MTs or by aligning spindle MTs due to a motor function. However, Slk19 does not have a predicted motor domain and so far, it was not known whether Slk19 can even bind to MTs by itself.

Here, it was shown that Slk19 does not possess an intrinsic MT-binding activity *in vitro* but can efficiently bind to MTs via prebound Stu1 or Ase1 (Figure 16B). These data are consistent with the *in vivo* data shown in this study. Also here, Slk19 localization to the metaphase spindle overlaps was dependent on Stu1 and Ase1 (Figure 11A, b-c and B). As for the sequestering process, the Stu1 CL domain confers the Slk19 interaction.

The *in vivo* data showed that Slk19 localizes to the metaphase spindle center rather than along the complete spindle, which is indicative for a localization at ipMT overlaps and a functional role at this specific site (Figure 7). The results of this study indicate that Slk19 contributes to increased ipMT crosslinking and spindle stabilization by enhancing the binding of the MT rescue factor Stu1 and the MT-crosslinking protein Ase1 at the metaphase spindle overlaps. This is supported by the experimental data listed in the following:

1) Deletion of Slk19 led to strongly reduced Ase1 amounts and moderately reduced Stu1 amounts at the metaphase spindle *in vivo* (Figure 12). Supportingly, also in the *in vitro* MT binding assays, Slk19 enhanced Ase1 and Stu1 binding at MTs (Figure 17).
2) Ase1 as well as Stu1 could both bind and crosslink MTs by themselves *in vitro* (Figure 16B, Figure 19A and B) as described before (Schuyler et al., 2003),(Funk et al., 2014). Importantly, it was shown here that Slk19 can enhance this MT crosslinking when incubated together with Stu1 or Ase1. In contrast, Slk19 alone could not crosslink MTs (Figure 19A and B).

The observed Slk19-dependent enrichment of Ase1 and Stu1 at the metaphase spindle could be explained by the tetrameric structure of Slk19 that is ideal to bind multiple copies of its interacting proteins and thus could allow the local enrichment of spindle proteins, such as the homodimer Ase1 (Schuyler et al., 2003) and the homodimer Stu1 (Funk et al., 2014). Therefore, the presented data suggest a model in which Slk19 promotes protein network formation at the metaphase spindle overlaps and thereby promotes MT crosslinking. This “enhancement model” is illustrated in Figure 20.

5.2.2 Slk19 is required for organized overlap formation

According to the suggested model (described above; illustrated in Figure 20), defective protein network formation due to Slk19 deletion should also lead to observable defects of the metaphase spindle overlaps *in vivo*. Indeed, the following defects at the spindle overlaps were shown in this study:

1) Thinned overlaps: *Δslk19* and *slk19Δcc1* cells (no Slk19 at the spindles) showed reduced tubulin levels at the spindle center (Figure 14), suggesting that there are less ipMT overlaps formed. Reduced tubulin levels at the spindle center might be a direct consequence of reduced overlap stabilization due to decreased levels of Ase1 and Stu1 at the metaphase spindles (Figure 12). This observation is accompanied by the increased appearance of long unaligned nrMTs in *Δslk19* and *slk19Δcc1* cells that randomly span the nucleus (Figure 9).
2) Acentric overlaps: In *WT* cells there are on average four ipMTs emanating from each SPB that create overlaps at the spindle center (Winey et al., 1995). Here, both the Stu1 and Ase1 signal peaks at the center of the metaphase spindle (Figure 15), which most probably represents a cumulative signal deriving from localization to all of the ipMT overlaps. In *Δslk19* cells however, both Ase1 and Stu1 showed altered localizations at the metaphase spindle overlaps (Figure 15). The weak remaining Ase1 signal at the spindle of *Δslk19* cells showed a non-centered localization pattern, which is indicative of shifted irregular MT overlaps. This shift in overlap positioning might result from more dynamic spindles in *Δslk19* cells (T. Zhang et al., 2006), possibly caused by defective protein network formation. Alternatively, the altered Ase1 localization could as well derive from reduced ipMTs that reach the middle of the spindle (as indicated above in point 1). If only two ipMT (one from each side) interdigitate to form an overlap region, this single overlap might appear acentric as assessed by the Ase1 localization. In contrast to the acentric Ase1 distribution, Stu1 showed a broader and evenly distributed spindle signal without a defined maximum in *Δslk19* cells.

Why do Ase1 and Stu1 behave differently? Ase1 has an intrinsic preference for binding to the ipMT overlap region (Schuyler et al., 2003),(Khmelinskii et al., 2007). In contrast, the results obtained in this study indicate that Slk19 is required to guide Stu1 to antiparallel MT overlaps in *WT* cells. In agreement with this, also Stu1ΔCL, which is defective in Slk19 interaction (Figure 10E), showed a broadened spindle localization (Figure 15). There are several ideas how Slk19 might direct Stu1 to this localization. However, the here preferred idea is that Slk19 might mediate the interaction of Stu1 with Ase1 and thereby mediates the overlap-specificity of Stu1. This is in agreement with the idea that Slk19 promotes protein network formation at the overlaps. Defects in this process could also explain the reported observations of bipolar attachment problems (Richmond et al., 2013) and short metaphase spindles (Zeng et al., 1999) in cells without Slk19. Moreover, both Ase1 and Slk19 are synthetically lethality with the same proteins, *Δkar3 or Δcin8*, which are involved in MT

alignment, crosslinking and metaphase spindle formation (Zeng et al., 1999),(Hepperla et al., 2014),(Hildebrandt et al., 2006) indicating that Ase1 and Slk19 probably contribute to the same cellular functions.

5.2.3 Stu1ΔCL rescues spindle defects caused by Slk19 and Ase1 deletion

Previous studies showed that *stu1ΔCL* cells possess long spindles (similar to *WT*) with increased kMT lengths and decreased inter-KT distances compared to *WT* cells (Funk et al., 2014), indicating that there is less tension at the spindles in those cells. Apparently, this *stu1ΔCL* mutant can rescue the metaphase spindle defects caused by *Δslk19* or *Δase1*, since *Δslk19 stu1ΔCL* cells as well as *Δase1 stu1ΔCL* cells showed long spindles (Figure 11) compared to *Δslk19* or *Δase1* cells carrying *WT STU1*.

How can *stu1ΔCL* cells form these long stable metaphase spindles despite its disturbed Slk19 interaction? The reason for this is currently not understood. Possibly, Stu1ΔCL possesses MT-crosslinking or MT-rescue functions that exceed those of *WT* Stu1 and this might result in more stable overlaps. Moreover, the reduced tension at the spindles in *stu1ΔCL* cells might require less stabilization via Ase1 and Slk19 to resist the forces exerted on the spindle.

It was shown here, that spindle bound Slk19 is strongly reduced in *stu1ΔC*L cells and that Ase1 is dependent on Slk19 for its efficient spindle localization (Figure 12). Thus, reduced Ase1 amounts at the spindles would also be expected in *stu1ΔC*L cells. Interestingly however, I found that Ase1 levels at the metaphase spindles in *stu1ΔC*L cells appear quite strong, similar to *WT* levels (Figure 11). This finding indicates that the reduced spindle binding of Slk19 in *stu1ΔCL* cells (Figure 11) is not a secondary defect due to reduced Ase1 levels at the metaphase spindles. Possibly, the low Slk19 amounts at the spindles in *stu1ΔCL* cells might be already sufficient to enable efficient Ase1 spindle binding. Nevertheless, this Ase1 enrichment at the spindle cannot be the cause for the long spindles in *stu1ΔC*L cells (mentioned above), since *Δslk19* or *Δase1* still allowed the formation of long spindles in *stu1ΔCL* cells (Figure 11). Thus, further research is required to understand the effects caused by the *stu1ΔCL* mutant.

5.2.4 Slk19's influence on the directionality of antiparallel MT crosslinking

For the establishment of a bipolar spindle, antiparallel MT crosslinking has to be favored over parallel MT bundling. Ase1 as well as its conserved orthologues have an intrinsic preference for antiparallel MT crosslinking (Schuyler et al., 2003),(Janson et al., 2007), (Mollinari et al., 2002),(Bieling et al., 2010),(Khmelinskii et al., 2007),(Loïodice et al., 2005). Does Slk19, or the proposed network formed via Slk19, might enhance this effect of antiparallel MT crosslinking?

One indication for this is that Slk19-OE partially rescued the monopolar spindle phenotype in Stu1-overexpressing cells (Figure 21). However, this hypothesis could not be verified by *in vitro* MT crosslinking experiments using polarity marked MTs (Figure 23). The preference of Ase1 to crosslink antiparallel MTs was not enhanced upon incubation of Ase1 together with Slk19. For Stu1 alone no preference in antiparallel MT crosslinking was observed and this, as well, was not changed by the incubation together with Slk19.

Nevertheless, the *in vitro* experiment was performed with only one set of protein concentrations and variations of individual parameters could be additionally analyzed in future experiments. Moreover, the situation might be different *in vivo* and might include a more complex protein network formation via Slk19 that could not be resembled within the here presented *in vitro* experiments. Thus, further research is required for clarification.

5.2.5 Slk19 affects cellular Ase1 protein levels

The Ase1 protein amount is strongly reduced (7.8-fold) at the metaphase spindles *in vivo* (Figure 12). However, the total Ase1 protein levels in the cell were only reduced approximately 2-fold in *Δslk19* or *slk19Δcc1* cells compared to *WT* cells (Figure13A and B). Therefore, these reduced cellular Ase1 protein levels cannot/not solely explain the strongly reduced Ase1 amounts at the metaphase spindles in these cells (Figure 12). So far it is unclear how the reduced cellular Ase1 protein level can be explained. Possibly, Slk19 is required for higher protein stability of Ase1 (e.g. by promoting correct folding) or maybe even for more effective Ase1 protein expression. However, so far Slk19 was not identified as transcription factor. Another explanation might be that Slk19 prevents premature degradation of Ase1. If the latter is the case, the impaired spindle binding of Ase1 in *Δslk19* or *slk19Δcc1* cells might promote premature degradation of unbound Ase1.

Previous studies also showed an altered Ase1 expression upon replication stress, which led to two N-terminally truncated Ase1 isoforms (due to transcription from alternative intragenic start sites). The short Ase1 isoforms still localized to the mitotic spindle and led to reduced binding of full length Ase1 (McKnight et al., 2014). However, this cannot be the explanation for the reduced Ase1 levels at the metaphase spindles of Δ*slk19* cells (shown in Figure 12): Ase1 was tagged C-terminally with mcherry in the analyses of this work, thus expression of N-terminally shortened Ase1 isoforms would still be detected at the spindle and thus would not be observed as a reduction of spindle-bound Ase1. Moreover, there were no shortened Ase1 isoforms observed in the Western blot analyses (Figure 13A).

In contrast to Ase1, total Stu1 protein levels were neither reduced in *Δslk19* nor in *slk19Δcc1* cells (Figure13A and B). This indicates that Stu1 does not require Slk19 for its protein stability or expression.

5.2.6 Comparison of Slk19 and its *S. pombe* homolog Alp7 in MT crosslinking

The *S. pombe* Slk19 homolog, Alp7, was shown to play a role for bipolar spindle formation and for MT crosslinking (Sato et al., 2004),(Thadani et al., 2009). This is in accordance with the finding that Slk19 contributes to MT crosslinking in budding yeast *in vivo* and *in vitro* (shown in this study in Figure 14, Figure 19). Unlike Slk19 however, that exerts this function indirectly via Ase1 and Stu1, Alp7 can bundle MTs *in vitro* by itself and is not dependent on other proteins for this function (Thadani et al., 2009).

Ase1 and Slk19 (in budding yeast) as well as Ase1 and Alp7 (in fission yeast) most likely contribute to similar cellular functions. Single deletions of these proteins are viable (Pellman et al., 1995),(Zeng et al., 1999),(Loïodice et al., 2005),(Oliferenko & Balasubramanian, 2002). However, fission yeast *Δase1 Δalp7* cells are lethal (Thadani et al., 2009) while budding yeast *Δase1 Δslk19* cells are not (Figure 13C). This might indicate that Ase1 and Alp7 in fission yeast might function in parallel pathways, for instance to stabilize MT overlaps, while Ase1 and Slk19 in budding yeast might function in the same pathway via a direct interaction network (as indicated by the viable *Δase1 Δslk19* double mutant). Thus, in budding yeast there must be (at least one) additional pathway contributing to spindle stabilization/crosslinking (e.g. via Stu1).

5.3 Metaphase spindle localization of Slk19 might be tension-regulated

Here it was shown that Slk19 amounts at the metaphase spindle center are increased in situations with high tension and decreased in situations with low/no tension at the KTs and the spindle. These findings suggest a tension-regulated mechanism controlling Slk19 spindle localization according to demand.

5.3.1 Enhanced Slk19 spindle localization correlates with increased tension

In '*Δspc105*' cells, the tension at KTs is increased compared to *WT* cells. This was deduced from the significantly reduced kMT lengths and increased KT-KT distances in '*Δspc105*' cells, while spindle lengths were only marginally reduced compared to *WT* (Figure 24A). In these '*Δspc105*' cells, the Slk19 signal was strongly present at the spindle center (Figure 7). Moreover though, this Slk19 signal at the metaphase spindle center was increased compared to *WT* cells (Figure 7C). This might be due to a larger pool of free Slk19, caused by defective KT binding, that can alternatively localize to the spindle overlaps. However, increased amounts of Slk19 at the spindle were also observed in *STU1*, *stu1ΔTOGL1* cells, in which binding of Slk19 to the KT was still functional according to the ChIP-assays (Figure 24B-E). Conclusively, this also shows that the increased recruitment of Slk19 to the spindle center does not significantly compete with its localization to the KTs.

Like in '*Δspc105*' cells, also *stu1ΔTOGL1* cells and *STU1*, *stu1ΔTOGL1* cells showed significantly reduced kMT lengths and increased KT-KT distances compared to *WT* (Figure 24A and B) (for the *stu1ΔTOGL1* cells this was also shown in Funk et al., 2014) and thus have increased tension. This is most probably due to defective KT localization of Stu1ΔTOGL1 and the resulting defect in kMT stabilization (Funk et al., 2014). The Slk19 localization in *stu1ΔTOGL1* cells was difficult to observe due to the reduced spindle length in those cells (Figure 24 B) (reduced spindle length in *stu1ΔTOGL1* cells also shown in Funk et al., 2014). However, *STU1*, *stu1ΔTOGL1* cells form long *WT*-like spindles despite short kMTs (shown in Figure 24B). Therefore, the Slk19 localization was analyzed in these cells. Furthermore, the long spindles in *STU1*, *stu1ΔTOGL1* cells might result in even higher tension at the KTs compared to *stu1ΔTOGL1* cells. A possible explanation for the phenotype in *STU1*, *stu1ΔTOGL1* cells (long spindles despite reduced kMT-lengths) might be that the heterodimers (Stu1-Stu1ΔTOGL1) are not fully functional anymore for KT binding and/or kMT stabilization but are still functional for spindle binding and stabilization. The strong localization of Slk19 at the spindle center might be involved in the latter process.

Taken together the increased tension at KTs of *'Δspc105'* cells and *STU1, stu1ΔTOGL1* cells correlates with elevated Slk19 amounts at the spindle center. Thus, the results support the hypothesis that there might be a tension regulated mechanism promoting Slk19 recruitment to the spindles if there is a special need for structural stabilization, e.g. due to increased tension at the spindle and KTs (illustrated in Figure 26C).

5.3.2 Decreased Slk19 spindle localization correlates with reduced tension

In *stu1ΔCL* cells, the tension at the KTs/spindle is most likely reduced compared to *WT* cells, since they show increased kMT lengths and reduced KT-KT distances (Funk et al., 2014). Here, it was shown that Slk19 levels at the spindle center are strongly reduced in *stu1ΔCL* cells (Figure 11). However, the defective Slk19 interaction in *stu1ΔCL* cells is most likely the cause for the reduced Slk19 levels at the spindles in those cells (Figure 10E). Therefore, this alone is no clear evidence for a tension-regulated mechanism.

However, tension is also strongly reduced in *ndc80Δ1-116* cells lacking the N-terminal tail of the outer KT protein Ndc80 (Suzuki et al., 2016). Also here, decreased Slk19 amounts were observed at the metaphase spindle center (localization only at KTs) (Figure 26).

A complete loss of tension can be achieved by depleting the cohesion subunit Scc1 in G1. A problem here was that a large proportion of those cells (60 %) showed uaKTs with sequestered Slk19 (uaKTs due to lack of tension as described in introduction chapter 1.4.2.2) (Figure 25A). This disturbed the Slk19 localization analysis. In *stu1ΔTOGL1* cells with defective sequestering, however, the Slk19 signal at the spindle center was also almost absent when Scc1 was depleted in G1 (although Tub1 signal was present) and only KT localization of Slk19 was observed (Figure 25B, a).

When Scc1 was depleted in metaphase-arrested cells (after assembly of a bipolar spindle and tension establishment) Slk19 was observed at the metaphase spindle center (less than *WT*, Figure 25B, b). This indicates that Slk19 only binds to the spindle after tension is established and that there is no (or only a slow) regulation mechanism for Slk19 removal from the spindle after tension is relieved. Another possible explanation for the remaining Slk19 signal at the spindle might be that Scc1 was not completely depleted in those cells, since Scc1 is loaded to the chromatin prior to S-phase of the cell cycle (Michaelis et al., 1997) and the effectiveness of protein depletion (by the AID-system) might be reduced once loaded to the chromatin.

Taken together, the mentioned results consistently support the proposed hypothesis of a dynamic regulation mechanism of Slk19 localization to the spindle in metaphase (see Figure 26C). The data suggest that Slk19 localization at the spindle center is enhanced after bi-orientation and tension establishment, and that the amount of Slk19 increases with increasing tension at the KTs and thus at the spindle. After cohesion cleavage, Slk19 remains at the spindle at least for a certain time. Whether there is a mechanism that actively removes Slk19 from the spindle overlaps when tension is relieved is so far not known.

5.3.3 Possible mechanisms triggering Slk19 enrichment at the metaphase spindle

The enrichment of Slk19 at the spindle is reminiscent of the sequestering process together with Stu1 at uaKTs. Possibly, Slk19 can also sequester at the spindles and this process might even employ similar mechanisms as the co-polymerization at uaKTs together with Stu1. In accordance with this, Slk19 requires Stu1 interaction for efficient binding to the spindle center as well as for sequestering. The cc1 domain of Slk19 that contributes to Stu1 interaction (Figure 6, Figure 10) was required for sequestering (Figure 3A, c) and for Slk19 localization to the metaphase spindle (Figure 8A and B). Analogously, the CL domain of Stu1 is required for both the sequestering of Slk19 at uaKTs (Kolenda et al., 2018) and for the efficient binding of Slk19 to the metaphase spindle (shown in Figure 11). Thus, a tension-regulated Stu1-dependent "Slk19 sequestering process" at the spindle center could be possible.

How is this process triggered? Conceivable mechanisms that might induce the enrichment of Slk19 at the spindle by demand could involve tension sensing mechanisms, e.g. via the CPC or Stu2 (described in introduction chapter 1.4.2.2).

Stu2 is a specific mechano-sensor required at the KT-MT interface to specifically stabilize tension bearing MT attachments (M. P. Miller et al., 2016),(M. P. Miller et al., 2019), (Aravamudhan et al., 2015),(Zahm et al., 2021). Interestingly (as mentioned in chapter 5.1.3), in fission yeast, the Stu2 homolog Alp14 is required to localize Alp7 (Slk19 homolog) to the KT-MT interface, where they are required as a complex for stable end-on attachment (Tang et al., 2013),(Sato et al., 2004),(Garcia et al., 2001). Thus, also in budding yeast, a

functional connection between the proteins (Stu2 and Slk19), including a possible tension-dependent regulation of Slk19 via Stu2, cannot be excluded so far.

Another idea is that Slk19 spindle localization is regulated by tension-dependent phosphorylation and dephosphorylation events, e.g. via the Ipl1 kinase located at the inner KTs (Ipl1 spatial separation model described in detail in introduction chapter 1.4.2.2) (T. U. Tanaka, 2010),(Biggins & Murray, 2001). Does this mean that all Slk19 must pass through the KT for its modification and regulated spindle binding? This situation seems rather unlikely, since Slk19 is also enriched at the spindle center in *'Δspc105'* cells (no Slk19 KT localization possible). Interestingly, it was shown that Ipl1 can also fulfill its tension-dependent function for biorientation when its localization to the inner KTs is hindered, but its accumulation and activation at the spindle is still possible (Campbell & Desai, 2013). Similarly, activated Ipl1 might also be sufficient to regulate Slk19 independently of the KT localization of the two proteins. However, the underlying mechanisms triggering Slk19 enrichment at the spindle upon increased tension and whether Ipl1 is involved in this process remains to be clarified.

5.4 Slk19 induces changes of the protein network at the anaphase midzone

5.4.1 The protein network at ipMT overlaps at the meta-to-anaphase transition

The data obtained within this study suggest that Slk19 is required for metaphase spindle stability by promoting protein network formation and MT crosslinking via Ase1 and Stu1 at the ipMT overlaps. Also in anaphase, Slk19 localizes to the ipMT overlap zone (referred to as midzone in anaphase) (Zeng et al., 1999). Compared to the overlap zone in metaphase, the anaphase midzone contains more protein components, which are focused or recruited to the midzone upon dephosphorylation events by Cdc14 at anaphase onset (Khmelinskii et al., 2007). These midzone components exert highly coordinated functions for MT stabilization, sliding and elongation (described in detail in introduction chapter 1.4.3.5). Thus, to combine these functions, the protein network at the anaphase spindle midzone must be very dynamic and flexible.

Changes in Slk19 and Stu1 binding at the anaphase midzone

It was shown that the binding mode of Stu1 at the spindle changes at the meta-to-anaphase transition from a sole MBD-dependent binding in metaphase, to a mode that does not require MBD and instead or additionally uses the D4 domain of Stu1 (Funk et al., 2014) (illustrated in Figure 27). Similar to the situation in metaphase, Stu1 is focused at the ipMT overlaps (midzone) in anaphase. In contrast to metaphase, this Stu1 localization seems to depend on D4 in anaphase. If D4 is replaced with the Gcn4 dimerization domain, the resulting hybrid protein (Stu1-ΔD4-Zipper) localizes (weakly) along the complete anaphase spindle (Funk et

al., 2014). If the altered Stu1 interactions in anaphase results in a weakened MBD-dependent ipMT binding and crosslinking, this may allow a higher flexibility at the spindle midzone (in comparison to the metaphase overlap zone) that allows MT gliding (according to the current model discussed in Funk et al., 2014). However, despite a possibly weakened direct MT interaction, MT stabilization at the midzone would still be guaranteed via the D4-dependent Stu1 localization (Funk et al., 2014).

Also Slk19 binding changes at the meta-to-anaphase transition: In metaphase, Slk19 localization at the overlap zone is markedly enhanced via an interaction with Stu1 that depends on the CL of Stu1 (see above and Figure 11A and B). In comparison to metaphase, the midzone localization of Slk19 occurs independently of the Stu1 CL domain in anaphase (Figure 11C). Again, this is likely to attenuate the MT-crosslinking network that was postulated for metaphase.

Thus, there are four questions: 1) What is the D4-interacting protein at the midzone? Since Stu1 (CL domain) interacts with Slk19 in metaphase, could Slk19 also be the interacting protein at the midzone in anaphase and is there a switch between the interaction domains from CL to D4 of Stu1? 2) How is this switch regulated? 3) What role does this switch (and Slk19) have for midzone formation and anaphase spindle function? 4) Is there an attenuation of Stu1 MT binding via MBD in anaphase?

These questions will be discussed in the following chapters.

5.4.2 Spindle localization of Slk19 is required in addition to Cdc14 activity for D4-dependent midzone localization of Stu1

As might be suspected, the regulation/activation of D4-dependent Stu1 localization is governed by FEAR/Cdc14. FEAR-defective *slk19ΔGD* or *Δspo12* cells (both with functional Slk19 spindle binding) showed clearly reduced D4-dependent Stu1 binding at the anaphase spindle as revealed when MBD-binding was disabled (in *stu1ΔML* cells) (illustrated in Figure 30),(shown in Figure 31A). The partial phenotype in these cells types (with some cells still showing D4-dependent Stu1 binding) might be explainable by a second later wave of Cdc14-release that is mediated by MEN (Stegmeier et al., 2002).

Furthermore, one can induce an artificial midzone in metaphase-arrested cells by using the Ase1-7A mutant (Khmelinskii et al., 2009) or by overexpression of Cdc14 (thesis of C. E. T. Funk, 2014). The latter was sufficient to trigger the localization of an isolated D4 domain (D4-GFP) to the ipMT overlaps in these cells (Figure 32A, b) (recruitment of D4 to metaphase spindle by Cdc15-OE also shown in the thesis of C. E. T. Funk, 2014). Thus, Cdc14 clearly regulates the D4-dependent binding of Stu1 to midzone proteins and since Slk19 is required for Cdc14 release via FEAR, it contributes in this way.

However, I showed here that Slk19 appears to contribute also in a more direct way. When Cdc14 is overexpressed in metaphase-arrested Δ*slk19* cells, D4 of Stu1 is not recruited to

the spindle as described above for *WT SLK19* cells (Figure 32A, c). Furthermore, in anaphase, *stu1ΔML Δslk19* cells showed a more severe (complete) defect in D4-dependent Stu1ΔML localization than cells with a mere FEAR defect (*slk19ΔGD* or *Δspo12* cells; see above) (Figure 31A). Importantly this defect could not be rescued by overexpression of Cdc14 or by the *ase1-7A* mutation that mimics Ase1-dephosphorylation by Cdc14 and thus at least partly reconstitutes the downstream effects of FEAR. Together this shows that Slk19 is needed beyond its FEAR function for D4-dependent binding of Stu1.

Finally, also Slk19Δcc6+7 that supports FEAR activation (Havens et al., 2010) but fails to localize to the spindle (Figure 8B and C) also fails to support the D4-dependent Stu1 binding (Figure 31A).This indicates that Slk19 is not only needed beyond its FEAR function but that its physical presence is required at the spindle.

In summary, the here presented data suggest that in anaphase D4 of Stu1 binds directly or indirectly to midzone-localized Slk19 and that this interaction is enabled by the activity of Cdc14.

How does Cdc14 induce the Slk19-dependent D4 binding of Stu1? As described in chapter 5.2, Slk19 most likely interacts with Ase1 in metaphase (Figure 11, Figure 12). Furthermore, the *in vitro* MT binding assays in this study showed that Slk19 not only interacts with the phosphomimetic Ase1-7D (reflects situation in metaphase) but also with the constitutively dephosphorylated Ase1-7A (reflects situation in anaphase) (Figure 32B). Thus, Slk19 probably also binds to the anaphase spindle via Ase1 (*in vivo*) and the Slk19-Ase1 interaction is most likely not the target of the Cdc14-regulation. Rather a direct dephosphorylation of Slk19 and/or D4 of Stu1 by Cdc14 might facilitate their interaction. Alternatively, Cdc14 may dephosphorylate proteins that mediate the D4-Slk19 interaction or may trigger a more complex signaling pathway.

5.4.3 Role of D4-dependent Stu1 localization for the anaphase spindle

Slk19-D4 interaction is per se not required for midzone formation

As judged by the Stu1 localization at the anaphase spindle, *Δslk19* cells show a broadened midzone/overlap zone (Figure 28A, b) (broadened Stu1 localization in *Δslk19* cells also shown in Khmelinskii et al., 2007). However, an *ase1-7A* mutant (that at least partly restores FEAR functions, see chapter above) was sufficient to rescue a defined midzone formation in *Δslk19* cells (Figure 29, c). Also *slk19Δcc6+7* cells, that have a functional FEAR but defective Slk19 spindle localization (and thus defective D4-dependent Stu1 localization) form a *WT*-like midzone in anaphase (Figure 28A, f).

The fact that Stu1 efficiently localized to these midzones (despite defective Slk19-D4 interaction) probably was fundamental for their formation. However, it also shows that Stu1 most likely binds to MTs directly (probably) via its MBD under these conditions (despite an

active FEAR pathway) and that localization at the ipMT overlaps is still favored. This result also has implications for the proposed regulation model of Stu1-MT interaction during the meta-to-anaphase transition (model described above in chapter 5.4.1 and in Funk et al., 2014), as will be discussed in more detail below in chapter 5.4.4. Moreover, the result that Stu1 can bind to ipMTs in a focused manner via the MBD also contradicts the finding that Stu1ΔD4-Zipper is not focused at the midzone but only binds weakly along the complete spindle (Funk et al., 2014). Conclusively, only dimerization via D4 may provide a Stu1 conformation that favors binding to ipMT overlaps.

Taken together, this data showed that the Stu1 D4-Slk19 interaction is per se not required for a defined midzone formation and that the role of Slk19 in midzone formation is predominantly driven through FEAR activation.

Stu1 D4-Slk19 interaction becomes close to essential when the MBD of Stu1 is defective

A large proportion of *stu1ΔML Δslk19* cells or *stu1ΔML slk19Δcc6+7* cells (defective MBD- and D4-dependent Stu1 binding) remained in metaphase also after a prolonged observation of over 5h (compared to *stu1ΔML SLK19* cells; data not shown). This indicates that these cells are quasi metaphase-arrested and that the Stu1 D4-Slk19 interaction becomes close to essential in *stu1ΔML* cells. Thus, Stu1 D4-Slk19 interaction could function as backup mechanism if MBD-dependent Stu1 binding fails or is attenuated in anaphase (as discussed also below in chapter 5.4.4).

Does the Stu1 D4-Slk19 interaction have another function for the anaphase spindle?

Slk19 has been reported to have a FEAR-independent function for the anaphase spindle (Havens et al., 2010). In particular, changed spindle dynamics and reduced anaphase spindle stability have been reported for *slk19Δcc6+7* cells (with defective Stu1 D4 binding). In those cells, the pause between the fast phase (pure sliding) and the slow phase (polymerization and sliding) of anaphase B (as seen in *WT* cells, described in introduction chapter 1.5.4.3) is lost, the spindle elongation rate is increased and anaphase spindles break more frequently (Sullivan et al., 2001),(Kahana et al., 1995),(Havens et al., 2010). This phenotype might be explained by a failure to stabilize and/or polymerize ipMTs sufficiently while sliding apart, resulting in compromised overlaps and finally broken spindles. Localizing the MT rescue factor Stu1 specifically to the midzone via the D4-Slk19 interaction might prevent just that.

5.4.4 Is there an attenuation of MBD-dependent Stu1 binding in anaphase?

The model from Funk et al., 2014 described in chapter 5.4.1, assumes that direct Stu1-MT interaction via the MBD is attenuated while Stu1 is instead anchored to the midzone via D4, in order to allow MT gliding and polymerization at the same time. An obvious candidate for

this regulation would have been FEAR/Cdc14. As pointed out by my results in this study, FEAR indeed facilitates the D4-dependent interaction.

However (as already mentioned above in chapter 5.4.3), Stu1 still localized efficiently to the anaphase midzone even when the FEAR pathway was active and the D4-dependent Stu1 localization was disabled by the *slk19Δ6+7* mutation (Figure 28A, g). Furthermore, the binding of Stu1ΔD4-Zipper to metaphase spindles remained unaltered upon the overexpression of Cdc14 (Figure 32A, a-b). Thus, FEAR, and any other regulation that may trigger anaphase and is unaltered in *slk19Δ6+7* cells, is not likely to directly attenuate a putative Stu1-MT interaction in anaphase. Rather it should be a direct consequence of the spindle localization of Slk19.

As mentioned above (chapter 5.4.3), only dimerization via the D4 domain seems to guarantee that Stu1 binds specifically to MT overlaps. Could the Slk19-D4 interaction (triggered by FEAR) cause a conformational change in D4 that interferes with this and thereby attenuates crosslinking? In that case, this attenuation would not occur in *slk19Δ6+7* cells and would result in a too rigid crosslinking in these cells (expectedly resulting in excessive stabilization and reduced dynamics of the spindle). However, the phenotype of *slk19Δ6+7* cells as described in chapter 5.4.3 is not conform with this model, since it shows increased spindle elongation dynamics that result in a destabilized spindle.

Thus, it is more than possible that there is no attenuation of Stu1 MBD-binding at all. Taken together the mentioned data indeed rather speak against this proposed model. Alternatively, anchoring Stu1 to the midzone via D4 (in addition to MT interaction) might make midzone localization of Stu1 (even) more efficient and might thus guarantee MT stabilization and polymerization of the gliding MTs. D4-dependent binding of Stu1 might also be a redundant mechanism (mentioned above) to assure Stu1 localization and thus anaphase spindle stabilization in case the MBD binding fails in this delicate situation of the cell cycle.

5.5 Slk19 might phase-separate at specific cellular locations

How can Slk19 be enriched by demand at such high levels as seen for the sequestering process or the enrichment at the spindle at high tension?

After an initial trigger (e.g. KT detachment triggering sequestering or increased tension triggering spindle enrichment), polymerization of the specific protein network must proceed and so far it is not well understood how this is achieved. Possibly, post-translational modifications of all involved proteins (Stu1, Slk19, Ase1) are required for this process (as discussed for the sequestering process in Kolenda et al., 2018 or for tension-dependent Slk19 spindle localization in chapter 5.3.3). Alternatively, the triggering process might induce a prion like folding cascade leading to a sequestering process at uaKTs or the spindle overlaps. In this case, the specific folding must be reversible very quickly to allow a dynamic regulation by demand. Another more favorable possibility might be that the observed

sequestering reflects a phase separation event that is initiated and locally restricted. This would allow the required dynamic formation and disassembly of the sequestering complex.

A possible phase separation leading to the sequestering process at uaKTs would include Stu1 and Slk19, while phase separation leading to enrichment at the MT overlaps might additionally involve Ase1. Since the protein interactions leading to phase separation are often weak (Alberti et al., 2018), this might also explain why Ase1 and Slk19 could not co-immunoprecipitate in the attempted Co-IP assays. In future experiments, specific cross-linking of the proteins might allow their co-immunoprecipitation.

How could Stu1/Slk19 *vs.* Stu1/Slk19/Ase1 separation be regulated? Distinct underlying mechanisms triggering the sequestering process *vs.* protein accumulation at the spindle (Mps1 activity upon KT detachment *vs.* tension-dependent regulation, e.g. possibly via Ipl1) might result in distinct site-specific modifications of the involved proteins and might thus allow differential regulation of Slk19, Stu1 and Ase1 within these processes.

Do these proteins meet the requirements for phase separation? Phase separation often involves proteins with intrinsically disordered prion-like domains (PLDs) or coiled coil domains (Alberti et al., 2018). Thus, Stu1, Slk19 and Ase1 and all possess protein regions that would theoretically allow phase separation: Stu1 possesses two long intrinsically disordered protein regions (IDPRs): aa 585–705 located within the ML-domain that is involved in MT binding (Funk et al., 2014) and aa 1048–1206 covering the CL domain that is required for both sequestering (Kolenda et al., 2018) and Slk19 enrichment at the spindle (Figure 11). The IDPRs of Slk19 include aa 1–197 covering almost the entire N-terminal GD, aa 215–299 (unknown function) and a C-terminal region from aa 691–724. Here, only a part of the C-terminal disordered region was shown to be required for sequestering or spindle localization (Figure 3A, e and Figure 8C). Slk19 also has a very high percentage of coiled coil domains (67.11 % of the protein, as predicted with the SOPMA tool; see also Figure 2A) that could also drive phase separation (Alberti et al., 2018). Thus, Slk19 cc1 or cc6+7, contributing to sequestering and spindle localization, could possibly also contribute to phase separation. The IDPRs of Ase1 include a short N-terminal sequence (aa 1–31) and a C-terminal region from aa 675–819 (unknown function).

An interesting observation in this context, is the finding that overexpression of Slk19 led to the formation of Slk19-clusters within the nucleus (Figure 22). These clusters were also formed in Δ*btn2* cells (Figure 22, c). Thus, they do not reflect a Btn2-dependent intranuclear quality control compartment for deposition of misfolded proteins (S. B. Miller et al., 2015). Furthermore, the Slk19 clusters did not represent completely misfolded proteins, since they were still able to recruit Stu1 (Figure 21A, c and Figure 22, d). They may therefore indicate a phase separation process induced by high protein concentrations (Alberti et al., 2019). The colocalization of Stu1 and Slk19 at the clusters is reminiscent of their interdependent sequestering at uaKTs. Unlike this however, the cluster formation within Slk19-OE cells was not dependent on Stu1 as seen in *'Δstu1'* cells (Figure 22, e). Thus, increased protein levels of Slk19 in the nucleus might induce phase separation independently of Stu1.

Alternatively, the Slk19-clusters might represent a Btn2-independent deposition of Slk19 (due to protein folding stress) that are still functional for Stu1 binding. Thus, clearly more research is needed on this point and on the initiation of the sequestering process.

5.6 Functional similarities between Slk19 and its human orthologue CENP-F

Slk19 shows regional sequence homologies with the human protein CENP-F/Mitosin (approximately 350-kDa, 3113 aa residues) (Xueliang Zhu et al., 1995),(Kitagawa & Hieter, 2001). CENP-F is suggested to be the functional orthologue of Slk19 in human cells since the two proteins share several functional similarities (Richmond et al., 2013). Like Slk19, CENP-F is a KT protein involved in several mitotic processes including chromosome segregation (reviewed in Varis et al., 2006).

CENP-F is a component of the corona at uaKTs

Most interestingly, CENP-F localizes to KTs in early prophase and is a component of the fibrous outer layer of the human KT named "corona" (Xueliang Zhu et al., 1995),(Rattner et al., 1993). The corona is strongly reminiscent of the sequestering complex in budding yeast: This crescent shaped structure, assembled at the outer layer of vertebrate KTs, only appears when KTs are detached from MTs, expands in early phases of mitosis and rearranges upon KT capture by end-on MT attachment (Dong et al., 2007a),(Magidson et al., 2015),(Hoffman et al., 2001). Like the suggested function of the sequestering complex in budding yeast, the expanded corona in vertebrate cells facilitates the initial KT capture (Sacristan et al., 2018),(Wynne & Funabiki, 2015). Also after end-on attachment of KTs and shedding of the corona, CENP-F remains localized at the KTs in metaphase (Rattner et al., 1993),(Kops & Gassmann, 2020). This constitutive KT localization of CENP-F is also reminiscent of the constitutive basal binding of Slk19 at KTs in metaphase (Figure 7A and Figure 8A). In vertebrate cells, the assembly of the expanding corona is dependent on the activity of multiple protein kinases including the checkpoint kinase Mps1 and Aurora B (Wynne & Funabiki, 2015). Similarly, it was shown in budding yeast that Mps1-activity is essential for the initiation of the sequestering process of Slk19 and Stu1 (Kolenda et al., 2018). Whether the budding yeast homolog of Aurora B, Ipl1, is involved in the initiation of the sequestering process of Slk19 and Stu1 is so far unknown and would be an interesting subject of further research. Although the corona in vertebrate cells contains more protein components compared to the sequestering complex in budding yeast, the process of co-polymerizing proteins at uaKTs might be a conserved mechanism to facilitate initial KT capture and to provide a close regulatory connection with the mitotic checkpoint at uaKTs (Kolenda et al., 2018),(Kops & Gassmann, 2020).

CENP-F is involved in tension-related processes

The data obtained in this study suggest a tension-regulated mechanism for the Slk19 spindle localization. Slk19 would thus be sensing tension in an indirect way (and possibly off the KT). Since Slk19 affects spindle stability, it would also influence/regulate tension at the KTs (more stable spindles allow higher tension). For CENP-F, there are indications that it might be involved in tension regulating mechanisms, since depletion of CENP-F results in reduced inter-KT distances (indicative for reduced tension at the KTs) and in more instable KT-MT attachments (Bomont et al., 2005). Moreover, the efficient localization of CENP-F to KTs is dependent on Bub1 (V. L. Johnson et al., 2004) and Shugoshin (Salic et al., 2004). Both of these proteins also contribute to the localization and regulation of the Aurora B kinase (Ipl1 in budding yeast) that is required for the correction of tensionless KT-MT attachments (Boyarchuk et al., 2007),(Liang et al., 2020),(Hadders et al., 2020),(Broad et al., 2020), (Meppelink et al., 2015),(Kawashima et al., 2010). Therefore, it might also be interesting to analyze whether the budding yeast homologs (Bub1 and Sgo1) are involved in Slk19 localization or even in tension-dependent regulation of Slk19.

CENP-F localizes to the spindle overlaps in anaphase

Similar to Slk19, CENP-F is also a dynamic chromosomal passenger protein that localizes to KTs in metaphase and localizes to the spindle midzone in anaphase (Rattner et al., 1993),(Xueliang Zhu et al., 1995),(Richmond et al., 2013),(Kitagawa & Hieter, 2001). Unlike CENP-F, Slk19 is present at the spindle already in metaphase and remains bound to KTs also in anaphase. In this study, Slk19 was shown to promote ipMT stabilization by promoting enhanced MT crosslinking (at least in metaphase; Figure 14 and Figure 19). So far it is unknown whether CENP-F also promotes crosslinking at its spindle localization. However, CENP-F possesses two MT-binding domains at either end of the molecule (Musinipally et al., 2013). Thus, it theoretically possesses the required properties for a MT-crosslinking function (like the fission yeast Slk19 homolog Alp7 that can also crosslink MTs, as mentioned in chapter 5.2.6). It was shown that neither the N-terminal nor the C-terminal MBD lead to increased MT crosslinking individually *in vitro* (Musinipally et al., 2013). Nevertheless, it would be most interesting to test whether CENP-F, as bipartite protein and functional homodimer (X. Zhu et al., 1995), is able to promote MT crosslinking in anaphase.

In summary, the functional similarities between budding yeast Slk19 and its human orthologue CENP-F are extraordinarily high. Thus, the functional insights gained on Slk19 using the comparatively simple model organism, *Saccharomyces cerevisiae*, could point the way for new research aspects on human CENP-F and could eventually give rise to new important insights into the CENP-F function in human cells.

6 Appendix

Statistical data:

For phenotype analyses, the table below lists the most common phenotypes with the respective absolute and/or relative frequencies and the total number of analyzed cells. Observed phenotypes were classified into different categories, which are listed under the respective table. For quantitative protein analyses, the table below lists the respective mean value and the number of measurements. Unless otherwise stated, two individual experiments (Exp.1/Exp.2) were performed from which the standard deviation (S.D.) was calculated (as described in the Methods chapter).

Figure 1A, Figure 3A and B, a Slk19 sequestering phenotype	Functional sequestering (% cells) [1]	∑Observed cells
WT	96.6	290
'Δstu2'	85.8	120
slk19Δ1-77	77.5	173
slk19ΔGD	86.5	104
slk19Δcc2	90.7	345
slk19Δcc3-5	96.1	127
slk19-cc1+2-cc6+7	91.1	101

[1] Remaining cells showed functional sequestering but with remaining Slk19 signal at the collapsed spindle.

Figure 1A and B, Figure 3A Slk19 sequestering phenotype	Only basal binding at uaKTs, defective sequestering (% cells)	∑Observed cells
'Δstu1'	96.3[1]	108
'Δstu2' 'Δstu1'	93.8[1]	112
'ndc80'	90.2[2]	123
slk19Δcc1	82.4[3]	91
slk19Δcc1+2	82.4[3]	111
slk19Δ1-708	85.5[3]	131

[1] Remaining cells showed localization only at collapsed spindle. [2] Remaining cells showed diffuse Slk19 signal. [3] Remaining cells showed localization only at collapsed spindle (5.4–12.2 %) or a diffuse signal (2.3–12.6 %).

Figure 1C Slk19 sequestering phenotype	Defective sequestering and basal binding, localization only at collapsed spindle (% cells)	∑Observed cells
'Δspc105'	86.9[1]	298

[1] Remaining cells showed sequestered (7 %) or partially sequestered Slk19 (6 %), probably due to incomplete Spc105 depletion.

Figure 1C, Figure 3A, Figure 5A, a Slk19 sequestering phenotype	No Slk19 localization (% cells)	∑Observed cells
'Δspc105' 'Δstu1'	89.1[1]	110
slk19Δcc6+7	100	100
slk19Δcc6	100	100
slk19Δcc7	100	100
slk19Δcc6+7-GCN4-Zipper	100	100

[1] Remaining cells still showed binding at uaKTs (8.2 %) or at SPBs (2.7 %), probably due to incomplete protein depletion.

Figure 5B, a Slk19 sequestering phenotype	Ectopic Slk19 clusters (% cells)	∑Observed cells
slk19Δcc6+7-CIN8-TD	73.11[1]	119

[1] Remaining cells showed diffuse Slk19 signal.

Figure 3B, b and C Stu1 sequestering phenotype	Functional sequestering (% cells)[1]	∑Observed cells
SLK19	93.8	112
slk19Δ1-77	64.2	134
slk19ΔGD	76.1	159
slk19Δcc3-5	88.2	136
slk19Δcc2	90.7	345
slk19-cc1+2-cc6+7	79.5	122

[1] Remaining cells showed functional sequestering but with remaining Slk19 signal at the collapsed spindle.

Figure 3C and Figure 5A, b and B, b Stu1 sequestering phenotype	Defective sequestering. basal Stu1 binding at uaKTs (% cells)	∑Observed cells
slk19Δcc1	100	100
slk19Δcc1+2	100	100
slk19Δcc6+7	100	100
slk19Δcc6+7-GCN4-Zipper	100	100
slk19Δcc6+7-CIN8-TD	100	100

Figure 6B Slk19-Stu1 CoIP with Nz-treated cells	Mean normalized* signal intensity, CoIP relative to IP [a.u.]	Statistics: two-tailed unpaired t-test
Slk19	1.00 (0.20)	-
Slk19ΔGD	0.94 (0.11)	p = .7576 compared to *WT*
Slk19Δcc1	0.36 (0.05)	p = .0489 compared to *WT*
Slk19Δcc1+2	0.34 (0.07)	p = .0487 compared to *WT*
Slk19Δcc6+7	0.20 (0.10)	p = .0379 compared to *WT*
Slk19Δ1-708	0.35 (0.02)	p = .0459 compared to *WT*

* Normalized to *WT* (*WT* = 1).

Figure 7A Metaphase cells	∑Observed cells (Exp.1/Exp.2)	*WT* phenotypes [1]	Observed cells	% cells	S.D. between two experiments [%]
WT	239 (n_1=120/n_2=119)	Slk19 clearly recognizable at spindle and at KTs	180	75.31	1.92
		Slk19 localizes predominantly to KTs, spindle localization unclear	59	24.69	1.92

Figure 7A Metaphase cells	∑Observed cells (Exp.1/Exp.2)	Cell categories	Observed cells	% cells	S.D. between two experiments [%]	Statistics: Two-tailed Fisher exact test
WT	239 (n_1=120/n_2=119)	Slk19 localization at KTs or at spindle and KTs	239	100	0	-
'Δspc105'	204 (n_1=96/n_2=108)	Slk19 localization at spindle only (between KTs) [2]	204	100	0	$p < .0001$ compared to *WT*

[1] Cells with declustered KTs, very small inter-KT distance and/or very short spindle length were not suitable for observation of distinct Slk19 localizations and thus were excluded from the statistics (on average 19.23 % of population). [2] Cells with remaining localization of Slk19 at KTs, probably due to incomplete depletion of Spc105, were excluded from the statistics (on average 15.78 % of population).

Figure 7B Quantitative ChIP	Normalized* enrichment (%) of centromeric over non-centromeric DNA (S.D.)**	Statistics: two-tailed unpaired t-test
WT	100 (23.91)	-
'Δspc105'	10.09 (13.18)	$p < .0001$ compared to *WT*

* Normalized to *WT* (*WT* = 100%). ** S.D. calculated from two individual experiments, each with three technical replicates.

Figure 7C Longitudinal RGB-plots	∑Observed cells (Exp.1/Exp.2)*
WT	32 (n_1=16/n_2=16)
'Δspc105'	28 (n_1=14/n_2=14)

* Mean value curves were calculated from the indicated number of cells. Figure 7C shows the average of the mean value curves obtained from two individual experiments as well as the associated standard deviations.

Figure 8A Metaphase cells	Slk19 localization at KTs and/or spindles [1]	∑Observed cells (Exp.1/Exp.2)	% cells	S.D. between two experiments [%]	Statistics: Two-tailed Fisher exact test*
WT	319	319 (n1=152/n2=167)	100	0	-
slk19Δ1-708	274	286 (n_1=146/n_2=140)	95.83	1.85	p < .0001
slk19Δcc3-5	294	294 (n_1=142/n_2=152)	100	0	p = 1
slk19Δcc2	281	281 (n_1=160/n_2=121)	100	0	p = 1
slk19Δcc1	210	243 (n_1=122/n_2=121)	86.44	6.32	p < .0001
slk19ΔGD	277	277 (n_1=148/n_2=129)	100	0	p = 1

Figure 8A Metaphase cells	Slk19 no localization/ diffuse [1]	∑Observed cells (Exp.1/Exp.2)	% cells	S.D. between two experiments [%]	Two-tailed Fisher exact test*
slk19Δcc6-7	245	245 (n_1=127/n_2=118)	100	0	p < .0001

* Compared to *WT*. [1] Cells were sorted into two categories: Type 1: Slk19 localization at KTs and/or spindles; Type 2: Slk19 no localization/ diffuse.

Figure 8B Metaphase cells (+IAA)	Slk19 localization at spindle only (between KTs) [1]	∑Observed cells (Exp.1/Exp.2)	% cells	S.D. between two experiments [%]	Statistics: Two-tailed Fisher exact test*
'Δspc105'	204	204 (n_1=96/n_2=108)	100	0	-
slk19Δcc3-5 'Δspc105'	246	246 (n_1=130/n_2=116)	100	0	p = 1
slk19Δcc2 'Δspc105'	240	240 (n_1=124/n_2=116)	100	0	p = 1
slk19ΔGD 'Δspc105'	198	198 (n_1=110/n_2=88)	100	0	p = 1

Figure 8B Metaphase cells (+IAA)	Slk19 no localization/diffuse [1]	∑Observed cells (Exp.1/Exp.2)	% cells	S.D. between two experiments [%]	Statistics: Two-tailed Fisher exact test*
slk19Δcc1 'Δspc105'	212	212 (n_1=115/n_2=97)	100	0	p < .0001
slk19Δ1-708 'Δspc105'	194	266 (n_1=147/n_2=119)	72.87 [2]	0.85	p < .0001
slk19Δcc6-7 'Δspc105'	71	71	100	-	p < .0001

* Compared to *'Δspc105'*. [1] Cells with remaining localization of Slk19 at KTs, probably due to incomplete depletion of Spc105, were excluded from the statistics (on average 13.58 % of population). Cells were sorted into two categories: Type 1: Slk19 localization at spindle only (between KTs); Type 2: Slk19 no localization/ diffuse. [2] Note: remaining cells showed only a very weak residual spindle localization of Slk19 (compared to *WT*).

Figure 8C Anaphase cells	Slk19 localization at KTs and midzone [1]	∑Observed cells	% cells	S.D. between two experiments	Statistics: Two-tailed Fisher exact test*
WT	127	194	65.58	0.95	-
slk19Δcc3-5	166	247	67.21	2.68	p = .7607
slk19Δcc2	96	181	53.13	1.54	p = .0157
slk19ΔGD	139	199	69.96	6.04	p = .3886

Figure 8C Anaphase cells	Slk19 localization only at KTs [1]	∑Observed cells	% cells	S.D. between two experiments	Statistics: Two-tailed Fisher exact test*
slk19Δ1-708	247	277	89.52	4.47	p < .0001
slk19Δcc1	217	217	100	0	p < .0001

Figure 8C Anaphase cells	Slk19 no localization/ diffuse [2]	∑Observed cells	% cells	S.D. between two experiments	Statistics: Two-tailed Fisher exact test*
slk19Δcc6-7	200	200	100	0	p < .0001

* Compared to *WT*. [1] Anaphase cells were sorted into two categories: Type 1: Slk19 localization at KTs and midzone; Type 2: Slk19 localization only at KTs. [2] For *slk19Δcc6-7,* cells were categorized as Type 1: Slk19 no localization/ diffuse; Type 2: Slk19 localization at KTs or at KT and midzone (*WT* localizations).

Figure 9 Spindle phenotypes	% cells (S.D.) 0.5–2.0 µm with nrMTs	% cells (S.D.) 2.0–3.0 µm with nrMTs	% cells (S.D.) 0.5–2.0 µm without nrMTs	% cells (S.D.) 2.0–3.0 µm without nrMTs	∑Observed cells (Exp.1/Exp.2)	Statistics: chi-square statistic
WT	3.04 (3.15)	24.72 (6.43)	11.49 (3.60)	60.75 (0.32)	237 (n_1=123/n_2=114)	-
Δslk19	48.77 (0.04)	2.35 (1.20)	42.71 (0.70)	6.17 (1.94)	324 (n_1=125/n_2=199)	p < .0001*
slk19Δcc1	53.91 (0.27)	1.23 (0.57)	40.34 (2.56)	4.52 (1.72)	243 (n_1=122/n_2=121)	p < .0001* p = .474**

* Compared to *WT*. ** compared to *Δslk19*.

Figure 10A Phenotypes	Slk19 localization at collapsed spindle	∑Observed cells (Exp.1/Exp.2)	% cells	S.D. between two experiments
'Δstu1'	249	249 (n_1=127/n_2=122)	100	0

Figure 10A Phenotypes	Slk19 localization at spindle only (between KTs)	∑Observed cells (Exp.1/Exp.2)	% cells	S.D. between two experiments
'Δspc105'	204	242 (n_1=118/n_2=124)	84.22[1]	4.05

Figure 10A Phenotypes	Slk19 no localization/ diffuse	∑Observed cells (Exp.1/Exp.2)	% cells	S.D. between two experiments
'Δstu1' Δspc105'	175	266 (n_1=127/n_2=139)	65.91[2]	3.67

[1] Remaining cells still showed localization of Slk19 at KTs, probably due to incomplete depletion of Spc105.
[2] Remaining cells showed a weak Slk19 signal at the spindle.

Figure 10C Stu1-Slk19 CoIP with metaphase-arrested cells	Mean normalized* signal intensity, CoIP relative to IP [a.u.]	Statistics: two-tailed unpaired t-test
Slk19	1.00 (0.14)	-
Slk19Δcc1	0.46 (0.08)	p = .0409 compared to *WT*

* Normalized to *WT* (*WT* = 1).

Figure 11A Phenotypes	Slk19 localization mainly at KTs (spindle localization unclear)	∑Observed cells (Exp.1/Exp.2)	% cells	S.D. between two experiments
stu1ΔCL	218	245 (n_1=/n_2=)	88.96[1]	1.02

Figure 11A Phenotypes	Weak localization at spindle	∑Observed cells (Exp.1/Exp.2)	% cells	S.D. between two experiments
stu1ΔCL 'Δspc105'	186	232 (n_1=116/n_2=116)	80.17[2]	7.31

Figure 11A Phenotypes	Slk19 no localization/ diffuse	∑Observed cells (Exp.1/Exp.2)	% cells	S.D. between two experiments
stu1ΔCL 'Δspc105' Δase1	260	260 (n_1=119/n_2=141)	100	0

Figure 11A Phenotypes	Slk19 localization at collapsed spindle	∑Observed cells (Exp.1/Exp.2)	% cells	S.D. between two experiments
'Δspc105' Δase1	211	252 (n_1=118/n_2=134)	83.84[3]	2.48

Figure 11A Phenotypes	Ase1 localization at metaphase spindles	∑Observed cells (Exp.1/Exp.2)	% cells	S.D. between two experiments
WT	200	200 (n_1=100/n_2=100)	100	0
stu1ΔCL	262	262 (n_1=119/n_2=143)	100	0

Figure 11A Phenotypes	Long spindles (spindles ≥ 2 µm)	∑Observed cells (Exp.1/Exp.2)	% cells	S.D. between two experiments
stu1ΔCL Δslk19	165	221 (n_1=105/n_2=116)	74.64[4]	0.51

[1] Remaining cells showed a weak Slk19 signal at the spindle. [2] Remaining cells showed residual Slk19 localization at KTs (spindle localization unclear). [3] Remaining cells showed a diffuse Slk19 signal (no localization). [4] Remaining cells had spindles < 2 µm.

Figure 11B Slk19 intensity in different cell types	Slk19 intensity normalized to mean spindle length [a.u.]	S.D. between two experiments [a.u.]	∑Observed cells (Exp.1/Exp.2)	Statistics: two-tailed unpaired t-test
'Δspc105'	45.51	2.35	300 (n_1=194/n_2=106)	-
'Δspc105' Δase1	33.17	2.04	185 (n_1=91/n_2=94)	p < .0001*
stu1ΔCL 'Δspc105'	14.72	2.87	169 (n_1=80/n_2=89)	p < .0001*
stu1ΔCL 'Δspc105' Δase1	2.90	0.13	206 (n_1=102/n_2=104)	p < .0001* p < .0001** p < .0001***

* Compared to *'Δspc105'*. ** compared to *'Δspc105' Δase1*. *** compared to *stu1ΔCL 'Δspc105'*.

Figure 12B Protein amounts at short metaphase spindles	Mean signal intensity of indicated protein (S.D.) [a.u.] at short spindles 1.8 +/- 0.2 µm	∑Observed cells (Exp.1/Exp.2)	Statistics: two-tailed unpaired t-test*
SLK19	Ase1: 72.12 (18.88) Stu1: 55.76 (8.31) Tub1: 129.42 (8.52)	100 (n_1=53/n_2=47)	-
Δslk19	Ase1: 9.19 (3.58) Stu1: 34.31 (7.47) Tub1: 91.58 (6.08)	106 (n_1=53/n_2=53)	Ase1: p < .0001 Stu1: p < .0001 Tub1: p < .0001
slk19Δcc1	Ase1: 12.50 (4.64) Stu1: 28.31 (6.57) Tub1: 94.63 (1.81)	88 (n_1=42/n_2=46)	Ase1: p < .0001 Stu1: p < .0001 Tub1: p < .0001
Δslk19, SLK19::LYS2	Ase1: 98.94 (7.56) Stu1: 96.14 (5.42) Tub1: 124.20 (1.79)	108 (n_1=68/n_2=40)	Ase1: p < .0001 Stu1: p < .0001 Tub1: p = .8684

Figure 12B Protein amounts at long metaphase spindles	Mean signal intensity of indicated protein (S.D.) [a.u.] at long spindles 2.4 +/- 0.2 µm	∑Observed cells (Exp.1/Exp.2)	Statistics: two-tailed unpaired t-test*
SLK19	Ase1: 80.62 (11.25) Stu1: 60.19 (2.01) Tub1: 148.29 (6.80)	97 (n_1=56/n_2=41)	-
Δslk19	Ase1: 10.49 (1.39) Stu1: 41.97 (2.49) Tub1: 125.34 (2.38)	176 (n_1=75/n_2=101)	Ase1: p < .0001 Stu1: p < .0001 Tub1: p < .0001
slk19Δcc1	Ase1: 16.20 (6.36) Stu1: 38.61 (8.96) Tub1: 122.92 (6.29)	115 (n_1=58/n_2=57)	Ase1: p < .0001 Stu1: p < .0001 Tub1: p < .0001
Δslk19, SLK19::LYS2	Ase1: 107.14 (1.15) Stu1: 108.20 (2.23) Tub1: 134.52 (0.82)	115 (n_1=62/n_2=53)	Ase1: p < .0001 Stu1: p < .0001 Tub1: p = .0055

* Compared to *WT*.

Figure 13B Quantification Western blot analysis	Mean normalized* signal intensity of Stu1 (S.D.)** [a.u.]	Statistics: two-tailed unpaired t-test
WT	1.00 (0.35)	-
Δslk19	1.02 (0.08)	p =.9009

Figure 13B Quantification Western blot analysis	Mean normalized* signal intensity of Ase1 (S.D.)** [a.u.]	Statistics: two-tailed unpaired t-test
WT	1.00 (0.28)	-
Δslk19	0.49 (0.10)	p = .0014
slk19Δcc1	0.60 (0.04)	p = .0059

* Normalized to *WT* (*WT* = 1). ** S.D. calculated from two individual experiments, each with three technical replicates.

Figure 14A Longitudinal RGB-plots	∑Observed cells (Exp.1/Exp.2)*
SLK19	35 (n_1=18/n_2=17)
Δslk19	35 (n_1=18/n_2=17)
slk19Δcc1	35 (n_1=18/n_2=17)
Δslk19, SLK19::LYS2	35 (n_1=17/n_2=18)

* Mean value curves were calculated from the indicated number of cells. Figure 14A shows the average of the mean value curves obtained from two individual experiments as well as the associated standard deviations.

Figure 14B Cross-sections	Mean max. Tub1 signal intensity (S.D.) [a.u.]	∑Observed cells (Exp.1/Exp.2)*	Statistics: two-tailed unpaired t-test
SLK19	$Tub1_{max}$= 186.20 (10.59)	171 (n_1=90/n_2=81)	-
Δslk19	$Tub1_{max}$= 137.48 (12.35)	186 (n_1=98/n_2=88)	p < .0001 compared to *WT*
slk19Δcc1	$Tub1_{max}$= 158.31 (3.01)	191 (n_1=101/n_2=90)	p < .0001 compared to *WT*
Δslk19, SLK19::LYS2	$Tub1_{max}$= 175.45 (2.28)	179 (n_1=83/n_2=96)	p = .0220 compared to *WT* p < .0001 compared to *Δslk19*

* Mean value curves were calculated from the indicated number of cells. Figure 14B shows the average of the mean value curves obtained from two individual experiments as well as the associated standard deviations.

Figure 15B Ase1 localization	Acentric maximum % cells (S.D.)	No defined maximum % cells (S.D.)	Centered maximum % cells (S.D.)	∑Observed cells (Exp.1/Exp.2)	Statistics: chi-square statistic
WT	10.65 (1.42)	5.11 (1.02)	84.24 (2.43)	217 (n_1=114/n_2=103)	-
Δslk19	46.51 (0.11)	11.63 (1.84)	41.86 (1.95)	172 (n_1=86/n_2=86)	p < .0001 compared to *WT*
stu1ΔCL	16.95 (2.22)	12.63 (3.89)	70.42 (1.68)	159 (n_1=78/n_2=81)	p = .0034 compared to *WT*

Figure 15B Stu1 localization	Acentric maximum % cells (S.D.)	No defined maximum % cells (S.D.)	Centered maximum % cells (S.D.)	∑Observed cells (Exp.1/Exp.2)	Statistics: chi-square statistic
WT	10.60 (0.11)	7.44 (1.84)	81.96 (1.95)	217 (n_1=114/n_2=103)	-
Δslk19	20.35 (4.11)	59.88 (5.76)	19.77 (1.64)	172 (n_1=86/n_2=86)	p < .0001 compared to *WT*
stu1ΔCL	10.04 (1.51)	75.52 (3.79)	14.43 (2.28)	159 (n_1=78/n_2=81)	p < .0001 compared to *WT*

Figure 17B *In vitro* enrichment of Ase1 via Slk19	Mean normalized* Ase1 signal intensity (S.D.) [a.u.]	∑Number of measurements (Exp.1/Exp.2)	Average length measured [µm] (Exp.1/Exp.2)	Statistics: two-tailed unpaired t-test
Ase1	2.46 (0.04)	222 (n_1=109/n_2=113)	l_1=10.35 / l_2=10.36	-
Ase1+Slk19	8.81 (0.83)	207 (n_1=103/n_2=104)	l_1=10.35 / l_2=10.28	p < .0001 compared to Ase1

Figure 17B *In vitro* enrichment of Stu1 via Slk19	Mean normalized* Stu1 signal intensity (S.D.) [a.u.]	∑Number of measurements (Exp.1/Exp.2)	Average length measured [µm] (Exp.1/Exp.2)	Statistics: two-tailed unpaired t-test
Stu1	1.55 (0.02)	213 (n_1=107/n_2=106)	l_1=11.17 / l_2=10.70	-
Stu1+Slk19	2.58 (0.18)	213 (n_1=108/n_2=105)	l_1=10.56 / l_2=10.51	p < .0001 compared to Stu1

* Normalized to MT length measured.

Figure 19B Enhanced crosslinking via Slk19	sum of overlaps [µm] / sum of Rho-MT [cm] (S.D.)	Sum of Rho-MT measured [µm] (Exp.1/Exp.2)	Statistics: two-tailed unpaired t-test
neg. control	28.86 (25.68)	7508.8 / 7417.9	-
Slk19	52.21 (7.33)	6798.6 / 8642.5	p = .3417 compared to neg. control
Ase1	476.28 (21.33)	7750.9 / 7165.6	p = .0040 compared to neg. control
Stu1	871.78 (71.18)	7141.1 / 7845.8	p = .0028 compared to neg. control
Ase1+Slk19	1434.28 (125.29)	7889.0 / 7226.1	p = .0087 compared to Ase1 p = .0041 compared to neg. control
Stu1+Slk19	2363.88 (280.96)	7460.6 / 9778.0	p = .0184 compared to Stu1 p = .0072 compared to neg. control
Ase1+Slk19Δcc1	428.06 (23.14)	11250.0 / 9471.5	p = .1625 compared to Ase1 p = .0037 compared to neg. control
Stu1+Slk19Δcc1	780.36 (118.39)	8361.3 / 7929.8	p = .4481 compared to Stu1 p = .0128 compared to neg. control
Ase1+Stu1	1180.49 (176.18)	7737.3 / 9700.5	p = .0117 compared to neg. control
Ase1+Stu1+Slk19	2736.34 (439.19)	7812.6 / 7572.0	p = .0433 compared to Stu1+Ase1 p = .0130 compared to neg. control

Figure 19C Crosslinking - premixed *vs.* successive	sum of overlaps [µm] / sum of Rho-MT [cm] (S.D.)	Sum of Rho-MT measured [µm] (Exp.1/Exp.2)	Statistics: two-tailed unpaired t-test
Ase1+Slk19, premixed	1434.28 (125.29)	7889.0 / 7226.1	-
Ase1+Slk19, successive	621.51 (1.93)	6328.8 / 7688.4	p = .0117 compared premix p = .0107 compared to Ase1 alone p = .0009 compared to neg. control
Stu1+Slk19, premixed	2363.88 (280.96)	7460.6 / 9778.0	-
Stu1+Slk19, successive	2316.27 (438.08)	7764.4 / 7631.2	p = .9089 compared premix p = .0179 compared to neg. control

Figure 21B Spindle phenotypes	Monopolar spindle % cells (S.D.)	Bipolar spindle % cells (S.D.)	∑Observed cells (Exp.1/Exp.2)
WT	3.54 (0.02)	96.47 (0.02)	396 (n_1=197/n_2=199)
Δslk19	7.09 (2.31)	92.91 (2.31)	378 (n_1=183/n_2=195)
Slk19-OE	29.42 (3.82)	70.58 (3.82)	281 (n_1=116/n_2=165)
Stu1-OE	43.15 (4.17)	56.85 (4.17)	676 (n_1=366/n_2=310)
Stu1-OE, *Δslk19*	63.85 (1.91)	36.15 (1.91)	372 (n_1=96/n_2=276)
Stu1-OE, Slk19-OE	29.87 (2.59)	70.13 (2.59)	227 (n_1=120/n_2=107)

Figure 21C Bipolar spindle lengths	Mean spindle length [µm]	∑Observed cells	Statistics: two-tailed unpaired t-test
Stu1-OE	1.41	157	-
Stu1-OE, *Δslk19*	1.34	108	p = .4437 compared to Stu1-OE
Stu1-OE, Slk19-OE	2.69	156	p < .0001 compared to Stu1-OE

Figure 23 Directionality of crosslinking	Parallel crosslinking % of observed MT pairs	Antiparallel crosslinking % of observed MT pairs	∑Counted MT pairs
Stu1	48.19	51.81	83
Stu1+Slk19	47.50	52.50	80
Ase1	28.79	71.21	66
Ase1+Slk19	32.05	67.95	78

Figure 24A Spindle length	Spindle length (S.D.) [µm]	∑Number of measurements (Exp.1/Exp.2)	Statistics: two-tailed unpaired t-test
WT	1.66 (0.16)	221 (n_1=106/n_2=115)	-
'Δspc105'	1.49 (0.03)	220 (n_1=109/n_2=111)	p < .0001 compared to *WT*

Figure 24A kMT length	kMT length (S.D.) [µm]	∑Number of measurements (Exp.1/Exp.2)	Statistics: two-tailed unpaired t-test
WT	0.48 (0.01)	230 (n_1=117/n_2=113)	-
'Δspc105'	0.32 (0.02)	243 (n_1=127/n_2=116)	p < .0001 compared to *WT*

Figure 24A KT-KT distance	KT-KT distance (S.D.) [µm]	∑Number of measurements (Exp.1/Exp.2)	Statistics: two-tailed unpaired t-test
WT	0.67 (0.02)	213 (n_1=107/n_2=106)	-
'Δspc105'	0.86 (0.04)	205 (n_1=103/n_2=102)	p < .0001 compared to *WT*

Figure 24B Spindle length	Spindle length (S.D.) [µm]	∑Number of measurements (Exp.1/Exp.2)	Statistics: two-tailed unpaired t-test
WT	2.64 (0.30)	207 (n_1=100/n_2=107)	-
STU1, stu1ΔTOGL1	2.46 (0.02)	221 (n_1=113/n_2=108)	p = .0006 compared to *WT*

Figure 24B kMT length	kMT length (S.D.) [µm]	∑Number of measurements (Exp.1/Exp.2)	Statistics: two-tailed unpaired t-test
WT	0.85 (0.12)	279 (n_1=130/n_2=149)	-
STU1, stu1ΔTOGL1	0.46 (0.11)	260 (n_1=120/n_2=140)	p < .0001 compared to *WT*

Figure 24B KT-KT distance	KT-KT distance (S.D.) [µm]	∑Number of measurements (Exp.1/Exp.2)	Statistics: two-tailed unpaired t-test
WT	0.97 (0.03)	225 (n_1=114/n_2=111)	-
STU1, stu1ΔTOGL1	1.48 (0.2)	234 (n_1=106/n_2=128)	p < .0001 compared to *WT*

Figure 24D Longitudinal RGB-plots	∑Observed cells (Exp.1/Exp.2)*
WT	22 (n_1=11/n_2=11)
STU1, stu1ΔTOGL1	31 (n_1=16/n_2=15)

* Mean value curves were calculated from the indicated number of cells. Figure 24D shows the average of the mean value curves obtained from two individual experiments as well as the associated standard deviations.

Figure 24E Quantitative ChIP	Normalized* enrichment (%) of centromeric over non-centromeric DNA (S.D.)**	Statistics: two-tailed unpaired t-test
WT	100 (23.91)	-
STU1, stu1ΔTOGL1	82.77 (15.04)	p = .1093 compared to *WT*

* Normalized to *WT* (*WT* = 100%). ** S.D. calculated from two individual experiments, each with three technical replicates.

Figure 25A *'Δscc1'* phenotype	Slk19 only at KT (% cells)	Slk19 sequestered at uaKT (% cells)	∑Observed cells
'Δscc1'	40	60	100

Figure 25B *'Δscc1' stu1ΔTOGL1* phenotype	Slk19 only at KT (% cells)	Slk19 at spindle and at KT (% cells)	∑Observed cells
Scc1 depletion in G1	72	28	200
Scc1 depletion in metaphase	26.54	73.46	162

Figure 26B Normalized* longitudinal RGB-plots	∑Observed cells (Exp.1/Exp.2)*
WT	22 (n_1=11/n_2=11)
ndc80Δ1-116	18 (n_1=10/n_2=8)
STU1, stu1ΔTOGL1	31 (n_1=16/n_2=15)

* Normalized to values ranging from 0–1.

Figure 28B Length of Stu1-GFP spread at the anaphase spindle	Mean spindle length [µm]	∑Observed cells	Statistics: two-tailed unpaired t-test
SLK19	2.28	182	-
slk19ΔGD	3.01	147	$p < 0.0001$
slk19Δcc1	3.51	188	$p < 0.0001$
slk19Δcc1+2	3.86	106	$p < 0.0001$
slk19Δcc2	2.37	122	$p = .2623$
slk19Δcc6+7	2.46	141	$p = .0258$
Δslk19	4.35	109	$p < 0.0001$

Figure 31A D4-dependent Stu1 binding In *'Δstu1', stu1ΔML* cells	Stu1ΔML at the anaphase spindle center (% cells)	No Stu1ΔML at anaphase spindle (% cells)	Metaphase cells (% cells)	∑Observed cells
SLK19	32.8	21.1	46.1	323
Δslk19	0.4	14.3	85.3	272
Δslk19 ase1-7A	8.9	15.3	75.8	157
Δspo12	17.5	20.8	61.7	149
Δslk19, Cdc14-OE	2.0	3.6	94.4	196
slk19Δcc6+7	7.4	6.6	86.0	113
slk19ΔGD	20.3	28.8	50.9	222
slk19Δcc1+2	9.8	12.5	77.7	264

Figure 32 D4-GFP spindle binding	D4 spindle binding (% cells)	No D4 spindle binding (% cells)	∑Observed cells (Exp.1/Exp.2)
SLK19	0	100	230 (n_1=117/n_2=113)
SLK19, Cdc14-OE	58.5	41.4	290 (n_1=111/n_2=179)
Δslk19, Cdc14-OE	0	100	200 (n_1=100/n_2=100)

7 References

Akhmanova, A., Hoogenraad, C. C., Drabek, K., Stepanova, T., Dortland, B., Verkerk, T., Vermeulen, W., Burgering, B. M., De Zeeuw, C. I., Grosveld, F., & Galjart, N. (2001). CLASPs Are CLIP-115 and -170 Associating Proteins Involved in the Regional Regulation of Microtubule Dynamics in Motile Fibroblasts. *Cell*, *104*(6), 923–935. https://doi.org/10.1016/S0092-8674(01)00288-4

Akiyoshi, B., Nelson, C. R., Ranish, J. A., & Biggins, S. (2009). Analysis of Ipl1-Mediated Phosphorylation of the Ndc80 Kinetochore Protein in Saccharomyces cerevisiae. *Genetics*, *183*(4), 1591. https://doi.org/10.1534/GENETICS.109.109041

Akiyoshi, B., Sarangapani, K. K., Powers, A. F., Nelson, C. R., Reichow, S. L., Arellano-Santoyo, H., Gonen, T., Ranish, J. A., Asbury, C. L., & Biggins, S. (2010). Tension directly stabilizes reconstituted kinetochore-microtubule attachments. *Nature*, *468*(7323), 576–579. https://doi.org/10.1038/nature09594

Al-Bassam, J., & Chang, F. (2011). Regulation of microtubule dynamics by TOG-domain proteins XMAP215/Dis1 and CLASP. *Trends in Cell Biology*, *21*(10), 604–614. https://doi.org/10.1016/j.tcb.2011.06.007

Al-Bassam, J., Larsen, N. A., Hyman, A. A., & Harrison, S. C. (2007). Crystal Structure of a TOG Domain: Conserved Features of XMAP215/Dis1-Family TOG Domains and Implications for Tubulin Binding. *Structure*, *15*(3), 355–362. https://doi.org/10.1016/J.STR.2007.01.012/ATTACHMENT/6B897AE6-97E4-4204-8459-DAB9648352FB/MMC1.PDF

Alberti, S., Gladfelter, A., & Mittag, T. (2019). Considerations and Challenges in Studying Liquid-Liquid Phase Separation and Biomolecular Condensates. *Cell*, *176*(3), 419–434. https://doi.org/10.1016/J.CELL.2018.12.035

Alberti, S., Saha, S., Woodruff, J. B., Franzmann, T. M., Wang, J., & Hyman, A. A. (2018). A User's Guide for Phase Separation Assays with Purified Proteins. *Journal of Molecular Biology*, *430*(23), 4806–4820. https://doi.org/10.1016/J.JMB.2018.06.038

Alberts, B., Johnson, A., Lewis, J., Raff, M., Roberts, K., & Walter, P. (2002). *An Overview of M Phase*. https://www.ncbi.nlm.nih.gov/books/NBK26931/

Alexandru, G., Uhlmann, F., Mechtler, K., Poupart, M. A., & Nasmyth, K. (2001). Phosphorylation of the Cohesin Subunit Scc1 by Polo/Cdc5 Kinase Regulates Sister Chromatid Separation in Yeast. *Cell*, *105*(4), 459–472. https://doi.org/10.1016/S0092-8674(01)00362-2

Allingham, J. S., Sproul, L. R., Rayment, I., & Gilbert, S. P. (2007). Vik1 Modulates Microtubule-Kar3 Interactions through a Motor Domain that Lacks an Active Site. *Cell*, *128*(6), 1161–1172. https://doi.org/10.1016/J.CELL.2006.12.046

Andy Choo, K. H. (2001). Domain Organization at the Centromere and Neocentromere. In *Developmental Cell* (Vol. 1, Issue 2, pp. 165–177). Cell Press. https://doi.org/10.1016/S1534-5807(01)00028-4

Aravamudhan, P., Chen, R., Roy, B., Sim, J., & Joglekar, A. P. (2016). Dual mechanisms regulate the recruitment of spindle assembly checkpoint proteins to the budding yeast kinetochore. *Molecular Biology of the Cell*, *27*(22), 3405. https://doi.org/10.1091/MBC.E16-01-0007

Aravamudhan, P., Goldfarb, A. A., & Joglekar, A. P. (2015). The kinetochore encodes a mechanical switch to disrupt spindle assembly checkpoint signalling. *Nature Cell Biology*, *17*(7), 868–879. https://doi.org/10.1038/ncb3179

Avena, J. S., Burns, S., Yu, Z., Ebmeier, C. C., Old, W. M., Jaspersen, S. L., & Winey, M. (2014). Licensing of Yeast Centrosome Duplication Requires Phosphoregulation of Sfi1. *PLOS Genetics*, *10*(10), e1004666. https://doi.org/10.1371/JOURNAL.PGEN.1004666

Azzam, R., Chen, S. L., Shou, W., Mah, A. S., Alexandru, G., Nasmyth, K., Annan, R. S., Carr, S.

A., & Deshaies, R. J. (2004). Phosphorylation by cyclin B-Cdk underlies release of mitotic exit activator Cdc14 from the nucleolus. *Science*, *305*(5683), 516–519. https://doi.org/10.1126/SCIENCE.1099402

Bakhoum, S. F., Thompson, S. L., Manning, A. L., & Compton, D. A. (2009). Genome stability is ensured by temporal control of kinetochore-microtubule dynamics. *Nature Cell Biology*, *11*(1), 27. https://doi.org/10.1038/NCB1809

Barrett, J. G., Manning, B. D., & Snyder, M. (2000). The Kar3p kinesin-related protein forms a novel heterodimeric structure with its associated protein Cik1p. *Molecular Biology of the Cell*, *11*(7), 2373–2385. https://doi.org/10.1091/MBC.11.7.2373/ASSET/IMAGES/LARGE/MK0701232009.JPEG

Bernander, R., & Ettema, T. J. G. (2010). FtsZ-less cell division in archaea and bacteria. *Current Opinion in Microbiology*, *13*(6), 747–752. https://doi.org/10.1016/J.MIB.2010.10.005

Bieling, P., Telley, I. A., & Surrey, T. (2010). A Minimal Midzone Protein Module Controls Formation and Length of Antiparallel Microtubule Overlaps. *Cell*, *142*(3), 420–432. https://doi.org/10.1016/J.CELL.2010.06.033

Biggins, S. (2013). The composition, functions, and regulation of the budding yeast kinetochore. *Genetics*, *194*(4), 817–846. https://doi.org/10.1534/genetics.112.145276

Biggins, S., & Murray, A. W. (2001). The budding yeast protein kinase Ipl1/Aurora allows the absence of tension to activate the spindle checkpoint. *Genes & Development*, *15*(23), 3118–3129. https://doi.org/10.1101/GAD.934801

Biggins, S., Severin, F. F., Bhalla, N., Sassoon, I., Hyman, A. A., & Murray, A. W. (1999). The conserved protein kinase Ipl1 regulates microtubule binding to kinetochores in budding yeast. *Genes & Development*, *13*(5), 532. https://doi.org/10.1101/GAD.13.5.532

Blake-Hodek, K. A., Cassimeris, L., & Huffaker, T. C. (2010). Regulation of microtubule dynamics by Bim1 and Bik1, the budding yeast members of the EB1 and CLIP-170 families of plus-end tracking proteins. *Molecular Biology of the Cell*, *21*(12), 2013–2023. https://doi.org/10.1091/MBC.E10-02-0083/ASSET/IMAGES/LARGE/ZMK0121094650007.JPEG

Bloom, J., & Cross, F. R. (2007). Spindle pole body Multiple levels of cyclin specificity in cell-cycle control. *NATURE REVIEWS | MOLECULAR CELL BIOLOGY*, *8*, 149. https://doi.org/10.1038/nrm2105

Bloom, K., & Costanzo, V. (2017). Centromere Structure and Function. In *Progress in molecular and subcellular biology* (Vol. 56, pp. 515–539). NLM (Medline). https://doi.org/10.1007/978-3-319-58592-5_21

Boettcher, B., & Barral, Y. (2013). The cell biology of open and closed mitosis. *Nucleus*, *4*(3), 160. https://doi.org/10.4161/NUCL.24676

Bokros, M., Sherwin, D., Kabbaj, M. H., & Wang, Y. (2021). Yeast Fin1-PP1 dephosphorylates an Ipl1 substrate, Ndc80, to remove Bub1-Bub3 checkpoint proteins from the kinetochore during anaphase. *PLoS Genetics*, *17*(5). https://doi.org/10.1371/JOURNAL.PGEN.1009592

Bomont, P., Maddox, P., Shah, J. V., Desai, A. B., & Cleveland, D. W. (2005). Unstable microtubule capture at kinetochores depleted of the centromere-associated protein CENP-F. *EMBO Journal*, *24*(22), 3927–3939. https://doi.org/10.1038/sj.emboj.7600848

Boyarchuk, Y., Salic, A., Dasso, M., & Arnaoutov, A. (2007). Bub1 is essential for assembly of the functional inner centromere. *Journal of Cell Biology*, *176*(7), 919–928. https://doi.org/10.1083/JCB.200609044

Bratman, S. V., & Chang, F. (2007). Stabilization of Overlapping Microtubules by Fission Yeast CLASP. *Developmental Cell*, *13*(6), 812–827. https://doi.org/10.1016/J.DEVCEL.2007.10.015

Brinkley, B. R., Ouspenski, I., & Zinkowski, R. P. (1992). Structure and molecular organization of

the centromere-kinetochore complex. *Trends in Cell Biology*, *2*(1), 15–20. https://doi.org/10.1016/0962-8924(92)90139-E

Broad, A. J., DeLuca, K. F., & DeLuca, J. G. (2020). Aurora B kinase is recruited to multiple discrete kinetochore and centromere regions in human cells. *Journal of Cell Biology*, *219*(3). https://doi.org/10.1083/JCB.201905144/133701

Bücking-Throm, E., Duntze, W., Hartwell, L. H., & Manney, T. R. (1973). Reversible arrest of haploid yeast cells at the initiation of DNA synthesis by a diffusible sex factor. *Experimental Cell Research*, *76*(1), 99–110. https://doi.org/10.1016/0014-4827(73)90424-2

Bugiel, M., Chugh, M., Jachowski, T. J., Schäffer, E., & Jannasch, A. (2020). The Kinesin-8 Kip3 Depolymerizes Microtubules with a Collective Force-Dependent Mechanism. *Biophysical Journal*, *118*(8), 1958–1967. https://doi.org/10.1016/J.BPJ.2020.02.030

Byers, B., & Goetsch, L. (1974). Duplication of Spindle Plaques and Integration of the Yeast Cell Cycle. *Cold Spring Harbor Symposia on Quantitative Biology*, *38*, 123–131. https://doi.org/10.1101/SQB.1974.038.01.016

Byers, B., & Goetsch, L. (1975). Behavior of spindles and spindle plaques in the cell cycle and conjugation of Saccharomyces cerevisiae. *Journal of Bacteriology*, *124*(1), 511. https://doi.org/10.1128/jb.124.1.511-523.1975

Calzada, A., Sacristán, M., Sánchez, E., & Bueno, A. (2001). Cdc6 cooperates with Sic1 and Hct1 to inactivate mitotic cyclin-dependent kinases. *Nature 2001 412:6844*, *412*(6844), 355–358. https://doi.org/10.1038/35085610

Camahort, R., Li, B., Florens, L., Swanson, S. K., Washburn, M. P., & Gerton, J. L. (2007). Scm3 Is Essential to Recruit the Histone H3 Variant Cse4 to Centromeres and to Maintain a Functional Kinetochore. *Molecular Cell*, *26*(6), 853–865. https://doi.org/10.1016/j.molcel.2007.05.013

Campbell, C. S., & Desai, A. (2013). Tension sensing by Aurora B kinase is independent of survivin-based centromere localization. *Nature 2013 497:7447*, *497*(7447), 118–121. https://doi.org/10.1038/nature12057

Cavanaugh, A. M., & Jaspersen, S. L. (2017). Big Lessons from Little Yeast: Budding and Fission Yeast Centrosome Structure, Duplication, and Function. *Https://Doi.Org/10.1146/Annurev-Genet-120116-024733*, *51*, 361–383. https://doi.org/10.1146/ANNUREV-GENET-120116-024733

Caydasi, A. K., Ibrahim, B., & Pereira, G. (2010). Monitoring spindle orientation: Spindle position checkpoint in charge. *Cell Division 2010 5:1*, *5*(1), 1–15. https://doi.org/10.1186/1747-1028-5-28

Chan, J., Jensen, C. G., Jensen, L. C. W., Bush, M., & Lloyd, C. W. (1999). The 65-kDa carrot microtubule-associated protein forms regularly arranged filamentous cross-bridges between microtubules. *Proceedings of the National Academy of Sciences of the United States of America*, *96*(26), 14931. https://doi.org/10.1073/PNAS.96.26.14931

Chandhok, N. S., & Pellman, D. (2009). A little CIN may cost a lot: revisiting aneuploidy and cancer. In *Current Opinion in Genetics and Development* (Vol. 19, Issue 1, pp. 74–81). Curr Opin Genet Dev. https://doi.org/10.1016/j.gde.2008.12.004

Chee, M. K., & Haase, S. B. (2010). B-Cyclin/CDKs Regulate Mitotic Spindle Assembly by Phosphorylating Kinesins-5 in Budding Yeast. *PLOS Genetics*, *6*(5), e1000935. https://doi.org/10.1371/JOURNAL.PGEN.1000935

Cheeseman, I. M., Anderson, S., Jwa, M., Green, E. M., Kang, J., Yates, J. R., Chan, C. S. M., Drubin, D. G., & Barnes, G. (2002). Phospho-Regulation of Kinetochore-Microtubule Attachments by the Aurora Kinase Ipl1p. *Cell*, *111*(2), 163–172. https://doi.org/10.1016/S0092-8674(02)00973-X

Cheeseman, I. M., Chappie, J. S., Wilson-Kubalek, E. M., & Desai, A. (2006). The Conserved KMN Network Constitutes the Core Microtubule-Binding Site of the Kinetochore. *Cell*, *127*(5), 983–

997. https://doi.org/10.1016/J.CELL.2006.09.039

Cheeseman, I. M., & Desai, A. (2008). Molecular architecture of the kinetochore-microtubule interface. In *Nature Reviews Molecular Cell Biology* (Vol. 9, Issue 1, pp. 33–46). Nature Publishing Group. https://doi.org/10.1038/nrm2310

Cheeseman, I. M., Drubin, D. G., & Barnes, G. (2002). Simple centromere, complex kinetochore: Linking spindle microtubules and centromeric DNA in budding yeast. In *Journal of Cell Biology* (Vol. 157, Issue 2, pp. 199–203). The Rockefeller University Press. https://doi.org/10.1083/jcb.200201052

Cho, U. S., & Harrison, S. C. (2012). Ndc10 is a platform for inner kinetochore assembly in budding yeast. *Nature Structural and Molecular Biology*, *19*(1), 48–56. https://doi.org/10.1038/nsmb.2178

Ciferri, C., Pasqualato, S., Screpanti, E., Varetti, G., Santaguida, S., Reis, G. Dos, Maiolica, A., Polka, J., Luca, J. G. De, Wulf, P. De, Salek, M., Rappsilber, J., Moores, C. A., Salmon, E. D., & Musacchio, A. (2008). Implications for Kinetochore-Microtubule Attachment from the Structure of an Engineered Ndc80 Complex. *Cell*, *133*(3), 427. https://doi.org/10.1016/J.CELL.2008.03.020

Cimini, D., Howell, B., Maddox, P., Khodjakov, A., Degrassi, F., & Salmon, E. D. (2001). Merotelic Kinetochore Orientation Is a Major Mechanism of Aneuploidy in Mitotic Mammalian Tissue Cells. *The Journal of Cell Biology*, *153*(3), 517. https://doi.org/10.1083/JCB.153.3.517

Ciosk, R., Zachariae, W., Michaelis, C., Shevchenko, A., Mann, M., & Nasmyth, K. (1998). An ESP1/PDS1 Complex Regulates Loss of Sister Chromatid Cohesion at the Metaphase to Anaphase Transition in Yeast. *Cell*, *93*(6), 1067–1076. https://doi.org/10.1016/S0092-8674(00)81211-8

Cleveland, D. W., Mao, Y., & Sullivan, K. F. (2003). Centromeres and kinetochores: From epigenetics to mitotic checkpoint signaling. In *Cell* (Vol. 112, Issue 4, pp. 407–421). Elsevier B.V. https://doi.org/10.1016/S0092-8674(03)00115-6

Cohen-Fix, O., Peters, J. M., Kirschner, M. W., & Koshland, D. (1996). Anaphase initiation in Saccharomyces cerevisiae is controlled by the APC-dependent degradation of the anaphase inhibitor Pds1p. *Genes & Development*, *10*(24), 3081–3093. https://doi.org/10.1101/GAD.10.24.3081

Cooper, G. M. (2000a). *Microtubules*. https://www.ncbi.nlm.nih.gov/books/NBK9932/

Cooper, G. M. (2000b). *The Eukaryotic Cell Cycle*. https://www.ncbi.nlm.nih.gov/books/NBK9876/

Cottingham, F. R., Gheber, L., Miller, D. L., & Hoyt, M. A. (1999). Novel Roles for Saccharomyces cerevisiae Mitotic Spindle Motors. *Journal of Cell Biology*, *147*(2), 335–350. https://doi.org/10.1083/JCB.147.2.335

Craig, J. M., Earnshaw, W. C., & Vagnarelli, P. (1999). Mammalian centromeres: DNA sequence, protein composition, and role in cell cycle progression. In *Experimental Cell Research* (Vol. 246, Issue 2, pp. 249–262). Academic Press Inc. https://doi.org/10.1006/excr.1998.4278

Crasta, K., Huang, P., Morgan, G., Winey, M., & Surana, U. (2006). Cdk1 regulates centrosome separation by restraining proteolysis of microtubule-associated proteins. *The EMBO Journal*, *25*(11), 2551–2563. https://doi.org/10.1038/SJ.EMBOJ.7601136

Cross, F. R. (1995). Starting the cell cycle: what's the point? *Current Opinion in Cell Biology*, *7*(6), 790–797. https://doi.org/10.1016/0955-0674(95)80062-X

De Rop, V., Padeganeh, A., & Maddox, P. S. (2012). CENP-A: The key player behind centromere identity, propagation, and kinetochore assembly. In *Chromosoma* (Vol. 121, Issue 6, pp. 527–538). Springer. https://doi.org/10.1007/s00412-012-0386-5

De Wulf, P., McAinsh, A. D., & Sorger, P. K. (2003). Hierarchical assembly of the budding yeast kinetochore from multiple subcomplexes. *Genes & Development*, *17*(23), 2902–2921.

https://doi.org/10.1101/gad.1144403

Diffley, J. F. X., Cocker, J. H., Dowell, S. J., & Rowley, A. (1994). Two steps in the assembly of complexes at yeast replication origins in vivo. *Cell*, *78*(2), 303–316. https://doi.org/10.1016/0092-8674(94)90299-2

Dong, Y., Vanden Beldt, K. J., Meng, X., Khodjakov, A., & McEwen, B. F. (2007a). The outer plate in vertebrate kinetochores is a flexible network with multiple microtubule interactions. *Nature Cell Biology 2007 9:5*, *9*(5), 516–522. https://doi.org/10.1038/ncb1576

Dong, Y., Vanden Beldt, K. J., Meng, X., Khodjakov, A., & McEwen, B. F. (2007b). The outer plate in vertebrate kinetochores is a flexible network with multiple microtubule interactions. *Nature Cell Biology*, *9*(5), 516–522. https://doi.org/10.1038/ncb1576

Duesberg, P., Rausch, C., Rasnick, D., & Hehlmann, R. (1998). Genetic instability of cancer cells is proportional to their degree of aneuploidy. *Proceedings of the National Academy of Sciences*, *95*(23), 13692–13697. https://doi.org/10.1073/PNAS.95.23.13692

Earnshaw, W. C., Allshire, R. C., Black, B. E., Bloom, K., Brinkley, B. R., Brown, W., Cheeseman, I. M., Choo, K. H. A., Copenhaver, G. P., Deluca, J. G., Desai, A., Diekmann, S., Erhardt, S., Fitzgerald-Hayes, M., Foltz, D., Fukagawa, T., Gassmann, R., Gerlich, D. W., Glover, D. M., … Cleveland, D. W. (2013). Esperanto for histones: CENP-A, not CenH3, is the centromeric histone H3 variant. *Chromosome Research*, *21*(2), 101–106. https://doi.org/10.1007/s10577-013-9347-y

Elserafy, M., Šarić, M., Neuner, A., Lin, T. C., Zhang, W., Seybold, C., Sivashanmugam, L., & Schiebel, E. (2014). Molecular mechanisms that restrict yeast centrosome duplication to one event per cell cycle. *Current Biology*, *24*(13), 1456–1466. https://doi.org/10.1016/J.CUB.2014.05.032/ATTACHMENT/A2BB074F-19DD-4131-92BD-BCA6D6BA6CE5/MMC2.XLS

Endow, S. A., Kang, S. J., Satterwhite, L. L., Rose, M. D., Skeen, V. P., & Salmon, E. D. (1994). Yeast Kar3 is a minus-end microtubule motor protein that destabilizes microtubules preferentially at the minus ends. *The EMBO Journal*, *13*(11), 2708–2713. https://doi.org/10.1002/J.1460-2075.1994.TB06561.X

Engel, S. R., Dietrich, F. S., Fisk, D. G., Binkley, G., Balakrishnan, R., Costanzo, M. C., Dwight, S. S., Hitz, B. C., Karra, K., Nash, R. S., Weng, S., Wong, E. D., Lloyd, P., Skrzypek, M. S., Miyasato, S. R., Simison, M., & Cherry, J. M. (2014). The Reference Genome Sequence of Saccharomyces cerevisiae: Then and Now. *G3: Genes|Genomes|Genetics*, *4*(3), 389. https://doi.org/10.1534/G3.113.008995

Epstein, C. B., & Cross, F. R. (1992). CLB5: a novel B cyclin from budding yeast with a role in S phase. *Genes & Development*, *6*(9), 1695–1706. https://doi.org/10.1101/GAD.6.9.1695

Eshel, D., Urrestarazu, L. A., Vissers, S., Jauniaux, J. C., Vliet-Reedijk, J. C. van, Planta, R. J., & Gibbons, I. R. (1993). Cytoplasmic dynein is required for normal nuclear segregation in yeast. *Proceedings of the National Academy of Sciences of the United States of America*, *90*(23), 11172. https://doi.org/10.1073/PNAS.90.23.11172

Feng, J., Huang, H., & Yen, T. J. (2006). CENP-F is a novel microtubule-binding protein that is essential for kinetochore attachments and affects the duration of the mitotic checkpoint delay. *Chromosoma*, *115*(4), 320–329. https://doi.org/10.1007/s00412-006-0049-5

Feng, Z., Wilson, S. E., Peng, Z. Y., Schlender, K. K., Reimann, E. M., & Trumbly, R. J. (1991). The yeast GLC7 gene required for glycogen accumulation encodes a type 1 protein phosphatase. *Journal of Biological Chemistry*, *266*(35), 23796–23801. https://doi.org/10.1016/S0021-9258(18)54353-2

Fernius, J., & Hardwick, K. G. (2007). Bub1 Kinase Targets Sgo1 to Ensure Efficient Chromosome Biorientation in Budding Yeast Mitosis. *PLoS Genetics*, *3*(11), 2312–2325. https://doi.org/10.1371/JOURNAL.PGEN.0030213

Fischböck-Halwachs, J., Singh, S., Potocnjak, M., Hagemann, G., Solis-Mezarino, V., Woike, S., Ghodgaonkar-Steger, M., Weissmann, F., Gallego, L. D., Rojas, J., Andreani, J., Köhler, A., & Herzog, F. (2019). The COMA complex interacts with Cse4 and positions Sli15/ipl1 at the budding yeast inner kinetochore. *ELife*, *8*. https://doi.org/10.7554/eLife.42879

Fitch, I., Dahmann, C., Surana, U., Amon, A., Nasmyth, K., Goetsch, L., Byers, B., & Futcher, B. (1992). Characterization of four B-type cyclin genes of the budding yeast Saccharomyces cerevisiae. *Molecular Biology of the Cell*, *3*(7), 805. https://doi.org/10.1091/MBC.3.7.805

Fitzgerald-Hayes, M., Clarke, L., & Carbon, J. (1982). Nucleotide sequence comparisons and functional analysis of yeast centromere DNAs. *Cell*, *29*(1), 235–244. https://doi.org/10.1016/0092-8674(82)90108-8

Foley, E. A., & Kapoor, T. M. (2013). Microtubule attachment and spindle assembly checkpoint signaling at the kinetochore. *Nature Reviews. Molecular Cell Biology*, *14*(1), 25. https://doi.org/10.1038/NRM3494

Foury, F. (1997). Human genetic diseases: a cross-talk between man and yeast. *Gene*, *195*(1), 1–10. https://doi.org/10.1016/S0378-1119(97)00140-6

Fraschini, R. (2019). Divide Precisely and Proliferate Safely: Lessons from Budding Yeast. In *Frontiers in Genetics* (Vol. 9, p. 738). Frontiers Media S.A. https://doi.org/10.3389/fgene.2018.00738

Freese, E. B., Chu, M. I., & Freese, E. (1982). Initiation of Yeast Sporulation by Partial Carbon, Nitrogen, or Phosphate Deprivation. *Journal of Bacteriology*, *149*(3), 840–851. https://jb.asm.org/content/149/3/840?ijkey=0c89dfcda2aa9bc97c6c0e0c246fe124f4b6e6f4&keytype2=tf_ipsecsha

Funk, C. E. T. (2014). *Distinct functions of the two TOGL domains in CLASP orchestrate mitosis in S. cerevisiae / [presented by Caroline Eva Theresia Funk]*.

Funk, C., Schmeiser, V., Ortiz, J., & Lechner, J. (2014). A TOGL domain specifically targets yeast CLASP to kinetochores to stabilize kinetochore microtubules. *The Journal of Cell Biology*, *205*(4), 555–571. https://doi.org/10.1083/jcb.201310018

Ganem, N. J., Godinho, S. A., & Pellman, D. (2009). A Mechanism Linking Extra Centrosomes to Chromosomal Instability. *Nature*, *460*(7252), 278. https://doi.org/10.1038/NATURE08136

García-Rodríguez, L. J., Kasciukovic, T., Denninger, V., & Tanaka, T. U. (2019). Aurora B-INCENP Localization at Centromeres/Inner Kinetochores Is Required for Chromosome Bi-orientation in Budding Yeast. *Current Biology*, *29*(9), 1536-1544.e4. https://doi.org/10.1016/J.CUB.2019.03.051

Garcia, M. A., Vardy, L., Koonrugsa, N., & Toda, T. (2001). Fission yeast ch-TOG/XMAP215 homologue Alp14 connects mitotic spindles with the kinetochore and is a component of the Mad2-dependent spindle checkpoint. *The EMBO Journal*, *20*(13), 3389. https://doi.org/10.1093/EMBOJ/20.13.3389

Gardner, M. K., Bouck, D. C., Paliulis, L. V., Meehl, J. B., O'Toole, E. T., Haase, J., Soubry, A., Joglekar, A. P., Winey, M., Salmon, E. D., Bloom, K., & Odde, D. J. (2008). Chromosome Congression by Kinesin-5 Motor-Mediated Disassembly of Longer Kinetochore Microtubules. *Cell*, *135*(5), 894–906. https://doi.org/10.1016/J.CELL.2008.09.046

Gardner, M. K., Haase, J., Mythreye, K., Molk, J. N., Anderson, M. B., Joglekar, A. P., O'Toole, E. T., Winey, M., Salmon, E. D., Odde, D. J., & Bloom, K. (2008). The microtubule-based motor Kar3 and plus end–binding protein Bim1 provide structural support for the anaphase spindle. *Journal of Cell Biology*, *180*(1), 91–100. https://doi.org/10.1083/JCB.200710164

Gonen, S., Akiyoshi, B., Iadanza, M. G., Shi, D., Duggan, N., Biggins, S., & Gonen, T. (2012). The structure of purified kinetochores reveals multiple microtubule-attachment sites. *Nature Structural and Molecular Biology*, *19*(9), 925–929. https://doi.org/10.1038/nsmb.2358

Gordon, D. J., Resio, B., & Pellman, D. (2012). Causes and consequences of aneuploidy in cancer.

Nature Reviews Genetics 2012 13:3, *13*(3), 189–203. https://doi.org/10.1038/nrg3123

Gordon, D. M., & Roof, D. M. (1999). The kinesin-related protein Kip1p of Saccharomyces cerevisiae is bipolar. *The Journal of Biological Chemistry*, *274*(40), 28779–28786. https://doi.org/10.1074/JBC.274.40.28779

Gordon, D. M., & Roof, D. M. (2001). Degradation of the kinesin Kip1p at anaphase onset is mediated by the anaphase-promoting complex and Cdc20p. *Proceedings of the National Academy of Sciences*, *98*(22), 12515–12520. https://doi.org/10.1073/PNAS.231212498

Gupta, A., Evans, R. K., Koch, L. B., Littleton, A. J., & Biggins, S. (2018). Purification of kinetochores from the budding yeast Saccharomyces cerevisiae. In *Methods in Cell Biology* (Vol. 144, pp. 349–370). Academic Press Inc. https://doi.org/10.1016/bs.mcb.2018.03.023

Gupta, M. L., Carvalho, P., Roof, D. M., & Pellman, D. (2006). Plus end-specific depolymerase activity of Kip3, a kinesin-8 protein, explains its role in positioning the yeast mitotic spindle. *Nature Cell Biology 2006 8:9*, *8*(9), 913–923. https://doi.org/10.1038/ncb1457

Guse, A., Carroll, C. W., Moree, B., Fuller, C. J., & Straight, A. F. (2011). In vitro centromere and kinetochore assembly on defined chromatin templates. *Nature*, *477*(7364), 354–358. https://doi.org/10.1038/nature10379

Güttinger, S., Laurell, E., & Kutay, U. (2009). Orchestrating nuclear envelope disassembly and reassembly during mitosis. *Nature Reviews Molecular Cell Biology 2009 10:3*, *10*(3), 178–191. https://doi.org/10.1038/nrm2641

Hadders, M. A., Hindriksen, S., Truong, M. A., Mhaskar, A. N., Pepijn Wopken, J., Vromans, M. J. M., & Lens, S. M. A. (2020). Untangling the contribution of Haspin and Bub1 to Aurora B function during mitosis. *Journal of Cell Biology*, *219*(3). https://doi.org/10.1083/JCB.201907087/133700

Haering, C. H., & Hasmyth, K. (2003). Building and breaking bridges between sister chromatids. *BioEssays*, *25*(12), 1178–1191. https://doi.org/10.1002/BIES.10361

Hanahan, D., & Weinberg, R. A. (2011). Hallmarks of Cancer: The Next Generation. *Cell*, *144*(5), 646–674. https://doi.org/10.1016/J.CELL.2011.02.013

Hara, M., & Fukagawa, T. (2020). Dynamics of kinetochore structure and its regulations during mitotic progression. In *Cellular and Molecular Life Sciences* (Vol. 77, Issue 15, pp. 2981–2995). Springer. https://doi.org/10.1007/s00018-020-03472-4

Harper, J. V., & Brooks, G. (2005). The Mammalian Cell Cycle. *Methods in Molecular Biology (Clifton, N.J.)*, *296*, 113–153. https://doi.org/10.1385/1-59259-857-9:113

Hartwell, L. H. (1974). Saccharomyces cerevisiae cell cycle. *Bacteriological Reviews*, *38*(2), 164. https://www.ncbi.nlm.nih.gov/pmc/articles/PMC413849/

Haruki, N., Harano, T., Masuda, A., Kiyono, T., Takahashi, T., Tatematsu, Y., Shimizu, S., Mitsudomi, T., Konishi, H., Osada, H., Fujii, Y., & Takahashi, T. (2001). Persistent Increase in Chromosome Instability in Lung Cancer: Possible Indirect Involvement of p53 Inactivation. *The American Journal of Pathology*, *159*(4), 1345–1352. https://doi.org/10.1016/S0002-9440(10)62521-7

Havens, K. A., Gardner, M. K., Kamieniecki, R. J., Dresser, M. E., & Dawson, D. S. (2010a). Slk19p of Saccharomyces cerevisiae regulates anaphase spindle dynamics through two independent mechanisms. *Genetics*. https://doi.org/10.1534/genetics.110.123257

Havens, K. A., Gardner, M. K., Kamieniecki, R. J., Dresser, M. E., & Dawson, D. S. (2010b). Slk19p of Saccharomyces cerevisiae regulates anaphase spindle dynamics through two independent mechanisms. *Genetics*, *186*(4), 1247–1260. https://doi.org/10.1534/genetics.110.123257

Hecht, A., & Grunstein, M. (1999). Mapping DNA interaction sites of chromosomal proteins using immunoprecipitation and polymerase chain reaction. *Methods in Enzymology*, *304*, 399–414. https://doi.org/10.1016/S0076-6879(99)04024-0

Hemmerich, P., Stoyan, T., Wieland, G., Koch, M., Lechner, J., & Diekmann, S. (2000). Interaction of yeast kinetochore proteins with centromere-protein/transcription factor Cbf1. *Proceedings of the National Academy of Sciences of the United States of America*, *97*(23), 12583–12588. https://doi.org/10.1073/pnas.97.23.12583

Henikoff, S., Ahmad, K., Platero, J. S., & Van Steensel, B. (2000). Heterochromatic deposition of centromeric histone H3-like proteins. *Proceedings of the National Academy of Sciences of the United States of America*, *97*(2), 716–721. https://doi.org/10.1073/pnas.97.2.716

Hepperla, A. J., Willey, P. T., Coombes, C. E., Schuster, B. M., Gerami-Nejad, M., McClellan, M., Mukherjee, S., Fox, J., Winey, M., Odde, D. J., O'Toole, E., & Gardner, M. K. (2014). Minus-End-Directed Kinesin-14 Motors Align Antiparallel Microtubules to Control Metaphase Spindle Length. *Developmental Cell*, *31*(1), 61–72. https://doi.org/10.1016/j.devcel.2014.07.023

Higuchi, T., & Uhlmann, F. (2005). Stabilization of microtubule dynamics at anaphase onset promotes chromosome segregation. *Nature*, *433*(7022), 171. https://doi.org/10.1038/NATURE03240

Hildebrandt, E. R., Gheber, L., Kingsbury, T., & Hoyt, M. A. (2006). Homotetrameric form of Cin8p, a Saccharomyces cerevisiae kinesin-5 motor, is essential for its in Vivo function. *Journal of Biological Chemistry*, *281*(36), 26004–26013. https://doi.org/10.1074/JBC.M604817200/ATTACHMENT/EA05671D-16AB-4C22-98F0-A06D6C61B9CB/MMC1.PDF

Hildebrandt, E. R., & Hoyt, M. A. (2000). Mitotic motors in Saccharomyces cerevisiae. *Biochimica et Biophysica Acta (BBA) - Molecular Cell Research*, *1496*(1), 99–116. https://doi.org/10.1016/S0167-4889(00)00012-4

Hildebrandt, E. R., & Hoyt, M. A. (2001). Cell Cycle-dependent Degradation of the Saccharomyces cerevisiae Spindle Motor Cin8p Requires APCCdh1 and a Bipartite Destruction Sequence. *Molecular Biology of the Cell*, *12*(11), 3402. https://doi.org/10.1091/MBC.12.11.3402

Ho, K. H., Tsuchiya, D., Oliger, A. C., & Lacefield, S. (2014). Localization and Function of Budding Yeast CENP-A Depends upon Kinetochore Protein Interactions and Is Independent of Canonical Centromere Sequence. *Cell Reports*, *9*(6), 2027–2033. https://doi.org/10.1016/j.celrep.2014.11.037

Hoffman, D. B., Pearson, C. G., Yen, T. J., Howell, B. J., & Salmon, E. D. (2001). Microtubule-dependent changes in assembly of microtubule motor proteins and mitotic spindle checkpoint proteins at PtK1 kinetochores. *Molecular Biology of the Cell*, *12*(7), 1995–2009. https://doi.org/10.1091/MBC.12.7.1995/ASSET/IMAGES/LARGE/MK0711544008.JPEG

Holland, A. J., & Cleveland, D. W. (2009). Boveri revisited: Chromosomal instability, aneuploidy and tumorigenesis. In *Nature Reviews Molecular Cell Biology* (Vol. 10, Issue 7, pp. 478–487). https://doi.org/10.1038/nrm2718

Holt, S. V, Vergnolle, M. A. S., Hussein, D., Wozniak, M. J., Allan, V. J., & Taylor, S. S. (2005). Silencing Cenp-F weakens centromeric cohesion, prevents chromosome alignment and activates the spindle checkpoint. *Journal of Cell Science*, *118*(Pt 20), 4889–4900. https://doi.org/10.1242/jcs.02614

Hornig, N. C. D., & Uhlmann, F. (2004). Preferential cleavage of chromatin-bound cohesin after targeted phosphorylation by Polo-like kinase. *The EMBO Journal*, *23*(15), 3144–3153. https://doi.org/10.1038/SJ.EMBOJ.7600303

Hoyt, M. A., He, L., Kek Khee Loo, & Saunders, W. S. (1992). Two Saccharomyces cerevisiae kinesin-related gene products required for mitotic spindle assembly. *Journal of Cell Biology*, *118*(1), 109–120. https://doi.org/10.1083/JCB.118.1.109

Hoyt, M. A., He, L., Totis, L., & Saunders, W. S. (1993). Loss of function of Saccharomyces cerevisiae kinesin-related CIN8 and KIP1 is suppressed by KAR3 motor domain mutations.

Genetics, *135*(1), 35–44. https://doi.org/10.1093/GENETICS/135.1.35

Hoyt, M. Andrew, Totis, L., & Roberts, B. T. (1991). S. cerevisiae genes required for cell cycle arrest in response to loss of microtubule function. *Cell*, *66*(3), 507–517. https://doi.org/10.1016/0092-8674(81)90014-3

Inoue, H., Nojima, H., & Okayama, H. (1990). High efficiency transformation of Escherichia coli with plasmids. *Gene*, *96*(1), 23–28. https://doi.org/10.1016/0378-1119(90)90336-P

Irniger, S., Piatti, S., Michaelis, C., & Nasmyth, K. (1995). Genes involved in sister chromatid separation are needed for b-type cyclin proteolysis in budding yeast. *Cell*, *81*(2), 269–277. https://doi.org/10.1016/0092-8674(95)90337-2

Jacobs, C. W., Adams, A. E., Szaniszlo, P. J., & Pringle, J. R. (1988). Functions of microtubules in the Saccharomyces cerevisiae cell cycle. *Journal of Cell Biology*, *107*(4), 1409–1426. https://doi.org/10.1083/JCB.107.4.1409

Janke, C., Magiera, M. M., Rathfelder, N., Taxis, C., Reber, S., Maekawa, H., Moreno-Borchart, A., Doenges, G., Schwob, E., Schiebel, E., & Knop, M. (2004). A versatile toolbox for PCR-based tagging of yeast genes: New fluorescent proteins, more markers and promoter substitution cassettes. *Yeast*, *21*(11), 947–962. https://doi.org/10.1002/yea.1142

Janson, M. E., Loughlin, R., Loïodice, I., Fu, C., Brunner, D., Nédélec, F. J., & Tran, P. T. (2007). Crosslinkers and Motors Organize Dynamic Microtubules to Form Stable Bipolar Arrays in Fission Yeast. *Cell*, *128*(2), 357–368. https://doi.org/10.1016/J.CELL.2006.12.030

Jaspersen, S. L., Charles, J. F., & Morgan, D. O. (1999). Inhibitory phosphorylation of the APC regulator Hct1 is controlled by the kinase Cdc28 and the phosphatase Cdc14. *Current Biology*, *9*(5), 227–236. https://doi.org/10.1016/S0960-9822(99)80111-0

Jaspersen, S. L., & Winey, M. (2004). THE BUDDING YEAST SPINDLE POLE BODY: Structure, Duplication, and Function. *Http://Dx.Doi.Org/10.1146/Annurev.Cellbio.20.022003.114106*, *20*, 1–28. https://doi.org/10.1146/ANNUREV.CELLBIO.20.022003.114106

Jensen, S., Segal, M., Clarke, D. J., & Reed, S. I. (2001). A Novel Role of the Budding Yeast Separin Esp1 in Anaphase Spindle Elongation: Evidence That Proper Spindle Association of Esp1 Is Regulated by Pds1. *The Journal of Cell Biology*, *152*(1), 27. https://doi.org/10.1083/JCB.152.1.27

Jiang, W., Jimenez, G., Wells, N. J., Hope, T. J., Wahl, G. M., Hunter, T., & Fukunaga, R. (1998). PRC1: A Human Mitotic Spindle–Associated CDK Substrate Protein Required for Cytokinesis. *Molecular Cell*, *2*(6), 877–885. https://doi.org/10.1016/S1097-2765(00)80302-0

Jin, Q. W., Fuchs, J., & Loidl, J. (2000). Centromere clustering is a major determinant of yeast interphase nuclear organization. *Journal of Cell Science*, *113*(11), 1903–1912. https://doi.org/10.1242/JCS.113.11.1903

Joglekar, A. P., Bloom, K., & Salmon, E. D. (2009). In Vivo Protein Architecture of the Eukaryotic Kinetochore with Nanometer Scale Accuracy. *Current Biology*, *19*(8), 694–699. https://doi.org/10.1016/j.cub.2009.02.056

Joglekar, A. P., Bouck, D. C., Molk, J. N., Bloom, K. S., & Salmon, E. D. (2006). Molecular architecture of a kinetochore-microtubule attachment site. *Nature Cell Biology*, *8*(6), 581–585. https://doi.org/10.1038/ncb1414

Joglekar, A. P., Bouck, D., Finley, K., Liu, X., Wan, Y., Berman, J., He, X., Salmon, E. D., & Bloom, K. S. (2008). Molecular architecture of the kinetochore-microtubule attachment site is conserved between point and regional centromeres. *Journal of Cell Biology*, *181*(4), 587–594. https://doi.org/10.1083/jcb.200803027

Johnson, D. G., & Walker, C. L. (2003). CYCLINS AND CELL CYCLE CHECKPOINTS. *Http://Dx.Doi.Org/10.1146/Annurev.Pharmtox.39.1.295*, *39*, 295–312. https://doi.org/10.1146/ANNUREV.PHARMTOX.39.1.295

Johnson, V. L., Scott, M. I. F., Holt, S. V., Hussein, D., & Taylor, S. S. (2004). Bub1 is required for kinetochore localization of BubR1, Cenp-E, Cenp-F and Mad2, and chromosome congression. *Journal of Cell Science*, *117*(8), 1577–1589. https://doi.org/10.1242/JCS.01006

Jones, M. H., Bachant, J. B., Castillo, A. R., Giddings, T. H., & Winey, M. (1999). Yeast Dam1p is required to maintain spindle integrity during mitosis and interacts with the Mps1p kinase. *Molecular Biology of the Cell*, *10*(7), 2377–2391. https://doi.org/10.1091/MBC.10.7.2377

Jossen, R., & Bermejo, R. (2013). The DNA damage checkpoint response to replication stress: A Game of Forks. *Frontiers in Genetics*, *0*(MAR), 26. https://doi.org/10.3389/FGENE.2013.00026

Juang, Y. L., Huang, J., Peters, J. M., McLaughlin, M. E., Tai, C. Y., & Pellman, D. (1997). APC-mediated proteolysis of Ase1 and the morphogenesis of the mitotic spindle. *Science*, *275*(5304), 1311–1314. https://doi.org/10.1126/SCIENCE.275.5304.1311/ASSET/88257266-8C84-42A1-A301-D60F54251824/ASSETS/GRAPHIC/SE0974836004.JPEG

Kachroo, A. H., Laurent, J. M., Yellman, C. M., Meyer, A. G., Wilke, C. O., & Marcotte, E. M. (2015). Systematic humanization of yeast genes reveals conserved functions and genetic modularity. *Science (New York, N.Y.)*, *348*(6237), 921. https://doi.org/10.1126/SCIENCE.AAA0769

Kahana, J. A., Schnapp, B. J., & Silver, P. A. (1995). Kinetics of spindle pole body separation in budding yeast. *Proceedings of the National Academy of Sciences*, *92*(21), 9707–9711. https://doi.org/10.1073/PNAS.92.21.9707

Kapitein, L. C., Janson, M. E., van den Wildenberg, S. M. J. L., Hoogenraad, C. C., Schmidt, C. F., & Peterman, E. J. G. (2008). Microtubule-driven multimerization recruits ase1p onto overlapping microtubules. *Current Biology : CB*, *18*(21), 1713–1717. https://doi.org/10.1016/j.cub.2008.09.046

Kapitein, L. C., Peterman, E. J. G., Kwok, B. H., Kim, J. H., Kapoor, T. M., & Schmidt, C. F. (2005). The bipolar mitotic kinesin Eg5 moves on both microtubules that it crosslinks. *Nature*, *435*(7038), 114–118. https://doi.org/10.1038/NATURE03503

Kawashima, S. A., Yamagishi, Y., Honda, T., Lshiguro, K. I., & Watanabe, Y. (2010). Phosphorylation of H2A by Bub1 prevents chromosomal instability through localizing shugoshin. *Science*, *327*(5962), 172–177. https://doi.org/10.1126/SCIENCE.1180189/SUPPL_FILE/PAP.PDF

Kemmler, S., Stach, M., Knapp, M., Ortiz, J., Pfannstiel, J., Ruppert, T., & Lechner, J. (2009). Mimicking Ndc80 phosphorylation triggers spindle assembly checkpoint signalling. *The EMBO Journal*, *28*(8), 1099–1110. https://doi.org/10.1038/emboj.2009.62

Kern, D. M., & Cheeseman, I. M. (2012). Kinetochore structure: Pulling answers from yeast. In *Current Biology* (Vol. 22, Issue 19, pp. R842–R844). Cell Press. https://doi.org/10.1016/j.cub.2012.08.001

Khmelinskii, A., Lawrence, C., Roostalu, J., & Schiebel, E. (2007). Cdc14-regulated midzone assembly controls anaphase B. *The Journal of Cell Biology*, *177*(6), 981–993. https://doi.org/10.1083/jcb.200702145

Khmelinskii, A., Roostalu, J., Roque, H., Antony, C., & Schiebel, E. (2009). Phosphorylation-dependent protein interactions at the spindle midzone mediate cell cycle regulation of spindle elongation. *Developmental Cell*, *17*(2), 244–256. https://doi.org/10.1016/j.devcel.2009.06.011

Khmelinskii, A., & Schiebel, E. (2008). Assembling the spindle midzone in the right place at the right time. In *Cell Cycle*. https://doi.org/10.4161/cc.7.3.5349

King, B. R., Meehl, J. B., Vojnar, T., Winey, M., Muller, E. G., & Davis, T. N. (2021). Microtubule-associated proteins and motors required for ectopic microtubule array formation in Saccharomyces cerevisiae. *Genetics*, *218*(2). https://doi.org/10.1093/GENETICS/IYAB050

King, E. M. J., Rachidi, N., Morrice, N., Hardwick, K. G., & Stark, M. J. R. (2007). Ipl1p-dependent

phosphorylation of Mad3p is required for the spindle checkpoint response to lack of tension at kinetochores. *Genes & Development*, *21*(10), 1163–1168. https://doi.org/10.1101/GAD.431507

Kitada, K., Johnson, A. L., Johnston, L. H., & Suginol, A. (1993). A multicopy suppressor gene of the Saccharomyces cerevisiae G1 cell cycle mutant gene dbf4 encodes a protein kinase and is identified as CDC5. *Molecular and Cellular Biology*, *13*(7), 4445–4457. https://doi.org/10.1128/MCB.13.7.4445-4457.1993

Kitagawa, K., & Hieter, P. (2001). Evolutionary conservation between budding yeast and human kinetochores. *Nature Reviews Molecular Cell Biology*, *2*(9), 678–687. https://doi.org/10.1038/35089568

Kitamura, E., Tanaka, K., Kitamura, Y., & Tanaka, T. U. (2007). Kinetochore microtubule interaction during S phase in Saccharomyces cerevisiae. *Genes & Development*, *21*(24), 3319–3330. https://doi.org/10.1101/gad.449407

Kitamura, E., Tanaka, K., Komoto, S., Kitamura, Y., Antony, C., & Tanaka, T. U. (2010). Kinetochores Generate Microtubules with Distal Plus Ends: Their Roles and Limited Lifetime in Mitosis. *Developmental Cell*, *18*(2), 248–259. https://doi.org/10.1016/J.DEVCEL.2009.12.018

Knockleby, J., & Vogel, J. (2009). The COMA complex is required for Sli15/INCENP-mediated correction of defective kinetochore attachments. *Cell Cycle (Georgetown, Tex.)*, *8*(16), 2570–2577. https://doi.org/10.4161/CC.8.16.9267

Knop, M., Siegers, K., Pereira, G., Zachariae, W., Winsor, B., Nasmyth, K., & Schiebel, E. (1999). Epitope tagging of yeast genes using a PCR-based strategy: more tags and improved practical routines. *Yeast (Chichester, England)*, *15*(10B), 963–972. https://doi.org/10.1002/(sici)1097-0061(199907)15:10b<963::aid-yea399>3.0.co;2-w

Kolenda, C., Ortiz, J., Pelzl, M., Norell, S., Schmeiser, V., & Lechner, J. (2018). Unattached kinetochores drive their own capturing by sequestering a CLASP. *Nature Communications*, *9*(1), 886. https://doi.org/10.1038/s41467-018-03108-z

Kollman, J. M., Polka, J. K., Zelter, A., Davis, T. N., & Agard, D. A. (2010). Microtubule nucleating γ-TuSC assembles structures with 13-fold microtubule-like symmetry. *Nature 2010 466:7308*, *466*(7308), 879–882. https://doi.org/10.1038/nature09207

Kops, G. J. P. L., & Gassmann, R. (2020). Crowning the Kinetochore: The Fibrous Corona in Chromosome Segregation. *Trends in Cell Biology*, *30*(8), 653–667. https://doi.org/10.1016/J.TCB.2020.04.006

Kornakov, N., Möllers, B., & Westermann, S. (2020). The EB1-Kinesin-14 complex is required for efficient metaphase spindle assembly and kinetochore bi-orientation. *The Journal of Cell Biology*, *219*(12). https://doi.org/10.1083/JCB.202003072/VIDEO-2

Koshland, D. E., Mitchison, T. J., & Kirschner, M. W. (1988). Polewards chromosome movement driven by microtubule depolymerization in vitro. *Nature*, *331*(6156), 499–504. https://doi.org/10.1038/331499a0

Kotwaliwale, C. V, Frei, S. B., Stern, B. M., & Biggins, S. (2007). A pathway containing the Ipl1/aurora protein kinase and the spindle midzone protein Ase1 regulates yeast spindle assembly. *Developmental Cell*, *13*(3), 433–445. https://doi.org/10.1016/j.devcel.2007.07.003

Kovacs, L. A. S., Nelson, C. L., & Haase, S. B. (2008). Intrinsic and Cyclin-dependent Kinase-dependent Control of Spindle Pole Body Duplication in Budding Yeast. *Https://Doi.Org/10.1091/Mbc.E08-02-0148*, *19*(8), 3243–3253. https://doi.org/10.1091/MBC.E08-02-0148

Labib, K., Tercero, J. A., & Diffley, J. F. X. (2000). Uninterrupted MCM2-7 function required for DNA replication fork progression. *Science (New York, N.Y.)*, *288*(5471), 1643–1647. https://doi.org/10.1126/SCIENCE.288.5471.1643

Laemmli, U. K. (1970). Cleavage of Structural Proteins during the Assembly of the Head of Bacteriophage T4. *Nature 1970 227:5259*, *227*(5259), 680–685. https://doi.org/10.1038/227680a0

Lamb, J. R., Michaud, W. A., Sikorski, R. S., & Hieter, P. A. (1994). Cdc16p, Cdc23p and Cdc27p form a complex essential for mitosis. *The EMBO Journal*, *13*(18), 4321. /pmc/articles/PMC395359/?report=abstract

Lampert, F., Hornung, P., & Westermann, S. (2010). The Dam1 complex confers microtubule plus end-tracking activity to the Ndc80 kinetochore complex. *Journal of Cell Biology*, *189*(4), 641–649. https://doi.org/10.1083/jcb.200912021

Leary, A., Sim, S., Nazarova, E., Shulist, K., Genthial, R., Yang, S. K., Bui, K. H., Francois, P., & Vogel, J. (2019). Successive Kinesin-5 Microtubule Crosslinking and Sliding Promote Fast, Irreversible Formation of a Stereotyped Bipolar Spindle. *Current Biology*, *29*(22), 3825-3837.e3. https://doi.org/10.1016/J.CUB.2019.09.030

Lechner, J., & Carbon, J. (1991). A 240 kd multisubunit protein complex, CBF3, is a major component of the budding yeast centromere. *Cell*, *64*(4), 717–725. https://doi.org/10.1016/0092-8674(91)90501-O

Lengauer, C., Kinzler, K. W., & Vogelstein, B. (1997). Genetic instability in colorectal cancers. *Nature*, *386*(6625), 623–627. https://doi.org/10.1038/386623a0

Lew, D J, & Reed, S. I. (1993). Morphogenesis in the yeast cell cycle: regulation by Cdc28 and cyclins. *Journal of Cell Biology*, *120*(6), 1305–1320. https://doi.org/10.1083/JCB.120.6.1305

Lew, Daniel J. (2003). The morphogenesis checkpoint: how yeast cells watch their figures. *Current Opinion in Cell Biology*, *15*(6), 648–653. http://www.ncbi.nlm.nih.gov/pubmed/14644188

Li, Y. Y., Yeh, E., Hays, T., & Bloom, K. (1993). Disruption of mitotic spindle orientation in a yeast dynein mutant. *Proceedings of the National Academy of Sciences*, *90*(21), 10096–10100. https://doi.org/10.1073/PNAS.90.21.10096

Liang, C., Zhang, Z., Chen, Q., Yan, H., Zhang, M., Zhou, L., Xu, J., Lu, W., & Wang, F. (2020). Centromere-localized Aurora B kinase is required for the fidelity of chromosome segregation. *Journal of Cell Biology*, *219*(2). https://doi.org/10.1083/JCB.201907092/VIDEO-2

Lianga, N., Doré, C., Kennedy, E. K., Yeh, E., Williams, E. C., Fortinez, C. M., Wang, A., Bloom, K. S., & Rudner, A. D. (2018). Cdk1 phosphorylation of Esp1/Separase functions with PP2A and Slk19 to regulate pericentric Cohesin and anaphase onset. *PLoS Genetics*, *14*(3), e1007029. https://doi.org/10.1371/journal.pgen.1007029

Liu, D., Vader, G., Vromans, M. J. M., Lampson, M. A., & Lens, S. M. A. (2009). Sensing chromosome bi-orientation by spatial separation of Aurora B kinase from kinetochore substrates. *Science*, *323*(5919), 1350–1353. https://doi.org/10.1126/science.1167000

Loïodice, I., Staub, J., Setty, T. G., Nguyen, N. P. T., Paoletti, A., & Tran, P. T. (2005). Ase1p organizes antiparallel microtubule arrays during interphase and mitosis in fission yeast. *Molecular Biology of the Cell*, *16*(4), 1756–1768. https://doi.org/10.1091/MBC.E04-10-0899

London, N., & Biggins, S. (2014). Mad1 kinetochore recruitment by Mps1-mediated phosphorylation of Bub1 signals the spindle checkpoint. *Genes and Development*, *28*(2), 140–152. https://doi.org/10.1101/gad.233700.113

London, N., Ceto, S., Ranish, J. A., & Biggins, S. (2012). Phosphoregulation of Spc105 by Mps1 and PP1 regulates Bub1 localization to kinetochores. *Current Biology : CB*, *22*(10), 900–906. https://doi.org/10.1016/j.cub.2012.03.052

Loog, M., & Morgan, D. O. (2005). Cyclin specificity in the phosphorylation of cyclin-dependent kinase substrates. *Nature 2005 434:7029*, *434*(7029), 104–108. https://doi.org/10.1038/nature03329

Luo, X., Tang, Z., Rizo, J., & Yu, H. (2002). The Mad2 spindle checkpoint protein undergoes similar

major conformational changes upon binding to either Mad1 or Cdc20. *Molecular Cell*, *9*(1), 59–71. https://doi.org/10.1016/S1097-2765(01)00435-X

Magidson, V., Paul, R., Yang, N., Ault, J. G., O'Connell, C. B., Tikhonenko, I., Mcewen, B. F., Mogilner, A., & Khodjakov, A. (2015). Adaptive changes in the kinetochore architecture facilitate proper spindle assembly. *Nature Cell Biology 2015 17:9*, *17*(9), 1134–1144. https://doi.org/10.1038/ncb3223

Maiato, H., DeLuca, J., Salmon, E. D., & Earnshaw, W. C. (2004). The dynamic kinetochore-microtubule interface. In *Journal of Cell Science* (Vol. 117, Issue 23, pp. 5461–5477). The Company of Biologists. https://doi.org/10.1242/jcs.01536

Maiato, H., Fairley, E. A. L., Rieder, C. L., Swedlow, J. R., Sunkel, C. E., & Earnshaw, W. C. (2003). Human CLASP1 Is an Outer Kinetochore Component that Regulates Spindle Microtubule Dynamics. *Cell*, *113*(7), 891–904. https://doi.org/10.1016/S0092-8674(03)00465-3

Majumdar, S., Kim, T., Chen, Z., Munyoki, S., Tso, S.-C., Brautigam, C. A., & Rice, L. M. (2018). An isolated CLASP TOG domain suppresses microtubule catastrophe and promotes rescue. *Molecular Biology of the Cell*, *29*(11), 1359. https://doi.org/10.1091/MBC.E17-12-0748

Manning, B. D., Barrett, J. G., Wallace, J. A., Granok, H., & Snyder, M. (1999). Differential Regulation of the Kar3p Kinesin-related Protein by Two Associated Proteins, Cik1p and Vik1p. *Journal of Cell Biology*, *144*(6), 1219–1233. https://doi.org/10.1083/JCB.144.6.1219

Manzoni, R., Montani, F., Visintin, C., Caudron, F., Ciliberto, A., & Visintin, R. (2010). Oscillations in Cdc14 release and sequestration reveal a circuit underlying mitotic exit. *Journal of Cell Biology*, *190*(2), 209–222. https://doi.org/10.1083/JCB.201002026

Margolin, W. (2005). FtsZ and the division of prokaryotic cells and organelles. *Nature Reviews Molecular Cell Biology 2005 6:11*, *6*(11), 862–871. https://doi.org/10.1038/nrm1745

Marston, A. L. (2014). Chromosome Segregation in Budding Yeast: Sister Chromatid Cohesion and Related Mechanisms. *Genetics*, *196*(1), 31–63. https://doi.org/10.1534/GENETICS.112.145144

McAinsh, A. D., Tytell, J. D., & Sorger, P. K. (2003). Structure, Function, And Regulation Of Budding Yeast Kinetochores. *Annual Review of Cell and Developmental Biology*, *19*, 519–539. https://doi.org/10.1146/annurev.cellbio.19.111301.155607

Mcclelland, S. E., & Mcclelland, S. E. (2017). Role of chromosomal instability in cancer progression. *Endocrine-Related Cancer*, *24*(9), T23–T31. https://doi.org/10.1530/ERC-17-0187

McEwen, B. F., Hsieh, C. E., Mattheyses, A. L., & Rieder, C. L. (1998). A new look at kinetochore structure in vertebrate somatic cells using high-pressure freezing and freeze substitution. *Chromosoma*, *107*(6–7), 366–375. https://doi.org/10.1007/s004120050320

McKnight, K., Liu, H., & Wang, Y. (2014). Replicative stress induces intragenic transcription of the ASE1 gene that negatively regulates Ase1 activity. *Current Biology : CB*, *24*(10), 1101. https://doi.org/10.1016/J.CUB.2014.03.040

Meiron, H., Nahon, E., & Raveh, D. (1995). Identification of the heterothallic mutation in HO-endonuclease of S. cerevisiae using HO/ho chimeric genes. *Current Genetics 1995 28:4*, *28*(4), 367–373. https://doi.org/10.1007/BF00326435

Mellor, J., Jiang, W., Funk, M., Rathjen, J., Barnes, C. A., Hinz, T., Hegemann, J. H., & Philippsen, P. (1990). CPF1, a yeast protein which functions in centromeres and promoters. *EMBO Journal*, *9*(12), 4017–4026. https://doi.org/10.1002/j.1460-2075.1990.tb07623.x

Meluh, P. B., & Rose, M. D. (1990). KAR3, a kinesin-related gene required for yeast nuclear fusion. *Cell*, *60*(6), 1029–1041. https://doi.org/10.1016/0092-8674(90)90351-E

Meluh, P. B., Yang, P., Glowczewski, L., Koshland, D., & Smith, M. M. (1998). Cse4p is a component of the core centromere of Saccharomyces cerevisiae. *Cell*, *94*(5), 607–613. https://doi.org/10.1016/S0092-8674(00)81602-5

Meppelink, A., Kabeche, L., Vromans, M. J. M., Compton, D. A., & Lens, S. M. A. (2015). Shugoshin-1 Balances Aurora B Kinase Activity via PP2A to Promote Chromosome Bi-orientation. *Cell Reports*, *11*(4), 508–515. https://doi.org/10.1016/J.CELREP.2015.03.052/ATTACHMENT/ECFF5973-C952-413F-9FEB-2B0A03BE562E/MMC1.PDF

Meraldi, P., McAinsh, A. D., Rheinbay, E., & Sorger, P. K. (2006). Phylogenetic and structural analysis of centromeric DNA and kinetochore proteins. *Genome Biology*, *7*(3), 23. https://doi.org/10.1186/gb-2006-7-3-r23

Michaelis, C., Ciosk, R., & Nasmyth, K. (1997). Cohesins: Chromosomal Proteins that Prevent Premature Separation of Sister Chromatids. *Cell*, *91*(1), 35–45. https://doi.org/10.1016/S0092-8674(01)80007-6

Mieck, C., Molodtsov, M. I., Drzewicka, K., Van Der Vaart, B., Litos, G., Schmauss, G., Vaziri, A., & Westermann, S. (2015). Non-catalytic motor domains enable processive movement and functional diversification of the kinesin-14 kar3. *ELife*, *2015*(4). https://doi.org/10.7554/eLife.04489

Miller, M. P., Asbury, C. L., & Biggins, S. (2016). A TOG Protein Confers Tension Sensitivity to Kinetochore-Microtubule Attachments. *Cell*, *165*(6), 1428–1439. https://doi.org/10.1016/j.cell.2016.04.030

Miller, M. P., Evans, R. K., Zelter, A., Geyer, E. A., MacCoss, M. J., Rice, L. M., Davis, T. N., Asbury, C. L., & Biggins, S. (2019). Kinetochore-associated Stu2 promotes chromosome biorientation in vivo. *PLOS Genetics*, *15*(10), e1008423. https://doi.org/10.1371/JOURNAL.PGEN.1008423

Miller, S. B., Ho, C.-T., Winkler, J., Khokhrina, M., Neuner, A., Mohamed, M. Y., Guilbride, D. L., Richter, K., Lisby, M., Schiebel, E., Mogk, A., & Bukau, B. (2015). Compartment-specific aggregases direct distinct nuclear and cytoplasmic aggregate deposition. *The EMBO Journal*, *34*(6), 778. https://doi.org/10.15252/EMBJ.201489524

Miranda, J. J. L., De Wulf, P., Sorger, P. K., & Harrison, S. C. (2005). The yeast DASH complex forms closed rings on microtubules. *Nature Structural and Molecular Biology*, *12*(2), 138–143. https://doi.org/10.1038/nsmb896

Mitchison, T., & Kirschner, M. (1984). Dynamic instability of microtubule growth. *Nature 1984 312:5991*, *312*(5991), 237–242. https://doi.org/10.1038/312237a0

Mittal, P., Chavan, A., Trakroo, D., Shah, S., & Ghosh, S. K. (2019). Outer kinetochore protein Dam1 promotes centromere clustering in parallel with Slk19 in budding yeast. *Chromosoma*, *128*(2), 133–148. https://doi.org/10.1007/S00412-019-00694-9/FIGURES/2

Mollinari, C., Kleman, J.-P., Jiang, W., Schoehn, G., Hunter, T., & Margolis, R. L. (2002). PRC1 is a microtubule binding and bundling protein essential to maintain the mitotic spindle midzone. *The Journal of Cell Biology*, *157*(7), 1175. https://doi.org/10.1083/JCB.200111052

MORTIMER, R. K., & JOHNSTON, J. R. (1959). Life Span of Individual Yeast Cells. *Nature*, *183*(4677), 1751–1752. https://doi.org/10.1038/1831751a0

Musinipally, V., Howes, S., Alushin, G. M., & Nogales, E. (2013). The Microtubule Binding Properties of CENP-E's C-Terminus and CENP-F. *Journal of Molecular Biology*, *425*(22), 4427–4441. https://doi.org/10.1016/J.JMB.2013.07.027

Nasmyth, K. (1993). Control of the yeast cell cycle by the Cdc28 protein kinase. *Current Opinion in Cell Biology*, *5*(2), 166–179. https://doi.org/10.1016/0955-0674(93)90099-C

Nasmyth, K. (1996). At the heart of the budding yeast cell cycle. *Trends in Genetics*, *12*(10), 405–412. https://doi.org/10.1016/0168-9525(96)10041-X

Neiman, A. M. (2005). Ascospore Formation in the Yeast Saccharomyces cerevisiae. *Microbiology and Molecular Biology Reviews*, *69*(4), 565–584. https://doi.org/10.1128/MMBR.69.4.565-584.2005

Nerusheva, O. O., Galander, S., Fernius, J., Kelly, D., & Marston, A. L. (2014). Tension-dependent removal of pericentromeric shugoshin is an indicator of sister chromosome biorientation. *Genes & Development*, *28*(12), 1291–1309. https://doi.org/10.1101/GAD.240291.114

Niedenthal, R. K., Sen-gupta, M., Andreas, W., & Hegemann, J. H. (1993). Cpf1 protein induced bending of yeast centromere DNA element I. *Nucleic Acids Research*, *21*(20), 4726–4733. https://doi.org/10.1093/nar/21.20.4726

Nishimura, K., Fukagawa, T., Takisawa, H., Kakimoto, T., & Kanemaki, M. (2009). An auxin-based degron system for the rapid depletion of proteins in nonplant cells. *Nature Methods*, *6*(12), 917–922. https://doi.org/10.1038/nmeth.1401

Nishitani, H., & Lygerou, Z. (2002). Control of DNA replication licensing in a cell cycle. *Genes to Cells*, *7*(6), 523–534. https://doi.org/10.1046/J.1365-2443.2002.00544.X

Norden, C., Mendoza, M., Dobbelaere, J., Kotwaliwale, C. V., Biggins, S., & Barral, Y. (2006). The NoCut Pathway Links Completion of Cytokinesis to Spindle Midzone Function to Prevent Chromosome Breakage. *Cell*, *125*(1), 85–98. https://doi.org/10.1016/J.CELL.2006.01.045

Norell, S., Ortiz, J., & Lechner, J. (2021). Slk19 enhances crosslinking of microtubules by Ase1 and Stu1. *Https://Doi.Org/10.1091/Mbc.E21-05-0279*, mbc.E21-04-0191. https://doi.org/10.1091/MBC.E21-05-0279

O'Shea, E. K., Klemm, J. D., Kim, P. S., & Alber, T. (1991). X-Ray Structure of the GCN4 Leucine Zipper, a Two-Stranded, Parallel Coiled Coil. *Science*, *254*(5031), 539–544. https://doi.org/10.1126/SCIENCE.1948029

O'Toole, E. T., Winey, M., & McIntosh, J. R. (1999). High-voltage electron tomography of spindle pole bodies and early mitotic spindles in the yeast Saccharomyces cerevisiae. *Molecular Biology of the Cell*, *10*(6), 2017–2031. https://doi.org/10.1091/MBC.10.6.2017/ASSET/IMAGES/LARGE/MK0690875012.JPEG

Oliferenko, S., & Balasubramanian, M. K. (2002). Astral microtubules monitor metaphase spindle alignment in fission yeast. *Nature Cell Biology 2002 4:10*, *4*(10), 816–820. https://doi.org/10.1038/ncb861

Orr, B., & Compton, D. A. (2013). A double-edged sword: How oncogenes and tumor suppressor genes can contribute to chromosomal instability. In *Frontiers in Oncology: Vol. 3 JUN* (pp. 164–164). https://doi.org/10.3389/fonc.2013.00164

Ortiz, J., Funk, C., Schäfer, A., & Lechner, J. (2009). Stu1 inversely regulates kinetochore capture and spindle stability. *Genes & Development*, *23*(23), 2778–2791. https://doi.org/10.1101/gad.541309

Ortiz, J., Stemmann, O., Rank, S., & Lechner, J. (1999). A putative protein complex consisting of Ctf19, Mcm21, and Okp1 represents a missing link in the budding yeast kinetochore. *Genes and Development*, *13*(9), 1140–1155. https://doi.org/10.1101/gad.13.9.1140

Page, B. D., Satterwhite, L. L., Rose, M. D., & Snyder, M. (1994). Localization of the Kar3 kinesin heavy chain-related protein requires the Cik1 interacting protein. *Journal of Cell Biology*, *124*(4), 507–519. https://doi.org/10.1083/JCB.124.4.507

Pagliuca, C., Draviam, V. M., Marco, E., Sorger, P. K., & De Wulf, P. (2009). Roles for the conserved spc105p/kre28p complex in kinetochore-microtubule binding and the spindle assembly checkpoint. *PloS One*, *4*(10), e7640. https://doi.org/10.1371/journal.pone.0007640

Palmer, D. K., O'Day, K., Trong, H. L. E., Charbonneau, H., & Margolis, R. L. (1991). Purification of the centromere-specific protein CENP-A and demonstration that it is a distinctive histone. *Proceedings of the National Academy of Sciences of the United States of America*, *88*(9), 3734–3738. https://doi.org/10.1073/pnas.88.9.3734

Palmer, R. E., Sullivan, D. S., Huffaker, T., & Koshland, D. (1992). Role of astral microtubules and actin in spindle orientation and migration in the budding yeast, Saccharomyces cerevisiae. *Journal of Cell Biology*, *119*(3), 583–593. https://doi.org/10.1083/JCB.119.3.583

Pardo, B., Crabbé, L., & Pasero, P. (2017). Signaling pathways of replication stress in yeast. *FEMS Yeast Research*, *17*(2), 101. https://doi.org/10.1093/FEMSYR/FOW101

Pasqualone, D., & Huffaker, T. C. (1994). STU1, a suppressor of a beta-tubulin mutation, encodes a novel and essential component of the yeast mitotic spindle. *Journal of Cell Biology*, *127*(6), 1973–1984. https://doi.org/10.1083/JCB.127.6.1973

Passmore, L. A., Barford, D., & Harper, J. W. (2005). Purification and Assay of the Budding Yeast Anaphase-Promoting Complex. *Methods in Enzymology*, *398*, 195–219. https://doi.org/10.1016/S0076-6879(05)98017-8

Pellman, D., Bagget, M., Tu, H., & Fink, G. R. (1995). Two microtubule-associated proteins required for anaphase spindle movement in Saccharomyces cerevisiae. *Journal of Cell Biology*, *130*(6), 1373–1385. https://doi.org/10.1083/JCB.130.6.1373

Peplowska, K., Wallek, A. U., & Storchova, Z. (2014). Sgo1 Regulates Both Condensin and Ipl1/Aurora B to Promote Chromosome Biorientation. *PLOS Genetics*, *10*(6), e1004411. https://doi.org/10.1371/JOURNAL.PGEN.1004411

Pereira, G., & Schiebel, E. (1997). Centrosome-microtubule nucleation. *Journal of Cell Science*, *110*(3), 295–300. https://doi.org/10.1242/JCS.110.3.295

Pereira, G., & Schiebel, E. (2003). Separase regulates INCENP-Aurora B anaphase spindle function through Cdc14. *Science (New York, N.Y.)*, *302*(5653), 2120–2124. https://doi.org/10.1126/science.1091936

Peters, J. M. (2002). The Anaphase-Promoting Complex: Proteolysis in Mitosis and Beyond. *Molecular Cell*, *9*(5), 931–943. https://doi.org/10.1016/S1097-2765(02)00540-3

Petry, S. (2016). Mechanisms of Mitotic Spindle Assembly. *Annual Review of Biochemistry*, *85*, 659–683. https://doi.org/10.1146/annurev-biochem-060815-014528

Pfaltzgraff, E. R., Roth, G. M., Miller, P. M., Gintzig, A. G., Ohi, R., & Bader, D. M. (2016). Loss of CENP-F results in distinct microtubule-related defects without chromosomal abnormalities. *Molecular Biology of the Cell*, *27*(13), 1990–1999. https://doi.org/10.1091/mbc.E15-12-0848

Pfiz, S., Zimmermann, J., & Hilt, W. (2002). The yeast kinetochore protein Slk19 is required to prevent aberrant chromosome segregation in meiosis and mitosis. *Genes to Cells : Devoted to Molecular & Cellular Mechanisms*, *7*(10), 1033–1042. http://www.ncbi.nlm.nih.gov/pubmed/12354097

Pfleger, C. M., Lee, E., & Kirschner, M. W. (2001). Substrate recognition by the Cdc20 and Cdh1 components of the anaphase-promoting complex. *Genes & Development*, *15*(18), 2396–2407. https://doi.org/10.1101/GAD.918201

Pinsky, B. A., Nelson, C. R., & Biggins, S. (2009). Protein Phosphatase I Regulates Exit from the Spindle Checkpoint in Budding Yeast. *Current Biology : CB*, *19*(14), 1182. https://doi.org/10.1016/J.CUB.2009.06.043

Podolski, M., Mahamdeh, M., & Howard, J. (2014). Stu2, the Budding Yeast XMAP215/Dis1 Homolog, Promotes Assembly of Yeast Microtubules by Increasing Growth Rate and Decreasing Catastrophe Frequency. *The Journal of Biological Chemistry*, *289*(41), 28087. https://doi.org/10.1074/JBC.M114.584300

Powers, A. F., Franck, A. D., Gestaut, D. R., Cooper, J., Gracyzk, B., Wei, R. R., Wordeman, L., Davis, T. N., & Asbury, C. L. (2009). The Ndc80 kinetochore complex uses biased diffusion to couple chromosomes to dynamic microtubule tips. *Cell*, *136*(5), 865. https://doi.org/10.1016/J.CELL.2008.12.045

Proudfoot, K. G., Anderson, S. J., Dave, S., Bunning, A. R., Sinha Roy, P., Bera, A., & Gupta, M. L. (2019). Checkpoint Proteins Bub1 and Bub3 Delay Anaphase Onset in Response to Low Tension Independent of Microtubule-Kinetochore Detachment. *Cell Reports*, *27*(2), 416-428.e4. https://doi.org/10.1016/J.CELREP.2019.03.027

Queralt, E., Lehane, C., Novak, B., & Uhlmann, F. (2006). Downregulation of PP2A(Cdc55) phosphatase by separase initiates mitotic exit in budding yeast. *Cell*, *125*, 719–732.

Queralt, Ethel, & Uhlmann, F. (2008). Separase cooperates with Zds1 and Zds2 to activate Cdc14 phosphatase in early anaphase. *Journal of Cell Biology*, *182*(5), 873–883. https://doi.org/10.1083/JCB.200801054

Rattner, J. B., Rao, A., Fritzler, M. J., Valencia, D. W., & Yen, T. J. (1993). CENP-F is a ca 400 kDa kinetochore protein that exhibits a cell-cycle dependent localization. *Cell Motility and the Cytoskeleton*, *26*(3), 214–226. https://doi.org/10.1002/cm.970260305

Richmond, D., Rizkallah, R., Liang, F., Hurt, M. M., & Wang, Y. (2013). Slk19 clusters kinetochores and facilitates chromosome bipolar attachment. *Molecular Biology of the Cell*, *24*(5), 566–577. https://doi.org/10.1091/mbc.E12-07-0552

Rizk, R. S., DiScipio, K. A., Proudfoot, K. G., & Gupta, M. L. (2014). The kinesin-8 Kip3 scales anaphase spindle length by suppression of midzone microtubule polymerization. *The Journal of Cell Biology*, *204*(6), 965–975. https://doi.org/10.1083/jcb.201312039

Robertst, B. T., Farr, K. A., & Hoyt, M. A. (1994). The Saccharomyces cerevisiae checkpoint gene BUB1 encodes a novel protein kinase. *Molecular and Cellular Biology*, *14*(12), 8282–8291. https://doi.org/10.1128/MCB.14.12.8282-8291.1994

Robinow, C. F., & Marak, J. (1966). A FIBER APPARATUS IN THE NUCLEUS OF THE YEAST CELL. *Journal of Cell Biology*, *29*(1), 129–151. https://doi.org/10.1083/JCB.29.1.129

Roccuzzo, M., Visintin, C., Tili, F., & Visintin, R. (2015). FEAR-mediated activation of Cdc14 is the limiting step for spindle elongation and anaphase progression. *Nature Cell Biology 2014 17:3*, *17*(3), 251–261. https://doi.org/10.1038/ncb3105

Roof, D. M., Meluh, P. B., & Rose, M. D. (1992). Kinesin-related proteins required for assembly of the mitotic spindle. *Journal of Cell Biology*, *118*(1), 95–108. https://doi.org/10.1083/JCB.118.1.95

Rose, A. (2007). Open Mitosis: Nuclear Envelope Dynamics. *Plant Cell Monographs*, *9*, 207–230. https://doi.org/10.1007/7089_2007_128

Rosenberg, J. S., Cross, F. R., & Funabiki, H. (2011). KNL1/Spc105 Recruits PP1 to Silence the Spindle Assembly Checkpoint. *Current Biology*, *21*(11), 942–947. https://doi.org/10.1016/j.cub.2011.04.011

Rossio, V., Michimoto, T., Sasaki, T., Ohbayashi, I., Kikuchi, Y., & Yoshida, S. (2013). Nuclear PP2A-Cdc55 prevents APC-Cdc20 activation during the spindle assembly checkpoint. *Journal of Cell Science*, *126*(19), 4396–4405. https://doi.org/10.1242/JCS.127365/263617/AM/NUCLEAR-PP2A-CDC55-PREVENTS-APC-CDC20-ACTIVATION

Rossio, V., & Yoshida, S. (2011). Spatial regulation of Cdc55–PP2A by Zds1/Zds2 controls mitotic entry and mitotic exit in budding yeast. *Journal of Cell Biology*, *193*(3), 445–454. https://doi.org/10.1083/JCB.201101134

Rudner, A. D., & Murray, A. W. (2000). Phosphorylation by Cdc28 Activates the Cdc20-Dependent Activity of the Anaphase-Promoting Complex. *Journal of Cell Biology*, *149*(7), 1377–1390. https://doi.org/10.1083/JCB.149.7.1377

Sacristan, C., Ahmad, M. U. D., Keller, J., Fermie, J., Groenewold, V., Tromer, E., Fish, A., Melero, R., Carazo, J. M., Klumperman, J., Musacchio, A., Perrakis, A., & Kops, G. J. (2018). Dynamic kinetochore size regulation promotes microtubule capture and chromosome biorientation in mitosis. *Nature Cell Biology 2018 20:7*, *20*(7), 800–810. https://doi.org/10.1038/s41556-018-0130-3

Salic, A., Waters, J. C., & Mitchison, T. J. (2004). Vertebrate Shugoshin Links Sister Centromere Cohesion and Kinetochore Microtubule Stability in Mitosis. *Cell*, *118*(5), 567–578. https://doi.org/10.1016/J.CELL.2004.08.016

Salmon, E. D., & Bloom, K. (2017). Tension sensors reveal how the kinetochore shares its load. In *BioEssays* (Vol. 39, Issue 7). John Wiley and Sons Inc. https://doi.org/10.1002/bies.201600216

Sanchez, A. D., & Feldman, J. L. (2017). Microtubule-organizing centers: from the centrosome to non-centrosomal sites. *Current Opinion in Cell Biology*, *44*, 93. https://doi.org/10.1016/J.CEB.2016.09.003

Sandall, S., Severin, F., McLeod, I. X., Yates, J. R., Oegema, K., Hyman, A., & Desai, A. (2006). A Bir1-Sli15 complex connects centromeres to microtubules and is required to sense kinetochore tension. *Cell*, *127*(6), 1179–1191. https://doi.org/10.1016/j.cell.2006.09.049

Sato, M., Koonrugsa, N., Toda, T., Vardy, L., Tournier, S., Millar, J. B. A., Oliferenko, S., & Balasubramanian, M. K. (2003). Deletion of Mia1/Alp7 activates Mad2-dependent spindle assembly checkpoint in fission yeast (multiple letters). In *Nature Cell Biology* (Vol. 5, Issue 9, pp. 764–766). Nature Publishing Group. https://doi.org/10.1038/ncb0903-764

Sato, M., Vardy, L., Garcia, M. A., Koonrugsa, N., & Toda, T. (2004). Interdependency of Fission Yeast Alp14/TOG and Coiled Coil Protein Alp7 in Microtubule Localization and Bipolar Spindle Formation. *Molecular Biology of the Cell*, *15*(4), 1609–1622. https://doi.org/10.1091/mbc.E03-11-0837

Saunders, W., Hornack, D., Lengyel, V., & Deng, C. (1997). The Saccharomyces cerevisiae Kinesin-related Motor Kar3p Acts at Preanaphase Spindle Poles to Limit the Number and Length of Cytoplasmic Microtubules. *Journal of Cell Biology*, *137*(2), 417–431. https://doi.org/10.1083/JCB.137.2.417

Saunders, W., Lengyel, V., & Hoyt, M. A. (1997). Mitotic spindle function in Saccharomyces cerevisiae requires a balance between different types of kinesin-related motors. *Molecular Biology of the Cell*, *8*(6), 1025–1033. https://doi.org/10.1091/MBC.8.6.1025

Saunders, W. S., & Hoyt, M. A. (1992). Kinesin-related proteins required for structural integrity of the mitotic spindle. *Cell*, *70*(3), 451–458. https://doi.org/10.1016/0092-8674(92)90169-D

Schiebel, E. (2000). γ-tubulin complexes: binding to the centrosome, regulation and microtubule nucleation. *Current Opinion in Cell Biology*, *12*(1), 113–118. https://doi.org/10.1016/S0955-0674(99)00064-2

Schiestl, R. H., & Gietz, R. D. (1989). High efficiency transformation of intact yeast cells using single stranded nucleic acids as a carrier. *Current Genetics 1989 16:5*, *16*(5), 339–346. https://doi.org/10.1007/BF00340712

Schneider, B. L., Patton, E. E., Lanker, S., Mendenhall, M. D., Wittenberg, C., Futcher, B., & Tyers, M. (1998). Yeast G1 cyclins are unstable in G1 phase. *Nature 1998 395:6697*, *395*(6697), 86–89. https://doi.org/10.1038/25774

Schueler, M. G., Higgins, A. W., Rudd, M. K., Gustashaw, K., & Willard, H. F. (2001). Genomic and genetic definition of a functional human centromere. *Science*, *294*(5540), 109–115. https://doi.org/10.1126/science.1065042

Schuyler, S. C., Liu, J. Y., & Pellman, D. (2003). The molecular function of Ase1p: Evidence for a MAP-dependent midzone-specific spindle matrix. *Journal of Cell Biology*, *160*(4), 517–528. https://doi.org/10.1083/jcb.200210021

Schwab, M., Lutum, A. S., & Seufert, W. (1997). Yeast Hct1 Is a Regulator of Clb2 Cyclin Proteolysis. *Cell*, *90*(4), 683–693. https://doi.org/10.1016/S0092-8674(00)80529-2

Schwob, E., & Nasmyth, K. (1993). CLB5 and CLB6, a new pair of B cyclins involved in DNA replication in Saccharomyces cerevisiae. *Genes & Development*, *7*(7a), 1160–1175. https://doi.org/10.1101/GAD.7.7A.1160

Severin, F., Habermann, B., Huffaker, T., & Hyman, T. (2001). Stu2 Promotes Mitotic Spindle Elongation in Anaphase. *Journal of Cell Biology*, *153*(2), 435–442. https://doi.org/10.1083/JCB.153.2.435

Shang, C., Hazbun, T. R., Cheeseman, I. M., Aranda, J., Fields, S., Drubin, D. G., & Barnes, G. (2003). Kinetochore protein interactions and their regulation by the aurora kinase Ipl1p. *Molecular Biology of the Cell*, *14*(8), 3342–3355. https://doi.org/10.1091/mbc.E02-11-0765

Shapira, O., Goldstein, A., Al-Bassam, J., & Gheber, L. (2017). A potential physiological role for bi-directional motility and motor clustering of mitotic kinesin-5 Cin8 in yeast mitosis. *Journal of Cell Science*, *130*(4), 725–734. https://doi.org/10.1242/JCS.195040/VIDEO-8

Shaw, S. L., Yeh, E., Maddox, P., Salmon, E. D., & Bloom, K. (1997). Astral Microtubule Dynamics in Yeast: A Microtubule-based Searching Mechanism for Spindle Orientation and Nuclear Migration into the Bud. *The Journal of Cell Biology*, *139*(4), 985. https://doi.org/10.1083/JCB.139.4.985

Shimogawa, M. M., Widlund, P. O., Riffle, M., Ess, M., & Davis, T. N. (2009). Bir1 Is Required for the Tension Checkpoint. *Molecular Biology of the Cell*, *20*(3), 915. https://doi.org/10.1091/MBC.E08-07-0723

Shirayama, Masaid, Tóth, A., Gálová, M., & Nasmyth, K. (1999). APCCdc20 promotes exit from mitosis by destroying the anaphase inhibitor Pds1 and cyclin Clb5. *Nature 1999 402:6758*, *402*(6758), 203–207. https://doi.org/10.1038/46080

Shirayama, Masaki, Zachariae, W., Ciosk, R., & Nasmyth, K. (1998). The Polo-like kinase Cdc5p and the WD-repeat protein Cdc20p/fizzy are regulators and substrates of the anaphase promoting complex in Saccharomyces cerevisiae. *The EMBO Journal*, *17*(5), 1336–1349. https://doi.org/10.1093/EMBOJ/17.5.1336

Sikorski, R. S., & Hieter, P. (1989). A system of shuttle vectors and yeast host strains designed for efficient manipulation of DNA in Saccharomyces cerevisiae. *Genetics*, *122*(1), 19–27. https://doi.org/10.1093/GENETICS/122.1.19

Silkworth, W. T., Nardi, I. K., Scholl, L. M., & Cimini, D. (2009). Multipolar Spindle Pole Coalescence Is a Major Source of Kinetochore Mis-Attachment and Chromosome Mis-Segregation in Cancer Cells. *PLoS ONE*, *4*(8). https://doi.org/10.1371/JOURNAL.PONE.0006564

Singh, S. K., Pandey, H., Al-Bassam, J., & Gheber, L. (2018). Bidirectional motility of kinesin-5 motor proteins: structural determinants, cumulative functions and physiological roles. *Cellular and Molecular Life Sciences 2018 75:10*, *75*(10), 1757–1771. https://doi.org/10.1007/S00018-018-2754-7

Sneddon, A. A., Cohen, P. T. W., & Stark, M. J. R. (1990). Saccharomyces cerevisiae protein phosphatase 2A performs an essential cellular function and is encoded by two genes. *The EMBO Journal*, *9*(13), 4339. https://doi.org/10.1002/j.1460-2075.1990.tb07883.x

Spence, J. M., Critcher, R., Ebersole, T. A., Valdivia, M. M., Earnshaw, W. C., Fukagawa, T., & Farr, C. J. (2002). Co-localization of centromere activity, proteins and topoisomerase II within a subdomain of the major human X α-satellite array. *EMBO Journal*, *21*(19), 5269–5280. https://doi.org/10.1093/emboj/cdf511

Stegmeier, F., Visintin, R., & Amon, A. (2002). Separase, polo kinase, the kinetochore protein Slk19, and Spo12 function in a network that controls Cdc14 localization during early anaphase. *Cell*, *108*, 207–220.

Stegmeier, Frank, Huang, J., Rahal, R., Zmolik, J., Moazed, D., & Amon, A. (2004). The Replication Fork Block Protein Fob1 Functions as a Negative Regulator of the FEAR Network. *Current Biology*, *14*(6), 467–480. https://doi.org/10.1016/J.CUB.2004.03.009

Stellfox, M. E., Bailey, A. O., & Foltz, D. R. (2013). Putting CENP-A in its place. *Cellular and Molecular Life Sciences*, *70*(3), 387–406. https://doi.org/10.1007/S00018-012-1048-8/FIGURES/6

Stoler, S., Keith, K. C., Curnick, K. E., & Fitzgerald-Hayes, M. (1995). A mutation in CSE4, an essential gene encoding a novel chromatin- associated protein in yeast, causes chromosome

nondisjunction and cell cycle arrest at mitosis. *Genes and Development*, *9*(5), 573–586. https://doi.org/10.1101/gad.9.5.573

Straight, A. F., Sedat, J. W., & Murray, A. W. (1998). Time-Lapse Microscopy Reveals Unique Roles for Kinesins during Anaphase in Budding Yeast. *Journal of Cell Biology*, *143*(3), 687–694. https://doi.org/10.1083/JCB.143.3.687

Subramanian, R., Wilson-Kubalek, E. M., Arthur, C. P., Bick, M. J., Campbell, E. A., Darst, S. A., Milligan, R. A., & Kapoor, T. M. (2010). Insights into Antiparallel Microtubule Crosslinking by PRC1, a Conserved Nonmotor Microtubule Binding Protein. *Cell*, *142*(3), 433–443. https://doi.org/10.1016/J.CELL.2010.07.012

Sullivan, D. S., & Huffaker, T. C. (1992). Astral microtubules are not required for anaphase B in Saccharomyces cerevisiae. *Journal of Cell Biology*, *119*(2), 379–388. https://doi.org/10.1083/JCB.119.2.379

Sullivan, M, Lehane, C., & Uhlmann, F. (2001). Orchestrating anaphase and mitotic exit: separase cleavage and localization of Slk19. *Nature Cell Biology*, *3*(9), 771–777. https://doi.org/10.1038/ncb0901-771

Sullivan, Matt, & Uhlmann, F. (2003). A non-proteolytic function of separase links the onset of anaphase to mitotic exit. *Nature Cell Biology*, *5*(3), 249–254. https://doi.org/10.1038/ncb940

Suzuki, A., Badger, B. L., Haase, J., Ohashi, T., Erickson, H. P., Salmon, E. D., & Bloom, K. (2016). How the kinetochore couples microtubule force and centromere stretch to move chromosomes. *Nature Cell Biology*, *18*(4), 382–392. https://doi.org/10.1038/ncb3323

Tanaka, K., Kitamura, E., Kitamura, Y., & Tanaka, T. U. (2007). Molecular mechanisms of microtubule-dependent kinetochore transport toward spindle poles. *Journal of Cell Biology*, *178*(2), 269–281. https://doi.org/10.1083/jcb.200702141

Tanaka, T. U. (2010). Kinetochore-microtubule interactions: Steps towards bi-orientation. *EMBO Journal*, *29*(24), 4070–4082. https://doi.org/10.1038/emboj.2010.294

Tanaka, T. U., & Desai, A. (2008). Kinetochore-microtubule interactions: the means to the end. In *Current Opinion in Cell Biology* (Vol. 20, Issue 1, pp. 53–63). Curr Opin Cell Biol. https://doi.org/10.1016/j.ceb.2007.11.005

Tanaka, T. U., Rachidi, N., Janke, C., Pereira, G., Galova, M., Schiebel, E., Stark, M. J. R., & Nasmyth, K. (2002). Evidence that the Ipl1-Sli15 (Aurora kinase-INCENP) complex promotes chromosome bi-orientation by altering kinetochore-spindle pole connections. *Cell*, *108*(3), 317–329. http://www.ncbi.nlm.nih.gov/pubmed/11853667

Tanaka, T. U., Stark, M. J. R., & Tanaka, K. (2005). Kinetochore capture and bi-orientation on the mitotic spindle. *Nature Reviews Molecular Cell Biology*, *6*(12), 929–942. https://doi.org/10.1038/nrm1764

Tanaka, Y., Nureki, O., Kurumizaka, H., Fukai, S., Kawaguchi, S., Ikuta, M., Iwahara, J., Okazaki, T., & Yokoyama, S. (2001). Crystal structure of the CENP-B protein-DNA complex: The DNA-binding domains of CENP-B induce kinks in the CENP-B box DNA. *EMBO Journal*, *20*(23), 6612–6618. https://doi.org/10.1093/emboj/20.23.6612

Tang, N. H., Okada, N., Fong, C. S., Arai, K., Sato, M., & Toda, T. (2014). Targeting Alp7/TACC to the spindle pole body is essential for mitotic spindle assembly in fission yeast. *FEBS Letters*, *588*(17), 2814–2821. https://doi.org/10.1016/j.febslet.2014.06.027

Tang, N. H., Takada, H., Hsu, K.-S., & Toda, T. (2013). The internal loop of fission yeast Ndc80 binds Alp7/TACC-Alp14/TOG and ensures proper chromosome attachment. *Molecular Biology of the Cell*, *24*(8), 1122–1133. https://doi.org/10.1091/mbc.E12-11-0817

Thadani, R., Ling, Y. C., & Oliferenko, S. (2009). The Fission Yeast TACC Protein Mia1p Stabilizes Microtubule Arrays by Length-Independent Crosslinking. *Current Biology*, *19*(21), 1861–1868. https://doi.org/10.1016/j.cub.2009.09.063

Thomas, W. E., Vogel, V., & Sokurenko, E. (2008). Biophysics of catch bonds. In *Annual Review of Biophysics* (Vol. 37, pp. 399–416). Annu Rev Biophys. https://doi.org/10.1146/annurev.biophys.37.032807.125804

Thompson, S. L., Bakhoum, S. F., & Compton, D. A. (2010). Mechanisms of Chromosomal Instability. *Current Biology*, *20*(6), R285–R295. https://doi.org/10.1016/J.CUB.2010.01.034

Thompson, S. L., & Compton, D. A. (2008). Examining the link between chromosomal instability and aneuploidy in human cells. *Journal of Cell Biology*, *180*(4), 665–672. https://doi.org/10.1083/jcb.200712029

Thornton, B. R., & Toczyski, D. P. (2003). Securin and B-cyclin/CDK are the only essential targets of the APC. *Nature Cell Biology 2003 5:12*, *5*(12), 1090–1094. https://doi.org/10.1038/ncb1066

Tien, J. F., Umbreit, N. T., Gestaut, D. R., Franck, A. D., Cooper, J., Wordeman, L., Gonen, T., Asbury, C. L., & Davis, T. N. (2010). Cooperation of the Dam1 and Ndc80 kinetochore complexes enhances microtubule coupling and is regulated by aurora B. *Journal of Cell Biology*, *189*(4), 713–723. https://doi.org/10.1083/jcb.200910142

Tomson, B. N., Rahal, R., Reiser, V., Monje-Casas, F., Mekhail, K., Moazed, D., & Amon, A. (2009). Regulation of Spo12 phosphorylation and its essential role in the FEAR network. *Current Biology : CB*, *19*(6), 449–460. https://doi.org/10.1016/j.cub.2009.02.024

Ubersax, J. A., Woodbury, E. L., Quang, P. N., Paraz, M., Blethrow, J. D., Shah, K., Shokat, K. M., & Morgan, D. O. (2003). Targets of the cyclin-dependent kinase Cdk1. *Nature*, *425*(6960), 859–864. https://doi.org/10.1038/nature02062

Uhlmann, F., Lottspelch, F., & Nasmyth, K. (1999). Sister-chromatid separation at anaphase onset is promoted by cleavage of the cohesin subunit Scc1. *Nature 1999 400:6739*, *400*(6739), 37–42. https://doi.org/10.1038/21831

Uhlmann, F., Wernic, D., Poupart, M.-A., Koonin, E. V, & Nasmyth, K. (2000). Cleavage of Cohesin by the CD Clan Protease Separin Triggers Anaphase in Yeast. *Cell*, *103*(3), 375–386. https://doi.org/10.1016/S0092-8674(00)00130-6

Varga, V., Helenius, J., Tanaka, K., Hyman, A. A., Tanaka, T. U., & Howard, J. (2006). Yeast kinesin-8 depolymerizes microtubules in a length-dependent manner. *Nature Cell Biology 2006 8:9*, *8*(9), 957–962. https://doi.org/10.1038/ncb1462

Varga, V., Leduc, C., Bormuth, V., Diez, S., & Howard, J. (2009). Kinesin-8 Motors Act Cooperatively to Mediate Length-Dependent Microtubule Depolymerization. *Cell*, *138*(6), 1174–1183. https://doi.org/10.1016/J.CELL.2009.07.032

Varis, A., Salmela, A. L., & Kallio, M. J. (2006). Cenp-F (mitosin) is more than a mitotic marker. *Chromosoma*, *115*(4), 288–295. https://doi.org/10.1007/S00412-005-0046-0/TABLES/2

Verzijlbergen, K. F., Nerusheva, O. O., Kelly, D., Kerr, A., Clift, D., Alves, F. de L., Rappsilber, J., & Marston, A. L. (2014). Shugoshin biases chromosomes for biorientation through condensin recruitment to the pericentromere. *ELife*, *2014*(3). https://doi.org/10.7554/ELIFE.01374

Vinh, D. B. N., Kern, J. W., Hancock, W. O., Howard, J., & Davis, T. N. (2002). Reconstitution and characterization of budding yeast γ-Tubulin complex. *Molecular Biology of the Cell*, *13*(4), 1144–1157. https://doi.org/10.1091/MBC.02-01-0607/ASSET/IMAGES/LARGE/MK0421806009.JPEG

Visintin, R., Craig, K., Hwang, E. S., Prinz, S., Tyers, M., & Amon, A. (1998). The phosphatase Cdc14 triggers mitotic exit by reversal of Cdk-dependent phosphorylation. *Mol. Cell*, *2*, 709–718.

Visintin, R, Hwang, E. S., & Amon, A. (1999). Cfi1 prevents premature exit from mitosis by anchoring Cdc14 phosphatase in the nucleolus. *Nature*, *398*(6730), 818–823. https://doi.org/10.1038/19775

Visintin, Rosella, Prinz, S., & Amon, A. (1997). CDC20 and CDH1: A family of substrate-specific activators of APC- dependent proteolysis. *Science*, *278*(5337), 460–463. https://doi.org/10.1126/SCIENCE.278.5337.460/ASSET/6DD96828-2432-4C3E-B0CC-75A3CAF3522D/ASSETS/GRAPHIC/SE427586105A.JPEG

Wan, X., O'Quinn, R. P., Pierce, H. L., Joglekar, A. P., Gall, W. E., DeLuca, J. G., Carroll, C. W., Liu, S. T., Yen, T. J., McEwen, B. F., Stukenberg, P. T., Desai, A., & Salmon, E. D. (2009). Protein Architecture of the Human Kinetochore Microtubule Attachment Site. *Cell*, *137*(4), 672–684. https://doi.org/10.1016/j.cell.2009.03.035

Wang, H. W., & Nogales, E. (2005). Nucleotide-dependent bending flexibility of tubulin regulates microtubule assembly. *Nature 2005 435:7044*, *435*(7044), 911–915. https://doi.org/10.1038/nature03606

Wang, P. J., & Huffaker, T. C. (1997). Stu2p: A Microtubule-Binding Protein that Is an Essential Component of the Yeast Spindle Pole Body. *Journal of Cell Biology*, *139*(5), 1271–1280. https://doi.org/10.1083/JCB.139.5.1271

Wang, Y., Zhang, X., Zhang, H., Lu, Y., Huang, H., Dong, X., Chen, J., Dong, J., Yang, X., Hang, H., & Jiang, T. (2012). Coiled-coil networking shapes cell molecular machinery. *Molecular Biology of the Cell*, *23*(19), 3911–3922. https://doi.org/10.1091/mbc.E12-05-0396

Wäsch, R., & Cross, F. R. (2002). APC-dependent proteolysis of the mitotic cyclin Clb2 is essential for mitotic exit. *Nature 2002 418:6897*, *418*(6897), 556–562. https://doi.org/10.1038/nature00856

Weaver, B. A., & Cleveland, D. W. (2006). Does aneuploidy cause cancer? *Current Opinion in Cell Biology*, *18*(6), 658–667. https://doi.org/10.1016/J.CEB.2006.10.002

Wei, R. R., Al-Bassam, J., & Harrison, S. C. (2007). The Ndc80/HEC1 complex is a contact point for kinetochore-microtubule attachment. *Nature Structural and Molecular Biology*, *14*(1), 54–59. https://doi.org/10.1038/nsmb1186

Wei, R. R., Schnell, J. R., Larsen, N. A., Sorger, P. K., Chou, J. J., & Harrison, S. C. (2006). Structure of a Central Component of the Yeast Kinetochore: The Spc24p/Spc25p Globular Domain. *Structure*, *14*(6), 1003–1009. https://doi.org/10.1016/J.STR.2006.04.007

Weir, J. R., Faesen, A. C., Klare, K., Petrovic, A., Basilico, F., Fischböck, J., Pentakota, S., Keller, J., Pesenti, M. E., Pan, D., Vogt, D., Wohlgemuth, S., Herzog, F., & Musacchio, A. (2016). Insights from biochemical reconstitution into the architecture of human kinetochores. *Nature*, *537*(7619), 249–253. https://doi.org/10.1038/nature19333

Welburn, J. P. I., Grishchuk, E. L., Backer, C. B., Wilson-Kubalek, E. M., Yates, J. R., & Cheeseman, I. M. (2009). The Human Kinetochore Ska1 Complex Facilitates Microtubule Depolymerization-Coupled Motility. *Developmental Cell*, *16*(3), 374–385. https://doi.org/10.1016/j.devcel.2009.01.011

Wevrick, R., & Willard, H. F. (1989). Long-range organization of tandem arrays of α satellite DNA at the centromeres of human chromosomes: High-frequency array-length polymorphism and meiotic stability. *Proceedings of the National Academy of Sciences of the United States of America*, *86*(23), 9394–9398. https://doi.org/10.1073/pnas.86.23.9394

Willard, H. F. (1990). Centromeres of mammalian chromosomes. *Trends in Genetics*, *6*(C), 410–416. https://doi.org/10.1016/0168-9525(90)90302-M

Winey, M., & Bloom, K. (2012). Mitotic Spindle Form and Function. *Genetics*, *190*(4), 1197–1224. https://doi.org/10.1534/GENETICS.111.128710

Winey, M., Mamay, C. L., O'Toole, E. T., Mastronarde, D. N., Giddings, T. H., McDonald, K. L., & McIntosh, J. R. (1995). Three-dimensional ultrastructural analysis of the Saccharomyces cerevisiae mitotic spindle. *Journal of Cell Biology*, *129*(6), 1601–1615. https://doi.org/10.1083/jcb.129.6.1601

Winey, M., & O'Toole, E. T. (2001). The spindle cycle in budding yeast. *Nature Cell Biology 2001*

3:1, *3*(1), E23–E27. https://doi.org/10.1038/35050663

Wong, J., Nakajima, Y., Westermann, S., Shang, C., Kang, J.-S., Goodner, C., Houshmand, P., Fields, S., Chan, C. S. M., Drubin, D., Barnes, G., & Hazbun, T. (2007). A protein interaction map of the mitotic spindle. *Molecular Biology of the Cell*, *18*(10), 3800–3809. https://doi.org/10.1091/mbc.e07-06-0536

Woodbury, E. L., & Morgan, D. O. (2006). Cdk and APC activities limit the spindle-stabilizing function of Fin1 to anaphase. *Nature Cell Biology 2006 9:1*, *9*(1), 106–112. https://doi.org/10.1038/ncb1523

Wynne, D. J., & Funabiki, H. (2015). Kinetochore function is controlled by a phospho-dependent coexpansion of inner and outer components. *Journal of Cell Biology*, *210*(6), 899–916. https://doi.org/10.1083/JCB.201506020

Yamagishi, Y., Sakuno, T., Goto, Y., & Watanabe, Y. (2014). Kinetochore composition and its function: Lessons from yeasts. In *FEMS Microbiology Reviews* (Vol. 38, Issue 2, pp. 185–200). Oxford Academic. https://doi.org/10.1111/1574-6976.12049

Yamashita, A., Sato, M., Fujita, A., Yamamoto, M., & Toda, T. (2005). The Roles of Fission Yeast Ase1 in Mitotic Cell Division, Meiotic Nuclear Oscillation, and Cytokinesis Checkpoint Signaling. *Molecular Biology of the Cell*, *16*(3), 1378. https://doi.org/10.1091/MBC.E04-10-0859

Yan, K., Zhang, Z., Yang, J., McLaughlin, S. H., & Barford, D. (2018). Architecture of the CBF3-Centromere Complex of the Budding Yeast Kinetochore. *Nature Structural & Molecular Biology*, *25*(12), 1103. https://doi.org/10.1038/S41594-018-0154-1

Ye, P., Peyser, B. D., Pan, X., Boeke, J. D., Spencer, F. A., & Bader, J. S. (2005). Gene function prediction from congruent synthetic lethal interactions in yeast. *Molecular Systems Biology*, *1*, 2005.0026. https://doi.org/10.1038/msb4100034

Yin, H., You, L., Pasqualone, D., Kopski, K. M., & Huffaker, T. C. (2002). Stu1p Is Physically Associated with β-Tubulin and Is Required for Structural Integrity of the Mitotic Spindle. *Molecular Biology of the Cell*, *13*(6), 1881. https://doi.org/10.1091/MBC.01-09-0458

Yoon, D.-S., Wersto, R. P., Zhou, W., Chrest, F. J., Garrett, E. S., Kwon, T. K., & Gabrielson, E. (2002). Variable Levels of Chromosomal Instability and Mitotic Spindle Checkpoint Defects in Breast Cancer. *The American Journal of Pathology*, *161*(2), 391–397. https://doi.org/10.1016/S0002-9440(10)64194-6

Zachariae, W., Schwab, M., Nasmyth, K., & Seufert, W. (1998). Control of cyclin ubiquitination by CDK-regulated binding of Hct1 to the anaphase promoting complex. *Science*, *282*(5394), 1721–1724. https://doi.org/10.1126/SCIENCE.282.5394.1721/ASSET/8114C849-9E5D-40B7-8A69-0C59A3C9B55D/ASSETS/GRAPHIC/SE488704804A.JPEG

Zachariae, W., Shin, T. H., Galova, M., Obermaier, B., & Nasmyth, K. (1996). Identification of Subunits of the Anaphase-Promoting Complex of Saccharomyces cerevisiae. *Science*, *274*(5290), 1201–1204. https://doi.org/10.1126/SCIENCE.274.5290.1201

Zahm, J. A., Stewart, M. G., Carrier, J. S., Harrison, S. C., & Miller, M. P. (2021). Structural basis of stu2 recruitment to yeast kinetochores. *ELife*, *10*, 1–17. https://doi.org/10.7554/ELIFE.65389

Zeng, X., Kahana, J. A., Silver, P. A., Morphew, M. K., McIntosh, J. R., Fitch, I. T., Carbon, J., & Saunders, W. S. (1999). Slk19p is a centromere protein that functions to stabilize mitotic spindles. *The Journal of Cell Biology*, *146*(2), 415–425. http://www.ncbi.nlm.nih.gov/pubmed/10427094

Zhang, K., Lin, W., Latham, J. A., Riefler, G. M., Schumacher, J. M., Chan, C., Tatchell, K., Hawke, D. H., Kobayashi, R., & Dent, S. Y. R. (2005). The Set1 Methyltransferase Opposes Ipl1 Aurora Kinase Functions in Chromosome Segregation. *Cell*, *122*(5), 723–734. https://doi.org/10.1016/J.CELL.2005.06.021

Zhang, T., Lim, H. H., Cheng, C. S., & Surana, U. (2006). Deficiency of centromere-associated protein Slk19 causes premature nuclear migration and loss of centromeric elasticity. *Journal of Cell Science*, *119*(Pt 3), 519–531. https://doi.org/10.1242/jcs.02757

Zhu, C., Lau, E., Schwarzenbacher, R., Bossy-Wetzel, E., & Jiang, W. (2006). Spatiotemporal control of spindle midzone formation by PRC1 in human cells. *Proceedings of the National Academy of Sciences*, *103*(16), 6196–6201. https://doi.org/10.1073/PNAS.0506926103

Zhu, X., Chang, K. H., He, D., Mancini, M. A., Brinkley, W. R., & Lee, W. H. (1995). The C Terminus of Mitosin Is Essential for Its Nuclear Localization, Centromere/Kinetochore Targeting, and Dimerization *. *Journal of Biological Chemistry*, *270*(33), 19545–19550. https://doi.org/10.1074/JBC.270.33.19545

Zhu, Xueliang, Mancini, M. A., Chang, K.-H., Liu, C.-Y., Chen, C.-F., Shan, B., Jones, D., Yang-Feng, T. L., & Lee, W.-H. (1995). Characterization of a novel 350-kilodalton nuclear phosphoprotein that is specifically involved in mitotic-phase progression. *Molecular and Cellular Biology*, *15*(9), 5017–5029. https://doi.org/10.1128/MCB.15.9.5017

Zimniak, T., Stengl, K., Mechtler, K., & Westermann, S. (2009). Phosphoregulation of the budding yeast EB1 homologue Bim1p by Aurora/Ipl1p. *The Journal of Cell Biology*, *186*(3), 379. https://doi.org/10.1083/JCB.200901036

8 Acknowledgement

First and foremost, I want to thank PD Dr. Johannes Lechner for giving me the great opportunity to work on such an exciting subject for my thesis, for his support during the last years, his good advice, inspiration and supervision. I strongly appreciate the time he has invested in supporting this project, even after his retirement.

Also, I would like to thank Dr. Jennifer Ortiz for her support in the laboratory, her helpful advice and for the interesting daily discussions not only about science, but also about many other interesting subjects. Her enthusiasm for a wide range of topics was contagious and inspiring.

Many thanks also go to Marina Pelzl for her excellent technical assistance, her steady helpfulness and great cooperation and in the laboratory and for discussing results and numerous ideas. I also want to thank Britta Klem for her great technical assistance as well as Jürgen Reichert and Petra Ihrig for their support in mass spectrometry analyses.

I would like to thank all the other the colleagues at the Heidelberg University Biochemistry Center (BZH) who have supported me in many different ways and have contributed to the success of this work and who made the time at the BZH memorable.

I would also like to say a big thank you to my entire family. Particularly, I want to thank Dr. Derrick Norell and Dr. Laura Haag who always encouraged me and supported me by sharing their own experiences of their PhD time. My thanks also go to Nadine Norell who always cheered me up in difficult times by humorous conversations and culinary delicacies. Of course, I also want to mention Ruby here.

Especially, I want to thank my mother Iris Norell and my partner Matthias Riebl, who always supported me in any possible way, who had an open ear for all my topics, who felt with me in difficult times and celebrated my successes with me in good times. They gave me the courage and confidence I needed and without them this work would have not been possible. The conversations with my family gave me the incentive to see things from different and inspiring perspectives.

Moreover, I would also like to thank my friends who always believed in me and who always gave me motivation and encouragement.

Last but not least, I also want to thank Georg Maier, who supported me during the finalization of my thesis and for giving me the flexibility I needed to finish this work.